

ELECTROMAGNETIC FLOWMETERS
WITH LARGE ELECTRODES

by

YOUSIF A. H. AL-KHAZRAJI
B.Sc. (Baghdad), M.Sc. (Surrey - UK)

Thesis submitted for the degree of Doctor of
Philosophy in the Faculty of Engineering
of the University of London and for the
Diploma of Membership of the Imperial College

Department of Mechanical Engineering
Imperial College of Science & Technology
London, SW7 2BX

TO MY PARENTS

ABSTRACT

This work is concerned with the analysis of the electromagnetic flowmeter with large electrodes. The interest in this type of flowmeter stems from the fact that a flowmeter, so designed, may be less sensitive to flow profile distortion than ^a/point electrode flowmeter. It is, therefore, valuable to examine the extent to which such a design is indeed immune to profile distortion. Computer programs have been developed for the purpose of predicting the magnetic field, virtual current, weight function and flow signal. With the help of these programs, the effects of the velocity profile on the flowmeter sensitivity were also predicted.

A major drawback of the large electrode flowmeter is the effect of dirt on the electrodes. The normal assumption is that the contact resistance for the electrode is uniform. If, however, the electrodes become partially fouled, this assumption will no longer be justified and the response of the flowmeter will be modified. In this work, the possible size of error was examined for a particular flowmeter geometry.

A series of experiments were carried out on a commercial flowmeter, with point and large electrodes, to find the effect of distorted profile and dirt on the sensitivity and the quadrature signal of the flowmeter. Also, the flowmeter magnetic field, the virtual current and the distorted velocity profiles were measured.

A numerical method has been developed to optimize the weight function uniformity for a certain magnetic

field and for any rectilinear flow pattern. Also, another numerical approach was developed to optimize a flowmeter designed for three-dimensional flows. This flowmeter has a typical commercial magnetic field.

A design of contactless electrode flowmeter with an improved weight function was constructed and a series of tests were carried out on its performance.

ACKNOWLEDGEMENTS

The work in this thesis was carried out under the supervision of Dr. R. C. Baker. I wish to express my sincere gratitude to Dr. Baker for his guidance and constant encouragement during the preparation and completion of this project.

I am grateful to the Ministry of Oil and Minerals of the Government of the Republic of Iraq for the financial support which made this work possible.

I wish to acknowledge the valuable discussions I have had with Dr. J. Hemp and Mr. R. Al-Rabeh throughout this work.

I am grateful to the British Science Research Council for supporting this project and to Flowmetering Instruments Limited, Stroud, Gloucestershire, England for their help.

I wish to extend appreciation to the technical staff of the Thermal Power Section, especially Mr. W. Lamburn for his help in the construction of equipment and in the experiments, to Mr. R. D. Bloxham for his help in the electronic part of the work.

Finally, I would like to thank the staff of the Mechanical Engineering Department, especially Mr. P. Saunders of the Design Office, Miss D. Day, the Department Librarian Miss E. M. Archer, the Assistant Librarian Mrs. S. D. Boote and Mrs. H. A. Bastin for typing this thesis.

LIST OF CONTENTS

	<u>Page</u>
ABSTRACT	1
ACKNOWLEDGEMENTS	3
LIST OF CONTENTS	4
NOTATION	9
LIST OF FIGURES	12
 <u>CHAPTER 1</u>	
<u>INTRODUCTION</u>	20
1.1 General	20
1.2 Electromagnetic Flowmeter Elements	21
1.3 Basic Theory	22
1.4 Flowmeter Sensitivity	26
1.5 Literature Review	27
1.5.1 Early Investigations	27
1.5.2 Large Electrode Flowmeters	30
1.5.3 Contactless Electrode Flowmeters	34
1.5.4 Optimization of Flowmeter Performance	35
1.6 The Present Work	37
1.6.1 Objectives	37
1.6.2 Layout of This Thesis	38
 <u>CHAPTER 2</u>	
<u>THEORETICAL ANALYSIS OF LARGE ELECTRODE FLOWMETERS</u>	40
2.1 Magnetic Field Distribution	40
2.1.1 Type 1 Flowmeters	40
2.1.1.1 Analytical Solution	41
2.1.1.2 Numerical Solution	42
2.1.1.3 Comparison Between Analytical and Numerical Solutions	45

	<u>Page</u>
2.1.1.4 The Magnetic Field Distribution Inside Flow Tubes	45
2.1.2 Type 2 Flowmeters	46
2.1.3 Type 3 Flowmeters	47
2.2 Virtual Current	48
2.2.1 Numerical Solution	48
2.2.2 Analytical Solution	49
2.3 Weight Function	50
2.3.1 The Non-Uniformity of Weight Function	51
2.4 Flowmeter Sensitivity	51
2.5 Theoretical Analysis of Some Technical Problems	52
2.5.1 The Effect of Dirt on the Electrodes	53
2.5.2 The Effect of Dirt on the Quadrature Signal	53
2.6 Analysis of Some Other Applications	54
2.6.1 Commercial Point Electrode Flowmeters	54
2.7 Accuracy of the Numerical Solutions	55
2.8 Discussion	56
2.8.1 Flowmeter Insensitivity	56
2.8.2 Operating Problems	58
 <u>CHAPTER 3</u> <u>LARGE ELECTRODE FLOWMETER EXPERIMENTS</u>	 60
3.1 Description of the Rig	60
3.2 Magnetic Field Measurements	65
3.3 Velocity Profile Measurements	67
3.4 Test Flowmeter	69

	<u>Page</u>	
3.4.1	The Converter and its Calibration	70
3.4.2	The Induced Flow Signal	71
3.4.3	The Quadrature Signal	71
3.5	Accuracy and Errors	72
3.6	Discussion	78
 <u>CHAPTER 4</u>	<u>VIRTUAL CURRENT EXPERIMENTS</u>	 81
4.1	Description of the Virtual Current Rig	81
4.2	Virtual Current Measurements	85
4.3	Accuracy and Errors	88
4.4	Results and Discussion	94
 <u>CHAPTER 5</u>	<u>OPTIMIZATION</u>	 96
5.1	Introduction	96
5.2	Superposition Method	96
5.2.1	Virtual Potential	96
5.2.2	Weight Function	99
5.3	Integrated Voltage Flowmeter for Rectilinear Flows	100
5.4	Optimization Method for Flowmeters Designed for Rectilinear Flows	102
5.5	Performance Measure in Three Dimensions	107
5.6	Ideal (Integrated Voltage) Flowmeter with a Uniform Magnetic Field	108
5.7	Integrated Voltage Flowmeter for Three- Dimensional Flows	110
5.8	Optimization Method for Flowmeters Designed for Three-Dimensional Flows	111
5.9	Conclusions and Discussion	116

	<u>Page</u>
<u>CHAPTER 6</u>	
<u>DESIGN OF CONTACTLESS ELECTRODE</u>	
<u>FLOWMETER WITH AN IMPROVED WEIGHT</u>	119
<u>FUNCTION</u>	
6.1 A Flowmeter Design Based on the Optimization Method	119
6.2 Contactless Electrodes	120
6.3 Some Considerations for the Optimized Flowmeter	122
6.3.1 Insulating Material Choice	122
6.3.2 Some Considerations for the Contactless Flowmeter	123
6.3.3 Choice of the Amplifier	124
6.3.4 The Capacitive Effect on the Phase of the Flow Signal	126
6.4 The Construction of the Optimized Flowmeter	128
6.4.1 Design of the Casting Mould	128
6.4.2 Casting Procedure	129
6.5 The Assembly of the Optimized Flowmeter	132
6.6 Accuracy and Errors	133
<u>CHAPTER 7</u>	<u>OPTIMIZED FLOWMETER EXPERIMENTS</u>
7.1 Introduction	136
7.2 Flowmeter Linearity	137
7.3 Zero Drift and Repeatability	137
7.4 Effect of Distorted Profiles	138
7.5 Effect of Dirt	138
7.6 Conclusions and Discussion	140
<u>CHAPTER 8</u>	<u>CONCLUSIONS AND FURTHER WORK</u>
8.1 Conclusions	142

	<u>Page</u>
8.2 Further Work	144
REFERENCES	146
TABLES	151
FIGURES	167
APPENDIX A	271
APPENDIX B	279
APPENDIX C	286
APPENDIX D	287
PUBLICATIONS	289

NOTATION

<u>A</u>	Flowmeter cross-sectional area.
<u>B</u>	Magnetic field vector.
<u>B_i</u>	Flow-induced magnetic field vector.
<u>c_{nm}</u>	Coefficients in Fourier series.
<u>C</u>	Capacitance given in Fig. 6.5.
<u>D</u>	Pipe diameter.
<u>D</u>	Displacement current vector.
<u>E</u>	Root mean square deviation of the weight function divided by \bar{W}_m .
<u>E</u>	Electric field vector.
<u>E_i</u>	Irrational electric field vector.
<u>E_s</u>	Solenoidal electric field vector.
(E _γ and E _G)	Error term incurred in approximating the second order partial derivatives.
<u>f</u>	Frequency.
<u>g'(z)</u>	Virtual current (J_v).
<u>G</u>	Virtual potential.
<u>h</u>	Grid size, pressure difference.
<u>i</u>	Current in the circuit given in Fig. 6.5.
<u>I</u>	Total current in the coil, current in the circuit given in Fig. 6.4.
<u>j</u>	Current density vector.
<u>J_v</u>	Virtual current vector.
<u>k</u>	Total number of test points, product of several correction factors.
<u>l</u>	Typical length.
<u>L</u>	Distance between two electrodes.

(L_1, L_2, L_3)	Distances given in Fig. 2.1.
m	Number of the artificial electrodes.
n	Number of the electrodes.
p	Ratio of electrode length to pipe diameter.
Q	Volume flow rate.
r	Co-ordinate radius.
R	Radius of flowmeter, resistance given in Fig. 6.5.
R_{eff}	Effective shunt resistance.
S	Sensitivity.
U	Electric potential.
U_{EE}	Potential difference induced between two electrodes.
\underline{v}	Velocity vector.
V	Volume.
V_m	Mean fluid velocity.
V_1, V_2	Voltages given in Fig. 6.5.
V_e	Signal detected by the electrode.
V_f	Flow signal.
\underline{w}	Weight vector.
\bar{w}	Asymmetric rectilinear profile weight function.
\bar{w}'	Axisymmetric rectilinear profile weight function.
\bar{w}_c	Weight function in the centre.
\bar{w}_m	Mean weight function over the cross-sectional area.
x_1	Half the axial length of the core given in Fig. 2.1.
(x, y, z)	Cartesian co-ordinate.
z	Complex number $(x + iy)$.
Z_f	Impedance between the fluid and the large electrode.
Z_s	Impedance between the large electrode and the earth.

Greek symbols

α	Coefficient for adjusting the virtual potentials, angle of large electrode given in Fig. 2.17.
β	Coefficient for adjusting the $\nabla\phi$, angle of large electrode given in Fig. 2.17.
γ	Magnetic potential, angle of large electrode given in Fig. 2.17.
δ	Angle of large electrode given in Fig. 2.17.
ϵ	Fluid permittivity, weight function non-uniformity.
θ	Polar co-ordinate.
μ	Permeability.
ρ	Density.
σ	Fluid conductivity.
τ	Element of volume.
ϕ	Harmonic potential.
ψ	Performance measure in a three-dimensional flow.
ω	Angular velocity = $2\pi f$.

LIST OF FIGURES

- Fig. 1.1 Components of an industrial flowmeter
- Fig. 1.2 Conventional point-electrode flowmeter
- Fig. 1.3 Large electrode flowmeter
- Fig. 1.4 Bevir's ideal flowmeter
- Fig. 2.1 Flowmeter Type 1
- Fig. 2.2 Cross-section of Type 1 flowmeter
- Fig. 2.3 Boundary conditions for γ (Type 1 flowmeter - analytical solution)
- Fig. 2.4 Finite-difference mesh (cartesian-notation)
- Fig. 2.5 Boundary conditions for γ (Type 1 flowmeter - numerical solution)
- Fig. 2.6 Comparison between analytical and numerical models of the magnetic field for Type 1 flowmeter
 - (a) $x = 0$
 - (b) $x = R$
 - (c) $x = 2R$
- Fig. 2.7 Finite-difference mesh (cylindrical-notation)
- Fig. 2.8 Comparison of experimental values of magnetic field with computed values (Type 1 flowmeter)
 - (a) $r = 0.8 R$
 - (b) θ -component, $r = 0.8 R$, $\theta = 54^\circ$
 - (c) r -component, $r = 0.8 R$, $\theta = 54^\circ$
 - (d) θ -component, $z = 0$, $\theta = 54^\circ$
 - (e) r -component, $z = 0$, $\theta = 54^\circ$
- Fig. 2.9 Flowmeter Type 2

- Fig. 2.10 Notation for the magnetic field of a finite length wire
- Fig. 2.11 Three-dimensional solution for the magnetic field (Type 2 flowmeter)
 - (a) r-component, $r = 0.8 R$
 - (b) θ -component, $r = 0.8 R$
 - (c) r-component, $z = 0.14 R$
 - (d) θ -component, $z = 0.14 R$
- Fig. 2.12 Two-dimensional solution for the magnetic field (Type 2 flowmeter)
 - (a) r-component
 - (b) θ -component
- Fig. 2.13 Flowmeter Type 3
- Fig. 2.14 Three-dimensional solution for the magnetic field (Type 3 flowmeter)
 - (a) r-component, $z = 0$
 - (b) θ -component, $z = 0$
 - (c) r-component, $r = 0.8 R$
 - (d) θ -component, $r = 0.8 R$
- Fig. 2.15 Diagram to indicate the boundary conditions for virtual potential G (large electrode - numerical solution)
- Fig. 2.16 Three-dimensional solution for the virtual potential
 - (a) $z = 0$
 - (b) $r = 0.93 R$
- Fig. 2.17 Conducting regions of electrodes for two-dimensional virtual current calculations
- Fig. 2.18 Weight function distribution for Type 1 flowmeter
(weight function in the centre $w_c = 0.378$)

- Fig. 2.19 Weight function distribution for Type 2 flowmeter ($w_c = 0.12$)
- Fig. 2.20 Weight function distribution for Type 3 flowmeter ($w_c = 0.394$)
- Fig. 2.21 Weight function distribution for Type 1 flowmeter with moderate fouling ($w_c = 0.542$)
- Fig. 2.22 Weight function distribution for Type 2 flowmeter with moderate fouling ($w_c = 0.15$)
- Fig. 2.23 Weight function distribution for Type 1 flowmeter with extreme fouling ($w_c = 0.41$)
- Fig. 2.24 Weight function distribution for Type 1 flowmeter with point electrode ($w_c = 0.056$)
- Fig. 3.1 Diagram of 100 mm ID flow rig
- Fig. 3.2 Photograph of 100 mm ID flow rig (weigh tank system)
- Fig. 3.3 Photograph of 100 mm ID flowmeter and instrumentation
- Fig. 3.4 Linearity of the reference flowmeter
- Fig. 3.5 The orifice plate arrangement
- Fig. 3.6 The weighing system assembly
- Fig. 3.7 Flow diverter valve assembly
- Fig. 3.8a The circuit of the electronic timer
- Fig. 3.8b The probe assembly for measuring the magnetic field
- Fig. 3.9 Comparison between AC and DC test values of the magnetic field for Type 1 flowmeter
- Fig. 3.10 Diagram of distortion discs

- Fig. 3.11 Traverse-Pitot tube assembly
- Fig. 3.12 Traverse-Pitot tube assembly
- Fig. 3.13 Undisturbed flow profile
- Fig. 3.14 Flow profile with concentric distortion disc
- Fig. 3.15 Flow profile with eccentric distortion disc
- Fig. 3.16 Calibration graph of the series 400 converter
- Fig. 3.17 The weighing machine linearity
- Fig. 3.18 Result of diverter adjustment tests
-
- Fig. 4.1 Photograph of the virtual current tank and associated electrics
- Fig. 4.2 Logic circuit for stepping motor controller
- Fig. 4.3 Comparison of experimental values of virtual potential with computed values (point-electrodes flowmeter)
- (a) $z = 0.38 R, r = 0.6 R$
 - (b) $r = 0.7 R, \theta = 72^\circ$
 - (c) $z = 0.38 R, r = 0.87 R$
 - (d) $z = 0, r = 0.73 R$
 - (e) $z = 0.38 R, \theta = 36^\circ$
 - (f) $z = 0, \theta = 0$
 - ..
 - (g) $r = 0.87 R, \theta = 0$
 - (h) $z = 0, r = 0.87 R$
- Fig. 4.4 Comparison of experimental values of virtual potential with computed values (large-electrodes flowmeter)
- (a) $z = 1.15 R, r = 0.87 R$
 - (b) $z = 1.15 R, r = 0.6 R$

- (c) $z = 0, r = 0.73 R$
- (d) $z = 1.15R, \theta = 36^\circ$
- (e) $z = 0, \theta = 0$
- (f) $r = 0.87 R, \theta = 0$
- (g) $z = 0, r = 0.87 R$

Fig. 4.5

Comparison of experimental values of virtual current with theoretical values (large-electrode flowmeter with moderate fouling)

- (a) r -component, $r = 0.62 R$
- (b) r -component, $r = 0.9 R$
- (c) θ -component, $r = 0.57 R$
- (d) θ -component, $r = 0.86 R$

Fig. 4.6

Comparison of experimental values of virtual potential with computed values (segmental electrodes flowmeter)

- (a) $z = 0, r = 0.87 R$
- (b) $z = 1.15 R, r = 0.87 R$
- (c) $z = 1.15 R, r = 0.6 R$
- (d) $z = 0, r = 0.73 R$
- (e) $z = 1.15 R, \theta = 36^\circ$
- (f) $z = 0, \theta = 0$
- (g) $r = 0.87 R, \theta = 0$

Fig. 5.1

Notation for the superposition method

Fig. 5.2

Virtual potential variation with angle for

$z = 0$ to show validity of superimposed solution

Fig. 5.3

Virtual potential variation with radius for

$z = 0$ to show validity of superimposed solution

- Fig. 5.4 Virtual potential variation with angle for
 $z = 1.15 R$ to show validity of superimposed
solution
- Fig. 5.5 Virtual potential variation with radius for
 $z = 1.15 R$ to show validity of superimposed
solution
- Fig. 5.6 Flowmeter tube showing the sets of electrodes
- Fig. 5.7a The effect of electrode length along the axis
on the weight function uniformity of the
optimized-Type 1 flowmeter
- Fig. 5.7b The effect of electrode length along the axis
on the weight function uniformity of the
optimized-Type 2 flowmeter
- Fig. 5.8 The swirl loops for testing the performance
of the flowmeter
- Fig. 5.9 Converting an ideal-rectangular flowmeter
into a circular one
- Fig. 5.10 The notation of a uniform magnetic field
- Fig. 5.11 Streamlines of weight function for an ideal
flowmeter
- Fig. 5.12 The boundary conditions for solving the
virtual potential of the artificial electrodes
- Fig. 5.13 The effect of the fixed β 's number on ψ
(optimized-flowmeter designed for three-
dimensional flow)
- Fig. 6.1 Optimized flowmeter with the strip electrodes
- Fig. 6.2 Optimized flowmeter with different insulating
wall thickness (different capacitance)

- Fig. 6.3 The inner and outer insulating walls of the optimized flowmeter
- Fig. 6.4 The flowmeter circuit showing the internal and loss impedance
- Fig. 6.5 Voltage follower circuit
- Fig. 6.6 The equivalent circuit of the contactless flowmeter
- Fig. 6.7 Mould of casting and constructing of contactless flowmeter electrode section
- Fig. 6.8 The casting mould assembly
- Fig. 6.9 Cast Araldite with the circular core
- Fig. 6.10 The resulting cast Araldite
- Fig. 6.11 Bare-flow tube for fabricating the optimized flowmeter
- Fig. 6.12 Construction of optimized-contactless flowmeter
- Fig. 6.13 Stage of fixing coils and yoke for the optimized-contactless flowmeter
- Fig. 7.1 Optimized-contactless flowmeter in 100 mm ID flow rig
- Fig. 7.2 Optimized-contactless flowmeter and instrumentation
- Fig. 7.3 Linearity of optimized-contactless flowmeter (converter-scale 1)
- Fig. 7.4 Linearity of optimized-contactless flowmeter (converter-scale 2)
- Fig. 7.5 Graph showing the repeatability of the optimized-contactless flowmeter

- Fig. C.1 Weight function distribution for Type 1 flowmeter (with point electrodes) when a quarter of the flow tube is empty ($w_c = 0.031$)
- Fig. C.2 Weight function distribution for Type 1 flowmeter (with point electrodes) when half the flow tube is full ($w_c = 0.056$)
- Fig. D.1 The large flowmeter assembly
- Fig. D.2 Notation for the mesh given in Appendix D
- Fig. D.3a Three-dimensional solution for the magnetic field - radial component (large flowmeter)
- Fig. D.3b Three-dimensional solution for the magnetic field - circumferential component (large flowmeter)
- Fig. D.4 Weight function distribution for the large flowmeter with point electrodes ($w_c = 0.074$)

CHAPTER 1
INTRODUCTION

1.1 General

When a conducting fluid flows through a magnetic field, a motion induced voltage is generated, the value of which is a function of the fluid flow rate. This fact was established by Faraday⁽¹⁸⁾ in 1832. The electromagnetic flowmeters are devices exploiting this principle.

The first and most important advantage of the electromagnetic flowmeter is that the output signal of these devices can, in principle at least, be made linearly proportional to the liquid flow rate. The conductivity variations of the metering fluid do not affect the measurement accuracy, provided the conductivity remains uniform and above a certain minimum value. The conductivity of distilled water represents this limit at the moment. It is also claimed by some of the manufacturers (see, for example, Flowmetering Instruments Ltd.⁽²¹⁾, Schlumberger⁽⁴⁰⁾ and Fischer and Porter⁽¹⁹⁾) of these devices that changes in the density, viscosity, pressure or temperature of the liquid have a negligible effect on the flowmeter performance. The electromagnetic flowmeter is also obstructionless and has no moving parts which facilitates the metering of difficult types of liquid, such as corrosive liquids, slurries, viscous materials and aseptic products. The pressure loss in the meter is very small and it is not more than an equivalent length of the same pipe.

The main disadvantage of the electromagnetic flow-

meter is its sensitivity to changes in the velocity profiles. Also, this type of flowmeter cannot handle gases and it is relatively expensive if compared to more conventional flowmeter types (e.g. orifice plates). In this thesis, attention is confined to flowmeters designed for low conductivity fluids and we do not consider those for liquid metals.

1.2 The Electromagnetic Flowmeter Elements

A typical industrial electromagnetic flowmeter for low conductivity fluids (see Fig. 1.1) is a combination of two main elements.

A. The Primary Element

This consists of the following:-

1. Metering Tube. This is often made of a non-magnetic material, usually stainless steel, to allow the magnetic field to penetrate through it.

2. Lining of the metering tube. This is manufactured from a non-conducting material to prevent signal shorting.

3. Coils. These are usually excited by an alternating current to produce an AC magnetic field. However, in some designs a pulsed excitation is used instead. The coil is sometimes surrounded with a steel yoke in order to strengthen the field inside the flow tube. In this case, it is laminated to reduce eddy currents.

4. Electrodes. The task of the electrodes is to pick up the induced signal. Because they are in contact with the fluid, their material must be carefully chosen. For a non-agressive liquid, usually a stainless steel material is used, and for an agressive one, some other material is used, such as platinum-iridium, titanium, etc.

5. Current transformer. This is used to produce a reference current proportional to the applied magnetic field.

6. Flanges. These are on the ends of the metering tube, and they are used to connect the meter with the pipe circuit.

B. The Secondary Element

This is usually known as the "converter". It rejects the unwanted signal (the quadrature) and amplifies the flow signal. The final output is given as a ratio of the flow signal to the coil current.

1.3 Basic Theory

The general theory of the electromagnetic flowmeter can be found in Shercliff's book⁽⁴³⁾. He has discussed several assumptions which simplify the governing equations. The "skin effect parameter" is assumed large in this work. This is defined as $(\mu\sigma\omega)^{-1/2}$, where μ is the permeability, σ is the fluid conductivity and ω is the frequency of the alternating magnetic field. The "magnetic Reynolds number" is also assumed small. It is given by $(\mu\sigma\omega l)$ where l is a

typical length and v is a typical velocity. Finally, the "dielectric relaxation number" is assumed small. This is defined as $(\omega\epsilon/\sigma)$, where ϵ is the absolute permittivity of the fluid.

Thus, if the skin effect parameter is large compared with a representative length scale of the flowmeter (for example, pipe diameter), and if the "magnetic Reynolds number" is much smaller than unity, then the inductance effects due to the AC applied magnetic field and to the fluid flow may be neglected when computing the distribution of the applied magnetic field and hence we may write for the applied magnetic field \underline{B} within the fluid:-

$$\nabla \times \underline{B} = 0 \quad (1.1)$$

$$\text{In addition, } \nabla \cdot \underline{B} = 0 \quad \text{always} \quad (1.2)$$

Also, if the "dielectric relaxation number" is much smaller than unity, the displacement current \underline{D} can be neglected, in comparison with the conducting current \underline{j} and thus Maxwell's equation gives:-

$$\nabla \times \underline{B}_i = \mu \underline{j}$$

where \underline{B}_i is the flow induced magnetic field. Consequently:-

$$\nabla \cdot \underline{j} = 0 \quad (1.3)$$

The value of the above parameters are calculated for a typical case below. If the flowmeter tube diameter is about 0.1 m, working at a frequency of 50 Hz and the metered fluid

is water ($\sigma \approx 10^{-2}$ mho/m, $\mu = 4\pi \times 10^{-7}$ tesla.m/Amp and $\epsilon_r = 80$)*, then the "skin effect parameter" is equal to 500 meters, the "magnetic Reynolds number" is 2×10^{-9} and the "dielectric relaxation number" is equal to 2.2×10^{-5} .

Ohm's law is given by:-

$$\underline{j} = \sigma (\underline{E} + \underline{v} \times \underline{B}) \quad (1.4)$$

where \underline{E} is the electric field defined by:-

$$\underline{E} = \underline{E}_i + \underline{E}_s \quad (1.5)$$

where \underline{E}_i is an irrotational electric field and \underline{E}_s is a solenoidal electric field (Shercliff⁽⁴⁴⁾), where:-

$$\nabla \cdot \underline{E}_s = 0 \quad (1.6)$$

and:-

$$\nabla \times \underline{E}_i = 0 \quad (1.7)$$

Therefore:-

$$\underline{E}_i = - \nabla U \quad (1.8)$$

where U is a scalar potential. Hence, the flowmeter formula is deduced (provided that σ is constant) from the above equations as shown below:-

* ϵ_r is the relative permittivity

$$-\nabla \cdot \underline{E} = \nabla \cdot (\underline{v} \times \underline{B}) \quad (1.9)$$

$$\nabla^2 U = \nabla \cdot (\underline{v} \times \underline{B}) \quad (1.10)$$

This can be simplified with the use of Equation (1.1) to:-

$$\nabla^2 U = \underline{B} \cdot (\nabla \times \underline{v}) \quad (1.11)$$

Bevir⁽⁸⁾ introduced the "virtual current" (\underline{J}_v) concept, which is defined as a current density set-up when a unit current is passed between the electrodes. He used the flowmeter Equation (1.10) to derive the following flowmeter signal (ΔU) in terms of \underline{v} , \underline{B} and \underline{J}_v :-

$$\Delta U = \int_V (\underline{v} \times \underline{B}) \cdot \underline{J}_v d\tau \quad (1.12)$$

where V is the flowmeter volume and τ is an element of volume. This equation may be written as:-

$$\Delta U = \int_V \underline{v} \cdot \underline{W} d\tau \quad (1.13)$$

where:-

$$\underline{W} = \underline{B} \times \underline{J}_v \quad (1.14)$$

\underline{W} represents the weight vector which is an extension of Shercliff's scalar weight function.

Bevir⁽⁸⁾ also showed that a necessary and sufficient condition for a flowmeter to be ideal (in which the flowmeter signal is independent of the velocity profile) is given by:-

$$\nabla \times \underline{W} = 0 \quad (1.15)$$

He showed that a flowmeter with point electrodes cannot be ideal due to the appearance of the virtual current singularity near to the electrode for which no magnetic field can satisfy Equation (1.15).

Bevir⁽⁹⁾ defined the asymmetric weight function by:-

$$\bar{W}(r, \theta) = \int_{-\infty}^{+\infty} w_z \, dz$$

and the axisymmetric weight function by:-

$$\bar{w}'(r) = \frac{1}{2\pi} \int_0^{2\pi} \bar{W}(r, \theta) \, d\theta$$

The first formula is used for asymmetric rectilinear profiles, and includes the second formula which is used only for axisymmetric profiles.

1.4 Flowmeter Sensitivity

The term sensitivity (S) is a measure of the performance of the induction flowmeter. Shercliff defined it as:-

$$S = \frac{\Delta U_{EE}}{BV_m L} \quad (1.16)$$

where ΔU_{EE} is the potential difference induced between two electrodes with a distance L apart, V_m is the mean fluid velocity and B is a representative value of the imposed magnetic field.

Bevir⁽⁹⁾ defined the flowmeter sensitivity, for parabolic and flat velocity profiles, by the following equation:-

$$S = \frac{\int_0^R \bar{w}'(r) v(r) r dr}{\int_0^R v(r) r dr} \quad (1.17)$$

in which the sensitivity has the same dimensions as that of \bar{w}' . This weight function is defined per unit μI (where I is the total current in the coil) and consequently, its dimensions are m^{-2} .

1.5 Literature Review

1.5.1 Early Investigations

Faraday⁽¹⁸⁾ in 1832, discussed the theory of the induction of electric currents in a moving conductor when it crosses a magnetic field. He tried to measure the induced voltages due to the flow of the River Thames through the earth's magnetic field by suspending two electrodes from wires hung from Waterloo Bridge. He was not able to obtain

results because much of the signal was short-circuited in the river bed and all he was able to get were spurious signals due to electrochemical and thermoelectric effects (Ref. 43).

The first instrument to approach a simple type of electromagnetic flowmeter was constructed by Williams⁽⁴⁹⁾ in 1930 out of academic interest. His apparatus consisted of a non-conducting circular tube under a uniform transverse magnetic field. The metered liquid was copper sulphate. He measured the induced voltage between two point electrodes placed diametrically opposite each other and found it to be proportional to the flow rate.

In 1936, Kolin⁽²⁸⁾ used the induction flowmeter to measure blood flow in blood vessels. In 1937, he developed his meter further to measure the flow of the blood without injury to the vessel (Kolin⁽²⁹⁾). In addition, Kolin⁽³⁰⁾ in 1941 employed an alternating magnetic field. This eliminates the polarization problem, but it introduces the difficulty of eliminating the unwanted AC signal. He managed to cancel the undesired voltage by the use of a compensating circuit.

Many workers analysed and discussed the various factors effecting the sensitivity of the electromagnetic flowmeter. Dennis and Wyatt⁽¹⁷⁾ tested the effect on the flowmeter sensitivity of haematocrit in the blood which makes the conductivity anisotropic. They found that the sensitivity decreased with the increasing haematocrit value for laminar and turbulent flows. The effects of the non-uniform conductivity of the fluid in the flowmeter were

also studied by Baker⁽⁵⁾ and Bevir⁽¹⁰⁾.

The principles of the electromagnetic flowmeter are applicable to the measurement of the flow of liquid metals and dielectric fluids (see, for example, Baker⁽⁷⁾, Cushing⁽¹⁶⁾ and Al-Rabeh et al⁽¹⁾). These applications are not discussed here. However, some of the theory and practice is inevitably common to both and is discussed here.

Baker⁽⁴⁾ was the first to solve the flowmeter equation in two dimensions for axisymmetric velocity profiles and general two-dimensional magnetic fields. His results give the potential distribution at any point inside the flow tube of the flowmeter (including the internal surface of the tube wall). Bevir, impressed by the elegance of the formula, attempted without success to generalize it to three-dimensions.

One piece of work relevant to this thesis is the numerical solution of the flowmeter equation by Baker⁽⁶⁾ using the finite-difference method. This allowed flexibility for complicated flow profile, pipe geometry or fluid properties. But the accuracy of numerical methods is generally less than analytical ones, because of the lattice spacing and the number of lattice points which are limited by the computer storage and by the form of the lattice described. The magnetic field considered in Ref. 6 was produced by laying coils in slots made on the flow tube wall which was of a high permeability magnetic material. The magnetic field B is given as:-

$$\underline{B} = \nabla \gamma$$

$$(1.18)$$

Then:-

$$\nabla^2 \gamma = 0 \quad (1.19)$$

where γ is the magnetic scalar potential. The value of γ was set to ± 1 on the pole pieces and zero elsewhere on the wall. The finite-difference method is used in three dimensions to solve the Laplace equation for the magnetic field (Equation (1.19)), and to solve the Poisson equation for the electric potential (Equation (1.11)). The value of the induced voltage (U) at the electrodes is obtained by extrapolation. Baker used this method to analyse the effect of a short magnetic field, a short insulating liner and an asymmetric rectilinear flow. His method is more convenient for the case when the velocity profile is axisymmetric, since only one-eighth of the flowmeter volume had to be solved. In the case of rectilinear asymmetric flow pattern, the Poisson equation has to be solved for a quarter or a half of the flowmeter volume. For a three-dimensional flow pattern, the Poisson equation has to be solved for the whole flowmeter volume. This results in a large increase in computing time and storage.

1.5.2 Large Electrode Electromagnetic Flowmeters

The most common kind of electromagnetic flowmeter is the point electrode type (Fig. (1.2)). This flowmeter is now produced commercially in large quantities and with a remarkable accuracy if certain conditions prevail. The problem with these flowmeters is their high sensitivity to

changes in the velocity profile. This sensitivity can be reduced by careful design. However, as shown in Bevir⁽⁸⁾, these flowmeters can never be made ideal for a general velocity profile. On the other hand, it is possible (in theory at least) to make a large electrode flowmeter ideal. The attraction of using large electrodes is thus apparent. Fig. (1.3) shows a flowmeter with large electrodes.

Smith⁽⁴⁷⁾ devised a method to derive the weight function for a circular and rectangular channel flowmeter. He assumed a positive unit charge at one electrode and a negative unit charge on the other instead of unity current source as in Bevir's analysis. Only the uniform magnetic field case was treated by Smith. He did not discuss the effect on the weight function distribution of electrode fouling.

The work of Bevir covered some analytical treatment of large electrode flowmeters. He found one class of flowmeters that satisfy the condition (1.15). These flowmeters consist of a rectangular channel, a uniform magnetic field and have in the field direction a constant width and invariant electrode shape. The electrode width is not restricted, it could be very narrow (transverse line electrodes) or large. Fig. (1.4) shows such an ideal flowmeter.

Due to mathematical difficulties, large electrode flowmeters of circular geometry have been analysed only in two dimensions. Most of the work on this subject is given by Bevir⁽⁹⁾. He found that the long flowmeter of constant sensitivity with an axisymmetric flow pattern requires

either a uniform magnetic field or a uniform virtual current. If the profile is not specified, it needs both. Bevir showed that the large electrode arrangement suffers a smaller variation in the sensitivity than the point electrode arrangement, due to the fact that large electrodes produce a more uniform virtual current. His two-dimensional theory also predicts that transverse line electrodes produce even more uniform weight functions than large electrodes and weaker singularities on the edges. Transverse line electrodes subtending an angle of 133° are shown to produce the best weight function distribution with a uniform magnetic field. Bevir gave the weight function distribution for various electrode shapes for both uniform and matching magnetic fields (the matching field is a mathematical term which is defined to be proportional to the reciprocal of the virtual current).

The main problem of large electrodes (including transverse line electrodes), is the contamination, which causes the contact resistance* between the electrode surface and the metering fluid to vary considerably resulting in a great change in the virtual current distribution. Bevir's analysis was concerned mainly with the case of symmetric electrode assemblies and did not analyse the case of the non-symmetric electrodes in order to estimate the effect on the distribution of the weight function of electrode fouling.

Arnold⁽²⁾ designed and built an electromagnetic flowmeter with large electrodes, a rectangular flow channel and uniform magnetic field. He claimed that its sensitivity was independent of the velocity profile, but he

* resistance is used as a general term covering impedance.

did not comment on the effect of the electrode contamination on the flowmeter sensitivity.

Wyatt⁽⁵¹⁾ constructed and tested a transverse line electrode flowmeter. He obtained a variation in the sensitivity of about 2% when using a concentrated jet of flow placed at different positions in the flowmeter. He also observed the effect of the large electrode fouling on the flowmeter performance. This he did by repeating the flow jet experiment half an hour after the flowmeter had been dried and then refilled with saline. He also noticed that the effect was reduced considerably if the flowmeter was washed with a detergent surfactant before refilling with saline.

One commercial concern (Schlumberger of France⁽³⁷⁾) is now marketing electromagnetic flowmeters with large electrodes. They claim that the total accuracy of this flowmeter is about 2% of the full scale and no straight lengths are needed before the flowmeter. To overcome the problems of electrode fouling, they provided their flowmeter with an "electrode cleaning system" (see Ref. 38). This is used periodically to remove the deposits from the surface of the electrodes. The cleaning is performed by passing a DC current of high density between the two electrodes to produce an electrolytic cleaning process. This current is reversed at a suitable low frequency to clean both of the electrodes. During the cleaning process, the flow signal cannot be recorded. This is one of the drawbacks of this system. In a patent held by Schlumberger⁽³⁹⁾, it is stated that it is preferable to use a number of small surface area

electrodes. These electrodes are suitably arranged so as to make the total surface area correspond to that of large electrodes and they are designed for easy removal.

1.5.3 Electromagnetic Flowmeters with Contactless Electrodes

The problems of electrode corrosion and deposits in electromagnetic flowmeters might be overcome by using contactless electrodes. This allows the induced flow signal to be picked up across the coupling capacity between the electrodes and the metered fluid. The difficulty arising from this technique is that the resulting flowmeter input impedance is very high which makes the measurement of the flow signal difficult and makes the use of an extremely high input impedance amplifier necessary.

The electromagnetic flowmeter with contactless electrodes has also been produced commercially by Fischer and Porter⁽²⁰⁾ and by Krohne⁽²⁷⁾. Fischer and Porter run their flowmeter on a low frequency (50 and 60 Hz) and claim that the total accuracy of their flowmeter is about 1% of the flow rate for flow velocity between 1 and 10 m/sec. They also claim that this flowmeter handles fluids with a resistivity up to 0.2 MΩ-m. Different tube materials have been used to line these flowmeters such as hard rubber, soft rubber and epoxy resin and PTFE for different applications. No specifications about the shape and the dimensions of the contactless electrode nor the magnetic field coil are given in their catalogue.

Hofmann⁽²⁷⁾ has designed and built an electro-

magnetic flowmeter with capacitive signal pick-off. He claimed that his flowmeter was capable of handling liquids with a minimum electrical conductivity of 4 $\mu\text{mhos}/\text{m}$. Hofmann's electrodes are circular in shape and relatively large in size and they are covered by the tube liner (Teflon). In addition to the technical problems which he described, the flowmeter sensitivity is still affected by the shape of the flow pattern.

1.5.4 Optimization of Flowmeter Performance

Many workers have tried with some success to design an electromagnetic flowmeter in which the sensitivity is less affected by the changes in the shape of the velocity profile using different techniques. Clark and Wyatt⁽¹³⁾ managed to reduce the strength of the applied magnetic field near the electrodes by placing a permalloy strip behind it, thus reducing the high sensitivity to the flow near the electrodes. The suitable size of the strip they obtained experimentally by the observation of the change in the flowmeter sensitivity versus flow rate, using different widths of the permalloy strip over the electrodes.

Rummel and Ketelsen⁽³⁶⁾ designed and built an electromagnetic flowmeter with point electrodes, in which diamond-shaped coils were used. The magnetic field strength at each side of the electrodes is low relative to the mid-part of the flow tube (a result of the coil shape). As a result of this, the flowmeter becomes less sensitive to the flow near the electrodes. They claimed that this type of flowmeter is almost unaffected by changes in velocity profile.

Wyatt⁽⁵⁰⁾ described a method to improve the electromagnetic flowmeter with point electrodes by optimizing the magnetic field for the least variation of the weight function. He obtained a two-dimensional magnetic field for a minimum E (root-mean-square deviation of the weight function over the cross-sectional area divided by the value of the mean weight function \bar{W}_m). The value of E is expressed by:-

$$E = \frac{1}{\bar{W}_m} \left[\frac{1}{\pi R^2} \int_0^R \int_0^{2\pi} (W - \bar{W}_m)^2 r dr d\theta \right]^{1/2} \quad (1.20)$$

where R is the flow tube radius and r is any radius. His axisymmetric weight function (W') for the improved fields was not satisfactory. It was worse than that for uniform magnetic field and point electrodes.

Hemp⁽²⁶⁾ optimized the point electrode flowmeter by finding a suitable three-dimensional magnetic field. He defined ϵ , which is a measure of the non-uniformity of the weight function (\bar{W}) over the cross-section of the flow tube, as:-

$$\epsilon = \frac{1}{\bar{W}_m} \left[\frac{1}{45} \sum_{i=1}^{45} (\bar{W}_i - \bar{W}_m)^2 \right]^{1/2} \quad (1.21)$$

where $\bar{W}_1, \bar{W}_2, \dots, \bar{W}_{45}$ are weight functions at 45 points distributed in a quadrant of the flowmeter cross-section, \bar{W}_m is the mean value of \bar{W} . The smaller the value of ϵ , the more uniform is the weight function. Hemp expressed the

magnetic field as a sum of harmonics with coefficients a_{nm} . The values of these coefficients are obtained for which ϵ is minimum. The improved magnetic field is produced by using complex coils which have been made in the form of an etched copper sheet and then placed in a suitable laminated iron tube. The field gave a getter uniformity of the weight function distribution. Also the axisymmetric weight function (w') for the improved field showed favourable distribution of w' . The maximum error expected from the reading of this flowmeter is about 10%, while for the conventional point electrode flowmeter, it is about 50%. The disadvantages of this design are the flowmeter length, which is rather longer (2.5 x diameter) than would be desired in practice, and the power consumption of the flowmeter is about 25 times that of a uniform magnetic field.

1.6 The Present Work

1.6.1 Objectives

The objectives of this work can be summarized in the following points:-

- (a) To develop computer programs for the purpose of predicting the magnetic field, virtual current, weight function and the flow signal.

- (b) To measure the flowmeter magnetic field, the virtual current, and the distorted velocity profiles and compare with (a).

- (c) To calculate and measure the effects on the flowmeter performance of the velocity profiles and of electrode fouling.
- (d) To optimize the uniformity of the weight function of an electromagnetic flowmeter, using numerical methods.
- (e) To construct a contactless electrode flowmeter and to assess its performance.

1.6.2 Layout of This Thesis

In Chapter 1, the electromagnetic flowmeter has been described and its basic theory given. A review of the work of others, which is of particular relevance to this thesis, has been made.

Chapter 2 contains the theoretical analysis of three types of electromagnetic flowmeter with large electrodes.

Chapter 3 describes the rig and the experimental techniques used to obtain the magnetic field and the distorted profiles. It also presents some experimental results.

Chapter 4 explains the virtual current rig and the tests carried out to measure the virtual current distribution resulting from the various electrode arrangements considered in the theoretical work.

Chapter 5 presents the numerical methods of the optimization used for large electrode flowmeters.

Chapter 6 describes the details of the construction of a contactless flowmeter designed to generate the improved

weight function distribution.

Chapter 7 presents the experiments and test results of the improved flowmeter.

Chapter 8 contains the conclusions of the thesis and some suggestions for further work.

CHAPTER 2

THEORETICAL ANALYSIS OF

LARGE ELECTRODE FLOWMETERS

In this chapter, three types of large electrode flowmeters have been analysed. Type 1 (the laboratory flowmeter, manufactured by Flowmetering Instruments Ltd.), type 2 (the square coil, air core flowmeter) and type 3 (the Bevir type flowmeter).

The magnetic field and the virtual current were solved analytically and numerically. A computer program was written for each of the above three types to give the weight function distribution.

2.1 Magnetic Field Distribution

Each of the flowmeter designs required a different approach to the solution and these are given below.

2.1.1 Type 1 Flowmeters

This configuration is composed of a stainless steel tube with an insulating lining covering the inner surface apart from the electrode area. The internal diameter of the flow tube is 99.5 mm. The type 1 flowmeter has a rectangular coil with rounded corners, wound around a laminated steel core, as shown in Fig. 2.1. Its dimensions are shown in Fig. 2.2. The whole flowmeter assembly is covered with a steel housing of 334 mm diameter and 310 mm long.

2.1.1.1 Analytical Solution

The three-dimensional distribution of the magnetic field, for the geometry shown in Figs. 2.1 and 2.3, is determined analytically by using the Fourier series. The boundary conditions used are given as follows.

At the core, inside the coil windings, γ (the magnetic scalar potential) is assumed constant and equal to ± 1 . Outside the coil windings (also at the core), γ is assumed constant and equal to zero. Along the axial direction (not at the core area) the value of γ is assumed to drop exponentially until it becomes zero at a distance far from the centre.

The γ -distribution for this solution is given by:-

$$\gamma(x, y, z) = \sum_{n=0}^{\infty} \sum_{m=0}^{\infty} c_{nm} \cdot \cos \left(\frac{\left(n + \frac{1}{2}\right)\pi x}{x_1 + L_1} \right) \cdot \cos \left(\frac{\left(m + \frac{1}{2}\right)\pi z}{L_3} \right) \cdot \frac{\sinh K_3 y}{\sinh K_3 L_2} \quad (2.1)$$

see Appendix A, where:-

$$n = 0, 1, 2, \dots$$

$$m = 0, 1, 2, \dots$$

$$c_{nm} = \left[2G \sin \theta - G(-1)^n \right] + \\ + \left[P \left(\frac{E_1 E_3 (-1)^n}{Q} - \frac{E_2 \left(\frac{\left(n + \frac{1}{2}\right)\pi}{x_1 + L_1} \cdot \sin \theta - \frac{\ln 2}{L_1} \cos \theta \right)}{Q} \right) \right] \quad (2.2)$$

$$\theta = \frac{\left(n + \frac{1}{2}\right) \pi X_1}{X_1 + L_1}$$

$$G = \frac{4(-1)^m}{\pi^2 \left(m + \frac{1}{2}\right) \left(n + \frac{1}{2}\right)}$$

$$P = \frac{4(-1)^m e^{\left(1 + \frac{X_1}{L_1}\right) \ln 2}}{\pi (X_1 + L_1) \left(m + \frac{1}{2}\right)}$$

$$Q = \left(\frac{\ln 2}{L_1}\right)^2 + \frac{\left(n + \frac{1}{2}\right)^2 \pi^2}{(X_1 + L_1)^2}$$

$$E_1 = e^{-\frac{\ln 2}{L_1} (X_1 + L_1)}$$

$$E_2 = e^{-X_1 \frac{\ln 2}{L_1}}$$

$$E_3 = \frac{\left(n + \frac{1}{2}\right) \pi}{X_1 + L_1}$$

$$K_3 = \pi \sqrt{\left(\frac{\left(n + \frac{1}{2}\right)}{X_1 + L_1}\right)^2 + \left(\frac{\left(m + \frac{1}{2}\right)}{L_3}\right)^2}$$

2.1.1.2 Numerical Solution

The magnetic field equations are solved numerically using the finite-difference approximation (Smith⁽⁴⁵⁾). From equation (1.1), a magnetic potential (γ) is given by:-

$$\underline{B} = \nabla \gamma \quad (2.3)$$

Substituting equation (2.3) in equation (1.2), the following Laplace equation is obtained:-

$$\nabla^2 \gamma = 0 \quad (2.4)$$

which can be expanded in the following general form (for Cartesian coordinates since the yoke has a rectangular shape, see Fig. 2.1):-

$$\nabla^2 \gamma = \frac{\partial^2 \gamma}{\partial x^2} + \frac{\partial^2 \gamma}{\partial y^2} + \frac{\partial^2 \gamma}{\partial z^2} = 0 \quad (2.5a)$$

To solve this equation numerically, the area of interest has to be divided into a grid, and the differential terms have to be expressed in terms of each point in the grid and the ones adjacent to it. The following equation is thus obtained for the notation given in Fig. 2.4:-

$$\begin{aligned} \nabla^2 \gamma &= \frac{\gamma_1}{\delta x^2} + \frac{\gamma_2}{\delta z^2} + \frac{\gamma_3}{\delta y^2} - 2 \left(\frac{1}{\delta x^2} + \frac{1}{\delta y^2} + \frac{1}{\delta z^2} \right) \gamma_4 + \\ &+ \frac{\gamma_5}{\delta y^2} + \frac{\gamma_6}{\delta z^2} + \frac{\gamma_7}{\delta x^2} = 0 \end{aligned} \quad (2.5b)$$

The value of γ can be derived for each point in the grid in terms of the adjacent γ 's. There will be a set of simultaneous equations, one for each grid point which, with the appropriate boundary conditions, can be solved. The

following boundary conditions are used to get γ distribution (see Fig. 2.5) :-

1. At the surface (AFHE), γ is set to 1 (when γ is at the yoke and inside the magnetic field windings).
2. At the surface (DGIC), γ is set to zero (when γ is at the yoke and outside the magnetic field windings).
3. At the surface (EHGD), γ is described by $\gamma_p = 1 - \left(\frac{x_s}{L_s}\right)^{0.3}$ where p is any point on the surface (EHGD), x_s is the distance between point p and the line (EH) and L_s is the width of the coil gap. The exponent was determined empirically by comparison with experimental results.
4. At the surface (ADCB), $\frac{\partial \gamma}{\partial x} = 0$ (surface of symmetry).
5. At the surface (ABMJ), $\frac{\partial \gamma}{\partial z} = 0$ (surface of symmetry).
6. At the surface (BCLM), $\gamma = 0$ (symmetry).
7. At the surface (FGKJ), γ decays exponentially along the flow axis.
8. At the surface (JKLM), $\gamma = 0$ (γ is far from the centre).

The coefficients of the simultaneous equations are formed into an upper triangle matrix, which is subsequently

solved by successive back substitutions to obtain γ .

2.1.1.3 Comparison Between Analytical and Numerical Solution

The problem with the analytical solution is that the effect of the coil gap width on the solution is not considered. While in the numerical solution this point could be taken into consideration, the value of γ at the coil gap is dropped from 1 (the inside edge of the coil) to zero (the outside edge of the coil), to get more realistic boundary conditions. This drop is described in the boundary conditions given in Section 2.1.1.2.

The field patterns obtained from the two solutions are compared for the same boundary conditions, in Figs. 2.6a, 2.6b and 2.6c, and it can be seen that a high level of agreement is achieved when the coil gap is zero. In the following work, assumption 3, page 44 was used.

2.1.1.4 The Magnetic Field Distribution Inside Flow Tubes

For the purpose of finding the weight function later on, the value of γ is needed at the nodes where the virtual current is known (the grid of virtual current is in cylindrical polar co-ordinates). Two ways could be followed, either interpolating (γ) values over all the grid points or alternatively interpolating γ along the flow tube wall only, and then solving the Laplace equation for this boundary condition. The second method is thought to be more accurate, and it has been used as explained below. The Laplace equation can be expanded in the following general form (for cylindrical polar coordinates):-

$$\nabla^2 \gamma = \frac{1}{r} \frac{\partial}{\partial r} \left(r \frac{\partial \gamma}{\partial r} \right) + \frac{1}{r^2} \frac{\partial^2 \gamma}{\partial \theta^2} + \frac{\partial^2 \gamma}{\partial z^2} = 0 \quad (2.6)$$

By applying the same method used previously (Section 2.1.1.2) (but for cylindrical grid instead of Cartesian), the following equation is then obtained for the notation given in Fig. 2.7:-

$$\begin{aligned} \nabla^2 \gamma &= \frac{\gamma_1}{\delta z^2} + \frac{\gamma_2}{r^2 \delta \theta^2} + \frac{\left[r - \frac{\delta r}{2} \right]}{r \delta r^2} \gamma_3 - \\ &- 2 \left(\frac{1}{\delta z^2} + \frac{1}{r^2 \delta \theta^2} + \frac{1}{\delta r^2} \right) \gamma_4 + \frac{\left[r + \frac{\delta r}{2} \right]}{r \delta r^2} \gamma_5 + \frac{\gamma_6}{r^2 \delta \theta^2} + \frac{\gamma_7}{\delta z^2} \end{aligned} \quad (2.5c)$$

The value of γ at each grid point inside the flow tube is determined as before. Thus the magnetic field (B) distribution can be calculated by applying equation (2.3). Fig. 2.8a shows the three-dimensional B -distribution inside the flow tube.

2.1.2 Type 2 Flowmeters

This flowmeter is similar to the type 1 flowmeter except that the magnetic-field-producing coil is square and is without a steel core, as shown in Fig. 2.9. The length of the square coil is 220 mm and the distance between the two coils is 283.7 mm.

The three-dimensional magnetic field distribution of this type is analysed by applying Biot-Savart formula (Seely⁽⁴¹⁾), from which the following expression may be deduced for the geometry and notation given in Fig. 2.10:-

$$\underline{B} = \frac{\mu_0 I}{4\pi R} (\cos \alpha_1 - \cos \alpha_2) \underline{\theta} \quad (2.7)$$

where μ_0 is the permeability of free space and $\underline{\theta}$ is the component normal to the plane containing \underline{i} and \underline{r} .

After applying the superposition principle, the magnetic field, for this coil configuration, at the lattice points may be directly obtained and it is shown in Figs. 2.11a, b, c and d.

The solution obtained has been checked by considering the special case where the coil is very long (in the axial direction) and the results agreed with those that can be obtained by applying the following two-dimensional equation:-

$$\underline{B} = \frac{\mu_0 I}{2\pi R} \quad (2.8)$$

The magnetic field distribution for this case is shown in Figs. 2.12a and b.

2.1.3 Type 3 Flowmeters

The magnetic field for this type of flowmeter results from using the tube wall as magnetic pole pieces and laying the wires in slots in the wall. The insulating liner is considered to be very thin. The length of the coil used is $0.8 \times$ diameter and the occupied angle is (90°), as shown in Fig. 2.13. The field within the pipe produced by this design of pole pieces may be obtained by the solution of the Laplace equation with known boundary conditions on the wall. In this work, a three-dimensional numerical

solution was used as in Section 2.1.1.4. The distribution of this field is shown in Figs. 2.14a, b, c and d.

2.2 Virtual Current

The solution of the virtual current also results from a potential function (G) which is governed by the Laplace equation as shown below:-

$$\text{Since } \nabla \times \underline{J}_v = 0 \quad (2.9)$$

$$\text{and } \nabla \cdot \underline{J}_v = 0 \quad (2.10)$$

$$\text{Hence } \underline{J}_v = \nabla G \quad (2.11)$$

$$\text{and } \nabla^2 G = 0 \quad (2.12)$$

The G -distribution depends on the flowmeter geometry and the shape of the electrodes. Type 1 and 3 flowmeters have the same electrode dimensions (the electrode occupied angle is 90° , and its length is $0.766 \times$ diameter where the diameter = 100 mm). Type 2 flowmeter has slightly different electrode dimensions (the electrode occupied angle is 80° , and its length is $0.7 \times$ diameter, where the diameter = 200 mm).

2.2.1 Numerical Solution

The potential function is solved numerically using a finite difference method for the three-dimensional case. The following boundary conditions are used to obtain the G -distribution (see Fig. 2.15):-

1. At the surface ABC, $J_z = 0$, hence $\frac{\partial G}{\partial z} = 0$ (surface

of symmetry).

2. At the surface ABED, $G = 0$ (due to the symmetry too).
3. At the surface ACFD, $G = \text{constant}$ at the electrode area and it is assumed equal to one. $J_r = 0$ on the insulating liner, hence $\frac{\partial G}{\partial r} = 0$.
4. At the surface BCEF, $J_\theta = 0$ hence $\frac{\partial G}{\partial \theta} = 0$ (symmetry).
5. At the surface DEF, it is assumed that $G = 0$ because it is far from the centre of the electrodes.

The flowmeter tube is divided into grids using cylindrical polar coordinates. Then by applying the above boundary conditions, the resulting set of simultaneous equations can be solved and the potential distribution inside the flow tube is obtained, as shown in Figs. 2.16a and b. Hence, the virtual current (J_v) can be determined by using equation (2.11).

2.2.2 Analytical Solution

The general formula of the two-dimensional virtual current for symmetric and unsymmetric electrodes is deduced analytically, using the complex variable methods. The unsymmetric electrode configurations simulate the situation of partial fouling of the electrodes. The general expression is given below for the notation referred to in Fig. 2.17 and

it was derived in collaboration with Dr. J. Hemp*.

$$J_v = g'(z) = \frac{i c . e^{i \left[\frac{\alpha + \beta + \gamma + \delta}{4} + \pi \right]}}{\left[(z - e^{i\alpha}) (z - e^{i\beta}) (z - e^{i\gamma}) (z - e^{i\delta}) \right]^{\frac{1}{2}}} \quad (2.13)$$

(see Appendix B), where c is a real number given by:-

$$\frac{1}{c} = \int_{\alpha}^{\beta} \operatorname{Re} \left[\frac{i e^{i\theta} . e^{i \left[\frac{\alpha + \beta + \gamma + \delta}{4} + \pi \right]}}{\left[(z - e^{i\alpha}) (z - e^{i\beta}) (z - e^{i\gamma}) (z - e^{i\delta}) \right]^{\frac{1}{2}}} \right] d\theta \quad (2.14)$$

The value of c has been calculated from equation (2.14) by using the computer.

2.3 Weight Function

Generally, the sensitivity dependence of the flow pattern is described in terms of a weight function (W). As mentioned before, the weight function can be obtained by forming the crossproduct of B and J_v (equation (1.14)). In this thesis, the flows considered are assumed to be rectilinear. All the flow is moving parallel to the axis. In this case, only the axial component of the weight function will be important and it may be integrated along the flow axis to obtain $W(r, \theta)$ as shown below:-

$$W(r, \theta) = \int_{-\infty}^{+\infty} W_z(r, \theta, z) dz \quad (2.15)$$

* Private communication

Plots of \bar{W} for each type of flowmeter are shown in Figs. 2.18, 2.19 and 2.20.

2.3.1 The Non-Uniformity of Weight Function

In order to find the susceptibility of a flowmeter to distorted profiles, it is necessary to define a quantity (ϵ) which measures the degree of non-uniformity of (\bar{W}) over the cross-sectional area (A) of the flow tube. This (ϵ) is similar to that mentioned by Wyatt⁽⁵⁰⁾ and Hemp⁽²⁶⁾ and it is given by:-

$$\epsilon = \frac{\int \left| (\bar{W} - \int \bar{W} dA/A) \right| dA}{\int \bar{W} dA} \times 100 \quad (2.16)$$

and the smaller the value of (ϵ), the more uniform is \bar{W} . This value (obtained numerically for a finite set of points) is given in Table 1 for the three flowmeter types.

2.4 Flowmeter Sensitivity

The value of $\bar{W}(r, \theta)$ may now be used to obtain the flow signal:-

$$\Delta U_{EE} = \int_A v_z \cdot \bar{W} \cdot dA \quad (2.17)$$

by applying the appropriate velocity profile to the integral. For a uniform velocity profile, the values in Table 1 were

obtained where the output voltages were divided by $\mu_0 Iv_m$ to give a sensitivity:-

$$S = \frac{\Delta U_{EE}}{\mu_0 Iv_m} \quad (2.18)$$

where I is the current turns in each field coil and v_m is the mean velocity. This differs from Shercliff's⁽⁴³⁾ sensitivity which was for a uniform field.

The sensitivities of the three flowmeters were obtained for different distorted velocity profiles* (where the peak flow is at the tube centre, near the electrode centre, at 45° to the electrode centre and at 90° to the electrode centre). Some other theoretical profiles have been proposed, i.e. "test profiles", where a bulk flow is assumed to pass through an orifice (which is a quarter of the area of the flow tube section), while the flow is zero elsewhere. Tables 2 and 3 show the percentage change of sensitivities of the three types of flowmeters as they are subjected to the above distorted flow profiles and "test profiles" respectively.

2.5 Theoretical Analysis of Some Technical Problems

The technical problem of large electrode electromagnetic flowmeters is the constancy of the resistance between the electrode surface and the metering liquid. The change of contact resistance is usually caused by the suspended dirt in a metering liquid, by the adherence of gas bubbles or by chemical action. This problem will affect

* these profiles were obtained from Pitot traverses 5.5 D downstream of the orifice. They were assumed to exist throughout the flowmeters for the purpose of computing Table 2.

the flowmeter sensitivity and the quadrature signal.

2.5.1 The Effect of Dirt on the Electrodes

The general approach previously used is now applied to obtain the modifications to the weight function which result from the fouling of the electrodes causing only part of them to operate. Because the geometry may now not be symmetrical, the solution obtained has to take in the whole cross section (which causes a computer storage problem) whereas previously the solution for one quadrant was adequate. For this reason, this effect is examined for a long two-dimensional flowmeter only, and for flowmeters based on types 1 and 2 which gave the better value of (ϵ).

A variety of situations are given in Table 4 which are selected to show the detrimental effect on (ϵ), on the weight function uniformity, and on the sensitivity S. Of these, the weight functions for moderate cases for types 1 and 2 are plotted in Figs. 2.21 and 2.22 and for the worst case for type 1 in Fig. 2.23.

2.5.2 The Effect of Dirt on the Quadrature Signal

Fig. 2.23 shows a weight function for large electrodes with extreme fouling. Because of the particular fouling shown, the quadrature pick-up is altered. The resulting ratio of quadrature to the flow signal is estimated as follows.

The quadrature signal will be:-

$$\Delta U_{\text{Quad.}} \approx \pi f B p d^2 \quad (2.19)$$

where f is the excitation frequency, B is the amplitude of the applied field and p is the ratio of electrode length to pipe diameter, d . The flow induced signal will be:-

$$\Delta U_{EE} \approx B v_m d$$

so the ratio:-

$$\frac{\Delta U_{Quad.}}{\Delta U_{EE}} \approx \frac{\pi f p d}{v_m}$$

for $f = 50$ Hz, $p = 0.7$ (a typical value), $d = 0.1$ m and $v_m = 1$ m/sec.

Hence: $\frac{\Delta U_{Quad.}}{\Delta U_{EE}} \approx 10$

2.6 Analysis of Some Other Cases

The computer programs which are used for the previous theoretical work have now been developed to analyse some other cases as explained below.

2.6.1 Commercial Point Electrode Flowmeters

The design of type 1 flowmeter has been analysed where the electrodes were small enough to be considered as point electrodes. The virtual current distribution inside the flow tube will be changed due to the alteration of the shape and area of the electrode. Applying this virtual current together with the magnetic field, the weight function

(\bar{W}) is obtained (equations 1.14 and 2.15). The plot of \bar{W} for this point electrodes flowmeter is shown in Fig. 2.24. The flowmeter weight function non-uniformity (ϵ) was calculated (equation (2.16)) and it was 47.8% which is very high relative to the large electrode. The sensitivity was also determined (equation (2.18)) and it was 1.06. The effect of the distorted profiles on the sensitivity of this type of flowmeter has also been examined theoretically by applying the distorted profiles and "test profiles" which have been mentioned before. Tables 5 and 6 show the percentage change of sensitivity as the flowmeter is subjected to the above profiles.

Some other applications of the electromagnetic flowmeter with point electrodes have been analysed theoretically, for example, partially empty flowmeter (Appendix C) and a large commercial design of electromagnetic flowmeter (Appendix D).

2.7 Accuracy of the Numerical Method

The accuracy of the finite difference method which was adopted in the numerical solution is subject to two sources of errors. The first of these (round-off errors) occurs due to the accuracy with which the variable values are described in the computer. Usually, this error is not serious with modern computers which are accurate to 29 significant digits. However, the second source is termed the truncation error, and it was caused by the approximation involved in replacing the differential equations by the difference equations. Such errors are dependent on the fineness of the

mesh. As the mesh is refined, the number of equations to be solved increases. Many writers have explained such errors in detail, such as Potter⁽³⁵⁾ and Conte⁽¹⁵⁾.

The error term (E_Y) incurred in approximating the second order partial derivatives, present in the Laplace's equation for the magnetic field, is given by Forsythe and Wasow⁽²²⁾ as follows:-

$$|E_Y| \leq \frac{1}{12} \left[\delta r^2 \frac{\partial^4 Y}{\partial r^4} + (r \delta \theta)^2 \frac{\partial^4 Y}{\partial \theta^4} + \delta z^2 \frac{\partial^4 Y}{\partial z^4} \right] \quad (2.20)$$

Also, the virtual current equation, as mentioned before, is governed by Laplace's equation, hence the error term (E_G) will be similar to that of equation (2.20), as shown below:-

$$|E_G| \leq \frac{1}{12} \left[\delta r^2 \frac{\partial^4 G}{\partial r^4} + (r \delta \theta)^2 \frac{\partial^4 G}{\partial \theta^4} + \delta z^2 \frac{\partial^4 G}{\partial z^4} \right] \quad (2.21)$$

Since the weight function is the multiplication of the magnetic field and the virtual current (equation (1.14)), the total error term for the weight function would be of the order of ($E_Y + E_G$).

2.8 Discussion

2.8.1 Flowmeter Insensitivity

The first part of the work presented in this chapter shows the effect of large electrodes on the weight function distribution. The results are strictly for a rectilinear

profile, but the results should give a reasonable guide to the performance for some more general velocity distribution, since usually after a few diameters from a disturbance the axial component of the velocity becomes the dominant component.

The flowmeter geometries represent three methods of construction which are used for commercial designs and which, it is reasonable to assume, would be acceptable for large electrode flowmeters. Type 1 has external rectangular magnetic coils bound round with a laminated yoke. Type 2 has rectangular coils with no yoke, and type 3 has internal coils in the industrial versions, although in this work these have been approximated by letting them into slots in the wall.

It has already been emphasised that no attempt at optimization has been made, but it is likely that changes to the geometry of the magnetic coil or the shape of the electrode could improve the uniformity of the weight functions.

The weight function uniformity for a type 3 flowmeter (Fig. 2.20) is probably worse than would be expected for a good point electrode flowmeter. However, the areas of high and low values alternate more for the large electrode flowmeters and the integrating effect of a flow profile over a large area will even this out even more. A similar effect is noticeable if the plots for types 1 and 2 are compared (Figs. 2.18 and 2.19). Although the high and low weight function areas for type 1 appear to be more extreme, in fact the areas which they occupy are less, and, as Table 1 indicates, the overall uniformity is better. This indicates that probably an optimization of the shape of the large

electrode is necessary to improve the performance of the electromagnetic flowmeters. However, the method of optimizing these flowmeters is not obvious due to the large number of parameters that need to be considered. An alternative method of optimization is the subject of Chapter 5.

2.8.2 Operating Problems

The single disadvantage which has resulted in a hesitancy in using the large electrode flowmeter is the effect on its performance of contamination of the electrodes. If some deposit forms on the surface due to the nature of the metered fluid, this will affect the contact resistance. The surface will not necessarily become electrically isolated. It is not easy to predict the nature and extent of such contamination which is dependent on the flowmeter design, the neighbouring pipework and particularly the fluid constituents.

In this chapter, some of the worst conditions have been examined which only give an indication of the extremes of error which could occur. Thus an error of 12% could result from the coating of all but one edge of each electrode with an insulating deposit for type 1, while for type 2, the error would only be about 5%. Also the quadrature pick-up which must affect the zero drift for AC excitation could rise to 10 times the flow signal for 1 m/sec for a 100 mm diameter flow head.

Fouling to a lesser extent than the extreme case considered above is expected to cause smaller change in the sensitivity.

Changes in the quadrature in this case (and hence the zero drift) are also likely to be smaller since the change in the area (of electrode) threading the magnetic field is correspondingly smaller.

CHAPTER 3

LARGE ELECTRODE FLOWMETER EXPERIMENTS

3.1 Description of the Rig

A 100 mm I.D. flow rig was built to test large electrode flowmeters, Fig. 3.1. This size of rig was selected because it would allow a flowmeter large enough for large electrodes to be inserted fairly easily. The water for this rig came from the departmental economy water supply. A plastic tube (ABS-durapipe) has been used for the construction of the rig whose elements are explained below. Photographs of the rig are shown in Figs. 3.2 and 3.3.

1. Valves

The water was controlled by an electrically operated master valve in the early stages of the flow rig. Two manual valves were used, one for the coarse flow rate control (100 mm diameter) and another (a 25.4 mm diameter bypass valve) for fine control. A steel pipe connected the electrically operated master valve to the manual valves, while the plastic pipe was used to connect the rest of the flow rig elements.

2. Reference Flowmeter

An electromagnetic flowmeter with point electrodes has been used in the flow circuit, and it has been calibrated against the weigh tank system. The flowmeter was then used as a reference to the test flowmeter. This device was manufactured by Flowmetering Instruments Ltd., Stroud,

Gloucestershire, and was of 100 mm I.D. MAGFLO type and of 300 flow sensor series used in conjunction with a series 400 converter. The magnetic field assembly was similar to that of the type 1 flowmeter design given in Section 2.1.1. The inside tube surface was insulated to prevent signal shorting. The point electrodes made contact with the fluid and, therefore, broke through the tube lining. The point electrode was shaped as a dome of 15.8 mm diameter.

After the control valve, a straight length of pipe (21 diameters) preceded the reference flowmeter to provide a fully developed velocity profile. This device has been tested with different flow rates to confirm its linearity for undistorted flow profiles. Fig. 3.4 shows the linearity graph for this flowmeter.

3. Orifice Plate

An orifice plate with a D and D/2 tapping arrangement has also been used in the rig flow circuit. It could be used (after being calibrated against the weigh tank assembly) as a second check on the flow rate of the test flowmeter. A straight length (after the reference flowmeter) of pipe (21D) preceded the orifice plate to provide an undistorted profile; and a 7.5D straight section followed the orifice plate downstream.

The orifice plate was made according to the British Standard⁽¹¹⁾, and it consisted of a brass plate having an axial hole (71 mm diameter) with a square edge on the upstream side and a bevel on the downstream side. The pressure tappings

were located at a distance of one pipe diameter upstream and one-half of the pipe diameter downstream of the plate. Fig. 3.5 shows the dimensions and the constructional arrangement of this type of orifice plate.

The wall tapping holes (2.5 mm bore) were connected to a vertical mercury manometer (7 mm bore) by using plastic pressure pipes. There was a small tap fitted at the highest point of each pressure pipe to release the air bubbles, because presence of the bubbles will affect the pressure difference readings. The volume flow rate (Q) in the pipe was then related to the manometer pressure difference readings as follows:-

$$Q = 359.2 k \sqrt{h/\rho} \quad \text{ft}^3/\text{hour} \quad (3.1)$$

where k is the product of several correction factors given in the British Standard, h is the pressure difference in inches of water and ρ is the water density (lb/ft^3).

4. Test Section

After two bends (7.5D between them) a further straight section (36D) preceded the "test section" and a 12.5D straight pipe length followed it. The "test section" had a 12.7D length and it could be adjusted to allow the insertion of a test flowmeter, distortion discs and a pitot traverse (the purpose of each will be explained later on in this chapter).

5. Weighing System Assembly

After the test section, the flow was directed towards a two tank weighing system to provide a final check on the rig flow rate. This system consisted of a flow-diverter valve, a weigh tank and a drain tank. The details of the assembly are shown in Fig. 3.6.

(a) Flow-Diverter Valve

The function of the diverter valve was to direct the flow to the drain or to the weigh tank as desired, without disturbing the rate of flow through the test section. In the valve diverter, the flowing water was made to pass through a slot of 305 mm long and 25.4 mm wide, so that it emerged as a jet with a long narrow cross-section. The particular anti-splash guards used in the rig were made of 1.58 mm mild steel in the form of an inverted V. It had a 356 mm width and the other dimensions are given in Fig. 3.7. The valve angular displacement was performed manually by pulling a connecting steel bar against a long tension spring used to bring the diverter valve back at the end of the stroke.

The diverter valve movement actuated a microswitch which started both a digital timer and two integrating counters, one on the reference electromagnetic flowmeter and the other on the test flowmeter. The actuation started when the diverter valve reached the "effective mid-point" during its travel. This "effective mid-point" is a "geometrical mid-point" if both the profile of the jet and the motion of the diverter are symmetrical at the mid-point.

Hayward⁽²⁵⁾ discussed a method of adjusting the position at which the microswitch operates at the "effective mid-point", i.e. finding the correct place of the microswitch relative to the diverter. Experiments have been carried out for this purpose as explained by Hayward⁽²⁵⁾. These are discussed in Section 3.5.1(b).

(b) Weigh Tank

A steel weigh tank of about 0.44 m^3 capacity was fixed on the platform of an Avery-bar type weighing machine of 1000 lb capacity, and with a 50 lb division for the course measurements and 0.25 lb for the fine measurements. No connection of any kind was attached to the tank when weighing determinations were being made. The tank was emptied by opening a 50 mm drain valve which allowed the water to drain by gravity.

(c) Drain Tank

Usually the flow goes to the drain tank, except during the test period. The drain tank was made of a plastic material of about 0.96 m^3 capacity. The reason for the use of this tank was because the drain pipe was too small for the high flow rate, and, therefore, this tank would help in regulating the drain congestion.

6. Electronic Timer

The electronic timer has been designed and built, especially for this rig, by Mr. Dennis Bloxham in the

Mechanical Engineering Department. The timer display had five digits and the decimal values can be selected either as 3, 2 or 1 decimal, and the total time limit for the three options was 100 sec, 1000 sec and 10,000 sec respectively. The time counting started or stopped either manually or by remote control (a microswitch was actuated when the flow diverter moved). The timer also actuated the integrating counter on the reference flowmeter and the test 100 mm flowmeter. The details of the circuit connections of this electronic timer are shown in Fig. 3.8.

3.2 Magnetic Field Measurements

A type 1 flowmeter was studied experimentally in this thesis. The details of this design have been explained in Chapter 2.

1. Hall Probe

The magnetic field distribution was measured by using a Hall probe. The Hall probe contained a crystal (1.27 mm thickness and 5.84 mm wide). If an imposed electrical current is passing along the crystal and if (at the same time) a magnetic field is applied perpendicular to the direction of the imposed current for the correct orientation of the crystal, an induced voltage will be generated in the direction perpendicular to both the magnetic field and the electric current. Hence, if the current is controlled and made constant, the generated voltage will be directly proportional to the strength of the magnetic field. A

special instrument was developed in the department to produce an almost constant current for the crystal and it also provided the value of the generated voltage across the crystal which can be read by using the digital voltmeter.

2. The Probe Holder Assembly

A special probe holder has been designed and built to facilitate the measurement of the magnetic field in three directions. The probe holder consisted of a rotatable perspex disc divided into divisions of 5 degrees, to allow the probe to move circumferentially. The radial movement of the probe was accomplished by a slide across the axis of the disc and graduated in 1/2 mm. The axial movement was made by another slide graduated also in 1/2 mm, and the total travel distance was from the flange to the centre of the flowmeter. The probe holder also had a facility for rotating the crystal face direction through 360° in 90° steps. Fig. 3.8b shows the probe and its holder assembly

3. Probe Calibration

A uniform magnetic field has been used to calibrate the Hall probe. The value of this field was measured by using two different search coils. The first was a circular search coil of 3.64 mm diameter and 59 turns. The second was a rectangular search coil of $10.68 \times 10^{-6} \text{ m}^2$ area and 30 turns. The average magnetic field reading was 1.067×10^{-2} tesla $\pm 1.9\%$. The probe was then used to measure the same magnetic field under both AC and DC excitations. The

average probe reading was $2.087 \text{ mV} \pm 0.3\%$. Hence, the calibration factor of this probe was calculated and it was $195.6 \text{ mV/tesla} \pm 1.9\%$.

4. Test Results

After mounting the probe and its holder on the face of the flowmeter flange, the readings of the probe were then recorded by using the digital voltmeter. The radial (B_r) and the circumferential (B_θ) components of the magnetic field were then measured at many different points. The results of this test were then compared with the equivalent theoretical results. Figs. 2.8a, b, c, d and e show this comparison.

The effect of the eddy currents on the magnetic field distribution has been tested by using the DC excitation current instead of the AC. This gave a negligible difference (within the Hall probe error) as can be seen in Fig. 3.9.

3.3 Velocity Profile Measurements

It has been mentioned before that, in general, the flow signal of the electromagnetic flowmeter depends on the velocity profile (equation (1.13)). However, a method has been adopted for the measurement of several flow patterns by using the pitot tube meter and the results were used in the computer programs to determine the corresponding flow signal.

1. Distortion Discs

The distorted profiles were produced by using perspex

discs upstream of the flowmeter which had holes cut in them allowing the water to emerge, in a specified area. One of the discs had a concentric circular orifice to simulate disturbance by an excessive cone angle in a tapered section, whilst the other disc had an eccentric circular orifice to simulate disturbance by a non-axial entry pipe. Both these orifices had a 1/4 area ratio. The two discs used in the tests are shown in Fig. 3.10. The disc with the eccentric hole could be set with three orientations, i.e. peak flow passing near the electrode, the peak flow passing at 45° from the electrode and 90° from the electrode.

2. The Pitot Tube

A total pressure pitot tube was used, in conjunction with wall static pressure holes, for measuring the velocity profiles of the undisturbed flow, peak flow at the centre and the eccentric flow. There were three static pressure tappings of 1.4 mm bore, distributed equally around the pipe periphery thus an average measurement of the pressure was obtained. The pitot tube bore was 0.61 mm, while the outside diameter was 1.06 mm (the details of drawings are shown in Figs. 3.11 and 3.12), and by traversing across the flow tube axis, the velocity readings at different radii were obtained. It also rotated circumferentially by sliding the device assembly on its end flanges. The total and static pressure tappings were connected to an inclined mercury manometer which gave a more sensitive pressure difference reading because of the inclination.

The distortion discs were set in many positions upstream of the pitot tube in order to measure the distorted profiles. The eccentric orifice plate created a jet flow with a recirculating region, in which the pitot device readings were not accurate due to the reverse flow in this region. The size of this recirculating flow region depends on the ratio of the orifice diameter to the flow tube diameter. It also depends on the value of the Reynolds number. It was found experimentally that there was no recirculating flow in the pitot tube region when the distortion disc was placed at 5.5 diameter upstream and the flow was at Reynolds number of 1.64×10^5 , i.e. more accurate readings would be obtained. However, when the concentric orifice plate was at 3.5 diameter upstream the pitot tube and the flow was at a Reynolds number of 1.64×10^5 , the recirculating region no longer was found to be affecting the pitot tube readings.

Fig. 3.13 shows the undistorted profile of the flow (36 diameter length of a straight pipe upstream). Fig. 3.14 shows the velocity profiles for the concentric orifice disc when it was at 3.5 and 5.5 diameter upstream from the pitot tube. Fig. 3.15 shows the velocity patterns for the eccentric orifice disc when it was at 5.5 diameter upstream from the measuring device. All these profiles were for a mean velocity of 1.643 meter/sec and a Reynolds number of 1.64×10^5 .

3.4 Test Flowmeter

A 100 mm I.D. electromagnetic flowmeter was provided

by Flowmetering Instruments Ltd. with specially prepared point electrodes, having holes bored to allow large electrodes to be fitted over them and bolted through. The large electrodes were made of a 1 mm thick brass, subtending an angle of 90° and 0.766 x diameter long and were fitted into the flowmeter. The resulting flowmeter corresponds to type 1 above (Section 2.1.1).

3.4.1 The Converter and Its Calibration

The test flowmeter was used in conjunction with a series 400 MAGFLO converter also manufactured by Flowmetering Instruments Ltd., Stroud. This converter was an essential part of the supporting electronics. It demodulated the signal by rejecting the quadrature signal using a reference voltage in phase with the magnetic field. Then it amplified this signal and converted it into DC. Using an analog multiplier, the converter gave the final output signal as a ratio of the flow signal to the reference signal which was proportional to the coil current and derived from a current transformer. The converter also used a "voltage to frequency converter" and this frequency (pulses) output could be read on an independent pulse counter. This made it possible either to read the instantaneous output of the converter on a DC voltmeter or to integrate this output over a specified period of time using the pulse counter and a stop watch (the electronic timer).

The calibration factor of this converter was obtained

by applying a known signal across the electrodes having the same phase as a flow signal. This was derived from a Hall probe placed in the magnetic field inside the test flowmeter. The integrator output was used to obtain the converter calibration factor, which was 4.25 (pulses/sec)/mV. Fig. 3.16 shows the graph of the calibration factor.

3.4.2 The Induced Flow Signal

The test flowmeter was placed in the flow circuit and experiments were carried out for different flow patterns (for a mean velocity of 1.643 meters/sec). These flow patterns were created by placing a distortion disc at 2.5 and 5.5 diameter from the centre of the flowmeter. The effect of these velocity profiles on the sensitivity of the test flowmeter and on the sensitivity of the point electrode flowmeter, when the flow was at Reynolds number of 1.64×10^5 , are shown in Table 7a and 7b respectively. Table 8 gives the comparison between the tested flowmeter signals and the equivalent computed signals, when the distortion disc was at 5.5 diameters from the centre of the test flowmeter and when the flow was at a Reynolds number of 1.64×10^5 .

3.4.3 The Quadrature Signal

Generally, the quadrature signal has an effect on the zero setting (baseline) of the converter when the electrodes are dirty (non-symmetric electrode area). However, in the experimental work, the electrodes were cleaned carefully before every run. Hence, the effect of the changing of the zero setting was reduced considerably and could thus

be ignored.

The effect of the dirt on both the test flowmeter sensitivity and on the zero setting, was then tested by dividing axially one electrode into two halves and covering one half with insulating material. Clear lacquer or adhesive grease was used to simulate the electrode fouling and then the flowmeter was placed in the flow circuit for examination. The percentage change of the sensitivity of this flowmeter was then obtained and it was 1.8%. Table 9 gives the values of the zero drift and the percentage changes, from the full scale (20 mV) of these zero drifts, when half of one electrode area and also when the whole of one electrode area (except one edge) was covered with the insulating material.

Also the induced flow signal of the half fouled electrode flowmeter was then tested for different velocity profiles, which were created by the distortion discs placed at 5.5 diameters from the centre of the flowmeter. The orientations of the eccentric hole were set such that the peak flow was passing near the fouled electrode. Table 10 gives the percentage change of the sensitivity of this flowmeter, in relation to the sensitivity of the flowmeter with clean electrodes and undisturbed profile.

3.5 Accuracy and Errors

1. Flow Rig Accuracy

There were many factors affecting the accuracy of the flow rig measurements. Some of these factors are explained below.

(a) Weighing Machine Accuracy

A small electronic weighing machine has been used to measure the accurate value of many cast iron weights. This machine was already calibrated by using very accurate dead weights (standard weights) and it gave an accuracy of - 0.1%. These cast iron weights were then used to calibrate the tank weighing machine. Sets of tests with different weight values were carried out and the maximum deviation between the corrected weights and the machine readings was 0.17%.

The linearity of the weighing machine has also been tested by loading it in both an ascending and a descending manner and no hysteresis was observed. Fig. 3.17 shows the linearity of the tank weighing machine.

(b) Diverter Trigger Accuracy

The position of the diverter trigger (microswitch) required adjustment in order to operate the trigger when the diverter was at the "effective mid-point". A series of experiments, similar to that explained by Hayward⁽²⁵⁾, has been carried out by plotting the measured flowrates (for the short and the long diversion time only) against the reciprocal of the diversion time. The result was a graph with a line through the experimental points and if this line is horizontal, it means that the setting of the diverter trigger is correct; if the line is inclined, it indicates that the trigger position still needs adjustment. Fig. 3.18 shows the graph of this experiment with the best trigger adjustment achieved and its inclination gave an error of 0.16%.

(c) Other Errors

There were many additional factors affecting the accuracy of the rig flow measurements and they are explained below.

The electronic timer display, as mentioned before, had five digits and the option of 2 decimals was used in the experimental work. However, the timer accuracy was ± 0.01 sec and for the average diversion time (30 sec), the error was 0.033%.

During the diversion period, some water usually splashed due to the diverting of the flow direction. Although the splashing was controlled considerably by covering the weighing tank with a plastic sheet, still a slight amount of this splashed water came out of the diverter valve. The total splashed water was estimated as a maximum of 0.1 kg per stroke (diversion period), and for the average weighing machine reading (340 kg of water) the error was 0.03%.

The volumetric flow rate was calculated from the measured mass flow rate. These calculations needed the density of the economy water which was measured by using a hydrometer. The accuracy of the hydrometer used was found to be within its resolution error which was $\pm 0.05\%$. The readings of different samples gave a maximum discrepancy from the average of $\pm 0.05\%$. Hence the total error of density measurement was 0.10%.

The temperature also affected the density of the metered liquids, and this effect was 0.015% per one degree centigrade for distilled water (British Standard⁽¹¹⁾) and this figure was used for the economy water. The error in the readings of thermometer (which was accurate to 0.1%)

is estimated as $\pm 0.2^{\circ}\text{C}$ resolution, which gave a total density error of 0.005%.

The true weight of the tank water was about (1/1000) greater than the apparent one, because of the buoyancy correction (Shafer et al⁽⁴²⁾) which resulted from the buoyant effect of air surrounding the tank. This effect gave an error of 0.1%.

2. Accuracy of the Orifice Plate

The orifice plate procedure for measuring the flow rate is given by the British Standard⁽¹¹⁾, and it has been adopted in this work. The orifice device readings have been corrected according to the correcting coefficients given by the standards. However, the readings were still subject to many sources of systematic and random errors which are explained below.

The major source of error in using the orifice plate was the manometer reading, which was subject to a fluctuation resulting from the nature of the flow through the orifice. The readings, however, were averaged and their accuracy was estimated to be $\pm 1 \text{ mm Hg}$, which gave an error of 1.4%.

The dynamic (absolute) viscosity of the fluid was also involved in the flow rate measurements, because of the requirements of the Reynolds number. The value of the dynamic viscosity of the ordinary water used in these measurements is given by the British Standard with a tolerance of 0.5%.

The water density also involved, as mentioned before,

was measured with an expected error of 0.096% (systematic plus random).

The temperature affected both the dynamic viscosity and the density of the water. In the ambient temperature and in the atmospheric pressure, the viscosity changed 1.5% per one degree centigrade, while the density changed 0.015%. Since the expected error in the thermometer was $\pm 0.2^{\circ}\text{C}$, the viscosity error due to the temperature variation was 0.3% and the density error for the same reason was 0.003%.

The total error in flow rate measurement by using the orifice plate was 2.3%, whilst, experimentally, the maximum difference between the flow rate measured by using the weighing tank and the orifice plate was 1.5%.

3. Magnetic Field Accuracy

The magnetic field measurement has been subjected to some errors arising from many sources. The greater source was the positioning of the Hall probe. The maximum expected error was estimated as 1 mm in the radial and axial direction, which gave a measured magnetic field with an error of 0.3% and 0.2% for both the radial and the axial positions respectively. Error in the directioning of the probe circumferentially was also estimated as 2.5 degrees and it added about 0.5% to the positioning error. Hence the total expected error due to the Hall probe position was added up to 0.802%.

It has been mentioned earlier that the calibration factor of the Hall probe had an accuracy of $\pm 1.94\%$, and this factor was obtained by using a known uniform magnetic

field which was already measured by using the search coils accurate to $\pm 0.9\%$ (see Baker⁽³⁾). Hence, the total error of the Hall probe calibration factor was $\pm 2.84\%$.

In addition, there were some other errors, affecting the Hall probe measurement, arising from the eddy currents, the external electric fields and the external magnetic fields.

4. Velocity Profiles Accuracy

The velocity profiles have been measured (as explained earlier) by using the total pressure pitot tube. This method of profile measurements needed many corrections (see British Standard⁽¹²⁾) as shown below.

- (a) Turbulence correction (λ) is the percentage by which the flow rate was reduced and it was found by calculating the Reynolds number based on the duct diameter. It was about - 0.28%.
- (b) Displacement correction (δ), which is the percentage by which the flow rate was reduced for the effect of pitot apparent displacement. This was found to be about - 0.3%.
- (c) Static hole size correction (d), which is the percentage by which the flow was increased. It was calculated from the empirical equation $d = 75 k_2 \Delta P$ (where k_2 and ΔP are found in the British Standard). The result was $d = 0.18\%$.

- (d) Blockage correction (k), which is due to the stem blockage and was about - 0.30%.

In addition, the manometer readings were averaged and the accuracy was estimated to be \pm 2 mm Hg which gave an error, for the average manometer head difference, of 1.8%. The density error (as explained before) was 0.1%, while the temperature effect on the water density was 0.003%.

5. Summary of Errors

- (a) The flow rate measurement, by using the "diverter-weighing" assembly, had a total possible error of 0.6%.
- (b) The flow rate measurement, by using the orifice plate, had a total possible error of 2.3%.
- (c) The magnetic field measurement, by using the Hall probe, had a total possible error of 3.64%.
- (d) The velocity profile measurement, by using the pitot tube, had a total possible error of 2.6%.

3.6 Discussion

Fig. 2.8a shows the predicted and measured magnetic field distribution of a type 1 flowmeter. The radial component (B_r) of this magnetic field showed good agreement

between test and computational values since the maximum error was 1.5% which was less than the possible error calculated above (3.64%). The circumferential component (B_θ) had a discrepancy of up to 4.8%. This could also be caused by the errors discussed before which amounted to 3.7% plus the numerical error in the magnetic field solution. Since the discrepancy was large only for (B_θ), this could be due to the fact that the positioning error of the probe in the θ -direction was larger than in the other directions.

The effect of the eddy currents on the magnetic field was very small (as shown in Fig. 3.9), and this could be due to the high resistance in the laminated core and in the stainless steel flow tube. Also the frequency 50 Hz was not high enough to create large eddy currents.

Table 7 shows the experimental results of the change of the flowmeter sensitivity subject to distorted profiles. The change of sensitivity was higher when the distortion disc was nearer to the flowmeter centre (2.5 diameters). This was perhaps because the velocity profiles were highly distorted near the disc where a recirculating region might appear. When the distortion disc was at 5.5 diameters, the change of sensitivity was reduced considerably, since the velocity profiles were more settled (less distorted) as the distortion disc was placed further from the flowmeter centre.

Table 8 shows the predicted and the experimental output signal of the type 1 flowmeter for different flow patterns created by the distortion disc placed at 5.5 diameters upstream. The discrepancy in the above comparison can be seen to be within 2.9%. This was considered satisfactory because

covered? - 172 ✓
Blowing - 0.0001

it was smaller than the total estimated error of 3.2% (the sum of a and d in Section 3.5.5).

The changes in the zero setting due to the alteration in the electrode area, obtained by covering a half of one electrode and a whole of one electrode, were found experimentally as shown in Table 9. It seemed that covering a larger area of electrode gave a larger change in the baseline (the reading when the flow is zero). This may indicate that as the distortion from symmetry of the large electrode increases, the zero drift increases too. Also, the flowmeter sensitivity increased by 1.8% when just half of one electrode was fouled. This change in sensitivity, due to the alteration in the electrode area, distorted the virtual current distributions. The sensitivity increased, since the effect of the electrode area on the signal short circuiting was partially reduced.

Table 10 shows the experimental results for the effect of the distorted profiles on the sensitivity of a flowmeter where half of one electrode is fouled. The distortion discs were placed at 5.5 D upstream the flowmeter centre. The sensitivity was increased when the peak velocity was near the electrode centre, because of the high weight function near the edge of the fouled area, whilst the sensitivity was reduced when the peak velocity was at the fouled area, because the value of the weight function was lower at the fouled area, as shown in the contour plotting of the weight function in Fig. 2.21.

CHAPTER 4

VIRTUAL CURRENT EXPERIMENTS

The virtual current rig (Fig. 4.1) was originally designed and built by M. Papworth at Warwick University. The rig was then moved to Imperial College. It consisted of a tank, a probe and a stepping motor. The complementary electrical equipment was built at Imperial College for the rig.

In this chapter, the virtual current rig is described and some experimental results obtained from it are presented.

4.1 Description of the Virtual Current Rig

Fig. 4.1 shows the rig which was used for measuring the virtual current. It consisted of the following parts.

1. The Tank

A plastic cylindrical tank 283 mm diameter, 1.5 m high and 16 mm thick represented the flowmeter tube. This tank was filled with tap water. The electrodes were fitted diametrically opposite each other on the wall at a height of 470 mm. The tank assembly stood on a ball race bearing to allow the rotation of the tank in steps of multiples of 9 degrees.

2. The Probe

A moveable (1.4m long) probe was immersed in the tank water. It was completely insulated from the water to prevent any potential shorting. At the tip of this probe

there was a small piece of bare copper wire connected to a fine wire inside the probe. This copper tip picked up the potential of the water at different places. It was moved radially by turning a wheel to shift the probe along the radius. The probe moved also circumferentially (relative to the cylinder) by fixing the probe and rotating the cylinder. Also this probe travelled axially in specified steps using a stepping motor.

3. The Stepping Motor

The axial motion of the probe was accomplished using a SLO-SYN stepping motor type SS400-1021. The motion was capable of 200 steps and developed a torque of 2.8 Nm when running at 5.3 volts DC and consuming 3.4 Amp.

The stepping motor drove a lead screw resulting in the axial motion of the probe upwards or downwards (by reversing the motion of the motor at the motor controller). The probe was shifted axially by 2.82 mm every one complete revolution of the motor.

4. Stepping Motor Controller

This equipment was used to control the direction and the travelling distance of the probe. The direction could be reversed by reversing the sequence of energizing the motor coil. The distance was controlled by setting the number of shifts and the value of the shift. This controller consisted of a power supply and a digicard (logic circuit) and dropping resistors (to make the power supply compatible with the digicard) of 1 ohm and 50 watts. The controller

also provided a small signal at the end of each shift, which was used to command the magnetic tape recorder to read the potential at different values inside the tank. Fig. 4.2 shows the logic circuit of this controller. This was designed by Mr. Dennis Bloxham of the Thermal Power Section.

5. The Transformer

An AC transformer was used to drop the mains voltage to the required level for the particular electrodes in use, and was also used as an isolator from the mains noise. It provided a voltage across the electrodes through the water. The value of this voltage was fixed by the output of the transformer, while the current was dependent on the size of the electrode.

A 10 ohm standard resistor was also used to measure the electrical current supplied by the transformer to the electrodes. The voltage across this resistor (which is proportional to the current) was then read by the magnetic tape recorder after it had been processed by the differential amplifier below.

6. The Differential Amplifier

The voltage of the probe was referenced relative to the potential of the water at a plane far from the electrode plane. Hence, two leads were required for measuring the voltage, and a differential amplifier was needed. Another differential amplifier was also required in order to measure the output of the standard resistor.

A Telequipment oscilloscope type DM63 with two

differential amplifiers was used. One was used for the probe signal and the other for the current measurement. The other advantage of using the differential amplifier was that its output could be adjusted (different gain scales) to fit the resolution of the magnetic tape recorder.

7. Magnetic Tape Recorder

The two single outputs from the two differential amplifiers were connected to two channels of the magnetic tape recorder. The voltage was then converted from analog to digital and recorded on a magnetic tape. The tape was then read into the computer using a special subroutine which converts the tape words to the computer words. The voltage range of this system was 0 to 10 volts. The magnetic tape recorder started to register the voltage when a signal from the stepping motor controller was in "enable" mode. This took place at the end of each shift.

8. Pulse Multiplier

The stepping motor controller produced a pulse at the end of each shift. This pulse passed through a multiplier which divided the pulse into 128 pulses of 0.15 ms duration. This allowed the recorder to read 128 values of the voltage in 19.2 ms. Since the frequency used in the experiment was 50 Hz (20 ms/cycle), the values of the sinusoidal voltage for slightly less than one cycle could be recorded. The maximum and the minimum values could be found from each set of 128 values by a simple computer program. The difference between these two values was the peak-to-peak voltage value from which

the RMS value of the voltage was obtained. The probe voltage was then divided by the current value to obtain a non-dimensional value of the potential (per unit current) of the water.

9. The Pulse Generator

Since there were two inputs (the probe signal and the supplied current signal) connected to the recorder, a pulse generator was needed to double each pulse from the multiplier before reaching the tape recorder. The latter registered the voltages from each input alternatingly.

4.2 Virtual Current Measurement

To verify the theoretical predictions, the stepping motor controller was set to allow the probe to move axially in steps of $0.38 \times R$. This was equal to the grid length along the axis in the numerical solution. R is the cylindrical tank radius (141.5 mm). Also the probe was shifted radially in steps of $0.133 \times R$. This was the grid length radially in the numerical solution. The cylinder wall was rotated circumferentially 9 degrees at a time. This movement was already set by the original rig design and could not be made to match the steps used in the numerical solution (12 degrees). This was one of the reasons for choosing the θ -direction as the abscissa for most of the results of this experiment.

The potential distribution for four different electrode arrangements were tested. The electrodes were

as follows:-

1. Point electrode of 6.3 mm diameter, made of steel and fitted flush with the walls. A voltage of 30 volts was applied across the two electrodes.
2. Large electrodes, made of brass sheet with a 72 degree angle span and 222 mm length. The voltage between them was 13 volts only.
3. Large fouled electrodes (same as above) with one of the electrodes half was covered with insulating material to represent the dirt effect. Since in this case the theoretical predictions were obtained by using a two-dimensional solution (Section 2.2.2), and for the purpose of comparison, the readings of the probe were taken only in one plane in the centre of the electrodes. This approximated to the behaviour of long electrodes.
4. Segmental electrodes made of aluminium sheet, with 160 degrees angle span, and 222 mm length. The aluminium surface was first insulated completely by covering it with Araldite AY103. Then a set of strips were made by painting on the Araldite layer with a conducting resin (Stycast 1970 with resistivity of 10^{-4} ohm-m). Each strip had 10 degrees span and there was a gap of 2 degrees between the strips.

Since the potential at each strip had to be different from the others, a set of resistors was built to regulate the voltage at each strip as required by the theoretical prediction (this is discussed in the next chapter). The total applied voltage across the segmental electrodes was 24 volts.

Comparison between the experimental results and the equivalent theoretical prediction was carried out as follows.

The theoretical and the experimental virtual potential values were compared as follows:-

$$\left(\frac{V_1}{V_n} \right)_{\text{theoretical}} \quad \text{compared with} \quad \left(\frac{V_1 / I_1}{V_n / I_n} \right)_{\text{experimental}}$$

where V_1 is the potential at any point.

I_1 is the current at the moment V_1 was measured.

V_n is the normalizing potential at point $r = R/2, \theta = 0,$

$z = 0.$

I_n is the current at the moment V_n was measured.

This method of normalization was carried out for the potential distribution of point, large and segmental electrodes, while for the fouled large electrode case, the theoretical and experimental virtual currents were compared after being normalized to the total virtual current across the surface of symmetry which is normal to the line connecting the electrodes. The reason for this departure was that the theoretical solution of this case gave the virtual current distribution directly.

4.3 Accuracy and Errors

The errors in these experiments arising from a number of sources are discussed below.

1. Probe Positioning Error

Since the probe was relatively long (1.4 m) and also very thin near the tip, this could create mispositioning in the radial and circumferential directions. This was estimated to be ± 1 mm radially and ± 2 degrees circumferentially. Also, an error in positioning axially was expected to be of the order of ± 2.8 mm. By observing the voltage versus position graphs and using the above positioning error values, the maximum possible error in the voltage readings can be estimated for the different types of electrodes as follows:-

- (a) Point electrodes. The maximum error in the voltage readings due to the error in positioning the probe radially, circumferentially and axially were estimated from the results to be within $\pm 1.7\%$, $\pm 2.5\%$ and $\pm 0.8\%$ respectively. Hence the total error in the voltage distribution for the point electrodes was 4.0%.

- (b) Large electrodes and segmental electrodes. The maximum error in the voltage readings due to the error in positioning the probe radially, circumferentially and axially were estimated in this case from the results obtained to be within $\pm 0.62\%$, $\pm 1.23\%$ and $\pm 1.22\%$ respectively. Hence the total error in the potential distribution for the large

and the segmental electrodes was $\pm 3.07\%$.

- (c) Large fouled electrode. In the case of a fouled electrode, the error in the voltage readings was due to mispositioning radially and circumferentially only, since the readings were taken in one plane in the centre of the electrodes. The maximum errors were estimated using the results obtained and found to be within $\pm 0.62\%$ and $\pm 1.23\%$. Hence the total error for the large fouled electrode was $\pm 1.85\%$.

2. The Magnetic Tape Recorder

The magnetic tape recorder used in the virtual current experiments had a "sample and hold" amplifier (SHA-2A) which held the voltage value in order to convert it from the analog to digital state. This type of amplifier had a gain non-linearity error of $\pm 0.01\%$. Also it had a gain error (follower connection) of 0.01% . The maximum rate of droop of this amplifier was $100 \mu V/\mu S$. Since the maximum voltage was 10 volts, and the time for "hold" was $1.2 \mu S$, the percentage error due to droop was 0.0012% for 10 volts. The total error of the "sample and hold" amplifier, therefore, was $\pm 0.0212\%$.

The magnetic tape recorder contained a fast analog to digital converter (type ADC 1103), which had the following errors.

An error relative to full scale was ± 0.5 LSB maximum (where LSB is the last significant bit and is equal to 9.775 mV for this system). This gave an error of $\pm 0.05\%$. Also this converter had a quantization error of

± 0.5 LSB maximum, which also gave an error of $\pm 0.05\%$. The gain temperature coefficient was $10 \text{ PPM}/{}^\circ\text{C}$ of the reading (maximum). Since the room temperature was 22°C and the standard temperature for calibration given by the manufacturers was 25°C , the temperature effect became $\pm 0.003\%$. Therefore, the total converter error was $\pm 0.1\%$.

The total error of the magnetic tape recorder was thus $\pm 0.12\%$.

3. Differential Amplifier

The Telequipment oscilloscope DM63 with two differential amplifiers, which was used in the experiment, had the following errors.

The common mode rejection ratio (cmrr) for the voltage range used in the experiments (20 mV - 10 V) at 50 Hz was 1 volt per 500 volts. Since the maximum input voltage (from the transformer) was 30 volts, cmrr equalled 0.06 volts. This gave an error of $\pm 0.6\%$ for each differential amplifier.

Hence the total error for the two amplifiers is $\pm 1.2\%$.

4. Standard Resistor

The value of the standard resistor was measured by using a digital voltmeter. Hence the accuracy of this instrument must be ascertained. The scale used was 10 ohms, then an error of $\pm 0.01\%$ of the reading plus $\pm 0.01\%$ of full scale was given by the manufacturers. Since the reading was 10.0 ohms, the accuracy was then $\pm 0.02\%$.

The room temperature was 22°C and the temperature coefficient was $\frac{1}{10} \times (\text{the above accuracy rating})/{^{\circ}\text{C}}$. A two-degree variation from 20°C , which was the standard temperature given by the manufacturers, was possible. Hence the temperature effect was $\pm 0.004\%$. The total standard resistor accuracy was thus $\pm 0.02\%$.

5. Errors Concerning the Segmental Electrode Resistors

The set of resistors, which was built to regulate the voltage on the segmental electrode strips, had a maximum discrepancy from the required value of $\pm 0.49\%$. Also the strips themselves had a maximum resistance of 8 ohms from the top electrode edge (where the strips were connected to the regulator of the resistors) to the centre of the strip. This resistance gave a maximum error of $\pm 0.79\%$. The resistance of the strips and the resistors were measured by the digital voltmeter. Hence an additional error due to the digital voltmeter of $\pm 0.024\%$ must be added. The total accuracy of the resistance of the segmental electrode was $\pm 1.3\%$ which gave a maximum error in the voltage distribution of $\pm 0.7\%$.

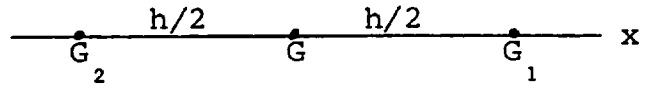
6. Error in Calculating the Gradient for the Case of Fouled Electrodes

In this case, the experiments should be compared with the analytical two-dimensional solution. Since this solution gave the value of virtual current rather than virtual potential, the calculations of the experimental virtual current from the virtual potential was required. This was done by taking the gradient of the potentials

numerically.

The gradient error was estimated as follows:-

G_1 and G_2 are expanded in a Taylor series in terms of G and its derivatives.



$$G_1 = G + \frac{h}{2} \frac{\partial G}{\partial x} + \frac{h^2}{4 x 2!} \frac{\partial^2 G}{\partial x^2} + \frac{h^3}{8 x 3!} \frac{\partial^3 G}{\partial x^3} + \dots$$

$$G_2 = G - \frac{h}{2} \frac{\partial G}{\partial x} + \frac{h^2}{4 x 2!} \frac{\partial^2 G}{\partial x^2} - \frac{h^3}{8 x 3!} \frac{\partial^3 G}{\partial x^3} + \dots$$

By subtracting the second of the above equations from the first, the following result is obtained:-

$$G_1 - G_2 = h \frac{\partial G}{\partial x} + \frac{h^3}{4 x 3!} \frac{\partial^3 G}{\partial x^3}$$

Hence:-

$$\frac{\partial G}{\partial x} = \frac{G_1 - G_2}{h} - \frac{h^2}{24} \frac{\partial^3 G}{\partial x^3}$$

Since the gradient term used in the calculations was $\left(\frac{G_1 - G_2}{h} \right)$, the error in the calculations of the gradient was:-

$$\left[\frac{h^2}{24} \frac{\partial^3 G}{\partial x^3} \right]$$

The maximum error was expected to appear at the electrode edge. The value of $\frac{\partial^3 G}{\partial x^3}$ was calculated there and it was $0.044/h^3$. Therefore, the error term $\left(\frac{h^2}{24} \frac{\partial^3 G}{\partial x^3} \right)$ was equal to 0.1. This gave an error in the calculations of the virtual current from the measured potential values of $\pm 1.9\%$.

7. Other Errors

There are some errors which cannot be accounted for because of the difficulties of estimating them. These errors are as follows:-

- (a) The water of the tank might carry some deposit which may deform the virtual current if deposited on the electrode surface during the experiment. Clean tap water was used, however, and the electrodes were well cleaned before the experiment, and the experiments were carried out immediately to reduce the chance of particle deposition on the electrode surface.
- (b) The applied voltage between the electrodes was 50 Hz AC and this may have a polarization effect on the electrodes.
- (c) Errors in measuring the tank diameter were not important due to the normalization of the results. However, changes in the diameter along the axis could introduce some errors which have not been considered.

8. Summary of Errors

- (a) The measured virtual potential distribution of the point electrodes had a possible total error of 5.4%.

- (b) The measured virtual potential distribution of the large electrodes had a possible total error of 4.4%.
- (c) The measured virtual potential distribution of the segmental electrodes had a possible error of 5.2%.
- (d) The measured virtual current distribution of the large fouled electrodes had a possible error of 5.1%.

4.5 Results and Discussion

The experimental and predicted (numerical) results of the virtual potential (or virtual current) were compared. Both curves were plotted in one graph using the plotting facility (visual display unit) at the computer centre of Imperial College.

Figs. 4.3a - 4.3h show the comparison of the experimental and the numerical potentials for the point electrode arrangement. The potentials were plotted against θ (circumferential co-ordinate), r/R (radial co-ordinate) and z/R (axial co-ordinate). The agreement was generally good although a maximum local discrepancy of 8% appeared. This occurred near the point electrode, because of the existence of the singularity there, and it could be referred to possible errors due to the finite grid size used in the numerical solution for the virtual potential.

Figs. 4.4a - 4.4g are the potential distribution for large electrodes. The agreement was also good although a maximum local discrepancy was 6.3%. This discrepancy occurred at the edges of the large electrode where the singularity existed.

Figs. 4.5a - 4.5d show the comparison of the virtual current distribution for the fouled large electrodes when half of one electrode was covered with insulating material. The agreement was, in general, good. Again a maximum local discrepancy of about 10% occurred near the edges of the electrodes. Similar arguments for the reasons of this discrepancy could be given here. In addition to that there was an error arising from the fact that the electrode had a finite length (222 mm) while it was assumed infinite in the theoretical two-dimensional solution.

Figs. 4.6a - 4.6g are the potential distribution for the segmental electrodes. The sharp changes in the values of the potential at the edges of the large electrode disappeared in the segmental one. This was due to the smooth changing of the potential on the strips. The agreement was also good although a maximum local discrepancy of 7% appeared. This discrepancy occurred on the lower edge of the segmental large electrode.

CHAPTER 5
OPTIMIZATION

5.1 Introduction

One of the fundamental problems concerning flowmeters with large electrodes is the singularity on the edge of the electrodes which produces a non-uniformity in the weight function distribution. However, numerical methods can be used here in order to optimize the performance of these flowmeters. The optimizing methods are used to find the best wall boundary condition possible which provides a suitable virtual current for a given constant magnetic field. In this thesis, the magnetic field of a typical commercial flowmeter (Type 1 flowmeter, Section 2.1.1) has been used.

Two flowmeter designs have been optimized here. In the first one, the fluid velocity is assumed to be parallel to the tube axis everywhere, while in the second flowmeter, a three-dimensional fluid flow is assumed. Finally, the details of the required potentials of the electrodes to generate the optimized flowmeters are given in this chapter.

5.2 Superposition Method

5.2.1 Virtual Potential

In Section 2.2.1, a numerical solution has been analysed for finding the virtual current distribution of the flowmeter with large electrodes. However, an alternative way of obtaining this virtual current is used here. It is performed by superimposing the virtual current of several point

electrodes in order to simulate one large electrode. The superposition method is described below.

Let the potential distribution, due to a point electrode on the surface, be given by the solution G_1 . It is well known that inside the flowmeter, this solution obeys the Laplacian:-

$$\nabla^2 G_1 = 0 \quad (5.1)$$

And let the potential distribution, due to another point electrode placed at a different point on the surface, be given by the solution G_2 . Inside the flowmeter, this also obeys the Laplacian:-

$$\nabla^2 G_2 = 0 \quad (5.2)$$

Since the Laplacian is linear, i.e. if G_1 and G_2 are both solutions of the Laplacian (5.1 and 5.2), then so also is:-

$$(aG_1 + bG_2)$$

for all constants (a) and (b) (Smith⁽⁴⁶⁾). The additive property is applicable at all points inside the flowmeter including the wall boundary.

Consider three adjacent points 1, 2 and 3 on the boundary (Fig. 5.1). In case (A), if G_1' is the potential at point 1 due to the existence of only one point electrode at point 1, and G_1'' and G_1''' are the potential at points 2 and

3 respectively, due also to the existence of the point electrode at point 1 (G_1). In case (B), the potential G_2' is assumed at point 2 due to the existence of a point electrode at point 2, and G_2' is the potential at points 1 and 3 due to the point electrode at point 2 (G_2). Also, it is assumed that at point 3 no electrode exists. Then by superimposing the two cases (A and B), the following results are obtained:-

$$\left. \begin{array}{l} \text{The potential at point 1 is } \alpha_1 G_1 + \alpha_2 G_2' \\ \text{The potential at point 2 is } \alpha_2 G_2 + \alpha_1 G_1' \\ \text{The potential at point 3 is } \alpha_1 G_1' + \alpha_2 G_2' \end{array} \right\} \quad (5.3)$$

where these α 's, in principle, can be adjusted to give some specified boundary condition on the flowmeter.

The large electrode is covered by points 1 and 2 (case C), and the assumption made on solving the Laplace equation for the potential distribution of a large electrode is that the potential is unity on the electrode area. Hence the potentials at these points are:-

$$G_1 \alpha_1 + G_2 \alpha_2 = 1 \quad (5.4)$$

$$G_1' \alpha_1 + G_2' \alpha_2 = 1 \quad (5.5)$$

Solving these two equations enables α_1 and α_2 to be found.

Hence the potential distribution of the superimposed case is as follows:-

$$\left. \begin{array}{l} \text{Potential at point 1} = 1 \\ \text{Potential at point 2} = 1 \\ \text{Potential at point 3} = \alpha_1 G'_1 + \alpha_2 G'_2 \end{array} \right\} \quad (5.6)$$

This method gives the virtual potential distribution very accurately as can be seen in Figs. 5.2 - 5.5, with a considerable saving of computing time. In these figures, the results of the computer program, using superposition, are compared with results from an earlier program (Section 2.2.1) which solved the virtual potential for the large electrode in one step.

5.2.2 Weight Function

In Section 5.2.1, it has been shown that the value of the virtual potential at any point inside the flowmeter, due to the existence of several point electrodes together, can be given in the following general expression:-

$$G = \alpha_1 G_1 + \alpha_2 G_2 + \alpha_3 G_3 + \dots + \alpha_n G_n \quad (5.7)$$

where n represents the total number of electrodes considered in the superposition method. Hence the superimposed virtual current (from Equation (2.11)) can be expressed as:-

$$\underline{J}_v = \nabla (\alpha_1 G_1 + \alpha_2 G_2 + \alpha_3 G_3 + \dots + \alpha_n G_n) \quad (5.8)$$

Since the grad operator is linear, Equation (5.8) can be rewritten as:-

$$\underline{J}_v = \alpha_1 \nabla G_1 + \alpha_2 \nabla G_2 + \alpha_3 \nabla G_3 + \dots + \alpha_n \nabla G_n \quad (5.9)$$

Since the magnetic field is considered the same for all the electrode arrangement and $\underline{W} = \underline{B} \times \underline{J}_v$, then the weight functions, due to the several point electrodes, can be superimposed, i.e. the weight function at any point inside the flowmeter is the sum of the contributions of all the point electrodes. Thus:-

$$W = \alpha_1 w_1 + \alpha_2 w_2 + \alpha_3 w_3 + \dots + \alpha_n w_n \quad (5.10)$$

where each term in the above equation is the resulting weight function of a point electrode placed at different positions within the flow tube. (Note that because of the symmetry assumed in the solution, one point electrode represents four point electrodes, two symmetrical and the other two are their images).

5.3 Integrated Voltage Flowmeter For Rectilinear Flows

The general flow signal (ΔU) of the electromagnetic flowmeter has been given in terms of the weight vector (Equation (1.13)). It may be expressed, for a circular flow tube, as follows:-

$$\Delta U = \int_{-\infty}^{+\infty} \int_0^{2\pi} \int_0^R \underline{V} \cdot \underline{W} r dr d\theta dz \quad (5.11)$$

where R is the flowmeter radius, \underline{V} is the fluid velocity vector and \underline{W} is the weight vector.

Since the assumption made in this work is that the flow is rectilinear, the axial component of the weight vector (w_z) is the only component needed to be considered. Therefore, Equation (5.11) becomes:-

$$\Delta U = \int_{-\infty}^{\infty} \int_0^{2\pi} \int_0^R v(r, \theta) w_z(r, \theta, z) r dr d\theta dz \quad (5.12)$$

where $v(r, \theta)$ is the fluid velocity parallel to the tube axis.

The important condition that makes such a flowmeter unaffected by changes in the flow profiles, is that the integral along the axis of w_z at any point in the flowmeter cross-section is made constant. In other words:-

$$\int_{-\infty}^{\infty} w_z(r, \theta, z) dz = k \quad (5.13)$$

where k is a constant.

Hence Equation (5.12) could be expressed as:-

$$\Delta U = k \int_0^{2\pi} \int_0^R v(r, \theta) r dr d\theta \quad (5.14)$$

Since the double integral term of Equation (5.14) is the fluid volumetric flow rate, the flow signal is directly proportional to the fluid flow and independent of the shape of the flow pattern.

5.4 Optimization Method for Flowmeters Designed for Rectilinear Flows

In this section, we seek an answer to the question: "Given the magnetic field distribution inside the flowmeter tube, what are the wall boundary conditions which generate the required virtual current in order to fulfil condition (5.13)?"

The optimization procedure for one set of electrodes (Fig. 5.6) is carried out as follows. The virtual potential distribution is first calculated inside the flowmeter for the case of a single point electrode placed at 1 (see Fig. 5.6) as explained earlier in Section 2.2.1. Therefore, the virtual current distribution can be obtained (by using Equation (2.11)). The weight function at each point inside the flowmeter can be determined from this virtual current and from the given magnetic field distribution (the magnetic field of type 1 flowmeter is used, see Section 2.1.1). The optimization method concentrates on the weight function at the test points near the boundary. This is because firstly the non-uniformity of the weight function is much higher on the flowmeter boundary than in the interior region, and secondly, it saves a considerable amount of the computing space, memory, and time.

The values of these weight functions, however, are then integrated along the tube axis (z) and the resulting integrated weight functions are called $\bar{w}_{1,1}$, $\bar{w}_{2,1}$, $\bar{w}_{3,1}, \dots, \bar{w}_{n,1}$ (where $\bar{w}_{i,j}$ is the integrated weight function for the i th test point when the electrode is placed at the j th point).

The virtual potential distribution for the case when

a point electrode is at point 2 (see Fig. 5.6) must be found. The solution for this can be obtained from the corresponding solution to the case when the electrode is at point 1. This is achieved simply by rotating the virtual potential by one grid point along the anti-clockwise direction. In order to maintain the symmetry of the virtual current inside the flow-meter, we also need the solution for an electrode at the image point of 2. Again, this can be obtained by rotating the virtual potential by one grid point along the clockwise direction. Then the weight function, due to these two new positions of the point electrode (point 2 and its image), at each test point near the boundary can be calculated. The weight functions are then integrated along the axis and labelled $\bar{w}_{1,2}$, $\bar{w}_{2,2}$, $\bar{w}_{3,2}$, $\bar{w}_{n,2}$. Also the values of the weight functions are obtained when the point electrode is shifted to points 3, 4, 5,, n.

By using the superposition method, the sum of the resulting weight function of each ith test point, when all the point electrodes exist together, has been calculated, using Equation (5.10) (e.g. at point 1 the sum of the weight function is $\alpha_1 \bar{w}_{1,1} + \alpha_2 \bar{w}_{1,2} + \alpha_3 \bar{w}_{1,3} + \dots + \alpha_n \bar{w}_{1,n}$).

The following set of simultaneous equations is then obtained (one equation for each ith test point):-

$$\begin{bmatrix} \bar{w}_{1,1} & \bar{w}_{1,2} & \bar{w}_{1,3} & \dots & \bar{w}_{1,n} \\ \bar{w}_{2,1} & \bar{w}_{2,2} & \bar{w}_{2,3} & \dots & \bar{w}_{2,n} \\ \bar{w}_{3,1} & \bar{w}_{3,2} & \bar{w}_{3,3} & \dots & \bar{w}_{3,n} \\ \vdots & & \vdots & & \vdots \\ \vdots & & \vdots & & \vdots \\ \vdots & & \vdots & & \vdots \\ \bar{w}_{n,1} & \bar{w}_{n,2} & \bar{w}_{n,3} & \dots & \bar{w}_{n,n} \end{bmatrix} \begin{bmatrix} \alpha_1 \\ \alpha_2 \\ \alpha_3 \\ \vdots \\ \vdots \\ \vdots \\ \alpha_n \end{bmatrix} = \begin{bmatrix} k_1 \\ k_2 \\ k_3 \\ \vdots \\ \vdots \\ \vdots \\ k_n \end{bmatrix} \quad (5.15)$$

In order to satisfy condition (5.13), the values of (k_i) have to be equal and can be any constant number. For this analysis, the value of 1 was selected. Then the values of the coefficients (α_i) which give the specified condition on the right hand side of the above matrix have to be calculated.

The solution of this system is obviously subject to the constraints which are imposed by us. Therefore, this system may or may not have an exact solution. Hence for general solutions the following method of least squares approximation (Thomas⁽⁴⁸⁾) was used.

The function $f(\alpha_1, \alpha_2, \dots, \alpha_n)$ is introduced and equated to the sum of the squares of the residue of each linear equation of the matrix (5.15), in other words:-

$$\begin{aligned} f = & (\alpha_1 \bar{w}_{1,1} + \alpha_2 \bar{w}_{1,2} + \dots + \alpha_n \bar{w}_{1,n} - k_1)^2 + \\ & + (\alpha_1 \bar{w}_{2,1} + \alpha_2 \bar{w}_{2,2} + \dots + \alpha_n \bar{w}_{2,n} - k_2)^2 + \\ & + \dots + (\alpha_1 \bar{w}_{n,1} + \alpha_2 \bar{w}_{n,2} + \dots + \alpha_n \bar{w}_{n,n} - k_n)^2 \end{aligned} \quad (5.16)$$

This sum of the squares depends upon the choice of the values

of α 's. Thus we try to find the values of α 's where the function (f) is minimum. To do this, we have to solve the following equations simultaneously:-

$$\frac{\partial f}{\partial \alpha_1} = 0, \quad \frac{\partial f}{\partial \alpha_2} = 0, \quad \frac{\partial f}{\partial \alpha_3} = 0, \dots, \quad \frac{\partial f}{\partial \alpha_n} = 0 \quad (5.17)$$

The following matrix is then set up as a result of applying Equation (5.17):-

$$\begin{bmatrix} \sum_{i=1}^n \bar{w}_{i,1} & \bar{w}_{i,1} & \sum \bar{w}_{i,2} \bar{w}_{i,1} & \dots & \sum \bar{w}_{i,n} \bar{w}_{i,1} \\ \sum \bar{w}_{i,1} \bar{w}_{i,1} & \sum \bar{w}_{i,2} \bar{w}_{i,2} & \dots & \sum \bar{w}_{i,n} \bar{w}_{i,2} \\ \vdots & \vdots & \ddots & \vdots \\ \vdots & \vdots & \ddots & \vdots \\ \vdots & \vdots & \ddots & \vdots \\ \sum \bar{w}_{i,1} \bar{w}_{i,n} & \sum \bar{w}_{i,2} \bar{w}_{i,n} & \dots & \sum \bar{w}_{i,n} \bar{w}_{i,n} \end{bmatrix} \begin{bmatrix} \alpha_1 \\ \alpha_2 \\ \vdots \\ \vdots \\ \alpha_n \end{bmatrix} = \begin{bmatrix} \sum_{i=1}^n k_i \bar{w}_{i,1} \\ \sum k_2 \bar{w}_{i,2} \\ \vdots \\ \vdots \\ \sum k_n \bar{w}_{i,n} \end{bmatrix} \quad (5.18)$$

The matrix (5.18) can be solved by using any standard solution procedure. We used a computer library subroutine based on Crout's factorization method (NAG Library - FO4ATF⁽³³⁾), in which the matrix (A) is decomposed into triangular form $A = LU$, where L is lower triangular and U is unit upper triangular. The coefficients are then found by forward and backward substitution in $Ly = \text{RHS}$ and $U\alpha = y$. The potential at each point electrode is then calculated using these α 's in Equation (5.7).

Knowing the required potentials on the first set of

point electrodes enables us to calculate the weight functions over the whole flowmeter volume by using these electrode potentials as boundary conditions for a specially written computer program (Section 2.3). The resulting weight functions are then integrated along the flow axis and \bar{W} is obtained. These results of \bar{W} 's are then examined and if the resulting non-uniformity of the weight function (ϵ) is not small enough, a second set of point electrodes is added to the previous set and the optimization procedure is repeated again. Adding a set of electrodes means making the electrode longer in the flow direction. Fig. 5.7a shows the value of (ϵ) drops with the increase of the electrode length in the flow direction. The following potentials of the electrodes are obtained by this optimization method for type 1 flowmeter but with a 76 mm flow tube diameter and with one diameter electrode length (three sets of point electrodes):-

(0.617, 0.595, 0.532, 0.442, 0.342, 0.243, 0.145, 0.048)

These electrode potentials are then used, as mentioned above, to find the flowmeter weight functions. The results gave a percentage non-uniformity (ϵ) of the weight function of 0.92%.

To show the applicability of the optimization procedure, the method has also been applied to the type 2 flowmeter (square-coil flowmeter without core). The value of ϵ has been reduced considerably for the optimized type 2 flowmeter. Fig. 5.7b shows the value of ϵ , decreasing with the increase of the strip-electrode length.

5.5 Performance Measure in a Three-Dimensional Flow

It is necessary to define a quantity ψ which measures the performance of a flowmeter subject to a specified three-dimensional flow in which the three components of the weight function are involved. The nature of this flow is described as follows.

Assume that for every test point inside the flowmeter there are three swirl loops, one in each direction, whose paths are defined by the adjacent grid lattice (see Fig. 5.8). The velocity of the fluid in each loop is assumed unity (lm/sec). This hypothetical picture of the flow is used here because it provides a severe test on the flowmeter performance. The signal given by each loop is then calculated by using Equation (1.13). Then the total swirl signal is determined by summing up the absolute value of the signal of each individual loop inside the flowmeter.

Next we assume a rectilinear flow parallel to the tube axis with a unit fluid velocity (lm/sec) through every grid lattice. In the same way, the total signal for this flow is calculated.

The performance measure ψ is defined by the ratio of the total swirl signal to the total rectilinear flow signal, in other words:-

$$\psi = \frac{\sum |Wdv|}{\sum \bar{W}dA} \quad (5.19)$$

where (dv) is the volume of each individual loop, A is the flowmeter cross-sectional area and \bar{W} is given by Equation (2.15). If the flowmeter is ideal, the swirl signal must be

zero and, therefore, the quantity (ψ) has to be zero too. The point electrode flowmeter, for example, gave ψ equal to 83.5%, while the flowmeter of Section 5.4 gave ψ equal to 23.5%.

5.6 Ideal (Integrated Voltage) Flowmeter With a Uniform Magnetic Field

An ideal flowmeter with a rectangular flow tube has been suggested by Bevir⁽⁸⁾ in which the condition $\text{curl } \underline{W} = 0$ is satisfied. Both line and large electrodes can be used provided they are of constant width in the direction of a uniformly applied magnetic field.

In this section, Bevir's ideal flowmeter has been converted into an integrated voltage flowmeter with a circular flow tube. The procedure starts by solving the three-dimensional Laplace equation numerically, for the virtual potential (G) inside the rectangular flowmeter, using cartesian co-ordinates. The boundary conditions are similar to those given in Section 2.2.1 apart from the shape of the electrode which is a line electrode in the present case. Knowing the virtual potential (G) distribution inside the flowmeter enables the value of (G) on the wall of a circular flow tube centred inside the rectangular tube (see Fig. 5.9) to be interpolated. A quadrature interpolation method can be used for this purpose (Harris⁽²⁴⁾). The resulting wall potentials can then be considered as the required electrode potentials which give the same type of virtual current inside the circular flow tube as that of the line electrode in the

rectangular flow tube.

Table 11 shows the resulting values of the electrode potentials (for a quarter flowmeter only) which are obtained by using this method. These results are then used as wall boundary conditions and together with the other boundary conditions (Section 2.1.1), the Laplace equation was solved, (using the finite difference method in polar-cylindrical coordinates) and the virtual potentials inside the flowmeter were obtained. The required virtual currents were then determined by using Equation (2.12).

Since Bevir's ideal flowmeter has a uniform magnetic field, a similar field has to be applied to the integrated voltage flowmeter. This field has the following components (the notation refers to Fig. 5.10):-

$$\left. \begin{aligned} B_r &= B_o \cos \theta \\ B_\theta &= -B_o \sin \theta \end{aligned} \right\} \quad (5.20)$$

where B_r and B_θ are the radial and circumferential components respectively of the uniform magnetic field.

The weight function distribution for this type of flowmeter was then calculated from both the uniform magnetic field and the required virtual currents (Equation (1.14)).

The results gave a percentage non-uniformity (ϵ) of the weight function of 0.25% which is very small if compared with the point electrode flowmeter (47.8%). The value of ψ has also been calculated and it can be seen in Table 12.

5.7 Integrated Voltage Flowmeter for Three-Dimensional Flows

The ideal flowmeter of the previous section (5.6) has practical drawbacks in that a uniform magnetic field is needed and also many sets of electrodes, in the flow direction, have to be provided which make the electrodes very long. However, in this section we try to approach the condition ($\nabla \times \underline{W} = 0$) from another angle, leading to a circular tube flowmeter with a short magnetic field and short electrodes.

The divergence of \underline{W} is given as follows:-

$$\nabla \cdot \underline{W} = \nabla \cdot (\underline{B} \times \underline{J}_v)$$

which further simplifies to:-

$$\nabla \cdot \underline{W} = \underline{J}_v \cdot (\nabla \times \underline{B}) - \underline{B} \cdot (\nabla \times \underline{J}_v)$$

But since $\nabla \times \underline{B} = 0$ (Equation (1.2)) and $\nabla \times \underline{J}_v = 0$ (Equation (2.9)), therefore:-

$$\nabla \cdot \underline{W} = 0 \quad (5.21)$$

From the condition ($\nabla \times \underline{W} = 0$), the value of \underline{W} can be represented as a gradient of a scalar potential (ϕ):-

$$\underline{W} = \nabla\phi \quad (5.22)$$

By combining Equations (5.21) and (5.22), the scalar potential ϕ is then given by:-

$$\nabla^2 \phi = 0 \quad (5.23)$$

Hence the scalar potential ϕ is a harmonic function.

If we can find the harmonic solution with properly adjusted boundary conditions so that its gradient components at every test point are equal to the corresponding components of the weight function, then Equation (5.22) is satisfied. This leads to the fulfilment of the condition $\text{curl } \underline{W} = 0$.

5.8 Optimization Method for Flowmeters Designed for Three-Dimensional Flows

In this section, we seek an answer to the question: "Given the magnetic field inside the flowmeter tube, what are the wall boundary conditions which make the weight functions of each test point inside the flowmeter equal to a gradient of some specific scalar potential (see Section 5.7)?"

The initial step for optimization of this case is similar to the one that was followed in Section 5.4, that is, the weight function is evaluated at each test point near the boundary using the known magnetic field and the virtual current which is generated by different positions of the electrodes. This time these weight functions are not integrated along the axial direction because the value of their components (W_r, W_θ, W_z) are required at every test point.

In order to obtain a harmonic potential (ϕ) and its gradient ($\nabla\phi$), sets of "artificial electrodes" at different nodes have to be considered. According to Bevir's ideal flowmeter (see Reference 8), the stream lines of the weight

functions are of the shape shown in Fig. 5.11. In order to make the stream lines of potential gradient similar to that of the weight function of the ideal flowmeter, sets of "artificial electrodes" have to be orientated as shown in Fig. 5.11.

The Laplace equation (5.23) is then solved numerically using the finite difference method, for cylindrical-polar coordinates in order to obtain the potential (ϕ) distribution for a single "artificial electrode". The following boundary conditions are used (the notations are referred to Fig. 5.12):-

1. At the surface ABC, $\frac{\partial \phi}{\partial z} = 0$
 2. At the surface ABDE, $\frac{\partial \phi}{\partial \theta} = 0$
 3. At the surface ACFE, $\frac{\partial \phi}{\partial \theta} = 0$
 4. At the surface FED, $\phi = 0$
 5. At the surface BCFD, $\frac{\partial \phi}{\partial r} = 0$ (Insulating surface)
 6. At the point electrode, $\phi = + 1$
-] (Surfaces of symmetry)

The resulting potential distribution can be used to calculate the three components of the potential gradient $(\nabla \phi)_r$, $(\nabla \phi)_\theta$ and $(\nabla \phi)_z$ at each test point near the boundary.

When the artificial point electrode is shifted circumferentially and/or axially, the components of the potential gradient can be calculated again in the same way as that explained in Section 5.4.

Now we have the weight function components which are produced by a set of electrodes whose surface potentials can be varied by adjusting the values of α in a similar way

as in Section 5.2. Similarly, we also have the potential gradient components which are produced by a set of artificial electrodes whose surface potential can also be varied by adjusting another set of values of, say, β . Since the required condition is $W = \nabla\phi$ (from Equation 5.22), then the term $(W - \nabla\phi)$ has to be minimized. Hence the condition which must be optimized can be expressed in the following matrix notation:-

$$\begin{bmatrix} W \\ \vdots \\ -\nabla\phi \end{bmatrix} \begin{bmatrix} \alpha \\ \beta \end{bmatrix} = \begin{bmatrix} \delta \end{bmatrix} \quad (5.24)$$

where δ is the right hand side column, and α and β both are column vectors. Here n and m are the total number of the electrodes and the artificial electrodes respectively. The relation (5.24) can be written out in full and takes the following form:-

$$\begin{bmatrix} w_{1,1} & w_{1,2} & \dots & w_{1,n} & -(\nabla\phi)_r^{1,1} & \dots & -(\nabla\phi)_r^{1,m} \\ r & r & & r & r & & r \\ w_{1,1} & w_{1,2} & \dots & w_{1,n} & -(\nabla\phi)_\theta^{1,1} & \dots & -(\nabla\phi)_\theta^{1,m} \\ \theta & \theta & & \theta & \theta & & \theta \\ w_{1,1} & w_{1,2} & \dots & w_{1,n} & -(\nabla\phi)_z^{1,1} & \dots & -(\nabla\phi)_z^{1,m} \\ z & z & & z & z & & z \\ w_{2,1} & \cdot & & \cdot & \cdot & & \cdot \\ r & \cdot & & \cdot & \cdot & & \cdot \\ w_{2,1} & \cdot & & \cdot & \cdot & & \cdot \\ \theta & \cdot & & \cdot & \cdot & & \cdot \\ w_{2,1} & \cdot & & \cdot & \cdot & & \cdot \\ z & \cdot & & \cdot & \cdot & & \cdot \\ \cdot & \cdot & & \cdot & \cdot & .. & \cdot \\ \cdot & \cdot & & \cdot & \cdot & & \cdot \\ \cdot & \cdot & & \cdot & \cdot & & \cdot \\ \cdot & \cdot & & \cdot & \cdot & & \cdot \\ \cdot & \cdot & & \cdot & \cdot & & \cdot \\ \cdot & \cdot & & \cdot & \cdot & & \cdot \\ \cdot & \cdot & & \cdot & \cdot & & \cdot \\ \cdot & \cdot & & \cdot & \cdot & & \cdot \\ \cdot & \cdot & & \cdot & \cdot & & \cdot \\ \cdot & \cdot & & \cdot & \cdot & & \cdot \\ \cdot & \cdot & & \cdot & \cdot & & \cdot \\ w_{k,1} & w_{k,2} & \dots & w_{k,n} & -(\nabla\phi)_r^{k,1} & \dots & -(\nabla\phi)_r^{k,m} \\ r & r & & r & r & & r \\ w_{k,1} & w_{k,2} & \dots & w_{k,n} & -(\nabla\phi)_\theta^{k,1} & \dots & -(\nabla\phi)_\theta^{k,m} \\ \theta & \theta & & \theta & \theta & & \theta \\ w_{k,1} & w_{k,2} & \dots & w_{k,n} & -(\nabla\phi)_z^{k,1} & \dots & -(\nabla\phi)_z^{k,m} \\ z & z & & z & z & & z \end{bmatrix} \begin{bmatrix} \alpha_1 \\ \alpha_2 \\ \alpha_3 \\ \cdot \\ \cdot \\ \cdot \\ \alpha_n \\ \beta_1 \\ \beta_2 \\ \beta_3 \\ \cdot \\ \cdot \\ \cdot \\ \beta_m \end{bmatrix} = \begin{bmatrix} \delta_1 \\ \delta_2 \\ \delta_3 \\ \cdot \\ \delta_{3k} \end{bmatrix} \quad (5.25)$$

where the $w_{i,j}$ and $(\nabla\phi)_{i,j}$ are the weight function and the potential gradient respectively for the i th test point when the electrode is placed at the j th point, and k is the total number of the test points.

The number of columns of matrix (5.25) is equal to $(n + m)$. Therefore, in order to have an efficient simultaneous system, $(n + m)$ linearly independent equations are needed. Each test point yields three equations (one in each co-ordinate direction). Therefore, the number of test points should be just over $(n + m)/3$.

First of all, a reasonable length for the electrodes has to be chosen (i.e. the value of n is fixed). In this case 4 sets of electrodes were selected (each set represents 8 electrodes, see Fig. 5.6). Next the length of the artificial electrodes is chosen to be the whole area of interest (see Fig. 5.11). In this case 7 sets of artificial electrodes are thought to be adequate (i.e. the value of m is fixed). Hence the number of the sets of the test points used should be just greater than $(4 + 7)/3 = 3.67$. Therefore, 4 sets of test points were used. When the resulting matrix was analysed (using the computer NAG library subroutine⁽³⁴⁾), the rank was equal to $(n + m)$. If the rank was less than $(n + m)$, then some more test points have to be considered.

In order to satisfy Equation (5.22), the values of the δ_i have to be set to zero. Hence the values of the coefficient α 's and β 's which give the specified condition on the right hand side of this system have to be calculated.

Since the matrix (5.25) forms a homogeneous system (where the right hand side is all zero), a trivial solution

is then expected to be obtained (Kreyszing⁽³¹⁾), where the α 's and β 's are all zeros. In order to achieve a non-trivial solution for this system, the following two ways have been tried. A linear equation is added to this matrix in which the sum of the integrated weight function (\bar{w}) in the flowmeter centre is made unity, i.e:-

$$\bar{w}_{c,1}^{\alpha_1} + \bar{w}_{c,2}^{\alpha_2} + \bar{w}_{c,3}^{\alpha_3} + \dots + \bar{w}_{c,n}^{\alpha_n} = 1.0 \quad (5.26)$$

where the subscript c is referred to the centre. The draw-back of this method is that the number of the matrix equations is increased whilst the number of the variables is still the same. This, obviously, increases the constraint on the solution of this system. An alternative way of obtaining a non-trivial solution can be achieved by fixing some of the β 's. The columns which are multiplied by these β 's are then transferred to the right hand side after changing signs. The resulting system, therefore, becomes non-homogeneous. The number of the fixed β 's has to be as small as possible since it creates some constraints on the solution.

Since the system is overdetermined and because of the right hand side constraints, no exact solution for this matrix can be achieved. However, the method of least squares approximation was used to solve this system. In this method, Equation (5.17) is applied by differentiating the function f (the sum of the squares of the residue of each linear equation) with respect to the whole α 's and β 's in the same way as that explained in Section 5.4. A square matrix is then set up as a result of this differentiation. The resulting square matrix

is then solved by using a computer library subroutine which was used to solve matrix (5.18). The solution contains the values of the coefficient α 's and β 's. The potential on each electrode is then calculated by using these α 's in Equation (5.7).

Table 13 gives the electrode potentials which are obtained by this optimization method for the type 1 flowmeter with a 99.5 mm flow tube diameter and with an electrode length of $1.3 \times$ diameter (4 sets of point electrodes). The resulting potentials are then used as boundary conditions (using a specially written computer program) in order to calculate the flowmeter weight functions (see Section 2.3). The results gave a percentage non-uniformity (ϵ) of the weight function of 1.4%. The value of the performance measure (ψ) has also been evaluated and it can be seen in Table 12.

5.9 Conclusions and Discussions

It has been shown in this chapter that it is possible to superimpose the virtual potentials of different point electrodes, as can be seen in Figs. 5.2 - 5.5. In the superposition method, the problem of mixed boundary conditions does not arise since the point electrodes are assumed very small and, therefore, no alterations in the nature of the wall boundary conditions are expected. This fact made it possible to use the superposition method to solve for the virtual current and the weight function.

An optimization method for a flowmeter intended for rectilinear flows has been explained in Section 5.4. The

optimized flowmeter was an adaptation of the commercial flowmeter described in Section 2.1.1. The predicted results of the optimized flowmeter gave $\epsilon = 0.92\%$, while the value of ψ for this flowmeter was 23.5%. The latter value is relatively high as expected, since the assumption made on the optimized flowmeter is that the flow profile is rectilinear whilst ψ refers to the three-dimensional flow behaviour. Table 16 gives the computed change of the sensitivity of the optimized flowmeter when subjected to distorted profiles. The computed values were based on the velocity profile measurements, where the distortion orifice was placed at 5.5 diameters upstream of the flowmeter mid-point. Because this distance is large comparatively, the flow profile is nearly rectilinear and the flowmeter behaviour approximates to the ideal case. Similar results with the orifice placed at 2.5 diameters cannot be calculated here due to the difficulties in measuring the velocity profile explained earlier in Chapter 3.

Thus it can be concluded that the optimization method is capable of giving the required electrode potentials for any flowmeter provided its magnetic field distribution inside the flowmeter is known in the r and the θ directions.

A method for converting Bevir's ideal flowmeter into a circular flow tube flowmeter has been described in Section 5.6. As a result of using the interpolation in this method, the potentials of the electrodes of the resulting flowmeter are subject to errors. However, the value of ϵ was calculated for this flowmeter and it was 0.25% which is very small and satisfactory in comparison with other designs. The value of ψ was 10.2% which might be even smaller if the exact potentials

on the electrodes were obtained. This value of ψ was used as a reference to compare with the performance measure of the other flowmeter types (see Table 12).

Another method of optimizing a flowmeter designed for three-dimensional flows has been discussed in Section 5.8. The optimized flowmeter was also an adaptation of the commercial design described in Section 2.1.1. The values of ϵ and ψ for this flowmeter were 1.4% and 9.95% respectively which are small in comparison with point electrode flowmeter performance ($\epsilon = 47.8\%$, $\psi = 83.5\%$). This method of optimization can be used for any type of flowmeter provided its magnetic field distribution inside the flowmeter is known in the r , θ and z directions. In this optimization method, some of the β 's have to be fixed in order to solve the matrix. Fig. 5.13 shows the effect of the number of the fixed β 's on the value of the performance measure ψ . It can be seen that as the number of the fixed β 's increases, the value of ψ is increased. This is due to the increasing effect of the constraints on the matrix solution.

The grid lattice for a quarter flowmeter tube was $8 \times 8 \times 8$. This size of lattice was used for the whole numerical optimization of this chapter. It was not possible to use a finer grid due to the limitation of the computer storage.

CHAPTER 6DESIGN OF A CONTACTLESS ELECTRODE
FLOWMETER WITH AN IMPROVED
WEIGHT FUNCTION6.1 A Flowmeter Design Based on the Optimization Method

A method of optimizing the performance of a typical-commercial flowmeter in which the flow profile is assumed rectilinear has been shown in the last chapter. The results of this optimization are used here in designing an integrated voltage flowmeter with strip electrodes (Fig. (6.1)). The required virtual potential on these strips were the values resulting from the optimization method. The magnetic field has to be the same field used in the optimization (type 1 flowmeter, Section 2.1.1).

Since the grid lattice used in the numerical optimization was $8 \times 8 \times 8$ for a quarter flowmeter tube, then only 8 strips with different virtual-potential appeared on each quarter of the flowmeter. The value of the resulting virtual-potential was very small on the 8th strip (the farthest from the conventional electrode position). Hence, the potential of this strip could be ignored. So we were left with 7 strips on each quarter of the flow tube.

The radial component of the virtual-current across each surface of the strip was calculated from the gradient of the values of the flowmeter virtual-potentials G (Section 5.4). The values of the virtual current were then normalized in order to obtain a unity total current from the large electrode. Also, the virtual-voltages on each strip were

divided by the total current for the same reason. The normalized values of voltages and currents on and from each strip electrode are shown in Table 14 (for one quarter of a large electrode). The first strip had only half the strip area of the others, since its place was at a plane of symmetry. Hence type 1 flowmeter with these virtual-voltages (or with the same virtual-voltage ratio) on each strip electrode will give a weight function distribution with a very small ϵ as predicted theoretically in the last chapter ($\epsilon = 0.92\%$).

6.2 Contactless Electrodes

The virtual-potentials of the strip electrodes of the optimized flowmeter cannot be maintained constant if the strips make contact with the metering liquid. This is because of the non-uniform contact resistance from the deposit of dirt, carried by the liquid, on the electrode surface. This deposit could result in serious deformation of the virtual current distribution. In order to avoid this problem, a contactless type of large electrode was considered. Two different types of contactless electrodes can be used.

1. In the first type, a material of high resistivity compared to that of the liquid is placed between the electrode and the metering liquid. Therefore, changes in contact resistance will result in much smaller deviation of the virtual current. There was difficulty in finding a suitably high resistive material (volume resistivity about

10^6 ohm-meter is necessary for meters intended for use with tap water). STYCAST 1970 (product of Emerson and Cumming Company), which is a metal filled epoxy resin having a resistivity of about 10^{-4} ohm-meter, was considered. This material must be mixed with a high resistivity resin diluent in order to obtain the required resistivity. A number of experiments in which STYCAST 1970 was mixed with a resin diluent in different proportions were carried out to give the required resistivity. In the experiments, a 3% by weight catalyst 9 was added to the mixture, stirred thoroughly and poured inside a small rectangular mould which was specially made of PTFE to prevent the casting mixture sticking to the mould. The whole assembly was then put in a vacuum chamber to extract all the air bubbles from the mixture. The mould was then put inside an oven at a temperature of about 75°C and left for one hour to complete the cure. The resistance of the specimen was measured by using a digital voltmeter, in order to find its resistivity. The results of the measurement showed that the resistance of the specimens was unstable due to the fact that the conducting filling cannot be dispersed uniformly in the mixture even if it is mixed thoroughly. This was probably due to gravity effects.

A different type of resistive material (ECCOBOND 60C which is a carbon filled resin and having a resistivity of 0.4 ohm-meter) was also tried. After casting and curing, the resistance of specimens made of this material mixed with a resin diluent was measured and the results also gave an unstable resistance. In addition, some air bubbles appeared

in the mixture during the curing time in spite of using a vacuum chamber. Hence it was decided not to use resistive material.

2. In the second type, a dielectric material was used instead of the resistive one, and was actually employed in designing the integrated voltage flowmeter. The flow signal can then be picked up by the large electrodes through the dielectric. The properties of the material used here as an insulator are considered in the next section.

The virtual-potential distribution on the meter boundary was achieved by changing the thickness of the dielectric material (i.e. changing the capacitance), as shown in the schematic drawing (6.2).

6.3 Some Consideration for the Optimized Flowmeter

6.3.1 Insulating Material Choice

It has been shown that the insulating wall between the large electrodes and the metering liquid has to be built with a variable thickness. The required insulating material, therefore, must have some specified properties. The relative permittivity of this material must be relatively high in order to reduce the flowmeter internal impedance. Also this material has to be hard to prevent the microphonic effect which could be detected by the electrodes as a result of the flowing of the metering liquids over the insulating wall. The most convenient material was the Araldite CY219 plus hardener HY219 and accelerator DY219.

This material was found hard experimentally and its relative permittivity was about 6.3 - 6.8 at 50 Hz (as claimed by the manufacturer).

Another insulating wall has to be built between the large electrodes and the outside of the flowmeter (Fig. (6.3)). The insulating material of this wall, therefore, has to be chosen for its strength in structure, (to keep the flowmeter assembly in one strong piece) and for its low relative permittivity, in order to obtain low coupling capacitance to earth. The material chosen was Araldite AY105 plus hardener HY951. The permittivity of this material, as given by the manufacturer, was about 3 at 50 Hz, and it was found experimentally that this material was also strong enough to form the outer part of the flowmeter assembly.

6.3.2 Some Calculations for the Contactless Flowmeter

The values of the insulating wall thickness of each strip electrode can be obtained by selecting a suitable value for the insulating thickness of any single strip. This value enabled the wall thickness of other strips to be found according to the virtual-potential distribution predicted on each strip. The minimum value of the thickness of the middle strip was dictated by the fabrication method to be employed. This value was 1.5 mm. Table 15 shows the resulting values of the insulating thickness and the capacitance of each strip. The capacitance between the large electrode and the metering liquid was then calculated and it was about 169.7 pF. Therefore, the total capacitance between the two large electrodes was 84.8 pF which gave a

flowmeter internal impedance of 3.8×10^7 ohm, for a 76 mm tube diameter and a 50 Hz frequency.

The signal leakage from the electrode to the earth throughout the outer wall was calculated as follows.

The capacitance between each strip electrode and the outside was determined and the total capacitance between the large electrode and the earth was found to be 8.7 pF. Then, assuming that Z_f is the impedance between the fluid and the large electrode, Z_s is the impedance between the large electrode and the earth, V_f is the flow signal and V_e is the signal detected by the electrode (see Fig. (6.4)):-

$$I = \frac{V_f}{Z_f + Z_s}$$

$$V_f - V_e = IZ_f$$

$$\frac{V_e}{V_f} = 1 - \frac{1}{1 + \frac{Z_s}{Z_f}} = 0.95$$

Therefore, the signal loss was 5%.

6.3.3 Choice of the Amplifier

Since the flowmeter output impedance was 3.8×10^7 Ω and the input impedance of the series 400 MAGFLO Converter (which was to be used for the optimized flowmeter) was 2×10^7 Ω, a buffer amplifier was necessary. The voltage follower LM310 was connected to each electrode. This is an operational amplifier internally connected as a Unity-gain

amplifier. The input resistance of this amplifier was $10^{12} \Omega$ and the input capacitance was 1.5 pF. Thus the total input impedance of this amplifier was $2 \times 10^9 \Omega$ for a 50 Hz frequency and this was just what was needed to couple the flowmeter to the converter.

Since the source internal impedance of a contactless flowmeter was of a capacitive type, no path for the DC bias current was available. Therefore, the amplifier input must be shunted by a resistor of at least 100 times the flowmeter internal impedance. Millman and Halkias⁽³²⁾ gave the AC voltage follower circuit (Fig. (6.5)) in which a feedback connection was used. This circuit was similar to that suggested by Mr. D. Harrison*. In order to make use of this circuit, the values of the resistance and capacitance of the circuit have to be calculated for our particular design. From Fig. (6.5), the gain characteristic is given by**:-

$$V_o = (V_i - V_o) \cdot \frac{A}{1 + j\omega T} \quad (\text{i.e. a single pole})$$

Where T is the open loop break frequency and where A is the open loop gain. Therefore:-

* Mr. D. Harrison, Flowmetering Instruments Limited, Stroud, Gloucestershire, GL5 2NN, England. Private communication, 1977.

** I am indebted to the external examiner for pointing this out to me. In my original approach the amplifier open loop gain was assumed infinity.

$$V_o = \frac{V_1}{\left(1 + \frac{1}{A} + \frac{j\omega T}{A}\right)}$$

Applying Kerchoff's law at node 1 we get:-

$$\frac{V_1 - V_2}{R} + (V_o - V_2) j\omega C - \frac{V_2}{R} = 0$$

Therefore:-

$$V_1 \left(\frac{1}{R} + \frac{j\omega C}{\left(1 + \frac{1}{A} + \frac{j\omega T}{A}\right)} \right) = V_2 \left(\frac{2}{R} + j\omega C \right) \quad (6.1)$$

$$i = \frac{V_1 - V_2}{R}$$

Using Equation (6.1) after rearrangement $V_1/i = R_{eff}$
(the effective shunt impedance):-

$$R_{eff} \approx \frac{R (2 + j\omega CR)}{1 + \frac{j\omega CR}{A} (1 + j\omega T)} \quad (6.2)$$

with the values $C = 0.22 \mu F$, $R = 10^7 \Omega$, $A = 10^4$ (from the catalogue), the amplifier break frequency open loop = 10 Hz and the operating frequency is 50 Hz. Therefore:-

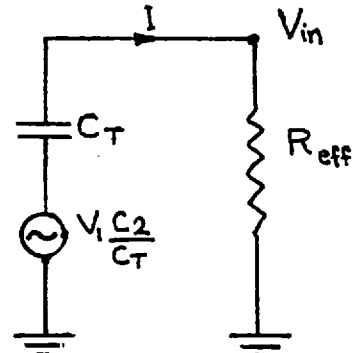
$$R_{eff} \approx 10^7 (113.1 + j 1043.2)$$

6.3.4 The Capacitive Effect on the Phase of the Flow Signal

The complex circuit of the optimized flowmeter consisted of electrode capacitance, C_2 , composite lead and earth capacitance, C'_3 , amplifier internal capacitance, C''_3 , and the preamplifier input impedance, R_{eff} . The equivalent circuit of this flowmeter is shown in Fig. 6.6. The flow signal was subjected to phase shift due to the existence of these capacitances. Hence it was necessary to calculate the phase angle of the flow signal at the preamplifier input in order to estimate the resulting error. For this flowmeter design, $C_1 = 0.1 \mu\text{F}$, $C_2 = 169.7 \text{ pF}$, $C'_3 = 8.7 \text{ pF}$, $C''_3 = 1.5 \text{ pF}$, and $f = 50 \text{ Hz}$. If $C_1 \gg C_2, C'_3, C''_3$, then the circuit of Fig. (6.6) can be represented as:-

where $C_T = C_2 + C'_3 + C''_3$, and V_{in} is the voltage at the amplifier input.

$$I = \left(V_1 \frac{C_2}{C_T} \right) \frac{1}{R_{\text{eff}} + z_T}$$



where $R_{\text{eff}} = 10^7 (113.1 + j 1043.2)$ and $z_T = \frac{-j}{\omega C_T} = -j 1.77 \times 10^7$; $V_{\text{in}} = I R_{\text{eff}}$. Therefore:-

$$V_{\text{in}} = \left(V_1 \frac{C_2}{C_T} \right) \frac{R_{\text{eff}}}{R_{\text{eff}} + z_T}$$

The signal phase shift is phase shift of:-

$$\frac{R_{\text{eff}}}{R_{\text{eff}} + z_T} = \frac{10^7 (113.1 + j 1043.2)}{10^7 (113.1 + j 1041.5)}$$

Therefore:-

$$\theta = \tan^{-1} 1.82 \times 10^{-4} = 0.01 \text{ degree}$$

where θ is the phase shift of the flow signal. This value was small and it was well within the error in setting the reference current-phase angle for the converter. The effect of this error was small and was neglected.

6.4 The Construction of the Optimized Flowmeter

6.4.1 Design of the Casting Mould

Fig. (6.2) shows that the insulating thickness of the Araldite varies in steps. This is due to the grid lattice used in the numerical solution of the potential distribution. It is preferable to make the insulating thickness change smoothly instead of in steps in the actual design. This is performed by fitting a curve through the middle of each strip. The form of the large electrode will, therefore, take the shape of this curve. In order to produce such a contactless large electrode, a special mould was designed and constructed in the Mechanical Engineering Department of Imperial College. The mould assembly was made of aluminium and it consisted of the following elements (Fig. (6.7) gives the dimensions of this mould):-

1. Outer Mould Casing

This was a cylinder of 111 mm internal diameter, 95 mm long and 4.8 mm thick. This diameter was purposely made large, in order to obtain an Araldite Casting with a

large diameter which could be machined to the required outside diameter.

2. Curve-former Core

The shape and the dimensions of this core can be seen in Fig. (6.7). It consisted of four segments with end plates which held the segments together in one piece. There was also a spigot on each end which was used to locate the core in the centre of the outer mould casting.

3. Central-circular Core

This was a 70 mm outside diameter core, consisting also of four segments with end plates which kept these segments in one piece. There was also a spigot on each end of this core, which was used for the same purpose as for the curve-former core. The diameter of this core was made smaller than the required bore, in order to achieve a small bore for the casting which could be machined to the required bore.

4. Locating Plate

Two locating plates with concentric holes of 28.6 mm diameter were used to position the core accurately in the outer casing. One of these plates had four eccentric holes of 9 mm diameter which were used for air release during the casting procedure.

6.4.2 Casting Procedure

The optimized flowmeter with the contactless large

electrodes has been made in the laboratory by casting the Araldite in two stages as described below:-

A. In the first stage of casting, the curve-former mould was fitted in the centre of the outer casing mould. This was accomplished with the help of the spigot and the locating plates. To prevent the casting material sticking to the mould surfaces, the mould was coated with a releasing agent (silicone grease).

The casting procedure started by mixing, at room temperature, Araldite AY105 with the hardener HY951 with a ratio of 100/10 by weight. The usable time of the resulting mixture was 45 - 60 minutes. This time was found to be enough for pouring the mixture into the mould then putting the assembly in a vacuum chamber for 20 - 30 minutes. In this way, all the air bubbles were extracted. The casting material was then cured by placing the casting assembly in the oven for 3 hours at 60°C. When the casting and curing processes were complete, the mould assembly was dismantled by removing one of the locating plates first. The curve-former core was extracted smoothly, and finally the outer mould casing was taken off the cured casting. The resulting casting had, therefore, an internal curve surface similar to that of the former core, while the outside surface was smooth and circular. Finally, two holes of 3.2 mm diameter were drilled through the centre of each side of the resulting casting. These holes were used for the leads for the connections to the large electrodes.

B. Before the second stage of casting was started, the large electrodes had to be fixed on the curved surface of the first stage casting. The electrodes used were made of phosphor bronze which had an electrical conductivity of 1.3×10^7 mho/meter. This electrode was 0.1 mm thick, 112 mm wide (in the θ -direction) and 76 mm long (in the axial-direction).

The casting mould was again made ready for the second stage. The resulting casting of the first stage (including the two fixed large electrodes) was placed back inside the outer casing mould. The circular core was then positioned in the centre of this assembly with the help of the locating plates and the spigots. The internal surfaces of the mould were also coated with the silicone grease for ease of release as mentioned earlier.

The procedure for casting started by mixing the Araldite CY219 and its hardener HY291 together at room temperature, and stirring them thoroughly. The mixing ratio was 100/50 by weight. The accelerator was then added to the mixture at a ratio of 5 parts to 100 parts of resin, the resulting mixture was well stirred until a uniform colour was obtained. The usable time of the mixture was dependent on the percentage of the accelerator used. For this case, the usable time was 45 - 60 minutes. During this time, the mixture was poured into the mould and then the air bubbles were extracted by using a vacuum chamber for about 30 minutes. Finally, the whole assembly was put again in the oven at about 60° temperature for 3 hours to complete the curing. The casting mould was then dismantled by removing

the upper locating plate first (see Fig. (6.8)). The outer mould casing was then pulled away from the cast Araldite as shown in Fig. (6.9). The central core was removed and the resulting-complete casting was obtained (see Fig. (6.10)). This casting procedure failed at the first and second attempts, but it was successful for the third trial.

6.5 The Assembly of the Optimized Flowmeter

The cast Araldite was used to assemble the optimized flowmeter after machining its bore to the required size (76 mm). Since the magnetic field used in the optimization method was the field of type 1 flowmeter, a similar magnetic field has to be produced for the optimized flowmeter. A bare stainless steel tube of 114.3 mm bore (similar to the tube of the type 1 flowmeter but without the lining, see Fig. (6.11)) was provided by Flowmetering Instruments Limited, in order to construct the optimized flowmeter with the same coil arrangements. Two holes of about 7.5 mm diameter located in the centre of this tube were used for the connections of the leads for the large electrodes. The outside diameter of the cast Araldite was then machined to 114.3 mm to fit the internal diameter of the stainless steel tube. Two extra lengths of ABS pipe of 114.3 mm outside diameter and 76 mm bore were used as a tube extension. These pipes extended from the edges of the cast Araldite to the flanges of the stainless steel tube. The ABS pipes were joined to the two edges of the cast Araldite by using a silicone rubber which acted as a sealing material as well as an adhesive. This assembly was then fitted

inside the stainless steel tube and the cast Araldite was positioned in the centre of the tube (see Fig. (6.12)). The new lining of the flowmeter was then the ABS pipe and the cast Araldite.

In order to minimize the signal losses from the leads of the electrodes, the buffer amplifier was placed very close to the large electrode (to reduce the lead length). In this case, the physical size of the amplifier (chip) must be small, since the flowmeter assembly was very compact. The LM310 chip had a 4 mm height and 8 mm diameter; this size was found suitable for the space available behind the electrodes. The chip was fixed at the centre of a circular-insulator board (26 mm diameter) plus two electrolytic ITT capacitors of 2.2 μ F used for smoothing the DC power supply to the chip.

The small board containing the electronics (Fig. (6.5)) was then placed on the outside surface of the stainless steel tube. The whole circuit was then covered with a screening cup in order to obtain a complete shield to the preamplifier assembly. The output of the preamplifier was then fed to the converter in the conventional manner. Finally, the coil assembly was replaced in position in order to obtain the same magnetic field inside the flow tube. Fig. (6.13) shows the stage at which the coils and the yoke were fixed on the stainless steel tube of the optimized contactless flowmeter.

6.6 Accuracy and Errors

In order to find out the actual thickness of the cast

Araldite (between the large electrode and the metering fluid), the dimensions (radii) of the curved core were measured by using the "Societe Genevoise Universal Measuring Machine" type MU-214B. The measuring accuracy of this machine, as given by the manufacturer, is as follows: If (L) is the length measured in mm, the measuring accuracy (p) in μ is given by $(p = 1 + 0.0025 L)$. Hence, for a maximum length measured by this machine (about 47.6 mm), the accuracy (p) is 1.12μ . This value gave a maximum error of $\pm 0.0024\%$.

A circular rotary table was mounted on the machine and used for laying out the curved core and for the measurements in polar coordinates. The length measurements were performed in a horizontal plane by measuring the movements of the longitudinal carriage in which a microscope of $\times 50$ magnification was mounted in order to read the carriage movement. Owing to the specially wide intervals of the graduation, actual readings to ± 0.0001 mm were easily estimated. This gave a maximum error of $\pm 0.0003\%$. The resolution of the angular readings were made to 10 seconds of arc on a vernier of the graduated drum mounted on the driving shaft controlling the rotation of the table. This gave a maximum error in the length measurements of $\pm 0.021\%$.

The curved aluminium core was centred on the rotary table by using a locating indicator which was mounted in a special tool holder belonging to the measuring machine. The centering was accurate to about 0.025 mm which gave a maximum reading error of $\pm 0.053\%$, while the resolution of this indicator, as given by the catalogue, was ± 0.002 mm.

which gave an error of $\pm 0.0042\%$.

Hence the total expected error from the measuring machine was $\pm 0.081\%$. The measurement of the curved core gave a maximum discrepancy of 5% from the design values. This was clearly due to errors in making the surface profile of the aluminium core.

After the first stage of the Araldite casting, the dimensions of the cast curved mould were then measured using a vernier graduated in 0.02 mm per division. In order to find out the error due to the shrinkage of the cast Araldite, these values were compared with the measured dimensions of the aluminium curved core. The comparison gave a maximum error of about $\pm 0.08\%$ plus a resolution error of $\pm 0.02\%$. Thus the total shrinkage effect added up to $\pm 0.1\%$. Hence the overall accuracy in producing the required profile amounted to 5.1%. The virtual-potentials of the strip electrodes were obtained using the above actual dimensions. These potentials were used (see Chapter 5) as the flowmeter boundary conditions from which the weight functions distribution of the actual optimized flowmeter was found. The results gave a percentage non-uniformity ϵ of the weight function of 3.1%. This value was higher than that predicted because of the errors considered above and due to the fact that the eighth strip electrode was ignored completely. Table 16 gives the computed change in flow signal, of the optimized flowmeter based on actual data, when subject to distorted profiles. The computed values were based on the velocity profile measurements, where the distortion orifice was placed at 5.5 diameters upstream the flowmeter mid-point.

CHAPTER 7OPTIMIZED FLOWMETER EXPERIMENTS7.1 Introduction

The procedure for designing and building the optimized flowmeter has been given in the last chapter. In this chapter, tests of the performance of this flowmeter are presented. The flowmeter was inserted in the test section of the flow rig (Figs. 7.1 and 7.2). Since the bore of the flowmeter was 76 mm and the pipes of the rig were 100 mm bore, a 241 mm long pipe with a 76 mm bore had been specially made to smooth the flow contraction in the upstream section of the flowmeter.

The electrodes and the reference current of the flowmeter were connected to the series 400 MAGFLO converter. The flowmeter coil was energized by about 1.2 amp derived from the mains (240 volts, 50 Hz). A DC power source of \pm 15 volts, operated from the mains voltage, was used to supply the pre-amplifier chips.

The quadrature signal was adjusted first when the flowmeter was full with stationary liquid (economy water). This was accomplished by adjusting the potentiometer of the quadrature loop until the output signal of the converter was eliminated or reduced considerably.

The optimized flowmeter was then ready to be operated and tested. If the converter DC output was negative for forward flow, then reversing the signal leads would correct the situation.

7.2 Flowmeter Linearity

The optimized flowmeter was inserted in the 100 mm line and its linearity was then examined. The flowrate was increased gradually in steps and the weight of liquid in the weighing tank (kg), the reading of the integrator (pulses) and the time of the division of the flow into the tank (using the electronic timer) were recorded for each step. The mean velocities versus the integrator output (pulses/sec) were then plotted in order to obtain the linearity of the optimized flowmeter. Figs. 7.3 and 7.4 show the linearity when the converter range was set to scales 1 and 2 respectively.

7.3 Zero Drift and Repeatability

In order to obtain the value of the zero drift for the optimized flowmeter, the flowmeter and the associated electronics were switched on for 12 hours during one day and for 10 hours during a second day. Most of this time the metering liquid was at rest and the flowmeter reading was registered at various intervals. Sometimes the flow was started just for a few minutes and stopped, then the flowmeter reading was recorded again. The range of the converter was set to scale 1 and the variation of the room temperature was $\pm 5\%$. The maximum zero drift was recorded and it was $\pm 0.2\%$ of full scale.

The repeatability of the optimized flowmeter was also obtained. This was performed by repeating the test on the flowmeter and the output of the converter (pulses/sec) was recorded. This series of tests was carried out over several days and each time the sensitivity of the optimized flowmeter, for a constant undisturbed flow rate, was obtained. The

reading of a bare thermocouple gave the temperature inside the flowmeter, this was nearly the same for each test. Fig. 7.5 shows the graph of the test results, from which the value of the repeatability was found and it was $\pm 0.25\%$.

7.4 Effect of Distorted Profiles

The effect of the distorted profiles on the optimized flowmeter was examined, using two distortion orifices, similar to those given in Fig. 3.10. These were made for this flowmeter (with an orifice area ratio of $\frac{1}{4}$) since the previous orifices were not suitable for the pipe-arrangement of the optimized flowmeter. Each distortion orifice was placed at two different positions. These were 2.5 and 5.5 diameters upstream from the flowmeter mid-point.

In order to ensure that the distorted profiles in the optimized flowmeter (76 mm bore) were geometrically similar to the profiles obtained in type 1 flowmeter (100 mm bore), the Reynolds number must be the same, i.e. 1.64×10^5 (Hansen⁽²³⁾). Since the mean velocity for type 1 flowmeter was 1.64 m/sec, the mean velocity in the optimized flowmeter, for the same Reynolds number, was calculated as 2 m/sec.

Table 17 shows the change in the optimized flowmeter signal when subjected to distorted profiles.

7.5 Effect of Dirt

The effect on the flowmeter performance of the electrode fouling has been shown in the previous chapters. In this section, the same effect on the optimized flowmeter was studied. Since the optimized flowmeter was designed in

such a way that the electrodes were not in contact with the metered fluid, a much smaller fouling effect was expected. However, tests were carried out in order to examine this effect on the quadrature signal and on the sensitivity of the optimized flowmeter.

Part of the inner surface of the optimized flowmeter (which corresponds to half an electrode) was coated with a layer of insulating material of about 0.1 mm thick. The material used was petroleum jelly with a volumetric resistivity of the order 10^{11} ohm-meter. The zero reading of the flowmeter was then read (when the flow tube was full with stationary liquid) and gave an increment of 0.02 mv compared to the reading of the clean flowmeter. The effect on the quadrature signal of half electrode fouling was calculated as 0.1% of full scale. A similar test was carried out by using the insulating material to coat half the inner surface of the flowmeter (which corresponds to the area of one electrode). The effect on the quadrature signal was also calculated as 0.15% of full scale.

In order to find the effect on the flowmeter sensitivity of the electrode fouling, the output signal of the fouled flowmeter was compared with the corresponding signal of the clean flowmeter. The results gave a change in the sensitivity of the optimized flowmeter, when part of the inner surface was coated, as 0.08% for undistorted velocity profile and for Reynolds number of 1.64×10^5 . The change in the sensitivity of the same flowmeter, when half of the inner surface was fouled, was found as 0.17%.

7.6 Conclusions and Discussion

The linearity of the optimized flowmeter was examined for the flow rates up to $0.87 \text{ m}^3/\text{min}$ which is the limit of the flow rig. The results gave a flow signal linearly proportional to the flow rate, as can be seen in Figs. 7.3 and 7.4.

The zero drift of the optimized flowmeter was measured and resulted in $\pm 0.2\%$ of full scale. This is due to small changes in the phase of the quadrature voltage, which produce signals indistinguishable from the flow signal. These changes could be caused by the eddy current and hysteresis loss in the iron-core which produce a phase angle between the exciting current and the magnetic field. Also, the zero drift could be caused by a voltage leakage between the coil and the electrodes and connecting leads. The interference at a frequency equal to, or at a harmonic of, the magnetic field frequency (mains frequency) has some effect on the flowmeter output, resulting in an alteration in the baseline reading.

The repeatability of the optimized flowmeter was examined and resulted in $\pm 0.25\%$ of full scale. This value was obtained from a series of tests in which each test consisted of several runs. The variation in the sensitivity of the optimized flowmeter for fixed flow conditions is shown in Fig. 7.5.

The effect of the distorted profiles on the performance of the optimized flowmeter was also examined. Table 17 shows the experimental results of the change of the flowmeter signal subject to distorted profiles. This change is obviously higher when the distortion orifice is closer to the flowmeter mid-point. The signal changes for the optimized flowmeter are less than the corresponding values of the type 1 and the

point electrode flowmeter. But the values for the optimized flowmeter, when the distortion orifice was at 2.5 diameters, are more than the expected values. This is because the velocity profile is not rectilinear at the region after the distortion orifices. It has a recirculating region which could extend to about 5 diameters downstream of the orifice. The results of the tests on the optimized flowmeter, when the distortion orifice was at 5.5 diameters, are improved considerably because everywhere the velocity profile is nearly rectilinear.

The effect on the optimized flowmeter of a fouled inner surface was studied. The results gave a change in the zero readings, when half and the whole of an electrode was contaminated, of 0.1% and 0.15% of full scale, respectively. These values are very small (as was expected for the contactless flowmeter) in comparison with the corresponding values of type 1 flowmeter (Table 9). Also these values are within the repeatability range of the flowmeter. The same fouling arrangements were also used to find the effect which they had on the sensitivity of the optimized flowmeter. The results showed a change in the flowmeter sensitivity, when compared to the values of a clean flowmeter, of 0.08% and 0.17% for both half and wholly fouled electrodes respectively. These changes are also small in comparison with the values of type 1 flowmeter in which a change in sensitivity of 1.8% was obtained when half of a large electrode was covered.

CHAPTER 8CONCLUSIONS AND FURTHER WORK8.1 Conclusions

In the introduction in Chapter 1, previous theoretical and experimental work on electromagnetic flowmeters was reviewed. The methods developed by Bevir (virtual current theory) provide the most powerful approach. In these, a weight function is used to identify the effect on the signal of flow in any particular region of the flow tube.

The work of this thesis is mainly concerned with the analysis of the electromagnetic flowmeter with large electrodes. Therefore, three flowmeter designs which are typical of recent commercial design practice have been analysed theoretically in Chapter 2. The three-dimensional weight function distribution for each flowmeter was obtained numerically using the finite-difference method. In this method, the accuracy of the solutions was found to be satisfactory. The plots of \bar{W} (the integrated weight function along the axial direction) for each flowmeter with large electrodes are shown in Figs. (2.18), (2.19) and (2.20). The uniformity of the weight function for type 1 flowmeter (with rectangular coils wound around a steel core) is better than that for type 2 (square coil without core). Although the high and low weight function regions for the first flowmeter appear to be more extreme in value, they occupy less area. The uniformity of the weight function of type 3 flowmeter (Bevir type) is worse than that of the other two designs.

The effect on the flowmeter performance of electrode

fouling was also analysed in Chapter 2. The results indicate that, due to the fouling effect, the response of the flowmeter is considerably altered. This alteration is smaller for type 2 flowmeter than for type 1.

Chapters 3 and 4 discuss the experimental work in which a wide variety of tests were used to demonstrate the validity of the solutions of Chapter 2. These were mainly for the magnetic field, the effect of distorted profiles and the virtual current. The results show a satisfactory agreement between tested and computed values. Also the effect of the eddy current on the magnetic field is found to be negligible.

The possibility of using the superposition method is discussed in Chapter 5. This method was then used to solve the virtual current and the weight function with a considerable saving on computing time. A method of optimizing flowmeters designed for rectilinear flows is also discussed in Chapter 5 where a good weight function uniformity was achieved. It was found that this method of optimization is capable of giving the required electrode potential for any flowmeter, provided its magnetic field distribution inside the flowmeter is known in the r and θ directions. Further discussion on optimizing flowmeters intended for three-dimensional flows is presented. The theoretical performance of the resulting flowmeter was satisfactory in comparison with any other design. In this case the magnetic field distribution inside the flowmeter has to be known in the three dimensions. The drawback of this design is that the resulting electrode potentials are not constant along the

flow direction, causing constructional difficulties.

A procedure for making an optimized flowmeter is discussed in Chapter 6. In this design, contactless large electrodes were considered and a dielectric material (Araldite CY219) was placed between the metering liquid and the electrode. It is found that a small error in the thickness of the dielectric wall causes a considerable effect on the uniformity of the flowmeter weight function. Hence careful constructing and machining for the casting mould is necessary.

In Chapter 7, some experimental tests of the performance of the optimized-contactless flowmeter are discussed. The results showed that the effects of the fouling and the distorted profiles are small. The flowmeter linearity, repeatability and zero drift were found satisfactory.

8.2 Further Work

The computer program developed for optimizing a flowmeter for rectilinear flows, using the present method, could easily be applied to optimize the magnetic field for given large electrodes. In this case, the virtual current distribution has to be known inside the flow tube. The results will be the boundary conditions for the scalar-magnetic potential (γ) which produces the required magnetic field. The problem of this method will lie in making a suitable coil which gives these boundary conditions.

Work could be carried out to make the integrated voltage flowmeter designed for three-dimensional flows. The

difficulty of constructing this design arises from the fact that the potentials of the electrodes are not constant along the axial direction. This problem may be overcome by careful design of a casting mould in which the cast-insulating wall thickness varies along the axial direction as well as the circumferential one. Also it would be interesting to measure the values of the virtual current resulting from these electrodes. This could be achieved by using the virtual current rig with suitably-built electrodes. The surface voltages of these electrodes have to be varied axially and circumferentially, in order to simulate the case of an integrated voltage flowmeter.

More work is recommended on improving the computer program which was based on the optimization method for a flowmeter designed for three-dimensional flows. There is a possibility of producing such a flowmeter in which these potentials are constant along the axial direction, although this will impose another constraint on the virtual current.

REFERENCES

1. AL-RABEH, R., BAKER, R. C. and HEMP, J.
"Induction flow-measurement theory for poorly conducting fluids".
Proc. R. Soc. London, Vol. 361, p. 93, 1978.
2. ARNOLD, J. S.
"An electromagnetic flowmeter for transient flow studies".
The Review of Scientific Instruments, Vol. 22, No. 1, p. 34, January, 1951.
3. BAKER, R. C.
"Electromagnetic wall velocimeters".
Ph.D. Thesis, University of Cambridge, February, 1967.
4. BAKER, R. C.
"Solutions of the electromagnetic flowmeter equation for cylindrical geometries".
Brit. J. Appl. Phys., Ser. 2, Vol. 1, p. 895, 1968.
5. BAKER, R. C.
"Effect of non-uniform conductivity fluids in electromagnetic flowmeters".
J. Phys. D: Appl. Phys., Vol. 3, p. 637, 1970.
6. BAKER, R. C.
"Numerical analysis of the electromagnetic flowmeter".
Proc. IEE, Vol. 120, No. 9, p. 1039, September, 1973.
7. BAKER, R. C.
"Electromagnetic flowmeters for fast reactor".
Progress in Nuclear Energy, Vol. 1, p. 41, 1977.
8. BEVIR, M. K.
"The theory of induced voltage electromagnetic flowmeters".
J. Fluid Mech., Vol. 43, p. 577, 1970.
9. BEVIR, M. K.
"Induced voltage electromagnetic flowmeters".
Ph. D. Thesis, University of Warwick, April, 1969.
10. BEVIR, M. K.
"The predicted effects on red blood cells on electromagnetic flowmeter sensitivity".
J. Phys. D: Appl. Phys., Vol. 4, p. 387, 1971.
11. BRITISH STANDARD 1042
"Methods for the measurement of fluid flow in pipes".
Part 1 Orifice plates, nozzles and venturi tubes, 1964.

12. BRITISH STANDARD 1042
 "Methods for the measurement of fluid flow in pipes".
 Part 2 Pitot tubes, 1973.
13. CLARK, D. M. and WYATT, D. G.
 "An improved perivascular electromagnetic flowmeter".
 Medical and Biological Engineering, Vol. 7, p. 185, 1969.
14. COHEN, A. M.
 "Numerical Analysis".
 McGraw-Hill Book Company (UK) Ltd., 1973.
15. CONT, S. D. and DE BOOR, C.
 "Elementary Numerical Analysis".
 McGraw-Hill Kogaknska Ltd., 1965.
16. CUSHING, V.
 "Electromagnetic flowmeter".
 The Review of Scientific Instruments, Vol. 36, No. 8,
 p. 142, August, 1965.
17. DENNIS, J. and WYATT, D. G.
 "Effect of haematocrit value upon electromagnetic
 flowmeter sensitivity".
 Circulation Research, Vol. 24, p. 875, 1969.
18. FARADAY, M.
 "Experimental researches in electricity".
 Vol. 1, p. 55, January, 1832.
19. FISCHER and PORTER.
 "Magnetic Flowmeters".
 Catalogue C1OD, 1967.
20. FISCHER and PORTER.
 "Capacitance type electromagnetic flowmeters".
 Catalogue D1O D1440 e1 - 2/75 N.
21. FLOWMETERING INSTRUMENTS LIMITED.
 "Technical instructions for 'MAGFLO' meters".
 Catalogue ICM-5, November, 1974.
22. FORSYTHE, G. E. and WASOW, W. R.
 "Finite-difference methods for partial differential
 equations".
 John Wiley & Sons, Inc., Publishers, 1960.
23. HANSEN, A. G.
 "Fluid Mechanics".
 Wiley international edition, p. 422, 1967.
24. HARRIS, L. D.
 "Numerical methods using Fortran".
 Charles E. Merrill Books, Inc., Columbus, Ohio, p. 79,
 1964.

25. HAYWARD, A. T. J.
 "The accurate calibration of oil and fuel meters".
 National Engineering Laboratory, East Kilbride, Glasgow.
26. HEMP, J.
 "Improved magnetic field for an electromagnetic flowmeter with point electrodes".
J. Phys. D: Appl. Phys., Vol. 8, p. 983, 1975.
27. HOFMANN, F.
 "Magnetic flowmeter with capacitive signal pick-off".
Flow Measurement of Fluids (FLOMEKO), ed. Spencer, E. A., Holland, 1978.
28. KOLIN, A.
 "An electromagnetic flowmeter. Principle of the method and its application to blood flow measurements".
Proc. of Society for Experimental Biology and Medicine. Vol. 35, p. 53, 1936.
29. KOLIN, A.
 "An electromagnetic recording flowmeter ".
American Journal of Physiology, Vol. 119, p. 355, 1937.
30. KOLIN, A.
 "An AC induction flowmeter for measurement of blood flow in intact blood vessels".
Proc. of the Society for Experimental Biology and Medicine, Vol. 46, p. 235, 1941.
31. KREYSZING, E.
 "Advanced engineering mathematics".
 John Wiley & Sons, Inc., p. 257, 1962.
32. MILLMAN, J. and HALKIAS, C.
 "Integrated electronics".
 McGraw-Hill Kogakusha Ltd., 1972.
33. NAG LIBRARY.
 "FO4ATF" simultaneous linear equations".
 NAGFLIB : 1200/646 : Mk5, November, 1974.
34. NAG LIBRARY.
 "FO1BKF" matrix operations, including inversion".
 NAGFLIB : 1336/0 : Mk5, January, 1976.
35. POTTER, D.
 "Computational physics".
 A Wiley-Interscience Publication, 1973.
36. RUMMEL, T. and KETELSEN, B.
 "Inhomogenous magnetic field enables inductive flow measurement of all practical flow profiles".
Regelungstechnik, Vol. 14, p. 262, 1966.
37. SCHLUMBERGER,
 "Electromagnetic flowmeter, Type BGE, BGA".
 Data sheet FT38 - 19/A and FT38 - 21/A.

38. SCHLUMBERGER,
 "Electromagnetic flowmeter, electrode cleaning system".
 Technical data sheet FT38 - 24/A.
39. SCHLUMBERGER,
 "Electromagnetic flowmeter".
 Patent No. 1 257 137, May, 1972.
40. SCHLUMBERGER,
 "The new range of DEBIMAG 11 electromagnetic flowmeters".
 Catalogue PB38 - 21 IMP 1256 RSC.
41. SEELY, S.
 "Introduction to electromagnetic fields".
 McGraw-Hill Inc., 1958.
42. SHAFFER, M. R., RUEGG, F. W. and WASHINGTON, D. C.
 "Liquid flowmeter calibration techniques".
 Transaction of the ASME, p. 1369, October, 1958.
43. SHERCLIFF, J. A.
 "The theory of electromagnetic flow-measurement".
 Cambridge University Press, 1962.
44. SHERCLIFF, J. A.
 "A textbook of magnetohydrodynamics".
 Pergamon Press, 1965.
45. SMITH, G. D.
 "Numerical solution of partial differential equations".
 Oxford University Press, 1965.
46. SMITH, M. G.
 "Introduction to the theory of partial differential equations".
 Van Nostrand Co. (Canada) Ltd., 1967.
47. SMYTH, C. C.
 "The circular and rectangular channel magnetic flowmeters, by means of Green's theorem and conformal mapping".
 J. of Physics E: Scientific Instruments, Vol. 4, p. 29, 1971.
48. THOMAS, G. B.
 "Calculus and analytic geometry".
 Addison-Wesley Publishing Co. Inc., 1961.
49. WILLIAMS, E. J.
 "The induction of electromotive forces in a moving liquid by a magnetic field and its application to an investigation of the flow liquids".
 The Proc. of the Physical Society, Vol. 42, p. 466, 1930.

50. WYATT, D. G.
"Velocity profile effects in electromagnetic
flowmeters".
In V. C. Roberts (ed.): Blood Flow Measurements,
p. 85, 1972.
51. WYATT, D. G.
"Theory, design and use of electromagnetic flowmeters".
Cardiovascular Flow Dynamics and Measurements,
Chapter 2, p. 89, 1977.

TABLE 1
UNIFORMITY OF WEIGHT FUNCTION ϵ
(EQUATION 2.16) AND SENSITIVITY S
(EQUATION 2.18)

Flowmeter Type	ϵ	S
1	13.4%	1.13
2	14.3%	0.39
3	48.7%	1.31

TABLE 2

DISTORTED PROFILES DUE TO AN ORIFICE DISC AT 5.5 DIAMETER FROM THE
CENTRE OF THE FLOWMETER WITH LARGE ELECTRODE
(THEORETICAL RESULTS AT Re = 1.64 x 10⁵)

Flow Pattern	Percentage change of the sensitivity relative to flat profile sensitivity		
	Type 1 Flowmeter	Type 2 Flowmeter	Type 3 Flowmeter
Undisturbed profile	+ 0.64	+ 0.63	- 0.15
Peak velocity at the centre	+ 0.64	+ 1.04	+ 1.10
Peak velocity at electrode	+ 0.67	+ 0.53	- 1.20
Peak velocity at 45° to electrode	+ 0.61	+ 0.38	- 0.95
Peak velocity at 90° to electrode	+ 0.62	+ 0.28	- 0.41

TABLE 3

EFFECT OF "TEST PROFILES" ON THE SENSITIVITY OF A FLOWMETER WITH LARGE ELECTRODE
(THEORETICAL RESULTS AT $Re = 1.64 \times 10^5$)

Flow Pattern (Test Profiles)	Percentage change of sensitivity relative to flat profile sensitivity		
	Type 1 Flowmeter	Type 2 Flowmeter	Type 3 Flowmeter
Peak at the centre	+ 0.04	- 5.90	- 15.2
Peak at the electrode	- 0.72	- 1.60	- 24.0
Peak at 45° to electrode	+ 1.56	- 1.24	- 4.9
Peak at 90° to electrode	- 3.20	- 8.80	- 10.6

TABLE 4

THE EFFECT ON THE SENSITIVITY S FOR A TWO-DIMENSIONAL FLOWMETER
OF SEVERE ELECTRODE FOULING (UNIFORM FLOW PROFILE ASSUMED)

Flowmeter Type	Fouling			
	S  ε	S  ε	S  ε	S  ε
1	1.49 14.3%	1.50 25.67%	1.38 49.7%	1.31 83.8%
2	0.44 14.0%	0.44 35.6%	0.42 38.5%	0.42 63.9%

TABLE 5

DISTORTED PROFILES DUE TO A DISTORTION ORIFICE AT 5.5 D FROM
THE CENTRE OF THE FLOWMETER WITH POINT ELECTRODE
(THEORETICAL RESULTS AT Re = 1.64 x 10⁵)

Flow Pattern	Percentage change of sensitivity relative to flat profile sensitivity
Undisturbed profile	+ 1.84%
Peak velocity at the centre	+ 1.48%
Peak velocity at the electrode	+ 3.40%
Peak velocity at 45° to electrode	+ 2.47%
Peak velocity at 90° to electrode	+ 1.06%

TABLE 6

EFFECT OF "TEST PROFILES" ON THE SENSITIVITY OF A FLOWMETER WITH POINT ELECTRODE
(THEORETICAL RESULTS AT $Re = 1.64 \times 10^5$)

Flow Pattern	Percentage change of sensitivity relative to flat profile sensitivity
Peak velocity at the centre	+ 4.3%
Peak velocity at the electrode	+ 22.5%
Peak velocity at 45° to electrode	- 5.7%
Peak velocity at 90° to electrode	- 17.4%

TABLE 7a .

EFFECT OF THE VELOCITY PROFILES ON THE SENSITIVITY
OF LARGE ELECTRODE FM
(EXPERIMENTAL RESULTS)

Flow Pattern	Percentage change of sensitivity compared to the sensitivity of undisturbed profile	
	2.5 D	5.5 D
Peak at the centre	- 3.47%	+ 0.20%
Peak at the electrode	+ 2.10%	+ 0.56%
Peak at 45° to electrode	+ 2.60%	- 0.30%
Peak at 90° to electrode	+ 4.79%	+ 0.04%

TABLE 7b

TEST AND COMPUTED RESULTS OF A POINT ELECTRODE FM
UNDER DISTORTED PROFILES

Orientation of distortion orifice	Percentage change in signal			
	Measured values compared with values for undisturbed profile			Calculated values compared with values for undistorted profiles
	2.5 D	4.5 D	5.5 D	5.5 D
Peak velocity at the centre	+ 6.5	+ 1.2	- 0.46	- 0.35
Peak velocity at the electrode	- 7.0	- 0.4	+ 1.00	+ 1.60
Peak velocity at 45° to electrode	- 7.3	- 2.8	+ 0.14	+ 0.60
Peak velocity at 90° to electrode	- 10.3	- 3.7	- 0.50	- 0.76

TABLE 8

COMPARISON BETWEEN TESTED AND COMPUTED FLOWMETER SIGNALS
(DISTORTED DISC IS AT 5.5 D) (LARGE ELECTRODE FM)

Flow Pattern	Tested output signal mV	Computed output signal mV	Percentage difference between tested and computed signals
No distorted disc	1.86	1.82	2.2%
Peak at the centre	1.86	1.82	2.2%
Peak at the electrode	1.87	1.82	2.8%
Peak at 45° to electrode	1.85	1.81	2.1%
Peak at 90° to electrode	1.86	1.81	2.7%

TABLE 9
EFFECT OF DIRT ON THE ZERO DRIFT
(EXPERIMENTAL RESULTS)

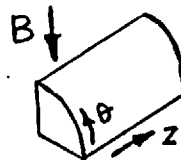
State	Percentage change of the zero drift from the full scale reading
Half of one electrode is covered	1.5%
One electrode is covered except one edge	17.0%

TABLE 10
EFFECT OF DISTORTED PROFILES ON THE HALF FOULED
ELECTRODE WHERE THE DISTORTION ORIFICES WERE
PLACED AT 5.5 D UPSTREAM THE FLOWMETER CENTRE
(EXPERIMENTAL RESULTS)

Flow Pattern	Percentage change of sensitivity relative to the sensitivity of clean electrode FM with undisturbed profile
Undisturbed profile	+ 1.8%
Peak velocity at the centre	+ 0.7%
Peak velocity at the electrode	+ 1.5%
Peak velocity at 45° to electrode	- 13.1%
Peak velocity at 90° to electrode	- 13.5%

TABLE 11

VIRTUAL POTENTIALS ON THE TUBE WALL RESULTING FROM THE METHOD GIVEN IN SECTION 5.6



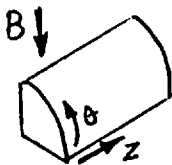
Set No.	Electrode potentials along the circumferential direction							
	$\theta \rightarrow$	0.645	0.617	0.541	0.439	0.331	0.229	0.134
z ↓ 1	0.379	0.371	0.348	0.307	0.250	0.184	0.112	0.037
2	0.221	0.218	0.209	0.191	0.163	0.125	0.078	0.027
3	0.131	0.130	0.125	0.116	0.101	0.079	0.050	0.017
4	0.078	0.077	0.075	0.070	0.061	0.048	0.031	0.011
5	0.046	0.045	0.044	0.041	0.036	0.029	0.018	0.006
6	0.025	0.025	0.024	0.023	0.020	0.016	0.010	0.004
7	0.011	0.011	0.011	0.010	0.009	0.007	0.005	0.002

TABLE 12
THE PERFORMANCE MEASURE (ψ) FOR DIFFERENT FLOWMETER DESIGNS

Flowmeter design types	The value of ψ			
	Swirl in the axial direction	Swirl in the radial direction	Swirl in the θ -direction	Swirl in the three directions together
Point electrode	17.26%	32.87%	33.36%	83.50%
Large electrode	2.19%	31.60%	20.70%	54.50%
Integrated voltage (Section 5.4)	1.50%	7.40%	14.50%	23.50%
Ideal integrated voltage (Section 5.6)	1.00%	4.36%	4.82%	10.20%
Integrated voltage (Section 5.8)	1.60%	2.70%	5.64%	9.95%

TABLE 13

VIRTUAL POTENTIAL ON THE TUBE WALL RESULTING FROM THE
OPTIMIZATION METHOD GIVEN IN SECTION 5.8



Set No.	θ	Electrode potentials along the circumferential direction						
1	1.088	1.040	1.020	0.743	0.578	0.351	0.197	0.065
2	0.951	0.936	0.770	0.641	0.432	0.309	0.176	0.058
3	0.645	0.595	0.554	0.416	0.333	0.218	0.130	0.043
4	0.497	0.482	0.405	0.312	0.202	0.135	0.077	0.026

TABLE 14
VIRTUAL VOLTAGES AND CURRENTS ON AND
FROM THE ELECTRODE STRIPS OF THE
OPTIMIZED FLOWMETER

V (volts)	6.4	6.2	5.5	4.6	3.5	2.5	1.5
I (m amp)	33.9	63.9	53.5	39.9	27.3	18.1	10.0

TABLE 15
INSULATING THICKNESS AND THE CAPACITANCE
OF THE STRIP ELECTRODES OF THE
OPTIMIZED FLOWMETER

ℓ (mm)	1.5	1.52	1.8	2.5	3.7	5.7	10.9
C (PF)	5.5	10.9	9.1	6.8	4.7	3.1	1.7

TABLE 16

SIGNAL CHANGE WHEN A DISTORTION ORIFICE WAS PLACED
AT 5.5 D UPSTREAM OF THE OPTIMIZED FLOWMETER
(COMPUTED RESULTS)

Orientation of distortion orifice	Percentage change in signal when the computed values were compared with values for undistorted profile	
	Optimized flowmeter (using design data)	Optimized flowmeter (using actual data)
Peak velocity at the centre	+ 0.06	+ 0.10
Peak velocity at the electrode	- 0.06	- 0.14
Peak velocity at 45° to electrode	- 0.04	- 0.05
Peak velocity at 90° to electrode	- 0.02	+ 0.04

TABLE 17

SIGNAL CHANGE WHEN A DISTORTION ORIFICE WAS
INTRODUCED UPSTREAM OF THE OPTIMIZED FLOWMETER
(EXPERIMENTAL RESULTS)

Orientation of distortion orifice	Percentage change in signal when the measured values were compared with values for undistorted profile	
	2.5 D	5.5 D
Peak velocity at the centre	- 1.1	+ 0.08
Peak velocity at the electrode	+ 0.8	+ 0.03
Peak velocity at 45° to electrode	+ 1.7	- 0.14
Peak velocity at 90° to electrode	+ 2.0	+ 0.15

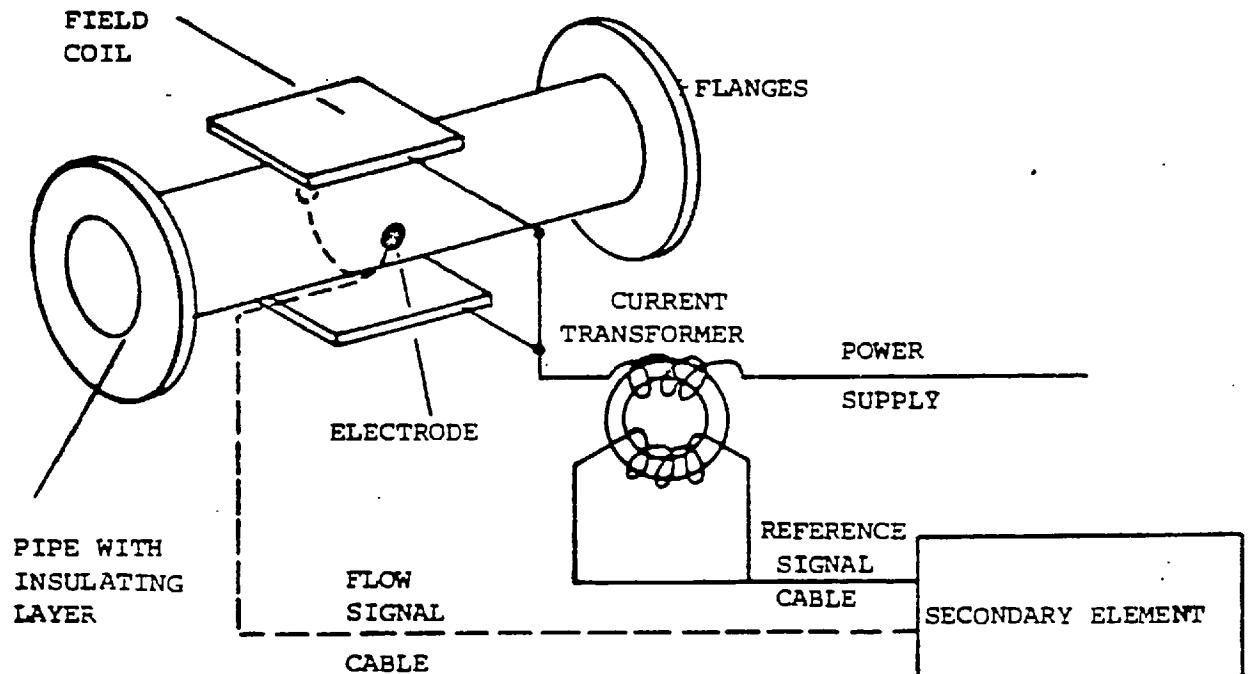


Fig. 1.1 Components of an industrial flowmeter

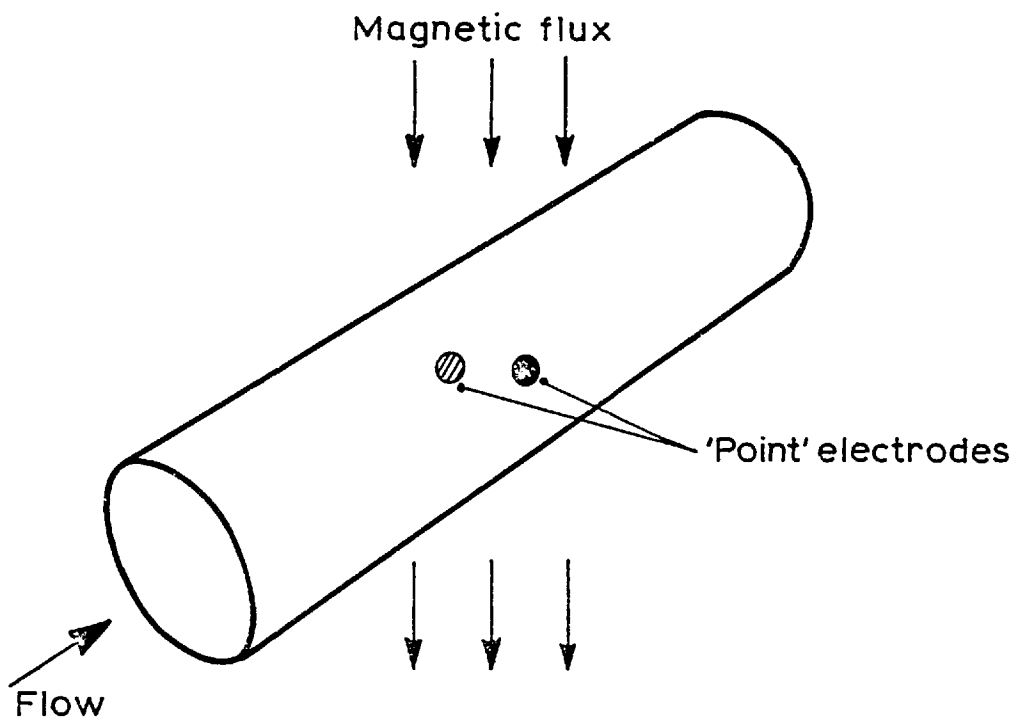


Fig. 1.2 Conventional point-electrode flowmeter

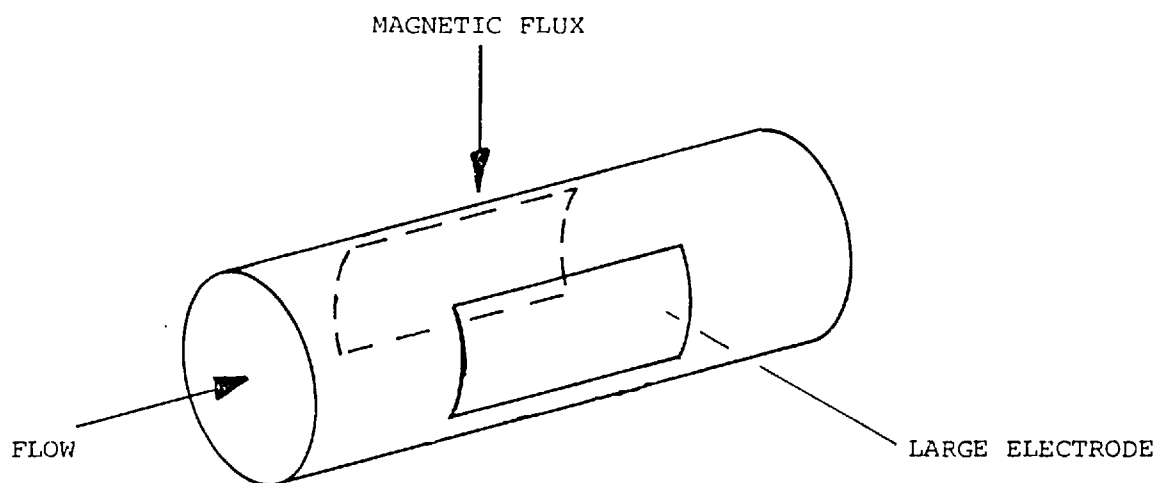


Fig. 1.3 Large electrode flowmeter

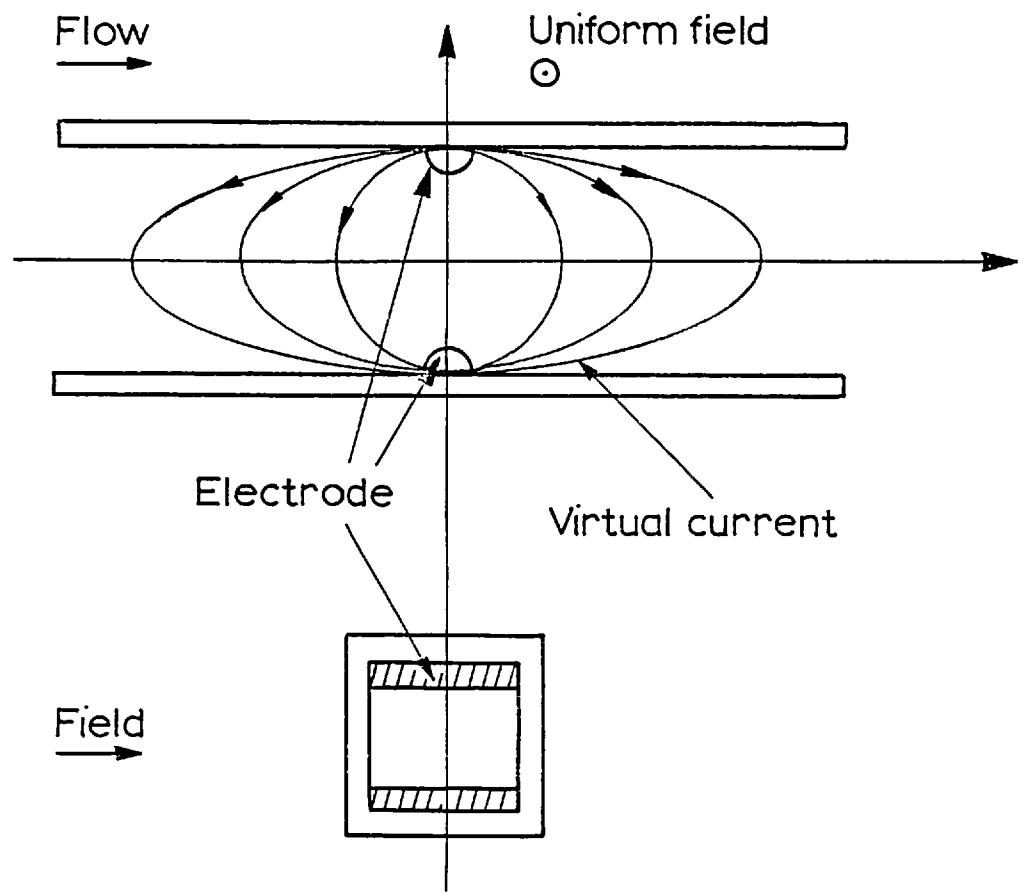


Fig. 1.4 Bevir's ideal flowmeter

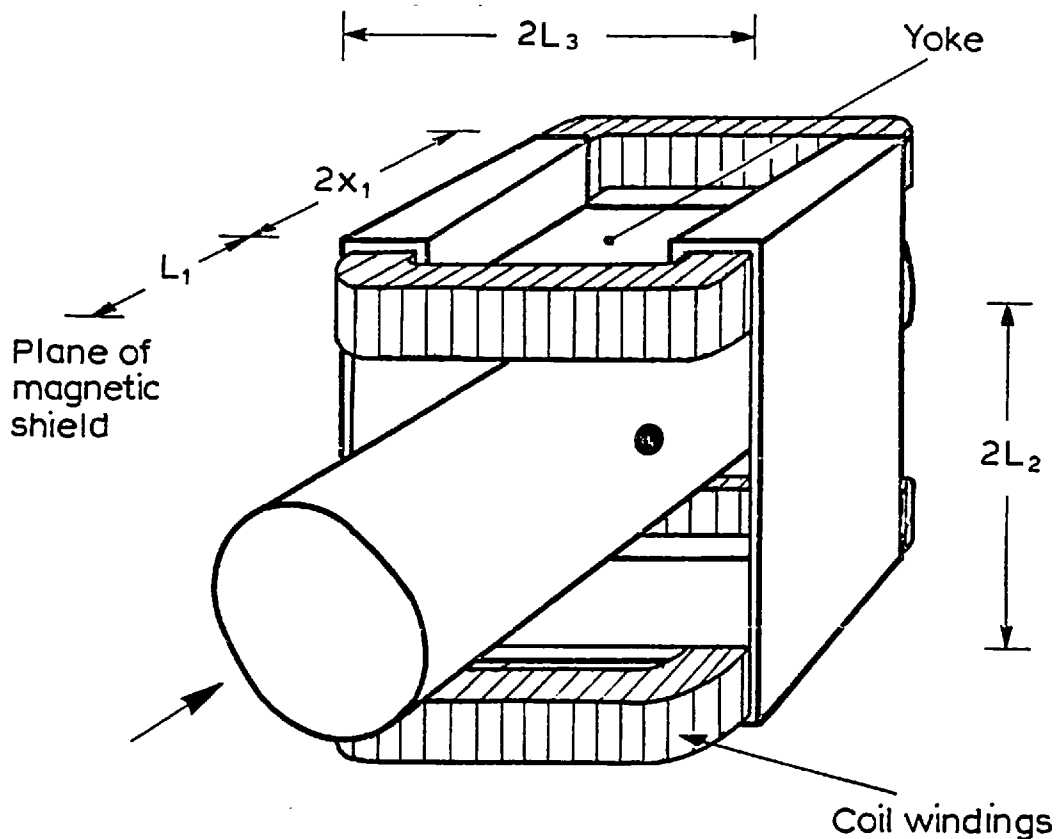


Fig. 2.1 Flowmeter Type 1

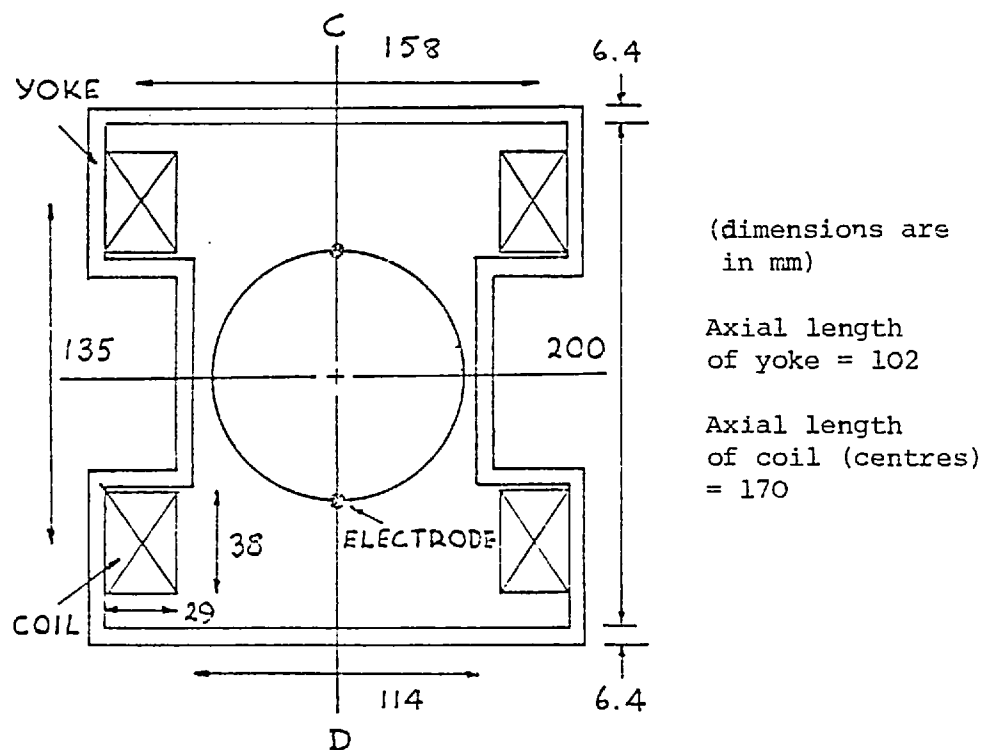


Fig. 2.2 Cross-section of Type 1 flowmeter

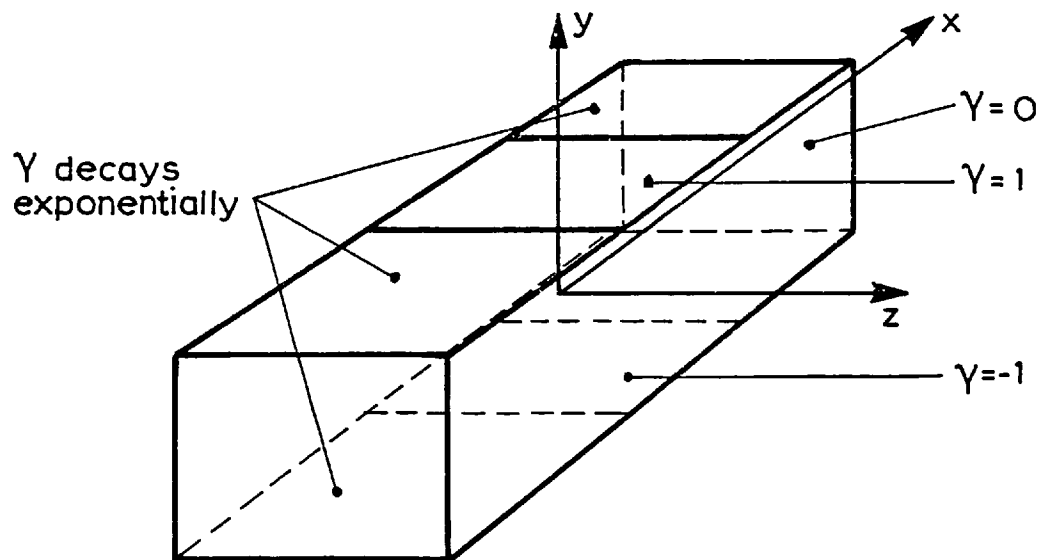


Fig. 2.3 Boundary conditions for γ (Type 1 flowmeter - analytical solution)

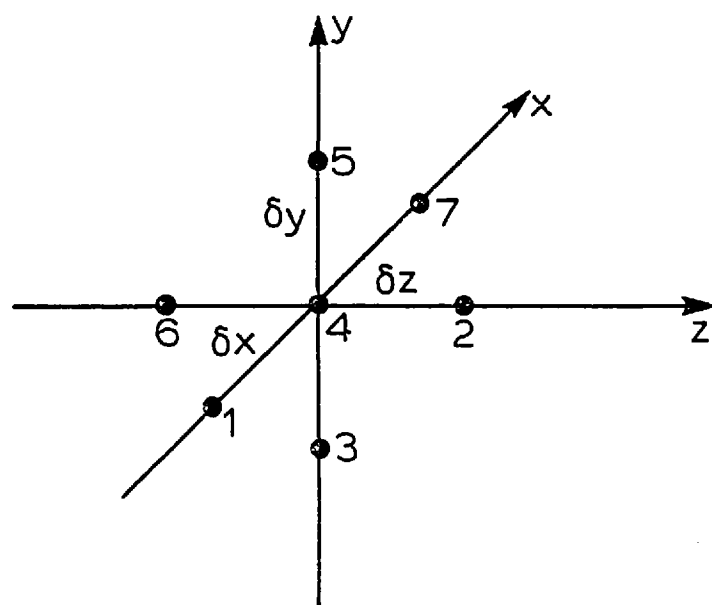


Fig. 2.4 Finite difference mesh (cartesian-notation)

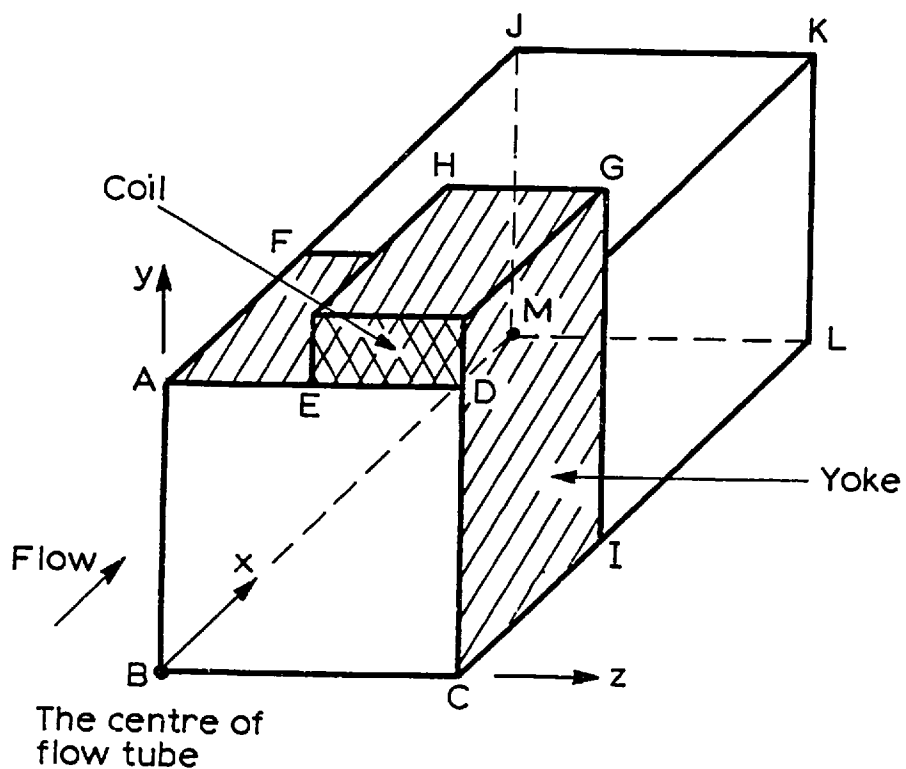


Fig. 2.5 Boundary conditions for γ (Type 1 flowmeter - numerical solution)

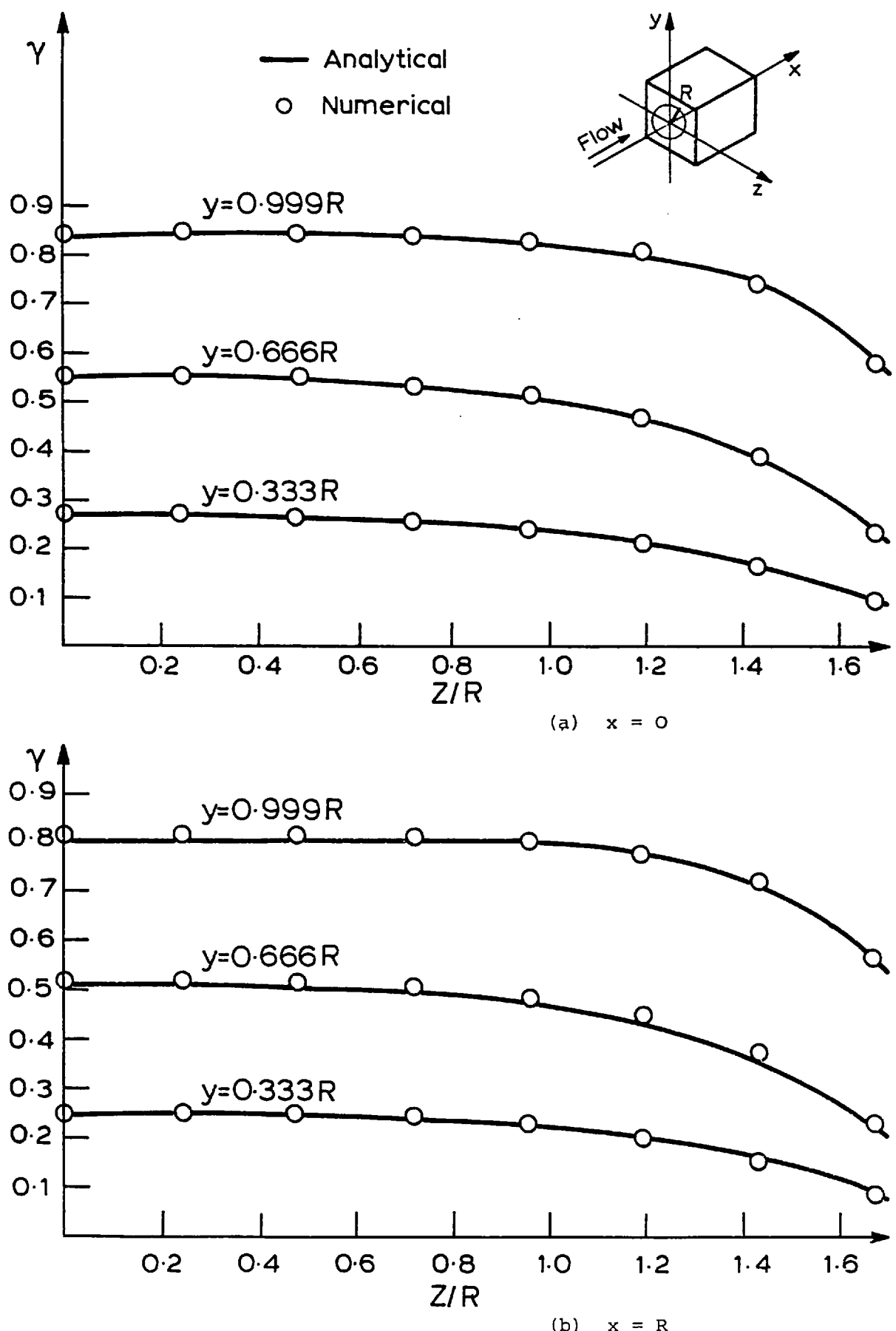


Fig. 2.6 Comparison between analytical and numerical models of the magnetic field for Type 1 flowmeter

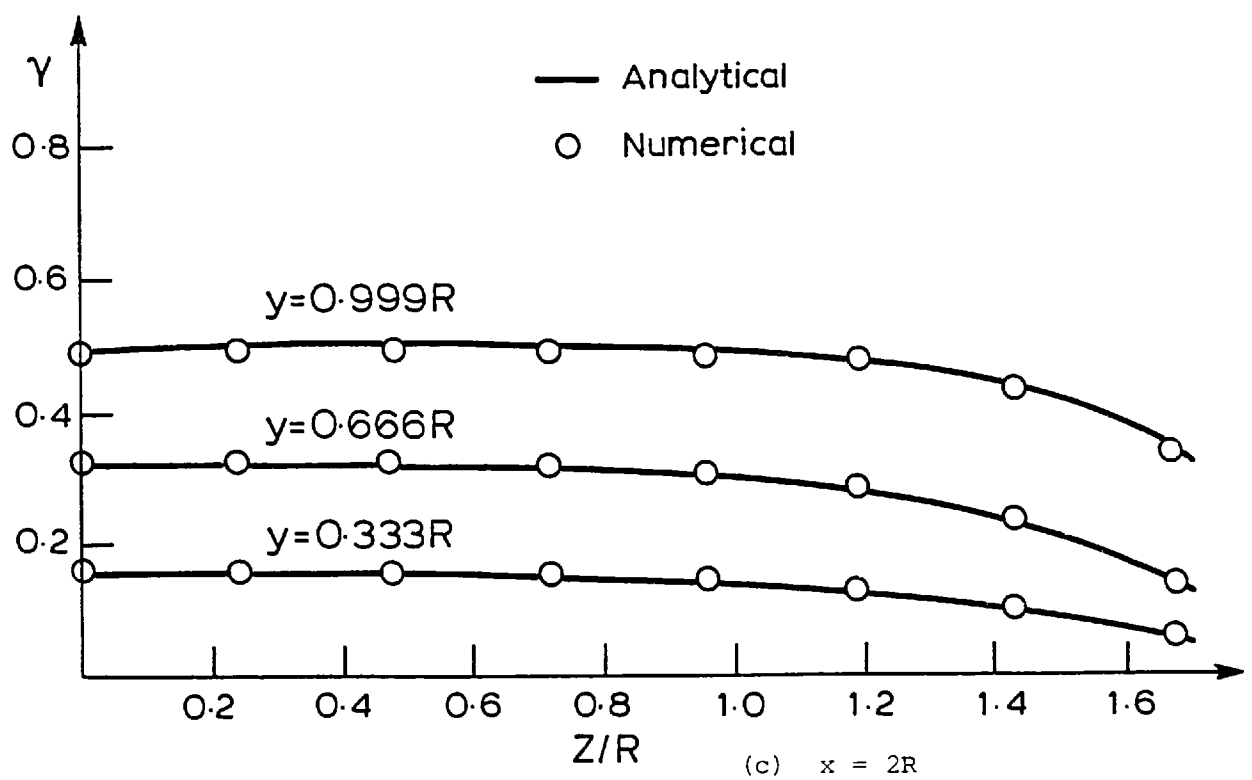


Fig. 2.6 (Continued)

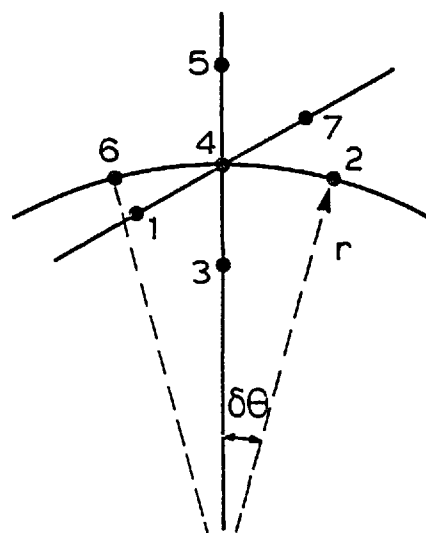


Fig. 2.7 Finite difference mesh (cylindrical-notation)

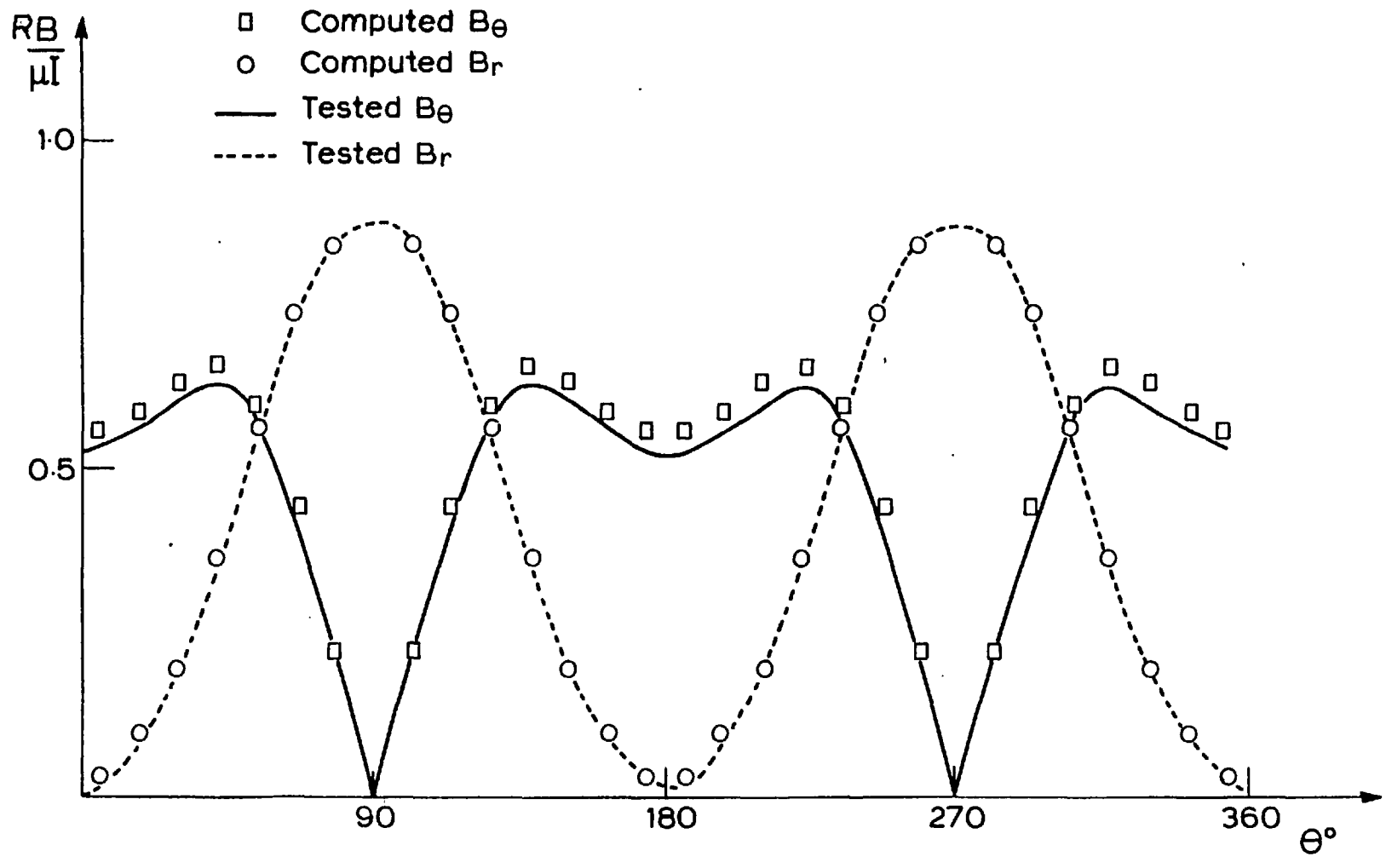
(a) $r = 0.8 R$ $z = 0$

Fig. 2.8 Comparison of experimental values of magnetic field with computed values (Type 1 flowmeter)

(The computed values are for unit $\mu I/R$)

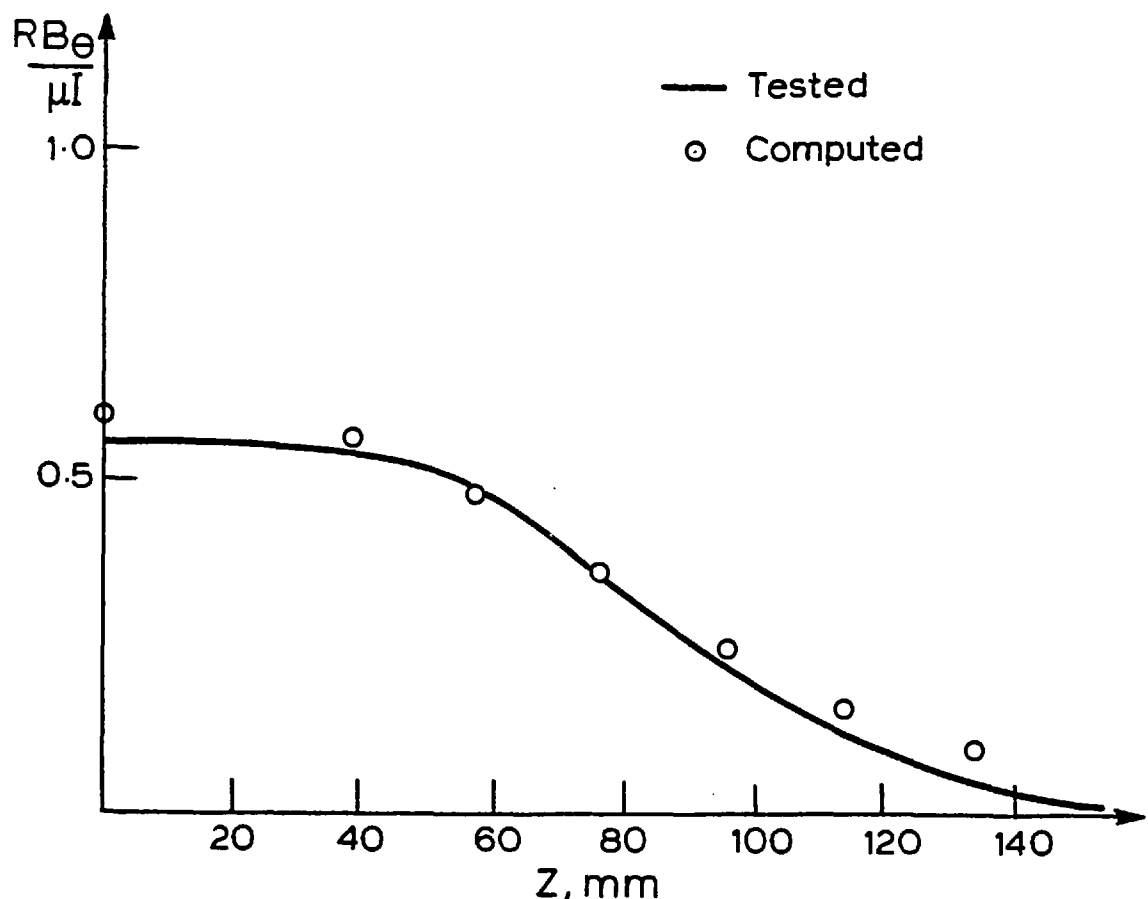
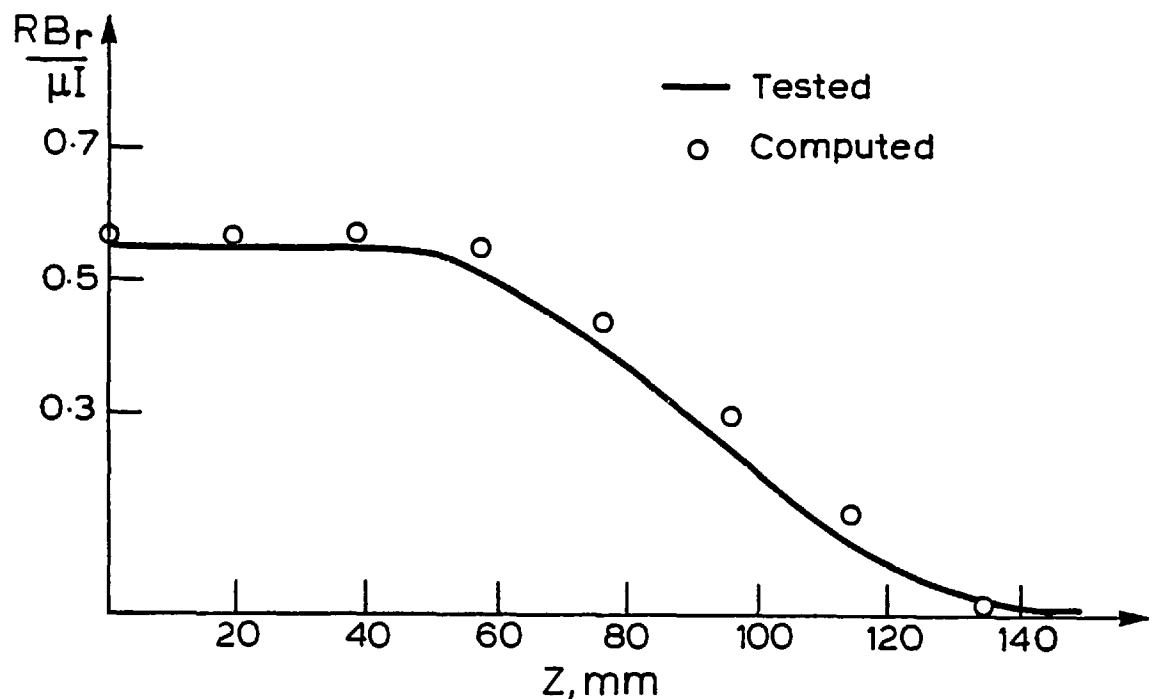
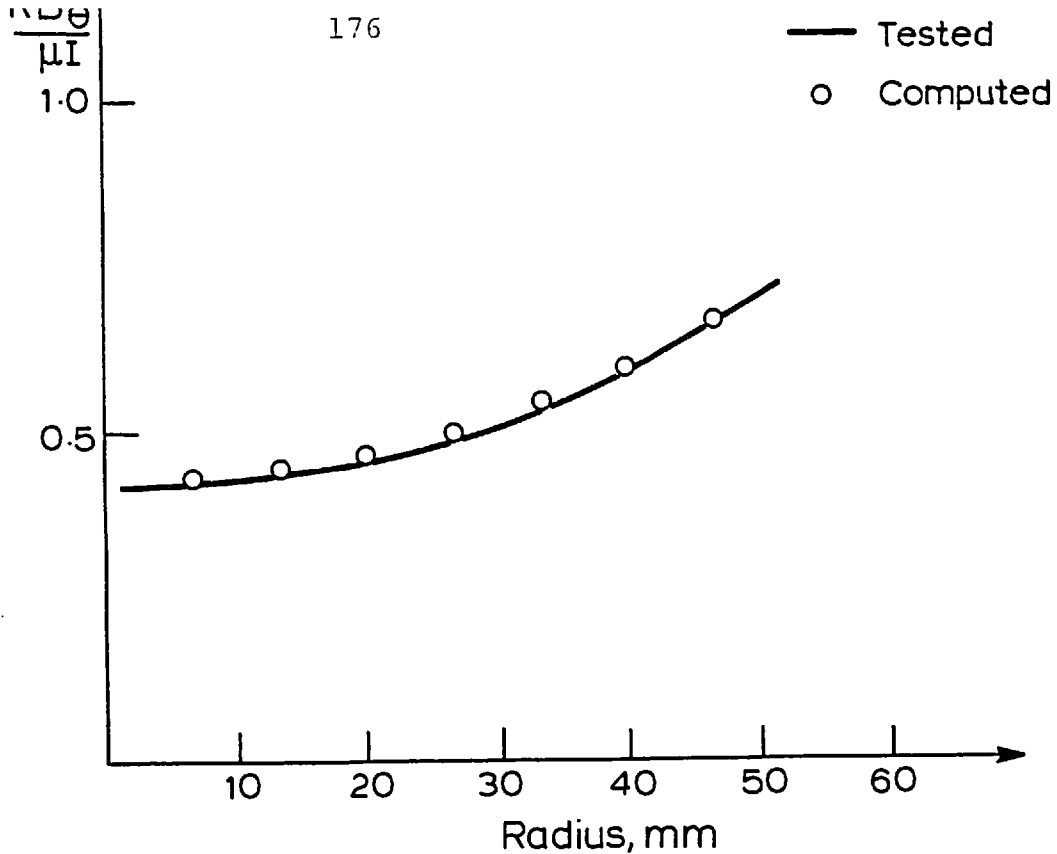
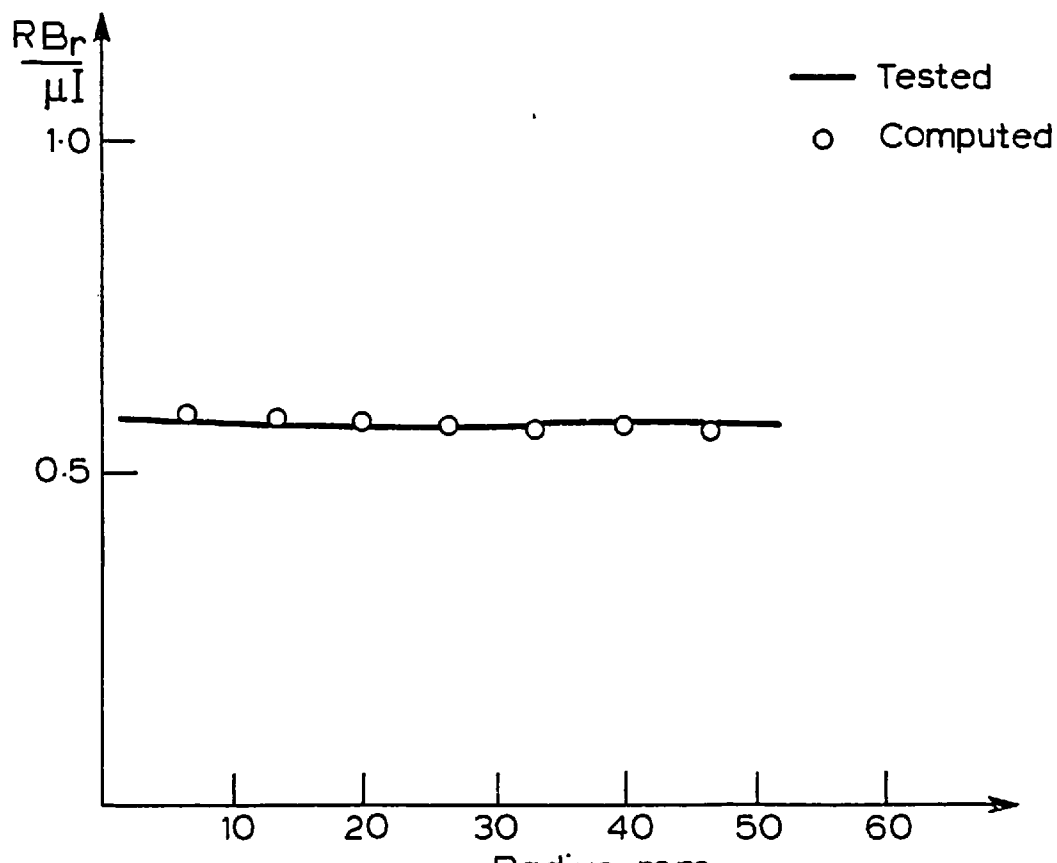
(b) θ -component, $r = 0.8 R$, $\theta = 54^\circ$ (c) r -component, $r = 0.8 R$, $\theta = 54^\circ$

Fig. 2.8 (Continued)



(d) θ -component, $z = 0$, $\theta = 54^\circ$



(e) r -component, $z = 0$, $\theta = 54^\circ$

Fig. 2.8 (Continued)

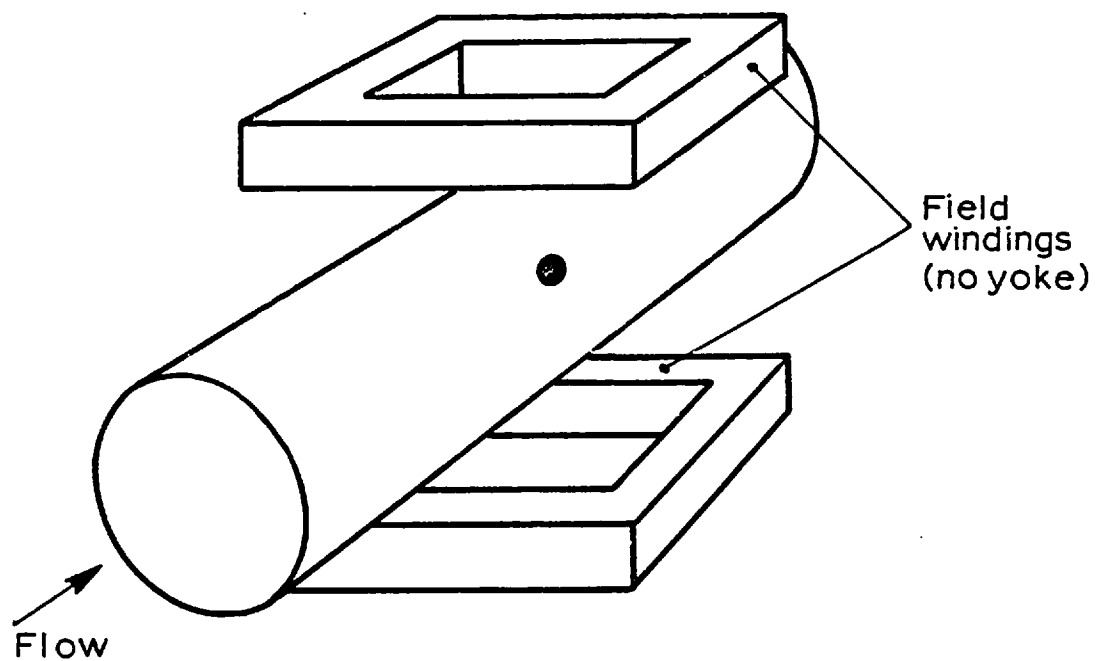


Fig. 2.9 Flowmeter Type 2

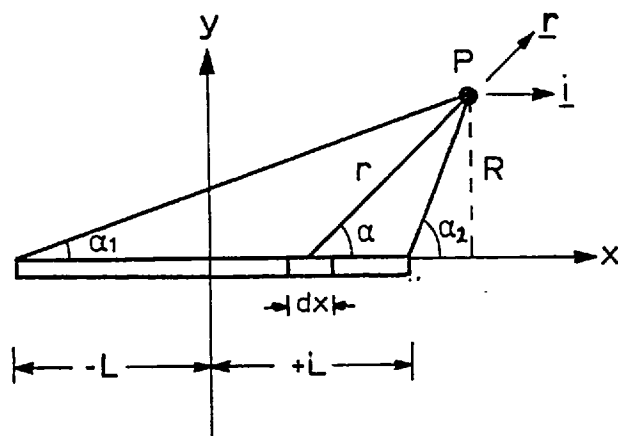


Fig. 2.10 Notation for the magnetic field of a finite length wire

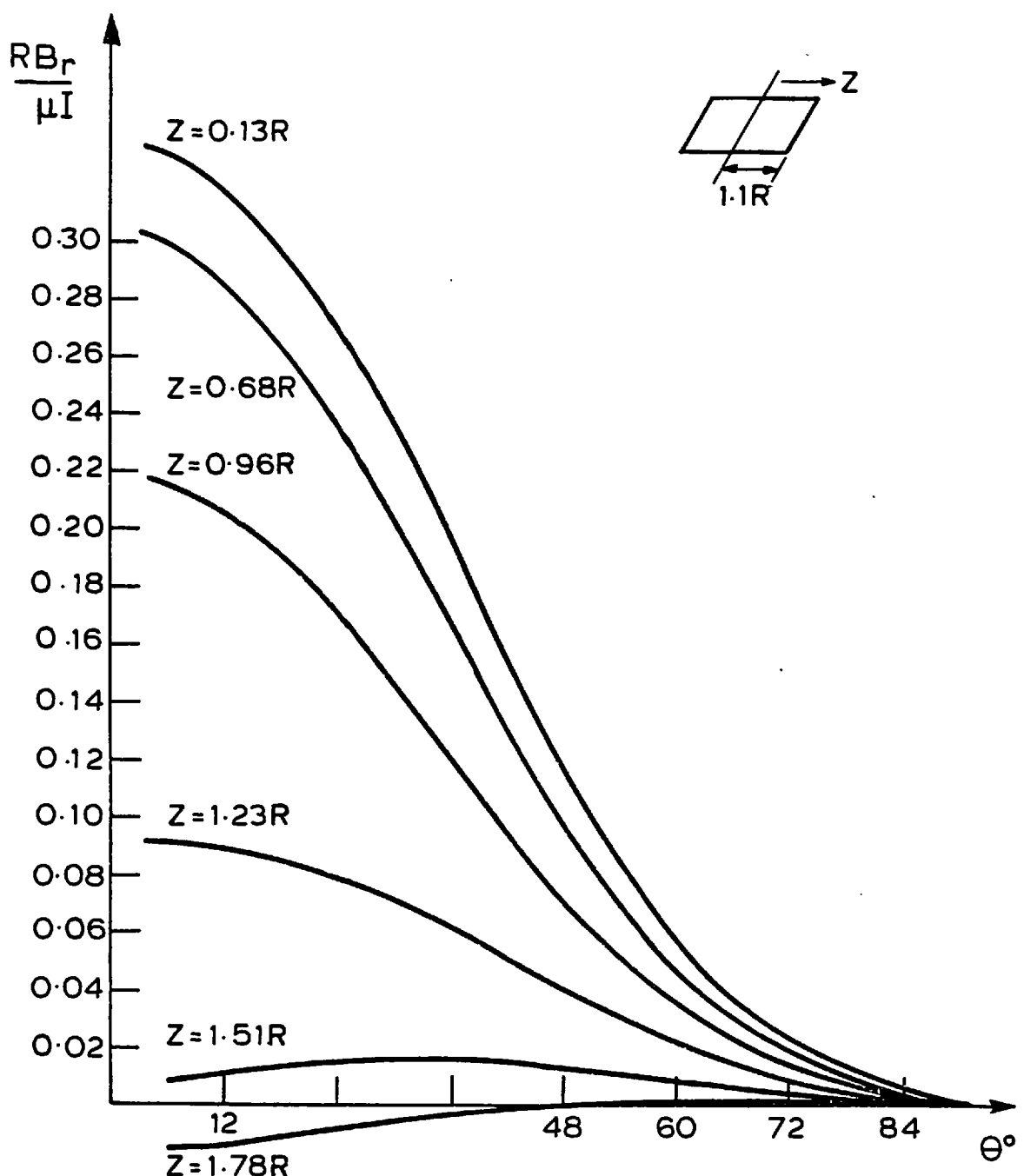
(a) r -component, $r = 0.8 R$

Fig. 2.11 Three-dimensional solution for the magnetic field (Type 2 flowmeter)

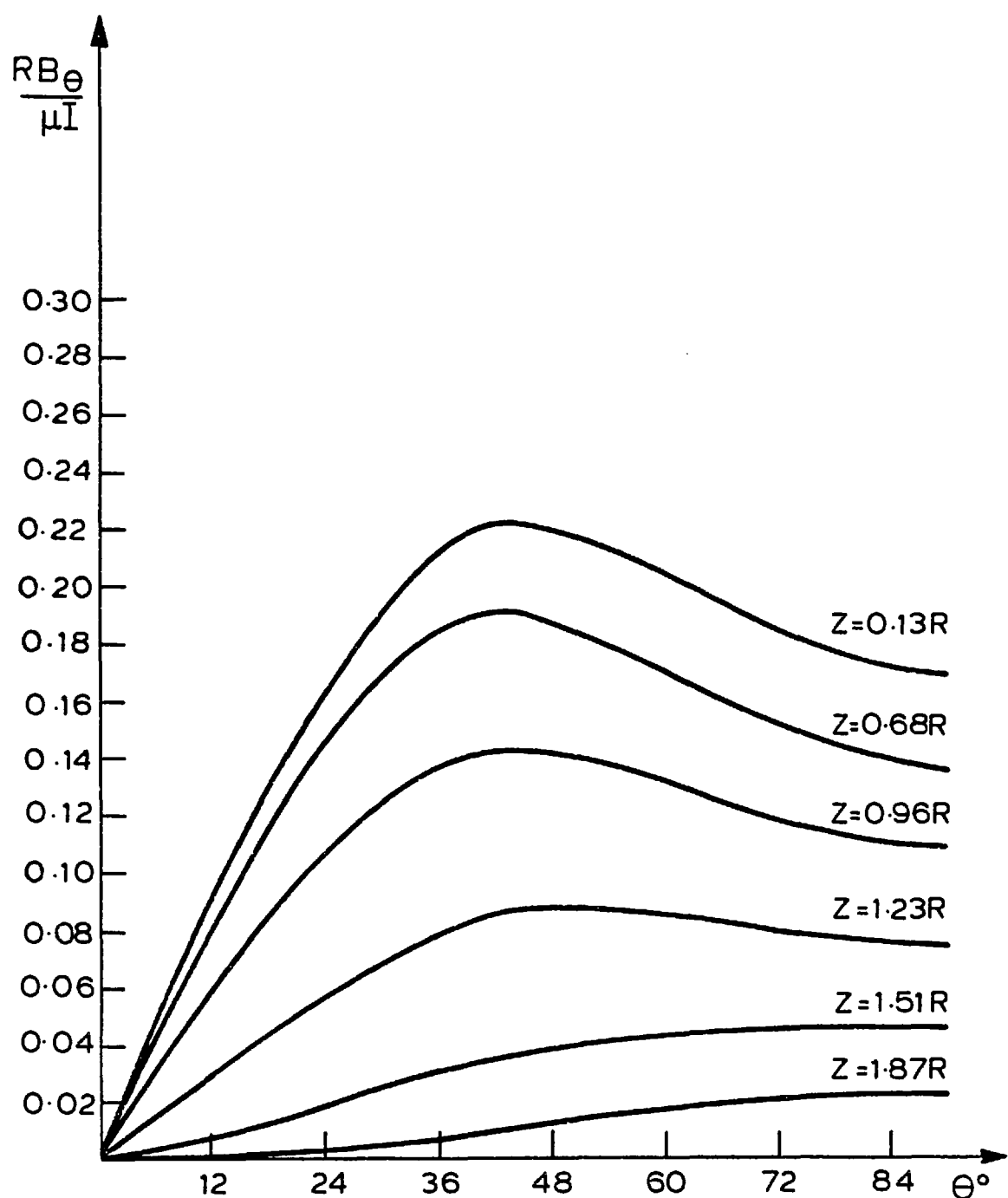
(b) θ -component, $r = 0.8 R$

Fig. 2.11 (Continued)

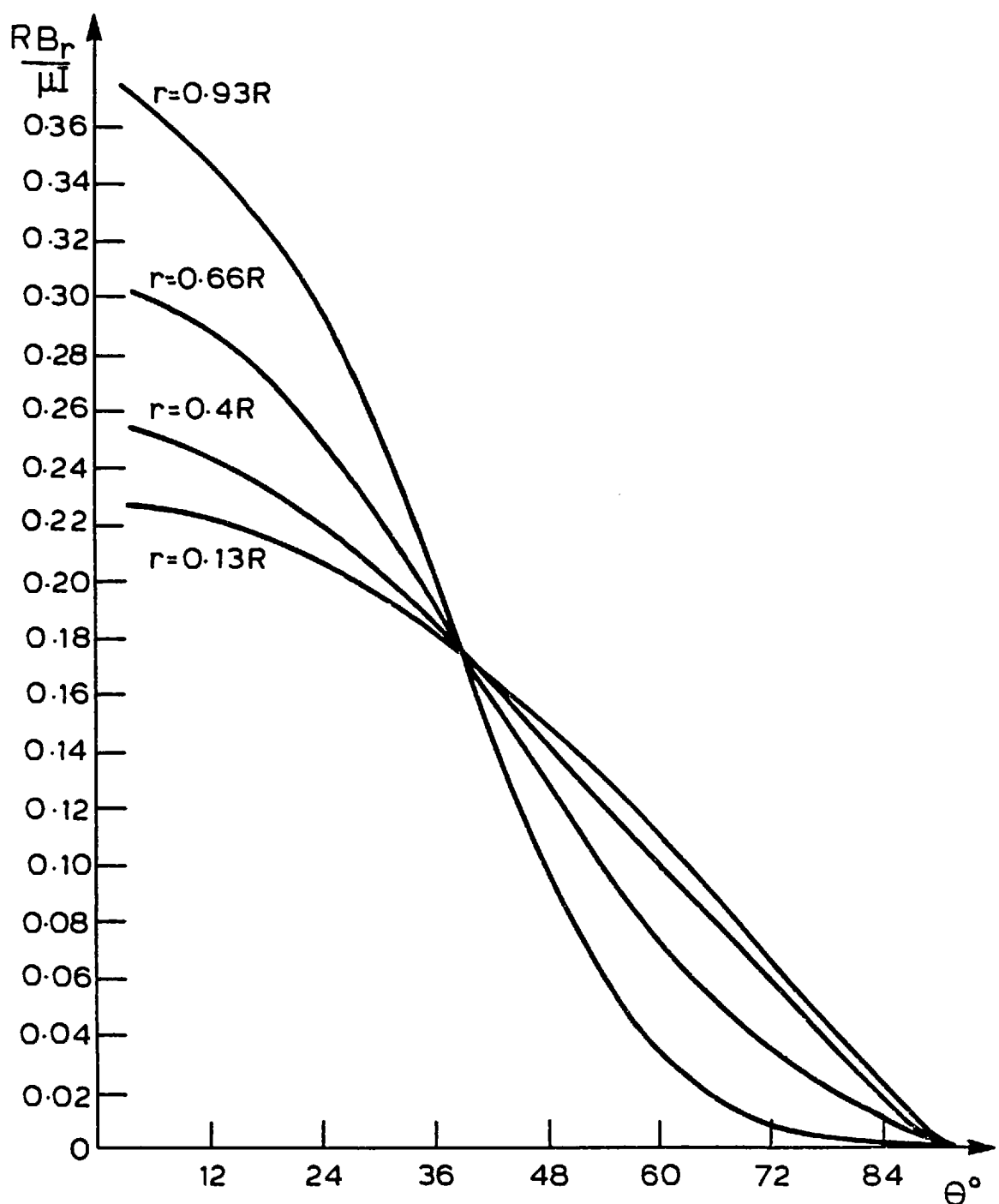
(c) r -component, $z = 0.14 R$

Fig. 2.11 (Continued)

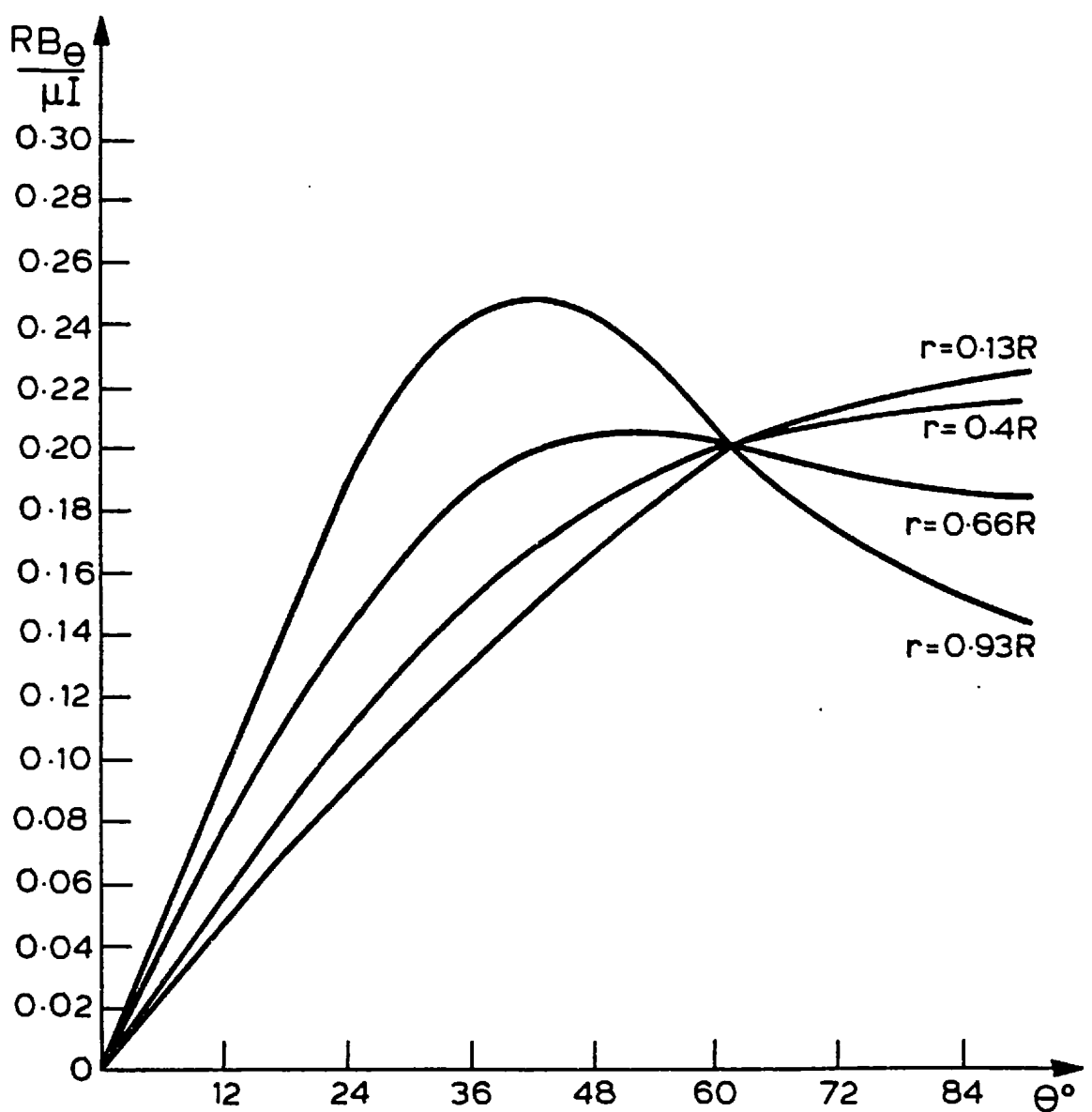
(d) θ -component, $z = 0.14 R$

Fig. 2.11 (Continued)

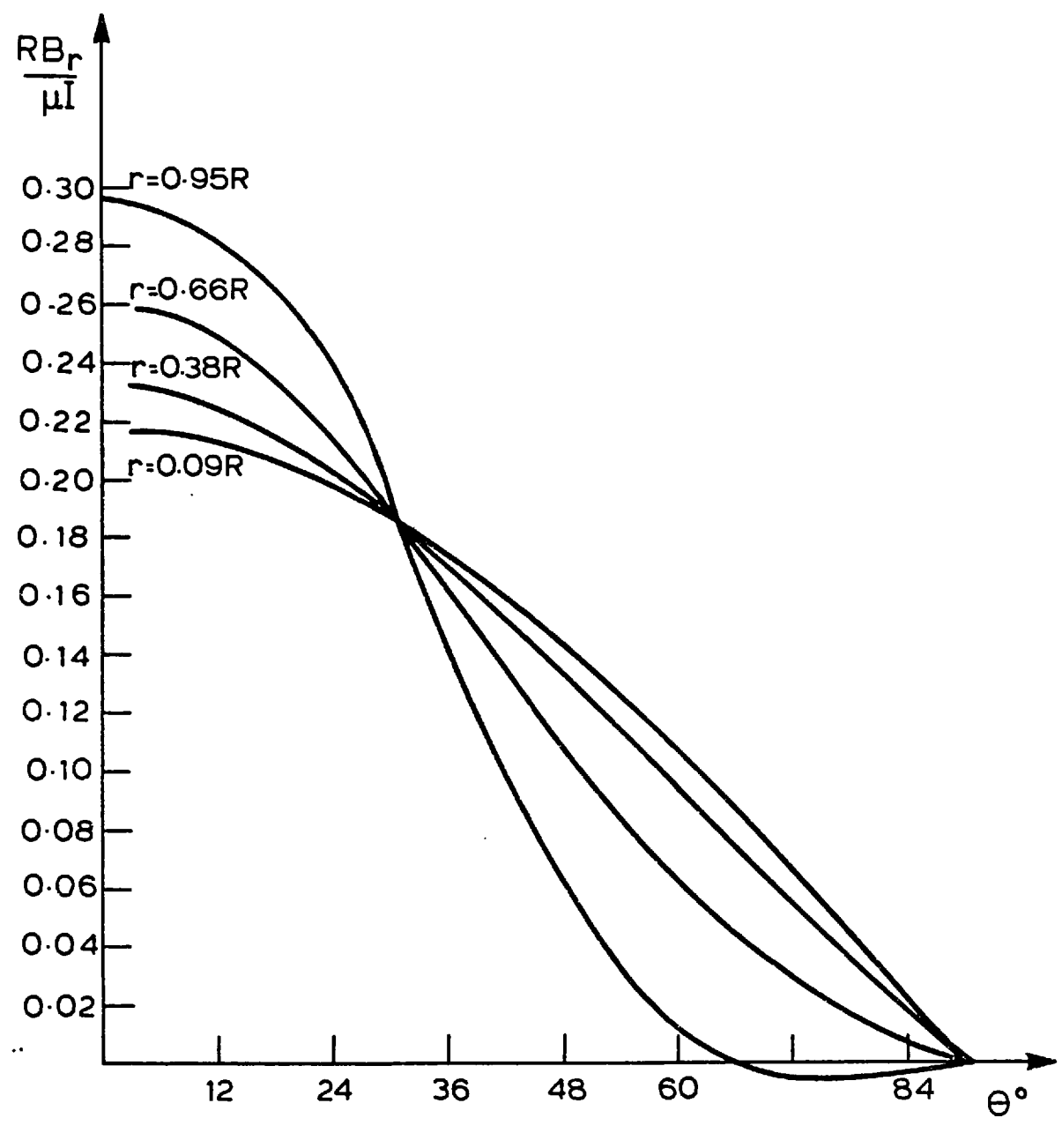


Fig. 2.12 Two-dimensional solution for the magnetic field (Type 2 flowmeter)

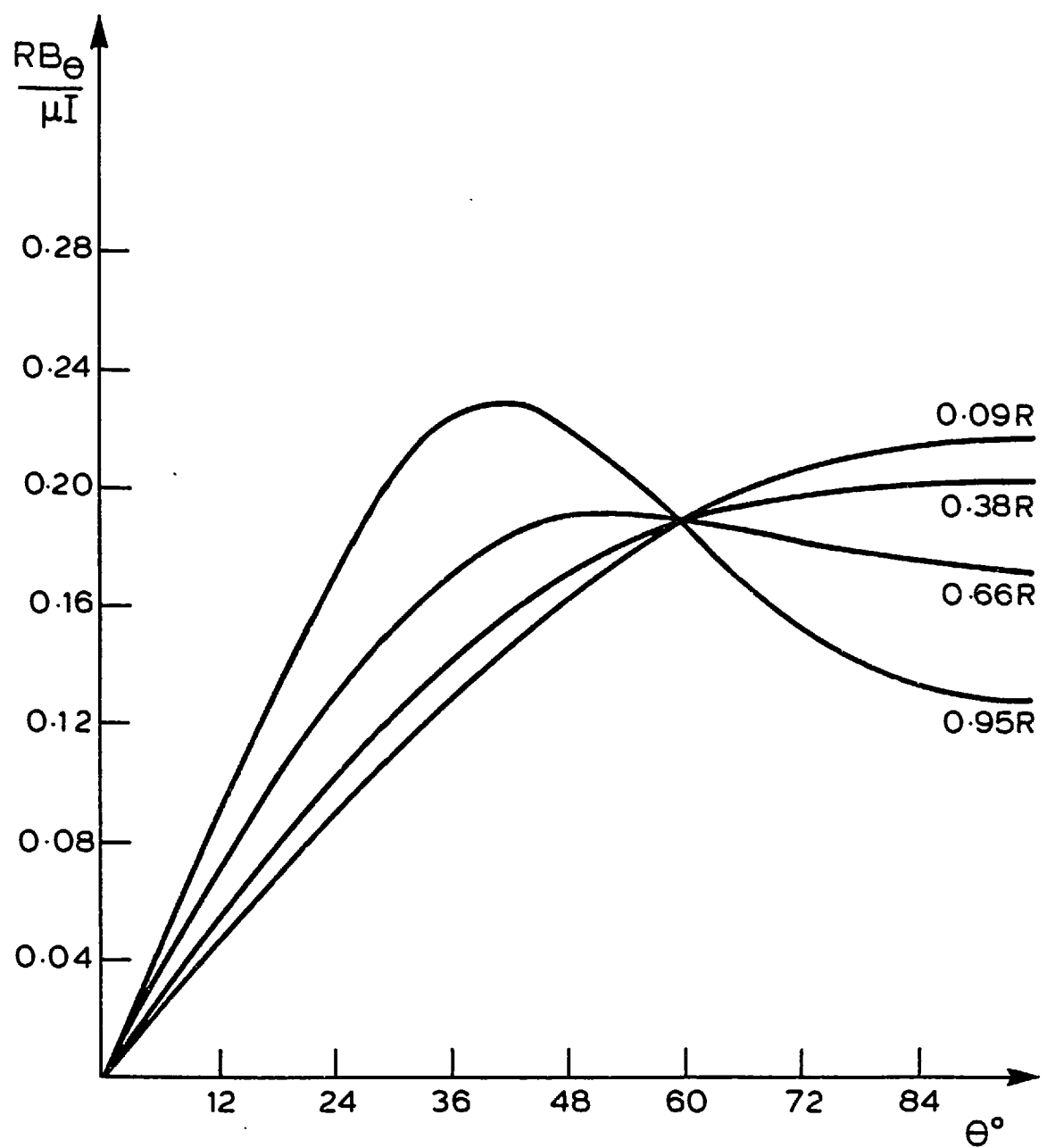
(b) θ -component

Fig. 2.12 (Continued)

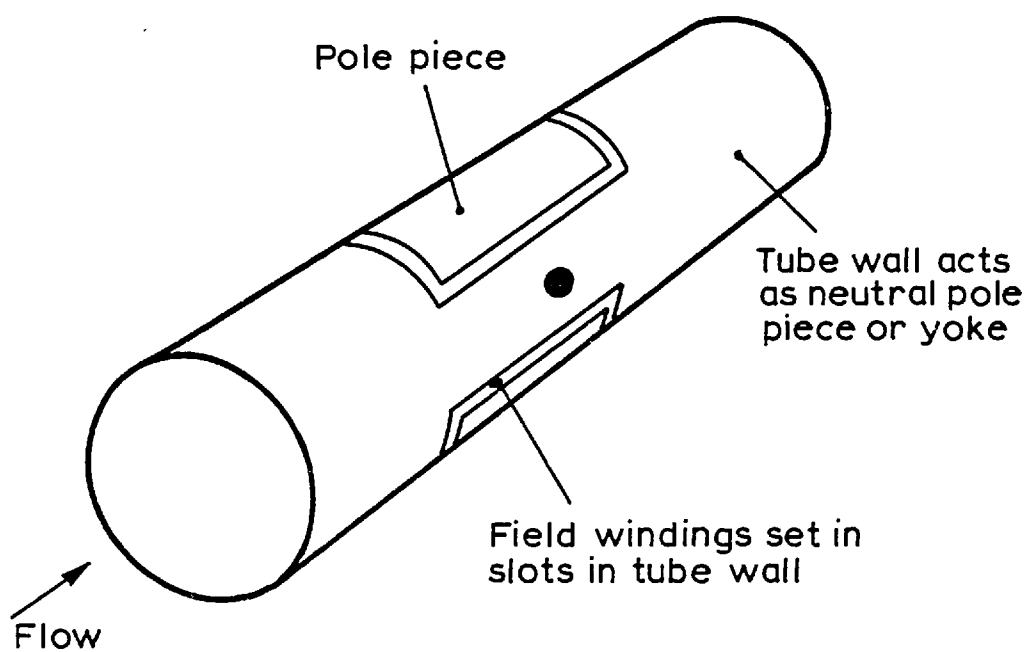


Fig. 2.13 Flowmeter Type 3

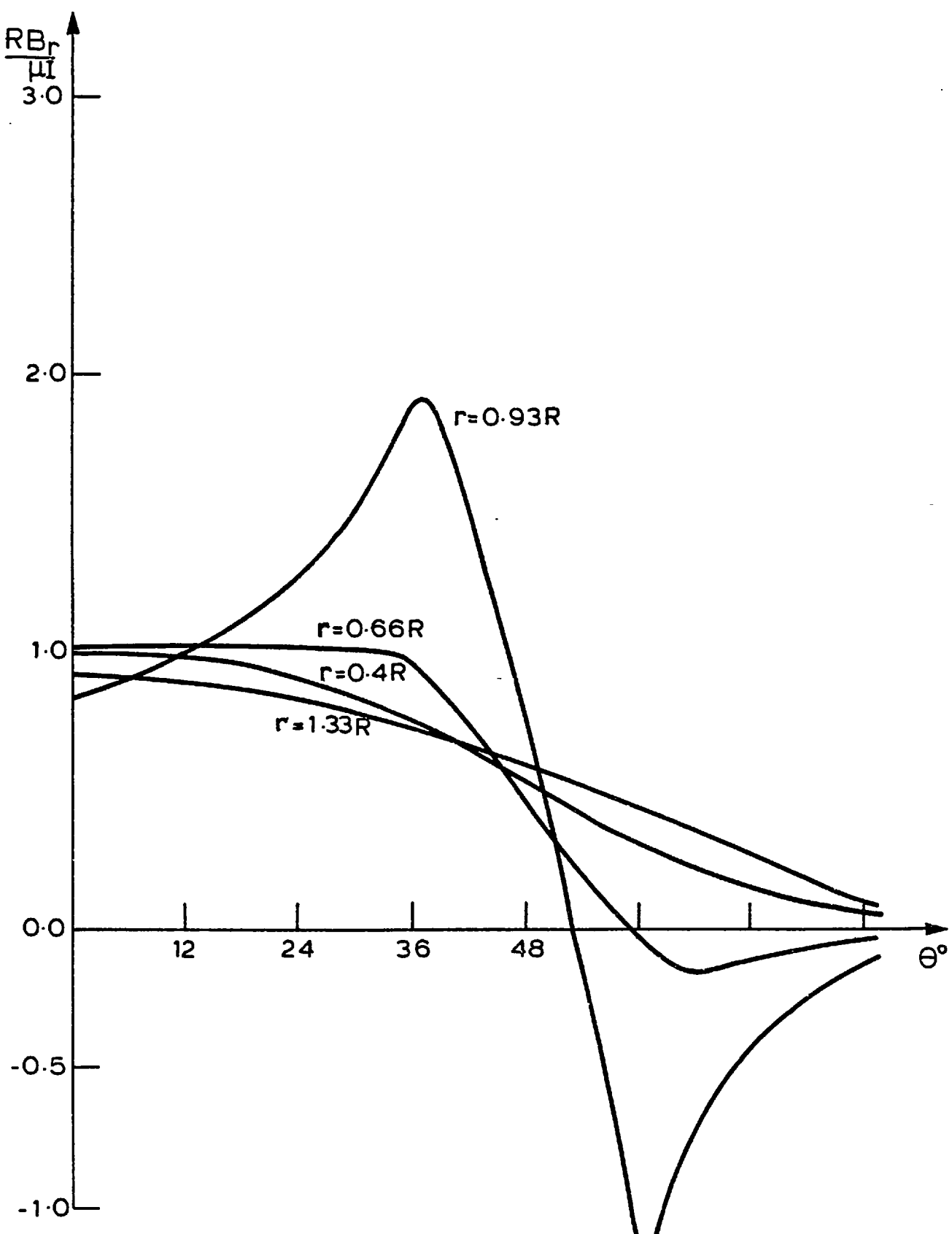
(a) r -component, $z = 0$

Fig. 2.14 Three-dimensional solution for the magnetic field (Type 3 flowmeter)

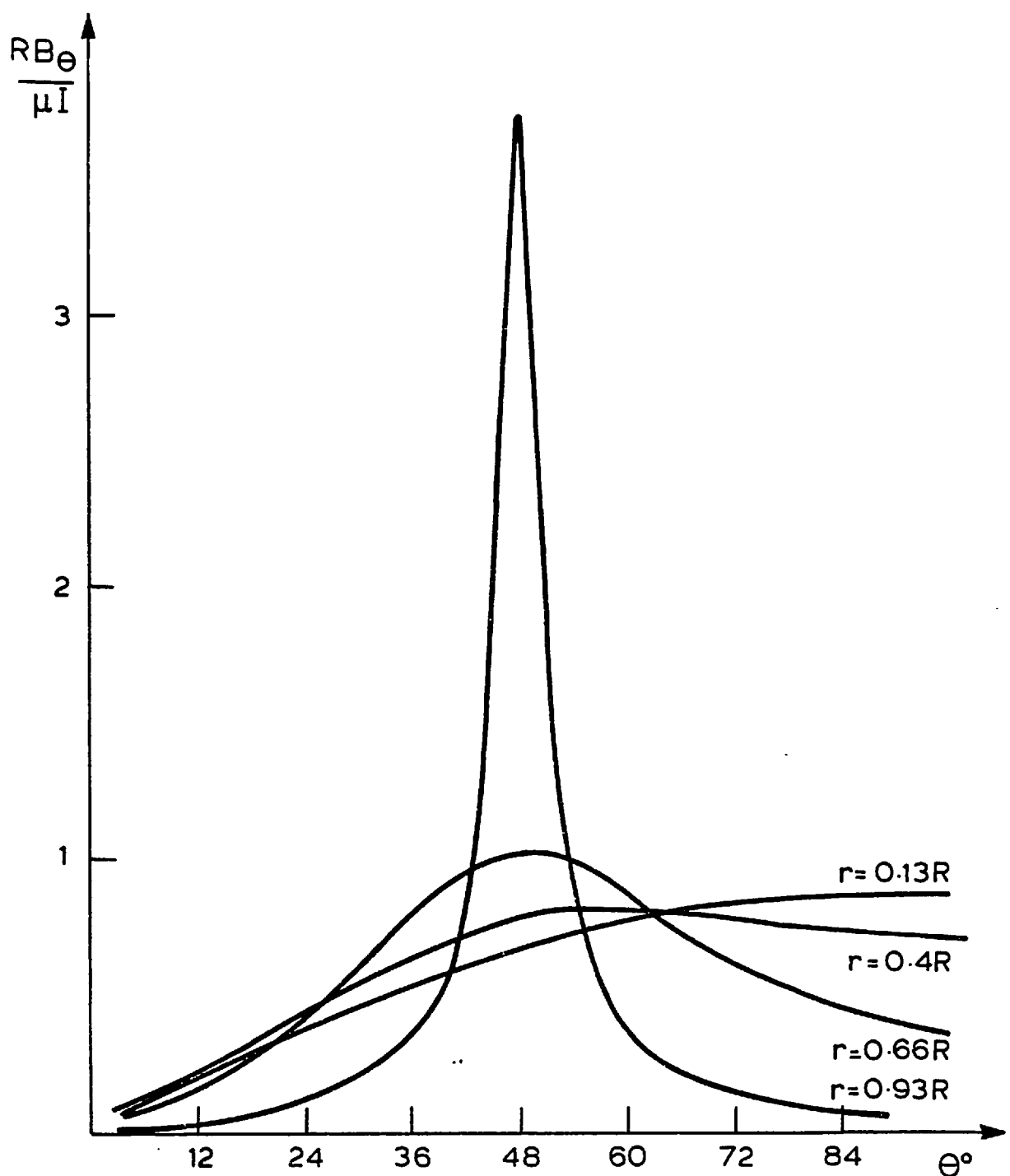
(b) θ -component, $z = 0$

Fig. 2.14 (Continued)

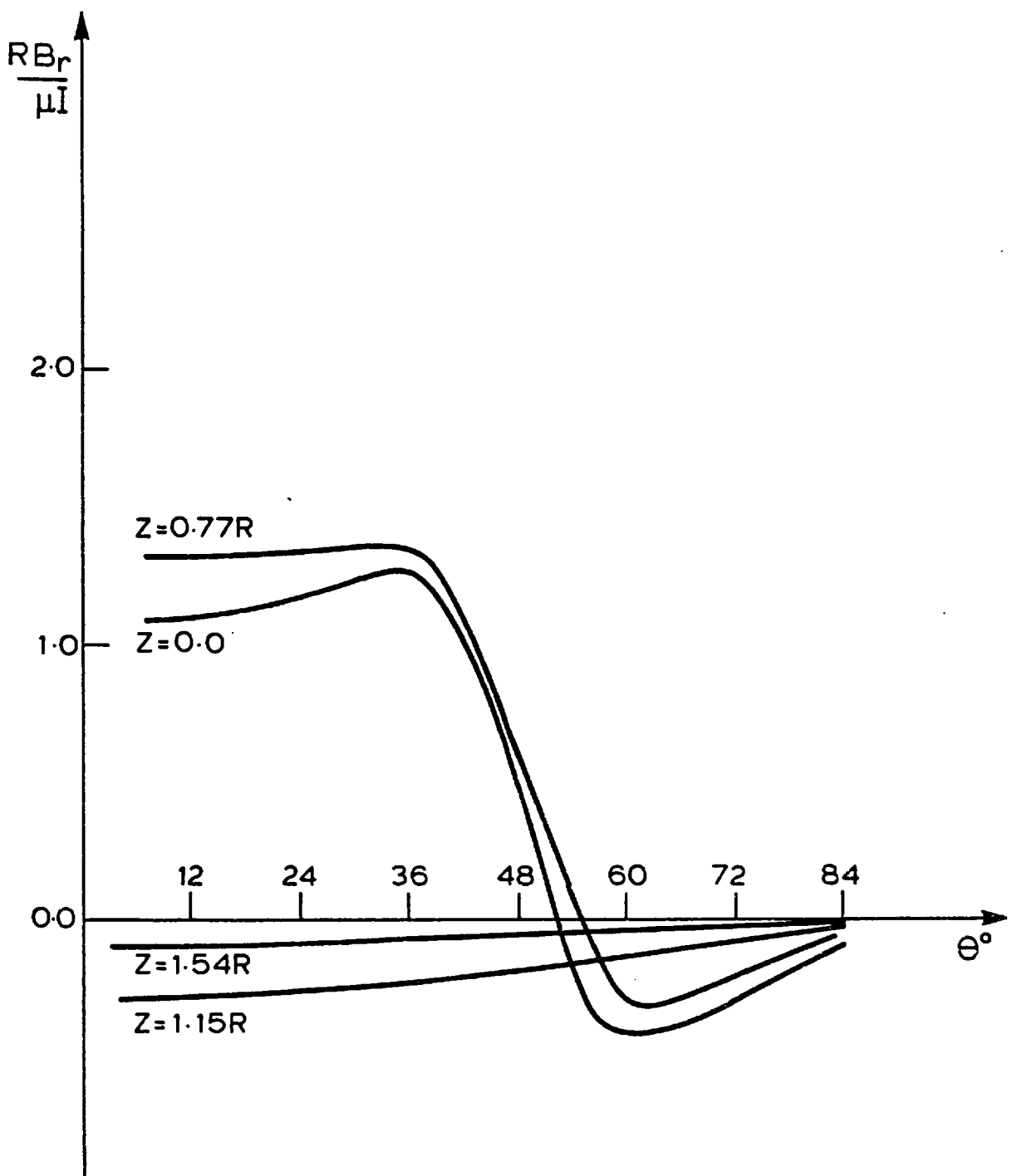
(c) r-component, $r = 0.8 R$

Fig. 2.14 (Continued)

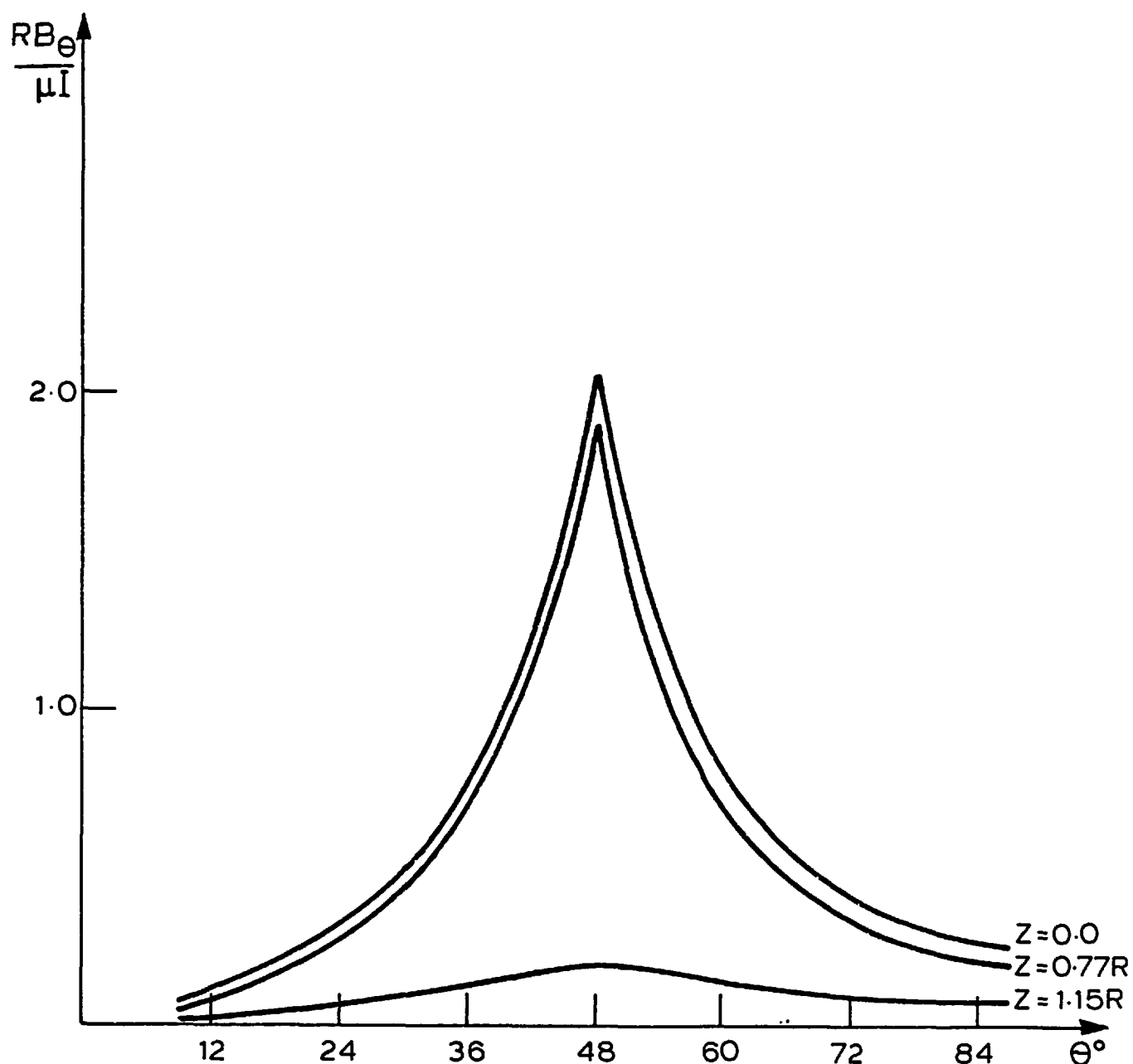
(d) θ -component, $r = 0.8 R$

Fig. 2.14 (Continued)

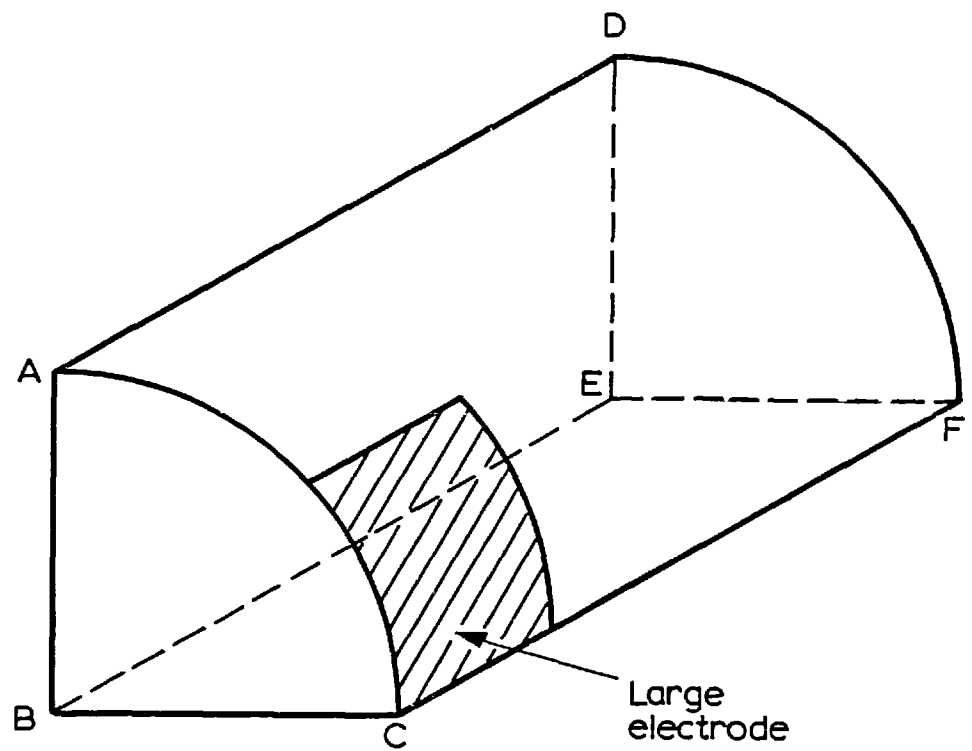


Fig. 2.15 Diagram to indicate the boundary conditions for virtual potential G (large electrode - numerical solution)

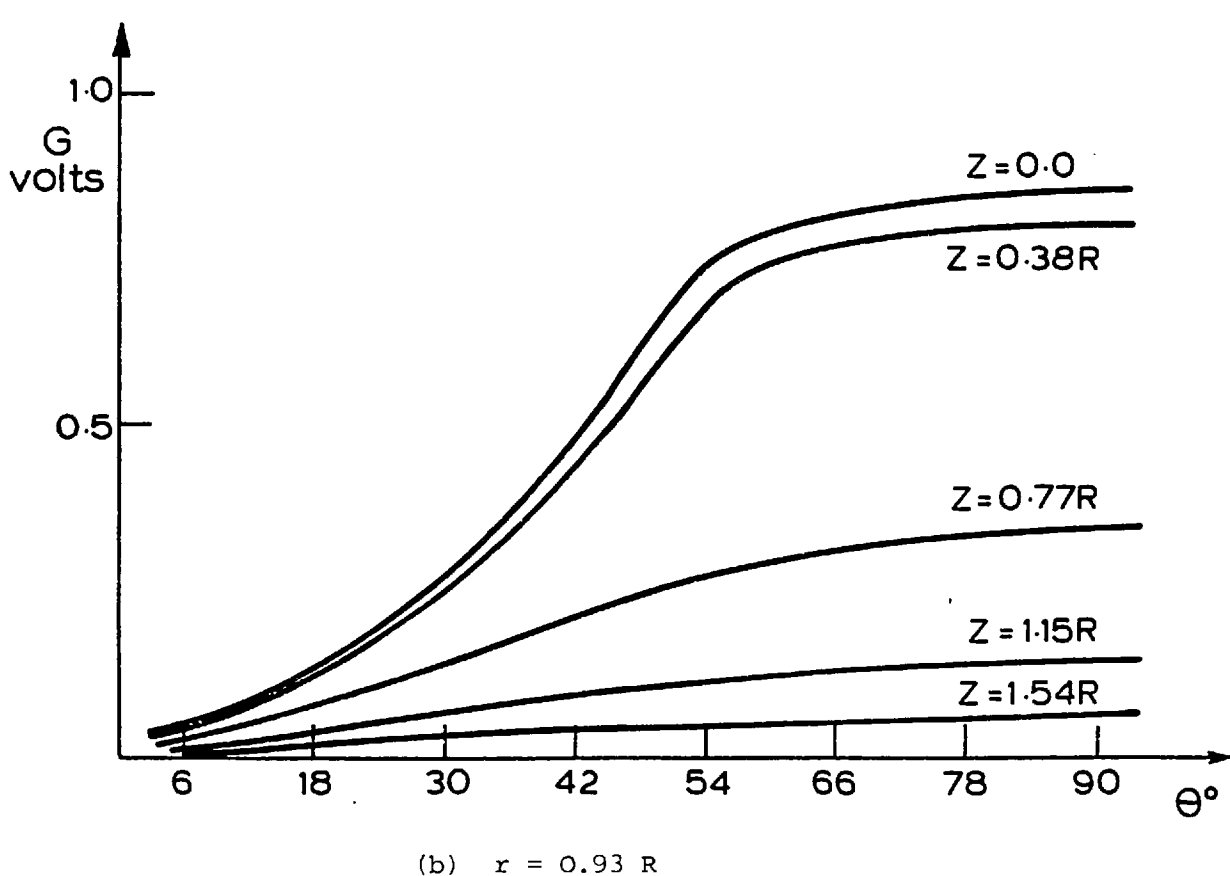
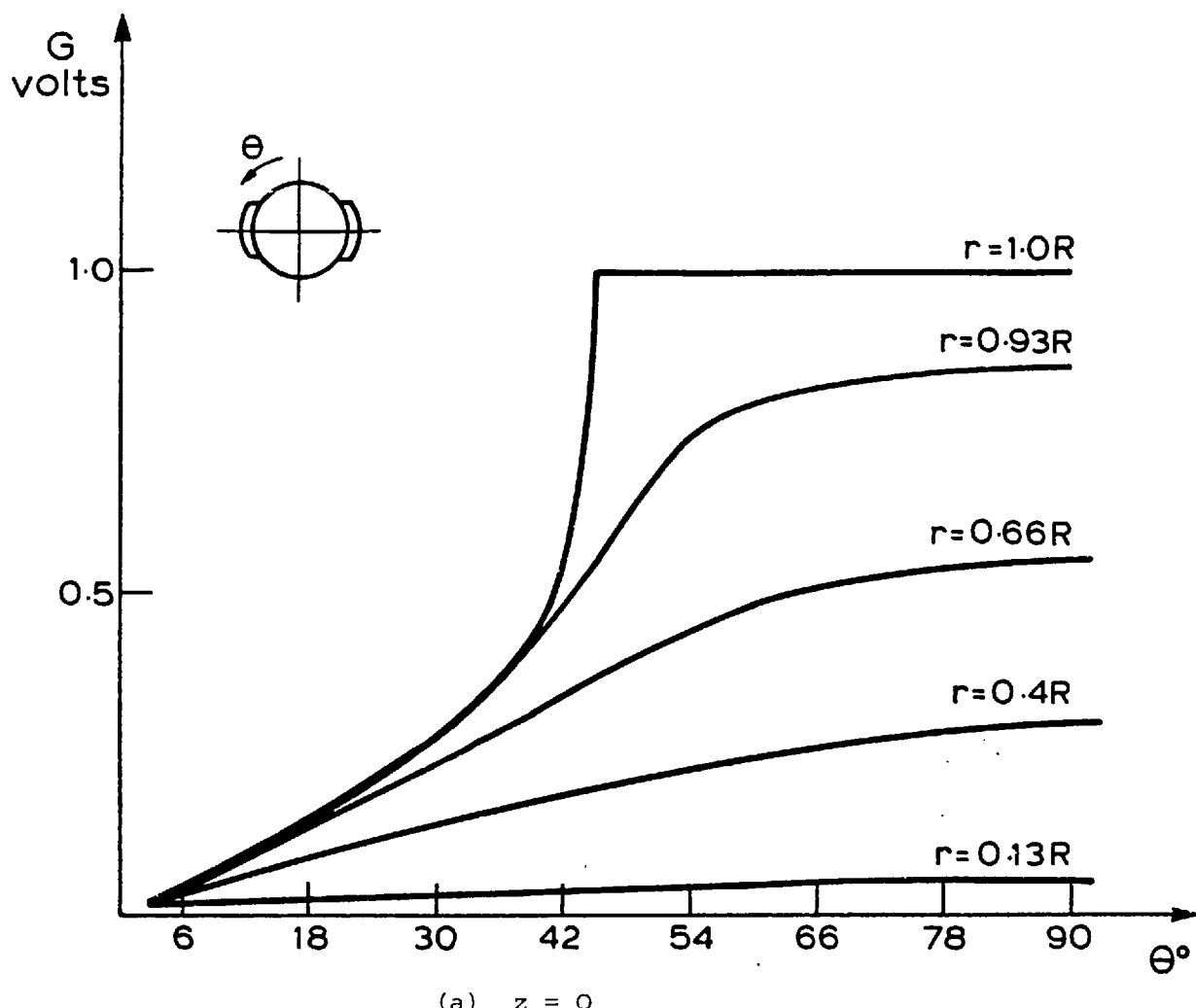


Fig. 2.16 Three-dimensional solution for the virtual potential

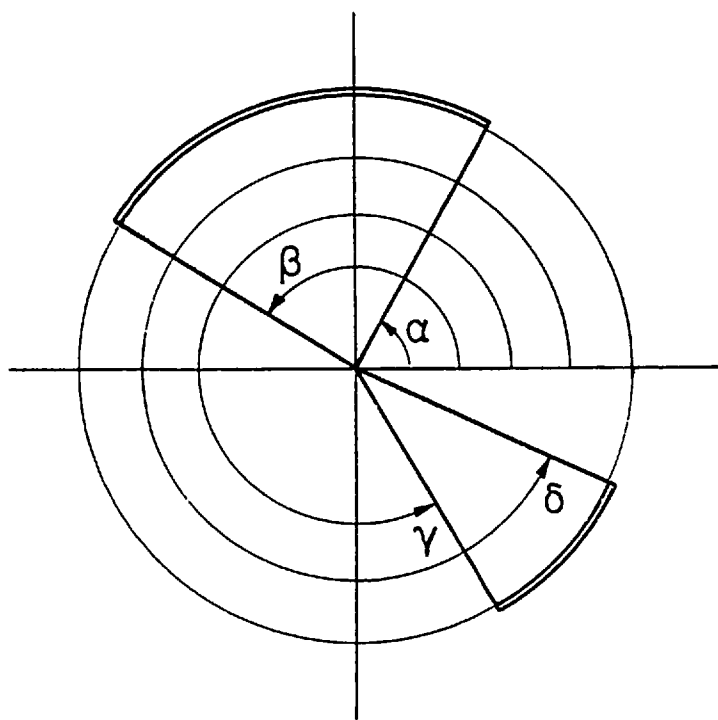


Fig. 2.17 Conduction regions of electrodes for two-dimensional virtual current calculations

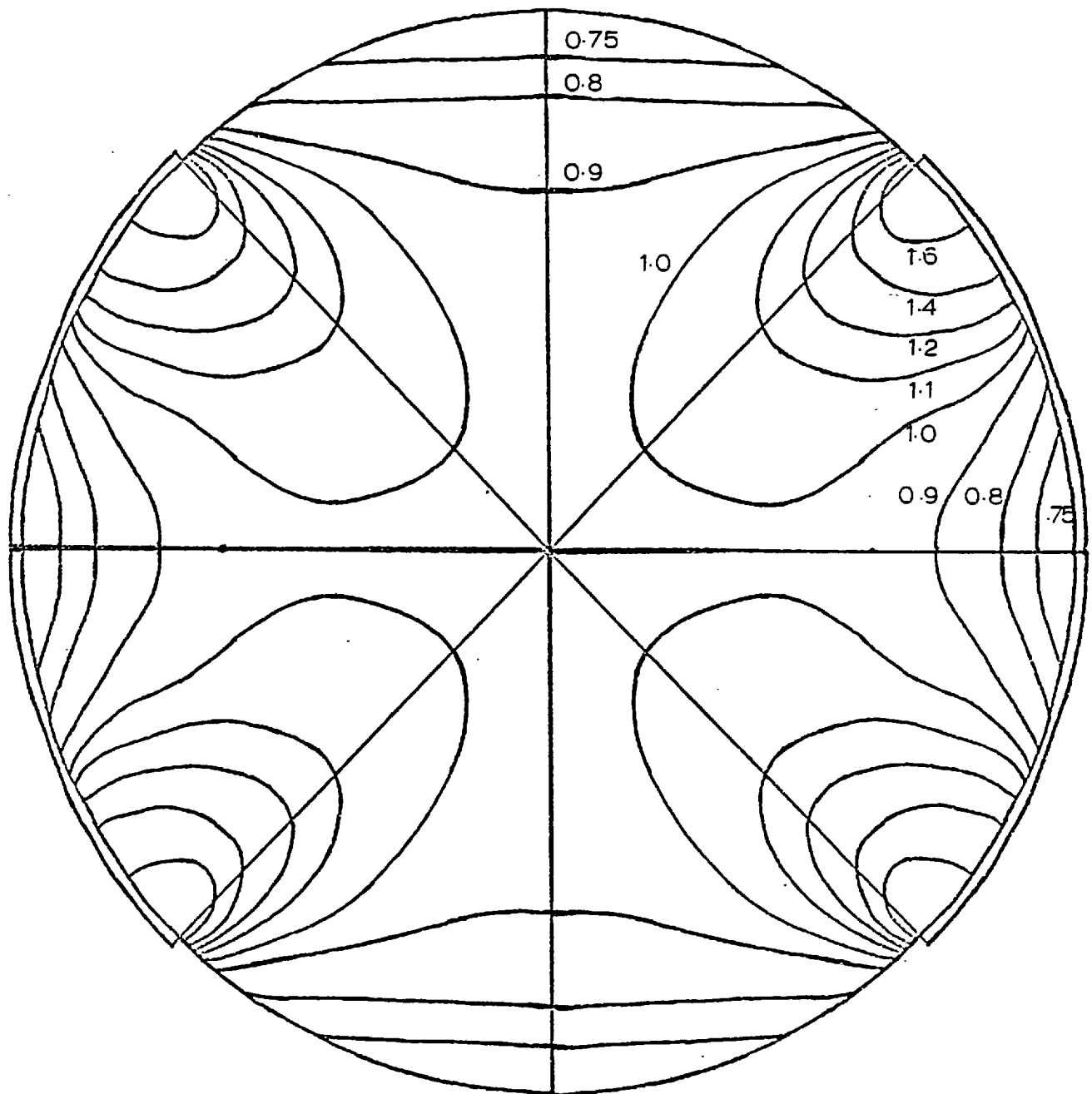


Fig. 2.18 Weight function distribution for Type 1 flowmeter
(weight function in the centre $w_c = 0.378$)

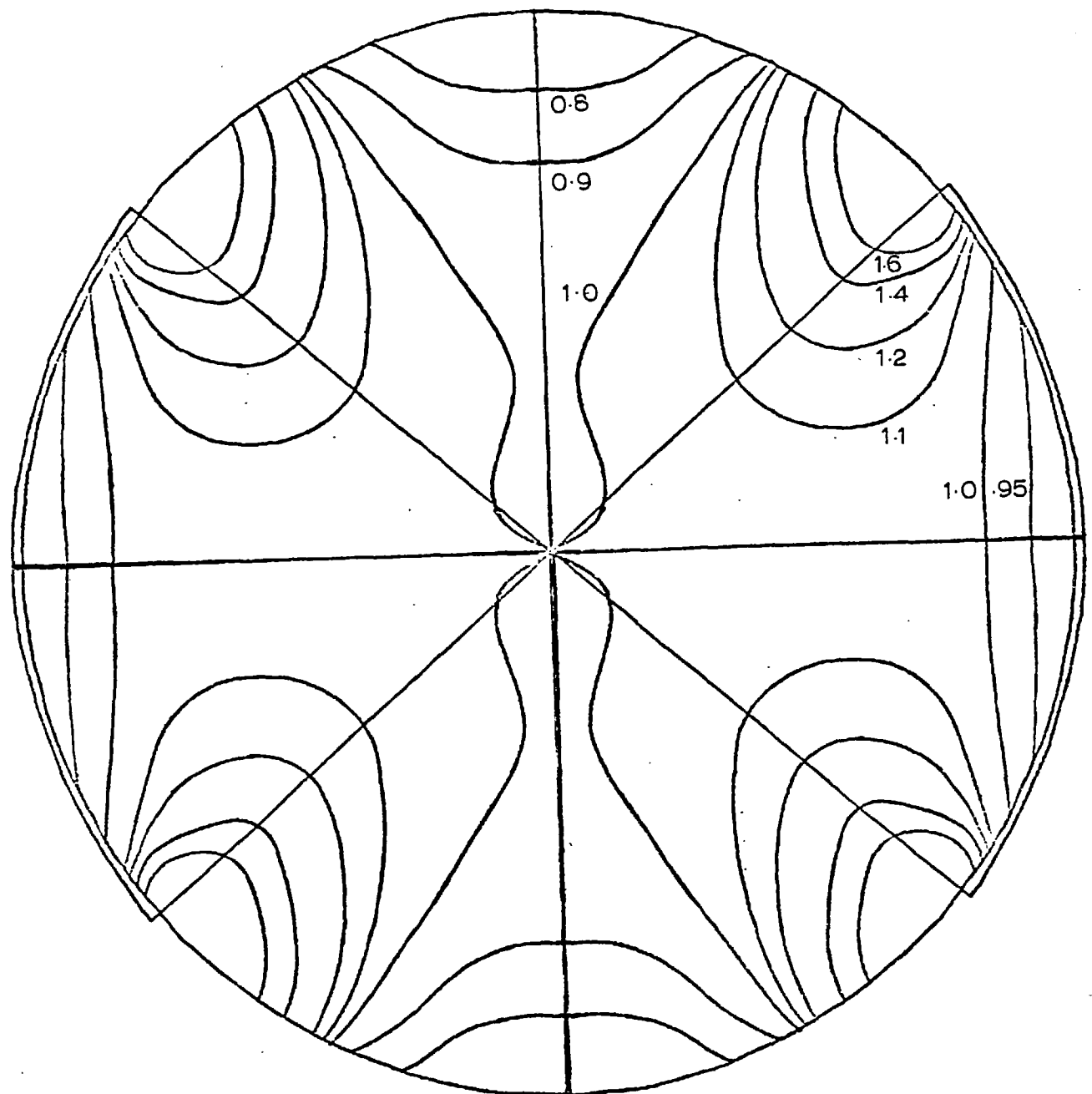


Fig. 2.19 Weight function distribution for Type 2 flowmeter ($w_c = 0.12$)

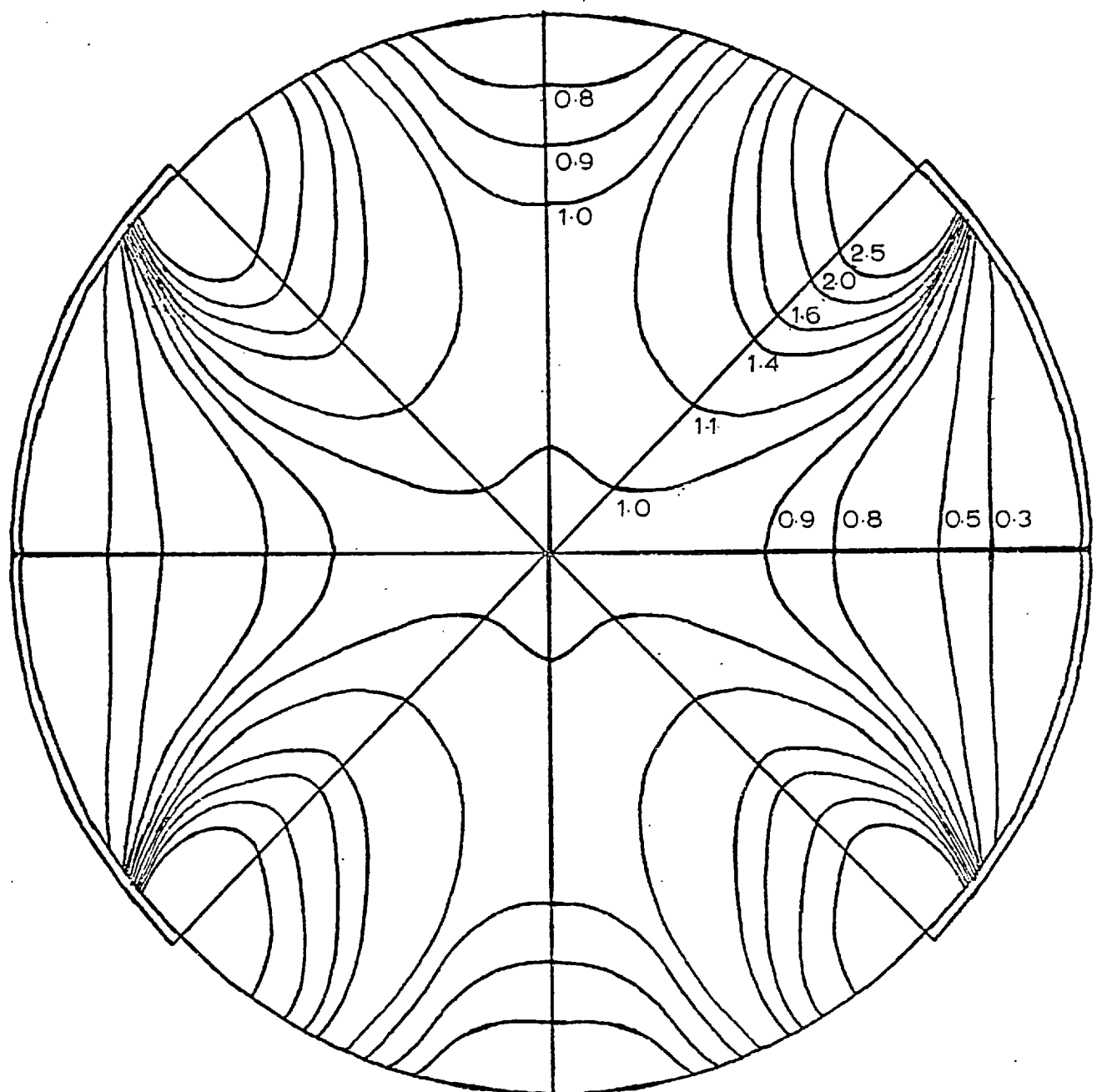


Fig. 2.20 Weight function distribution for Type 3 flowmeter ($w_c = 0.394$)

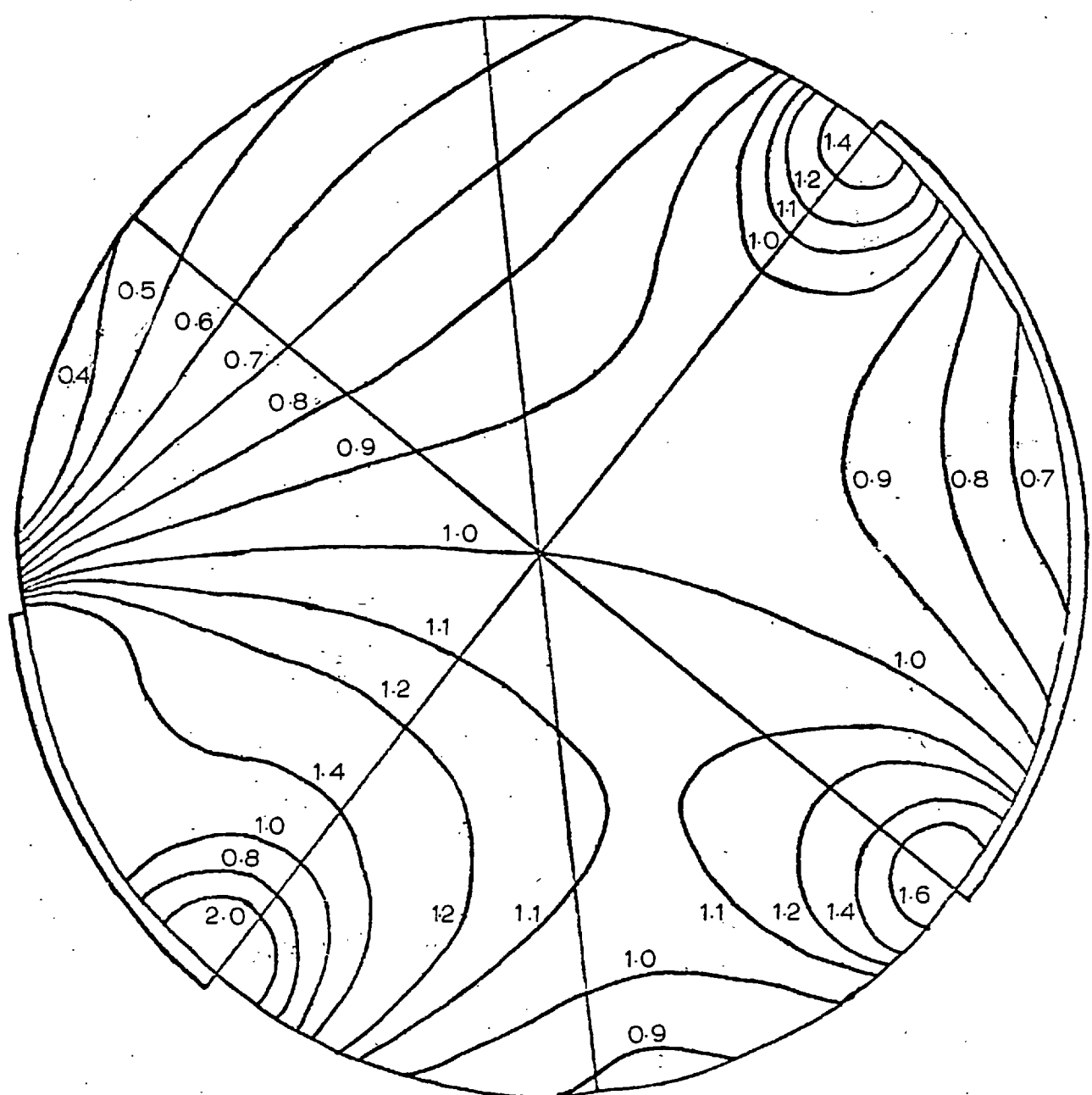


Fig. 2.21 Weight function distribution for Type 1 flowmeter with moderate fouling ($w_c = 0.542$)

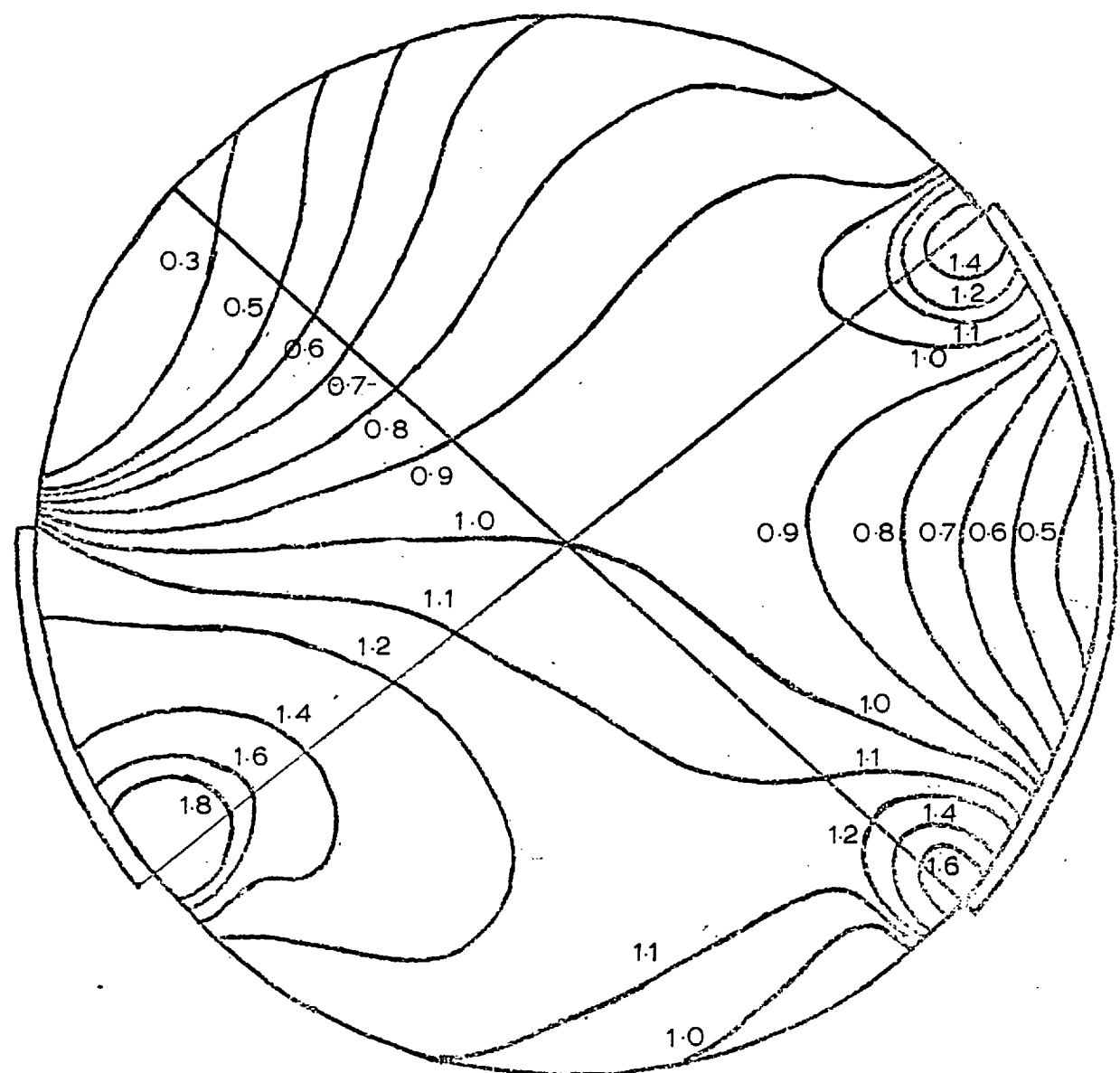


Fig. 2.22 Weight function distribution for Type 2 flowmeter with moderate fouling ($w_c = 0.15$)

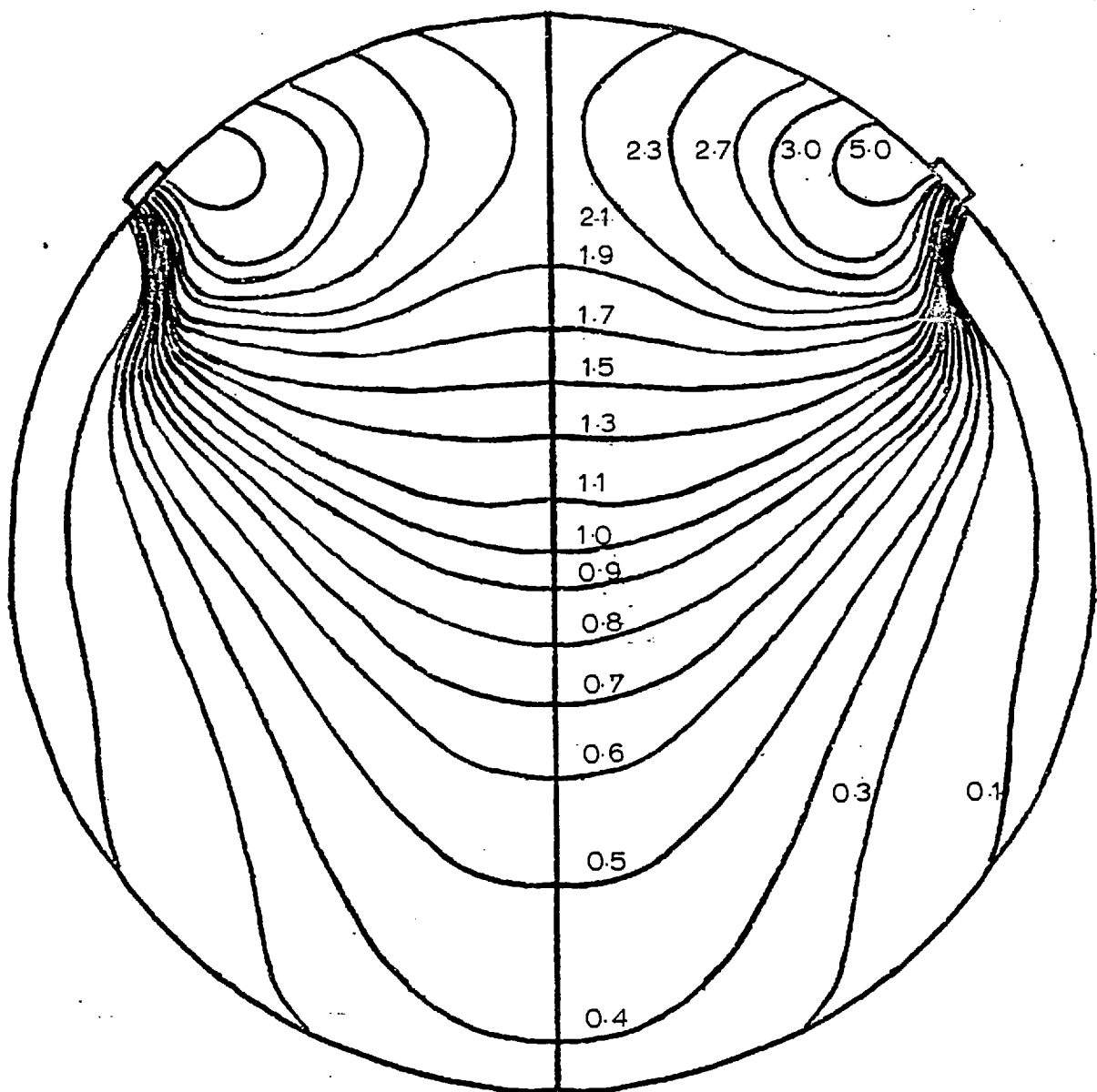


Fig. 2.23 Weight function distribution for Type 1 flowmeter with extreme fouling ($w_c = 0.41$)

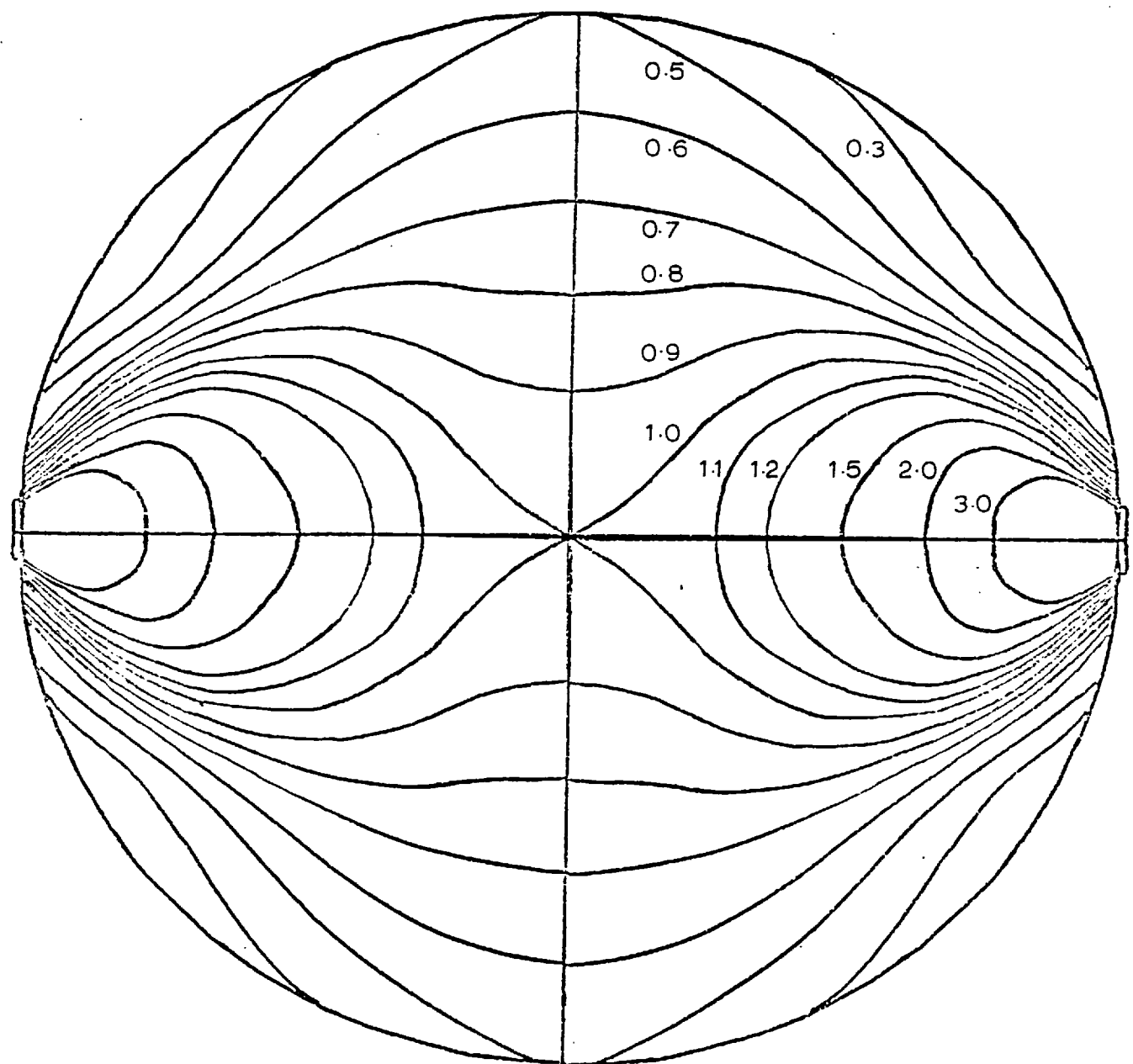


Fig. 2.24 Weight function distribution for Type 1 flowmeter with point electrode ($w_c = 0.056$)

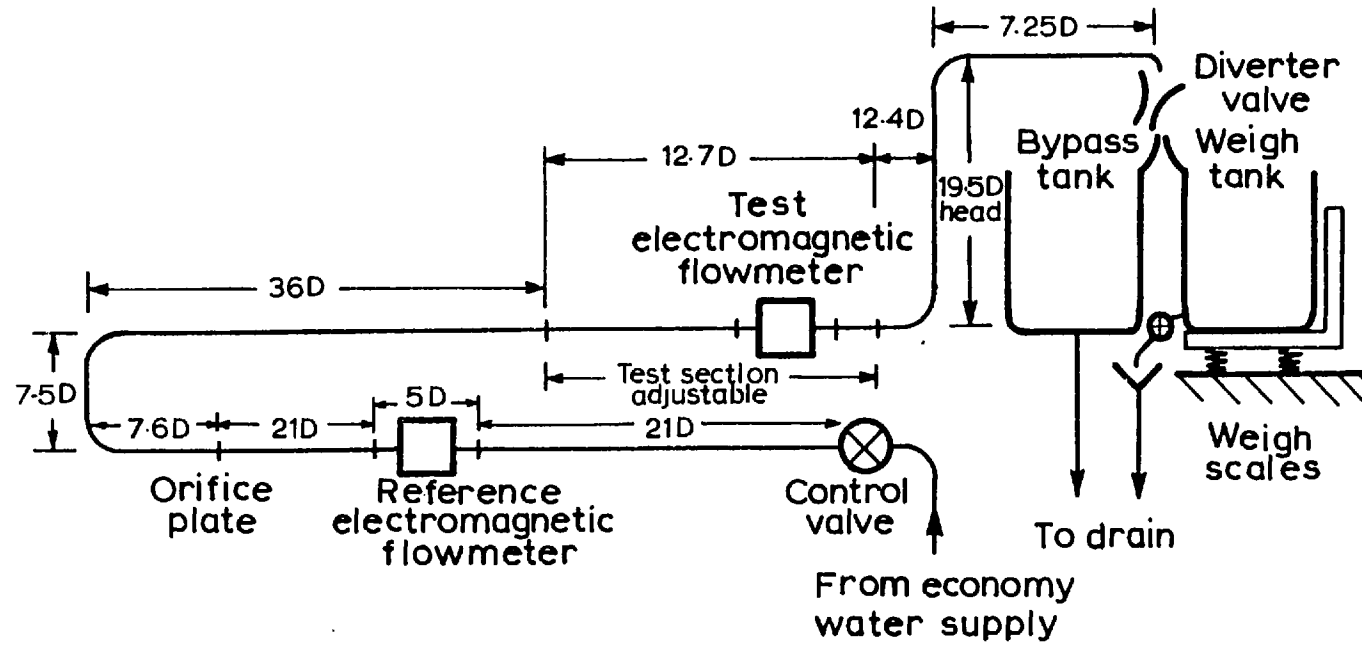


Fig. 3.1 Diagram of 100 mm ID flow rig

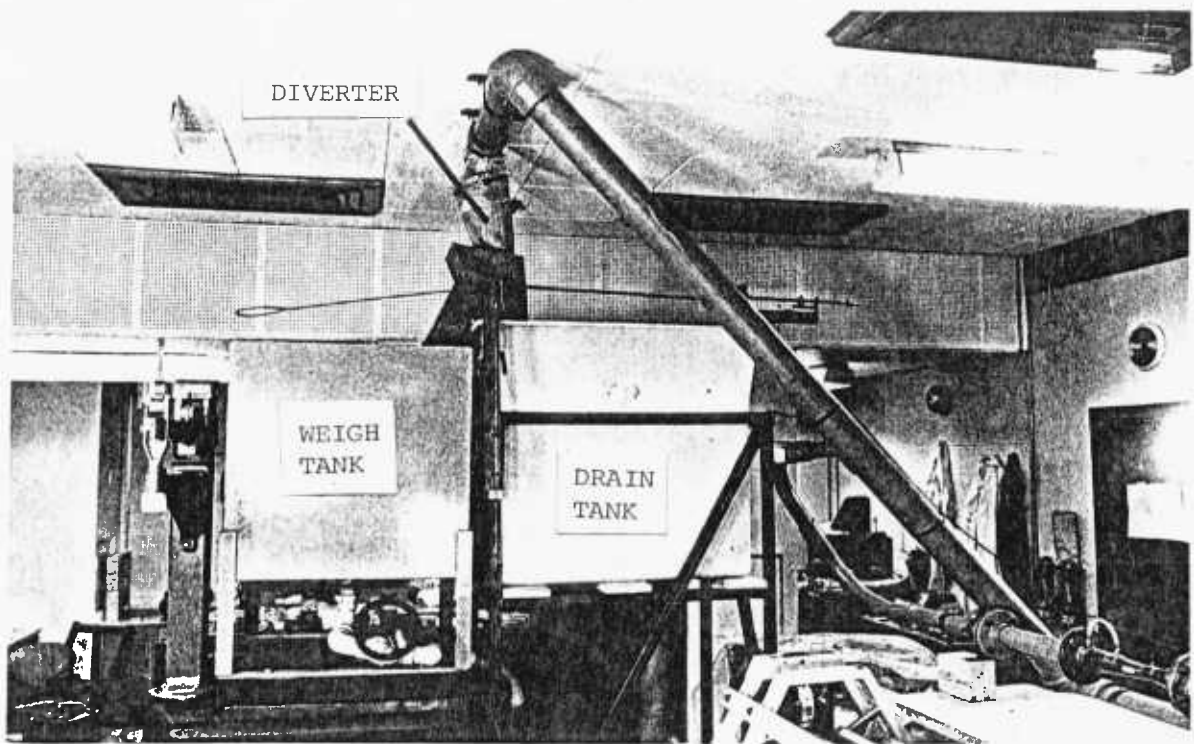


Fig. 3.2 Photograph of 100 mm ID test rig (weigh tank system)

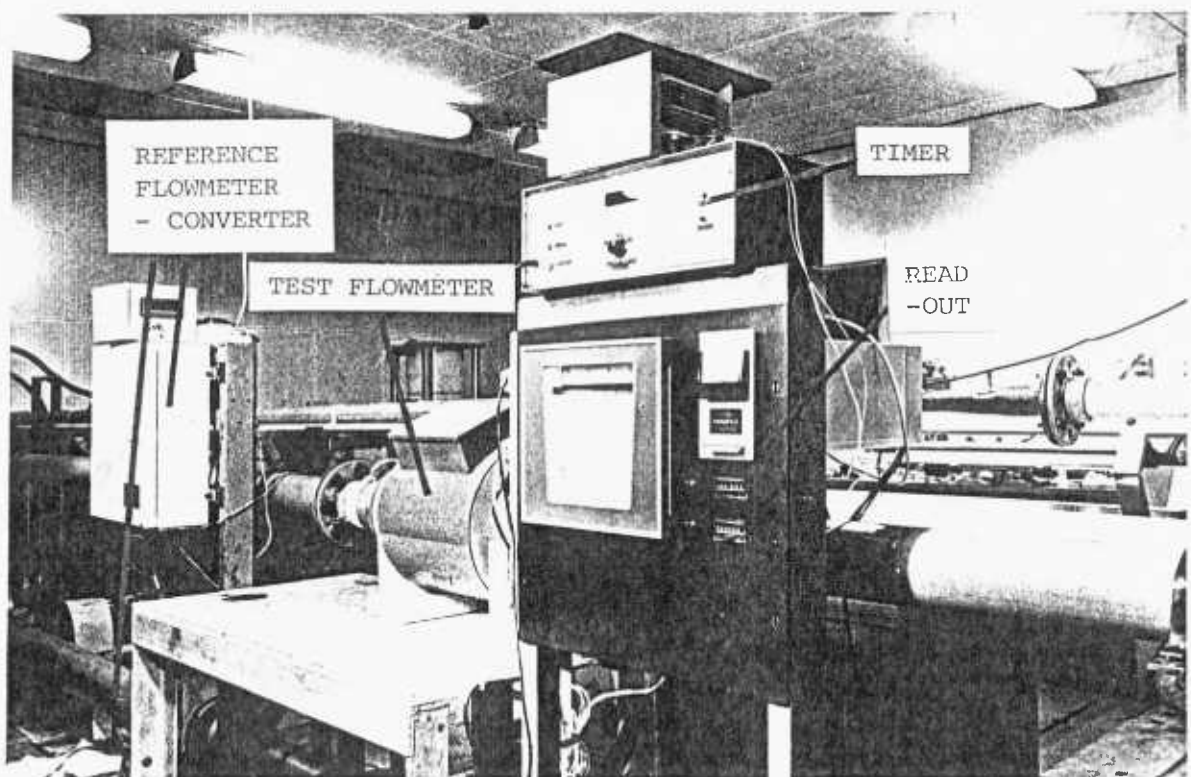


Fig. 3.3 Photograph of 100 mm ID flowmeter and instrumentation

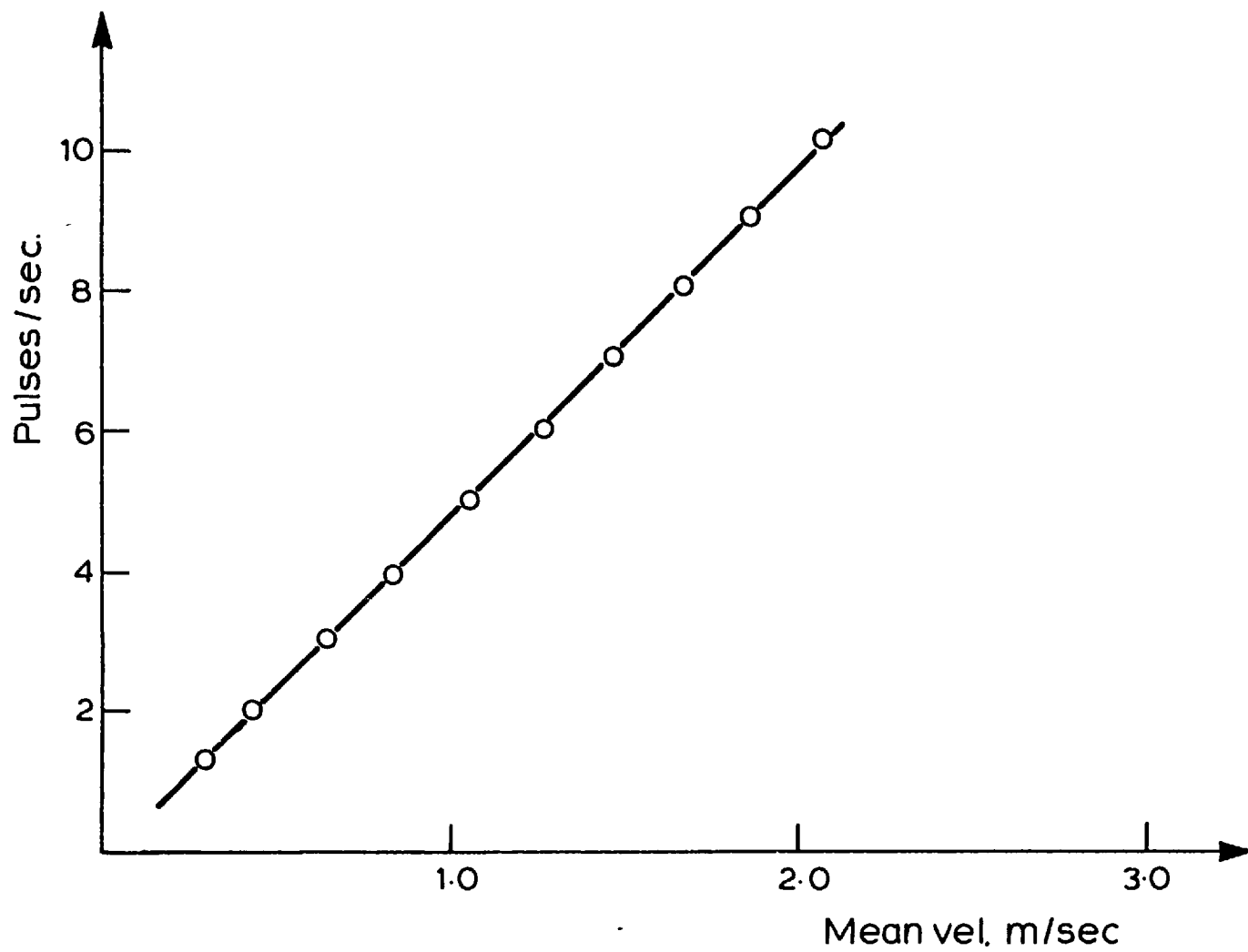


Fig. 3.4 Linearity of the reference flowmeter

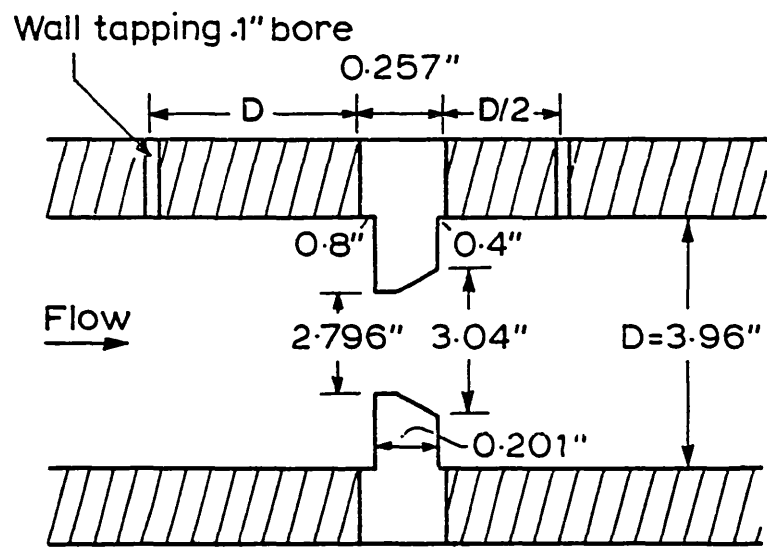


Fig. 3.5 The orifice plate arrangement

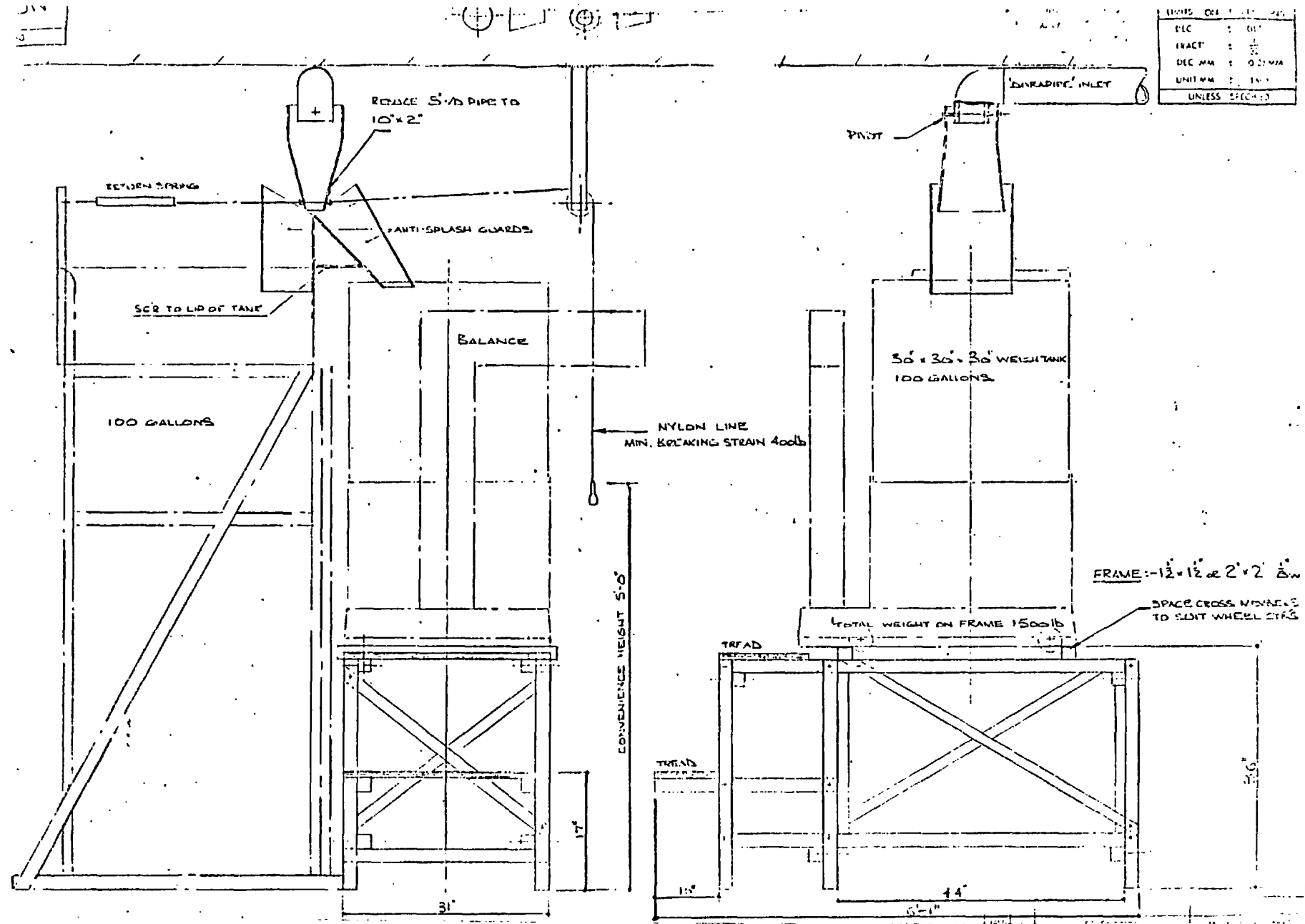


Fig. 3.6 The weighing system assembly

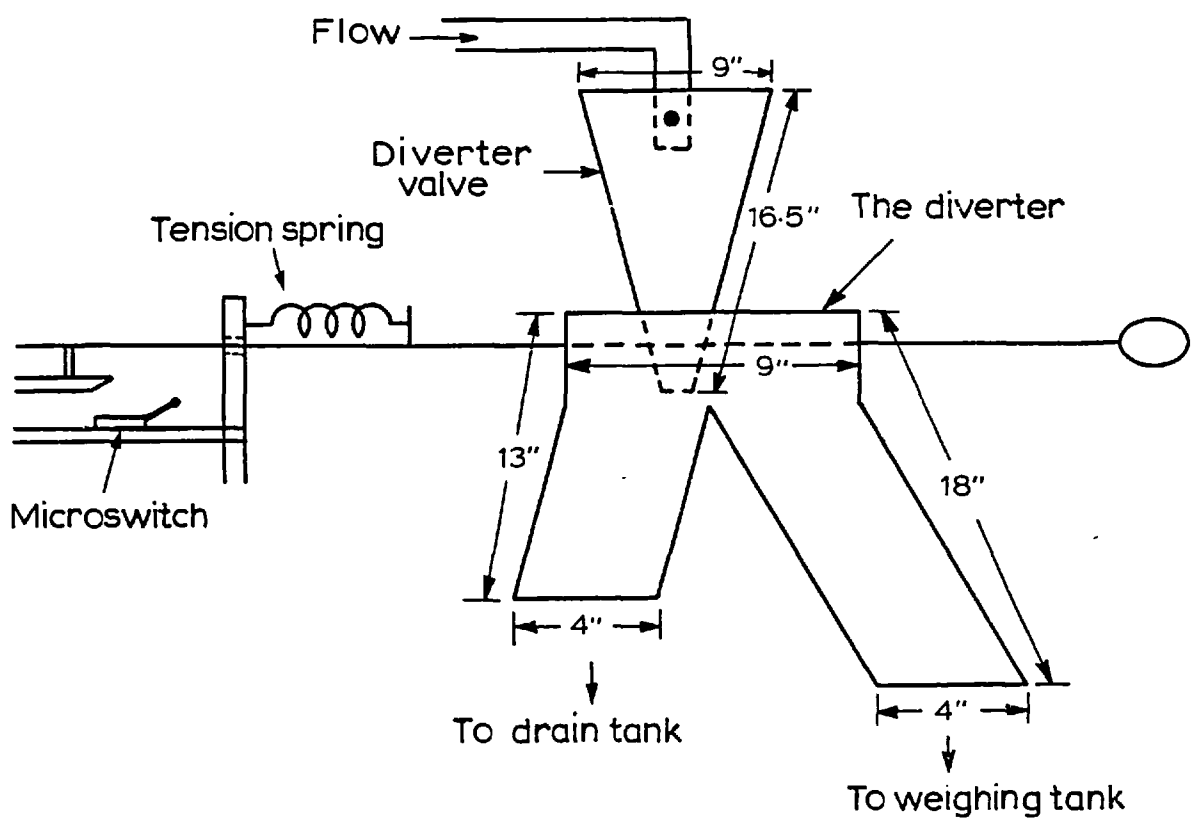


Fig. 3.7 Flow diverter valve assembly

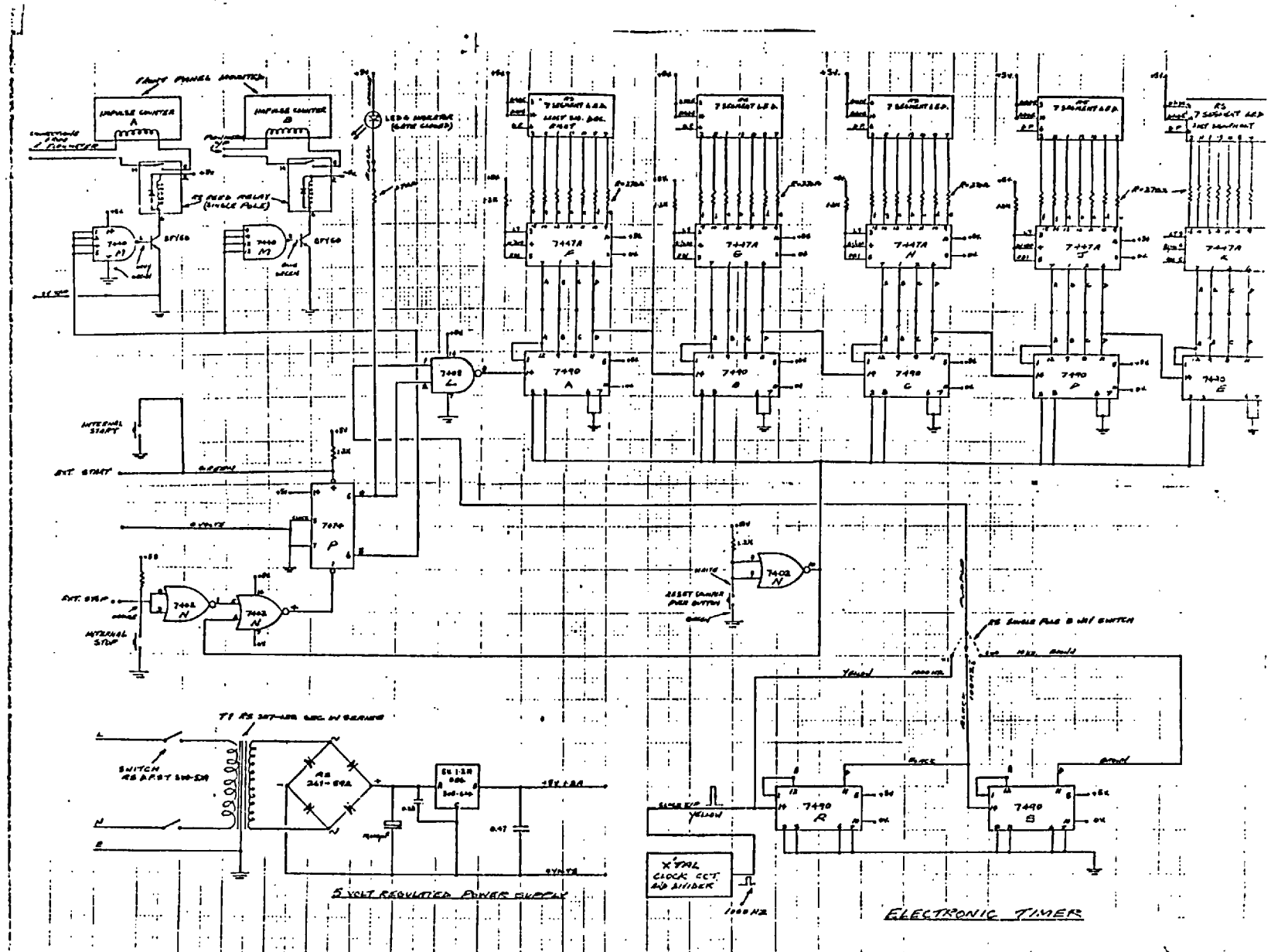


Fig. 3.8a The circuit of the electronic timer

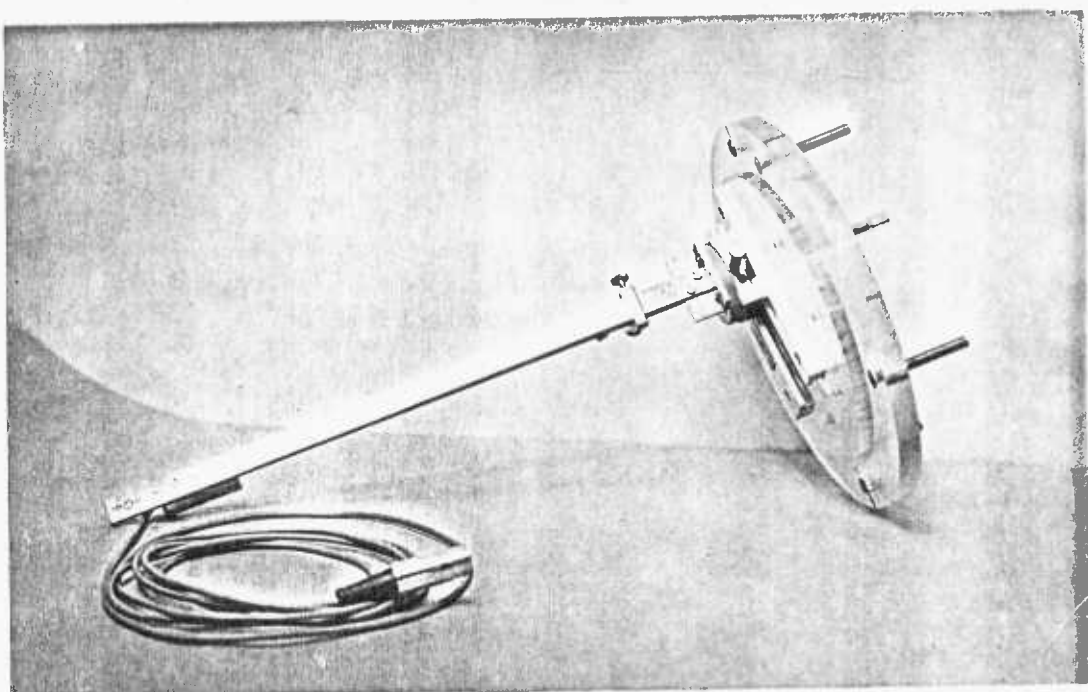


Fig. 3.8b The probe assembly for measuring the magnetic field

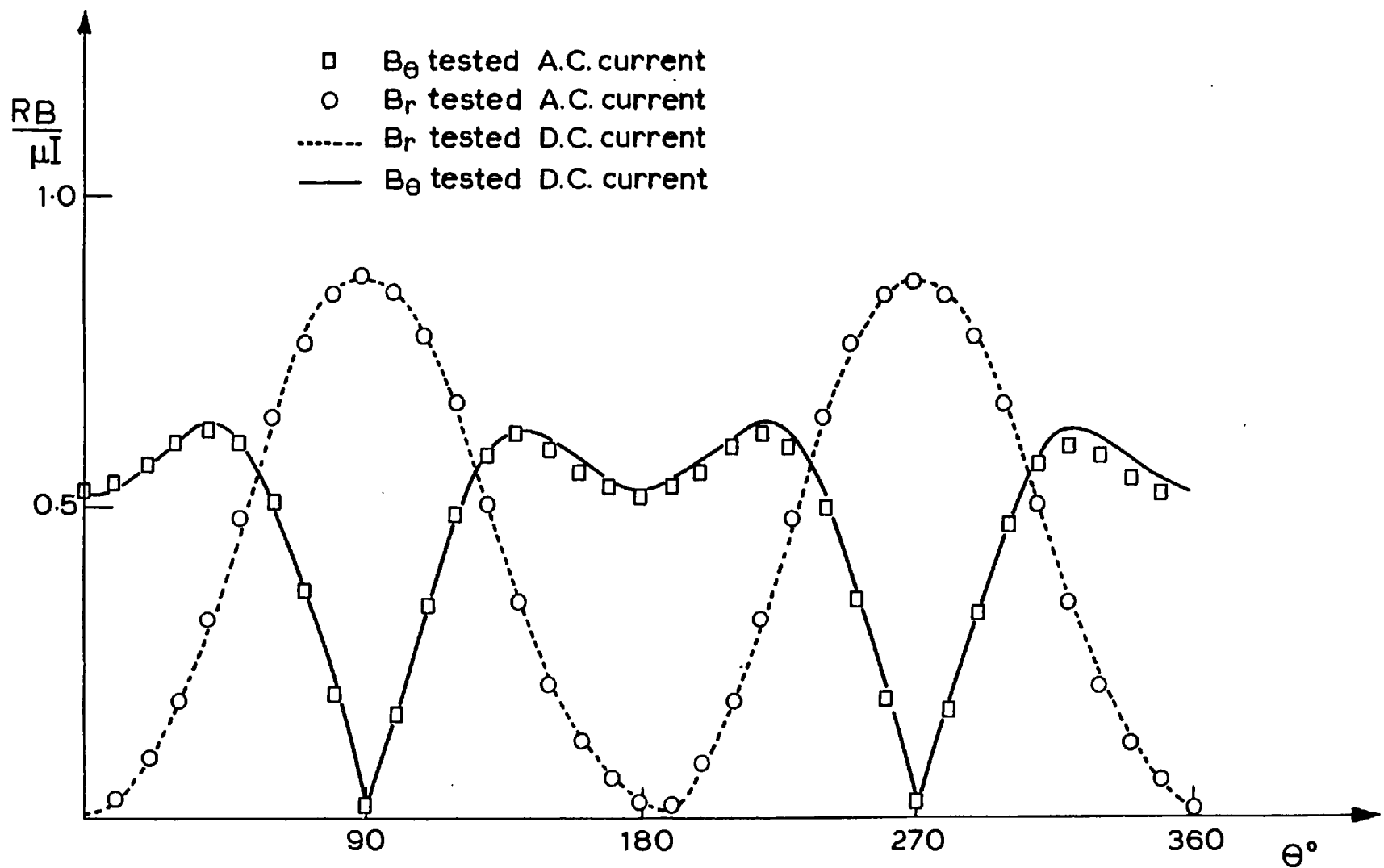


Fig. 3.9 Comparison between AC and DC test values of the magnetic field for Type 1 flowmeter

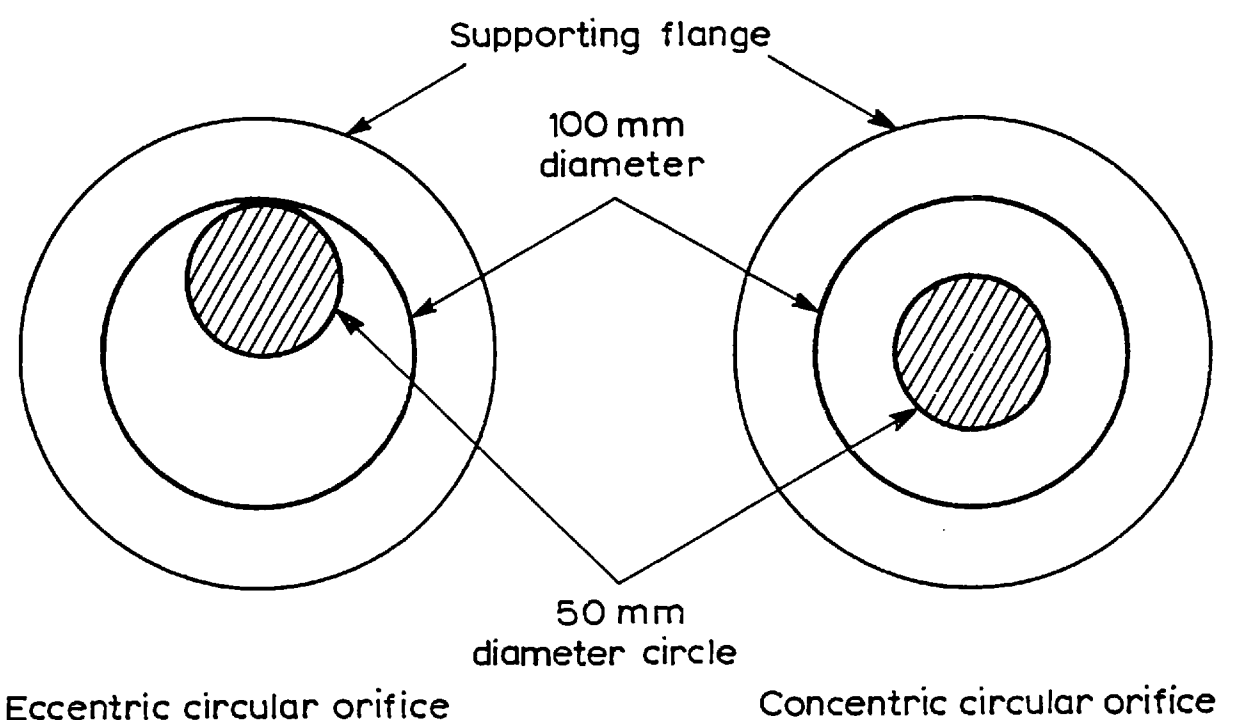


Fig. 3.10 Diagram of distortion discs

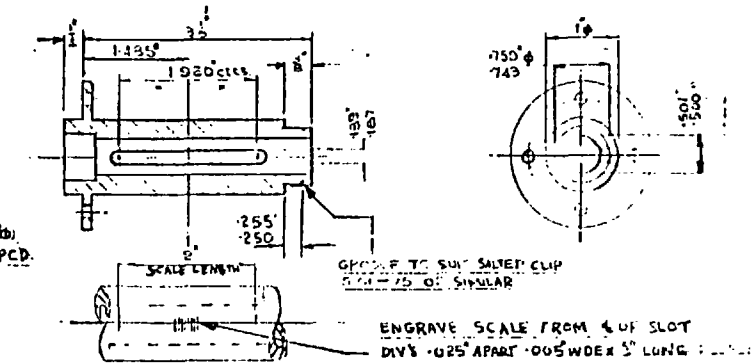
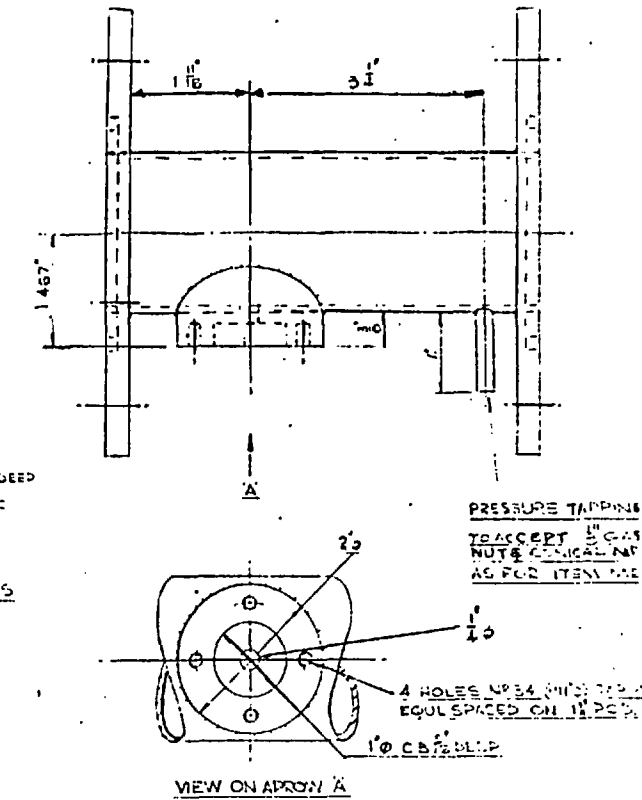
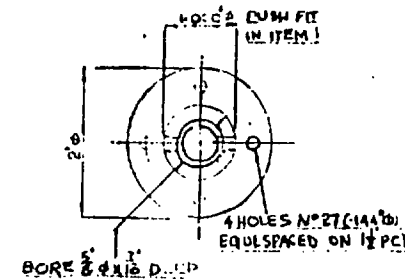
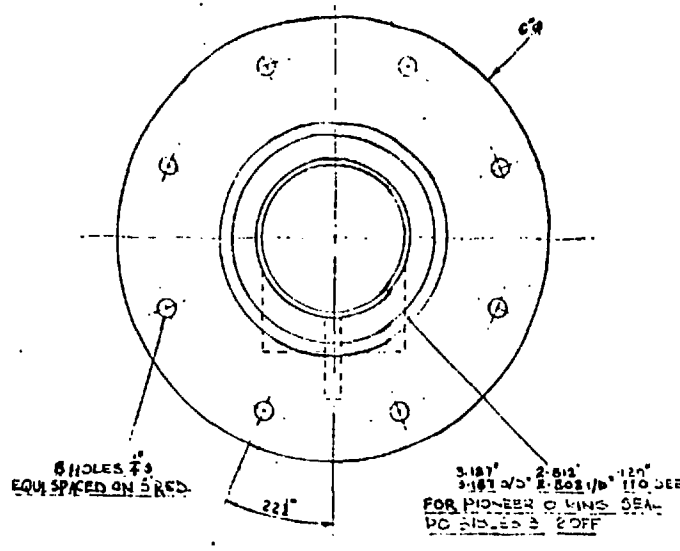
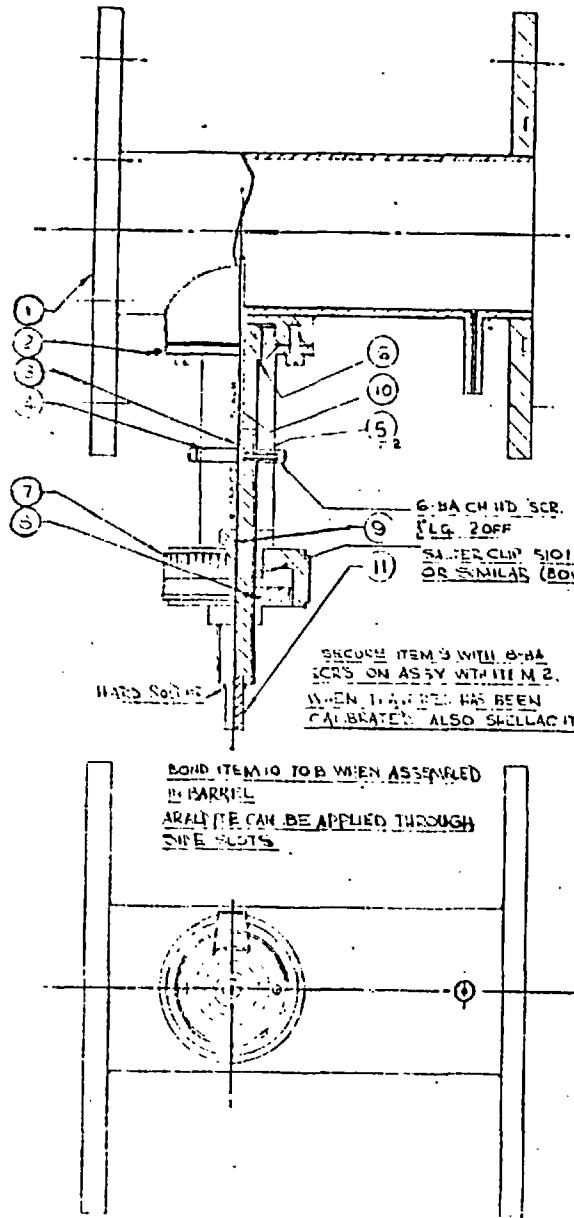
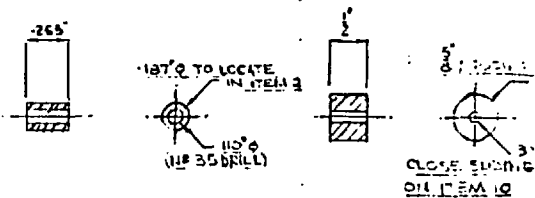
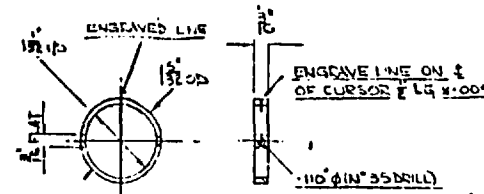
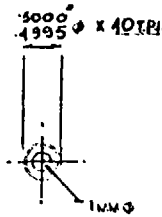
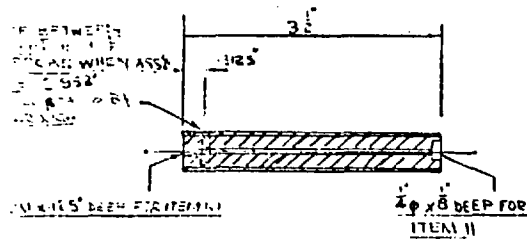
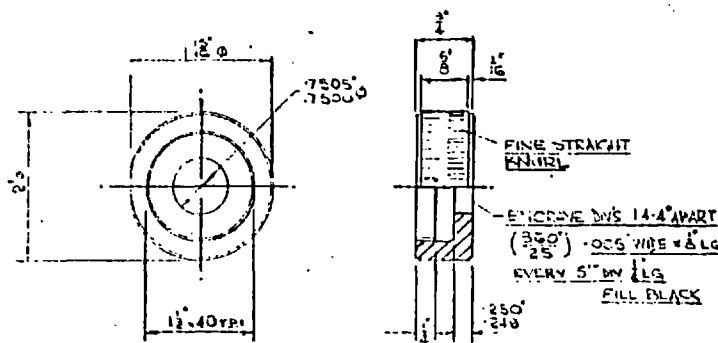


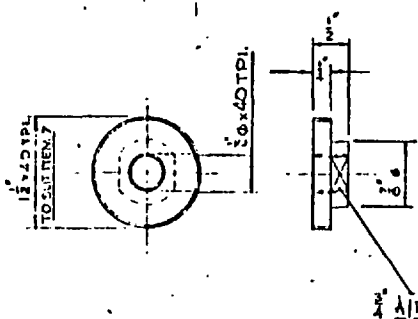
Fig. 3.11 Traverse-Pitot tube assembly



(3) SCREW MATL. PHOSPHOR BRONZE 1 OFF

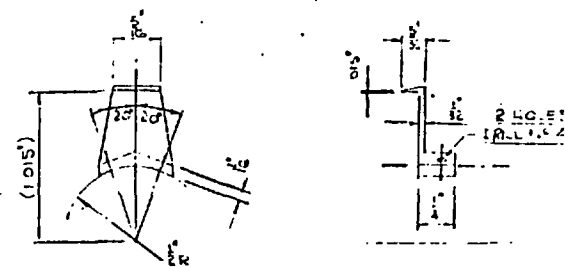


(4) CURSOR MATL. PERSPEX 1 OFF

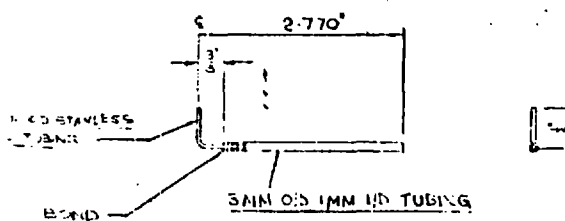


(5) SPACER MATL. NYLON 2 OFF

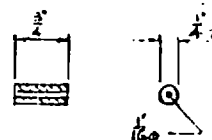
ITEMS 5 & 9 SCALE 2:1



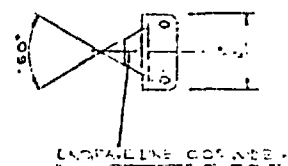
(7) THIMBLE MATL. ALUMINUM ALLOY 1 OFF



(8) ADJUSTABLE NUT MATL. HARD BRASS 1 OFF



(9) FILMIA BRACKET MATL. BRASS 1 OFF



(10) PROBE MATL. STAINLESS STEEL 1 OFF

(11) TUBE MATL. BRASS 1 OFF

Fig. 3.12 Traverse-Pitot tube assembly

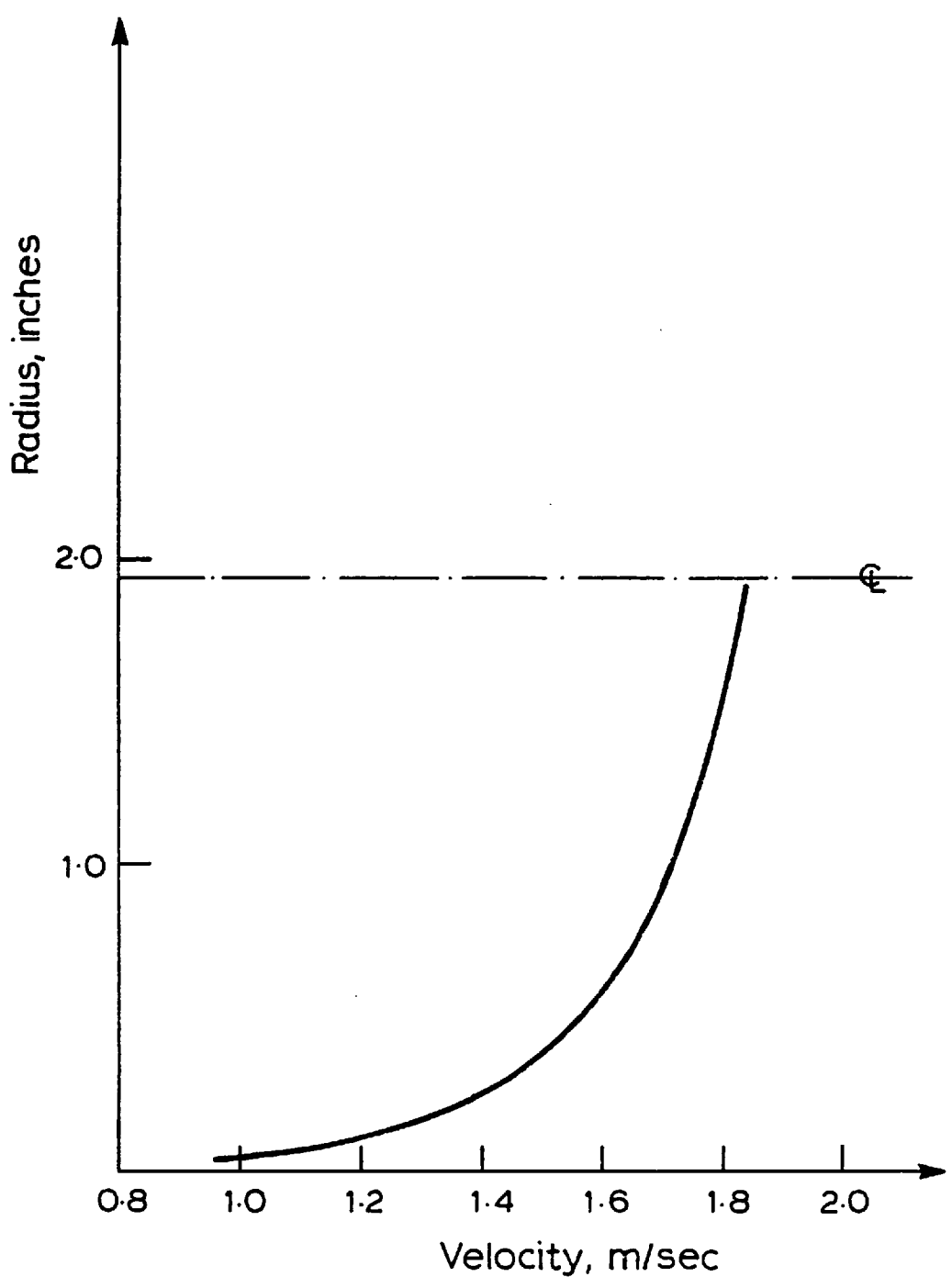


Fig. 3.13 Undisturbed flow profile

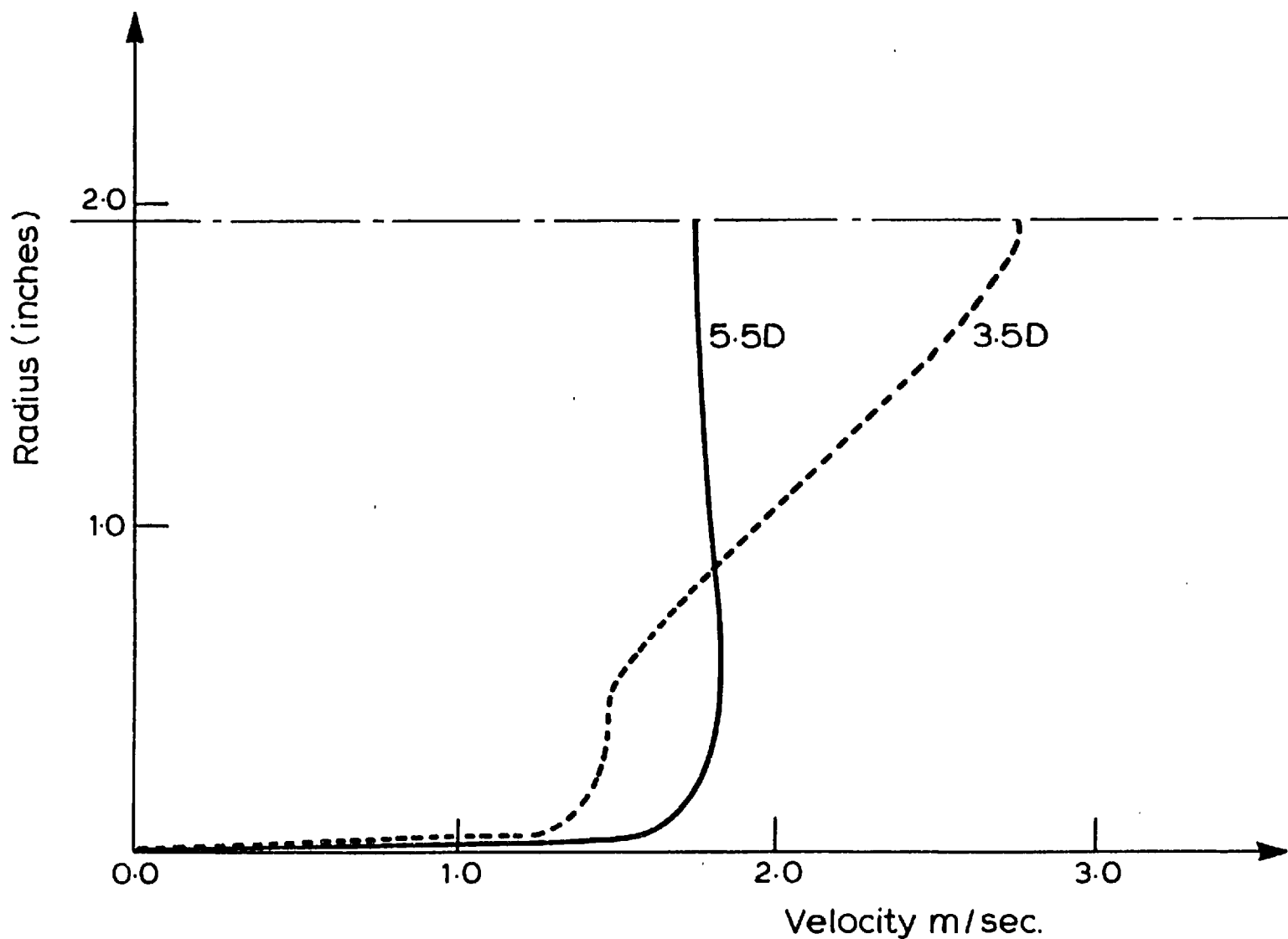


Fig. 3.14 Flow profile with concentric distortion disc

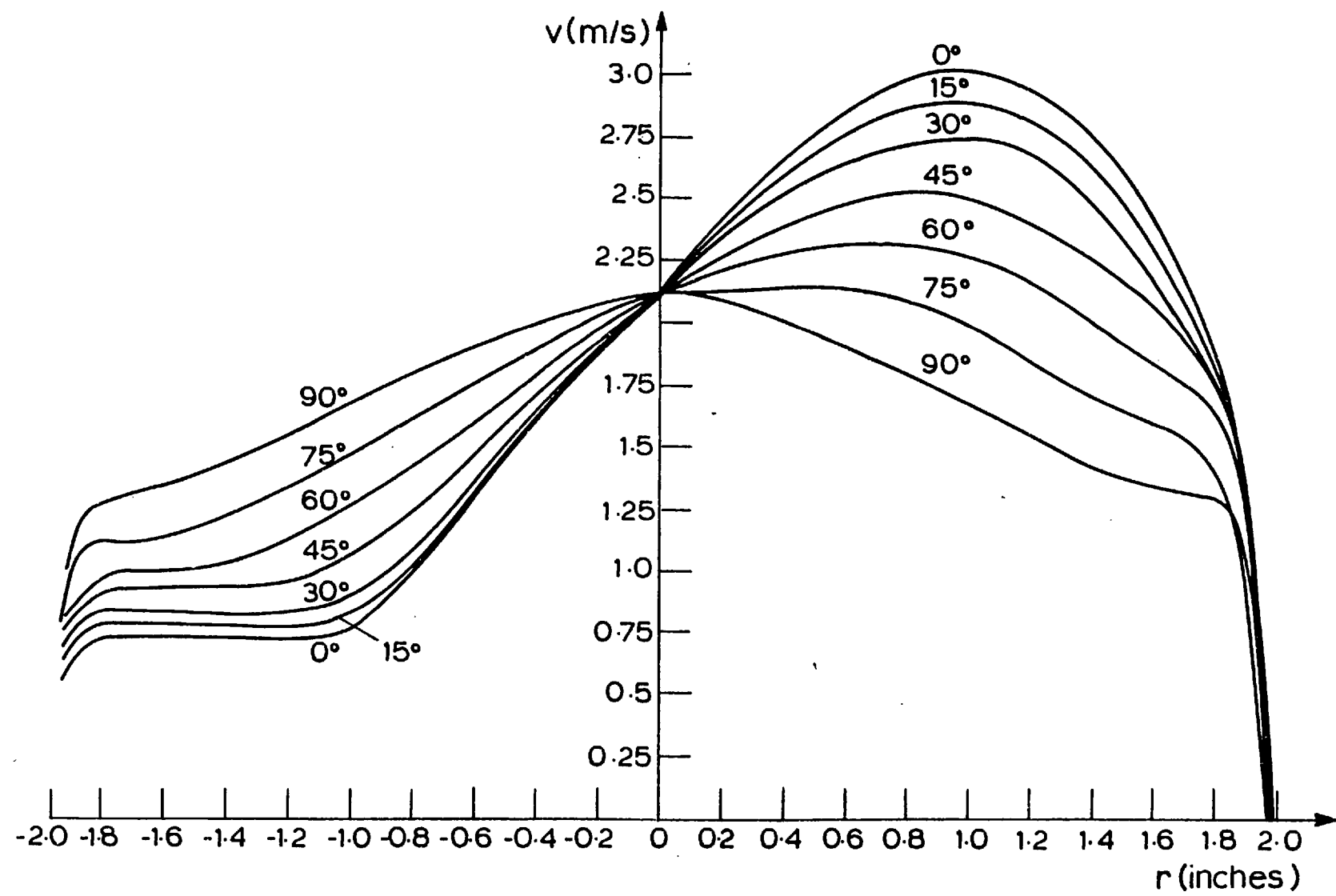


Fig. 3.15 Flow profile with eccentric distortion disc

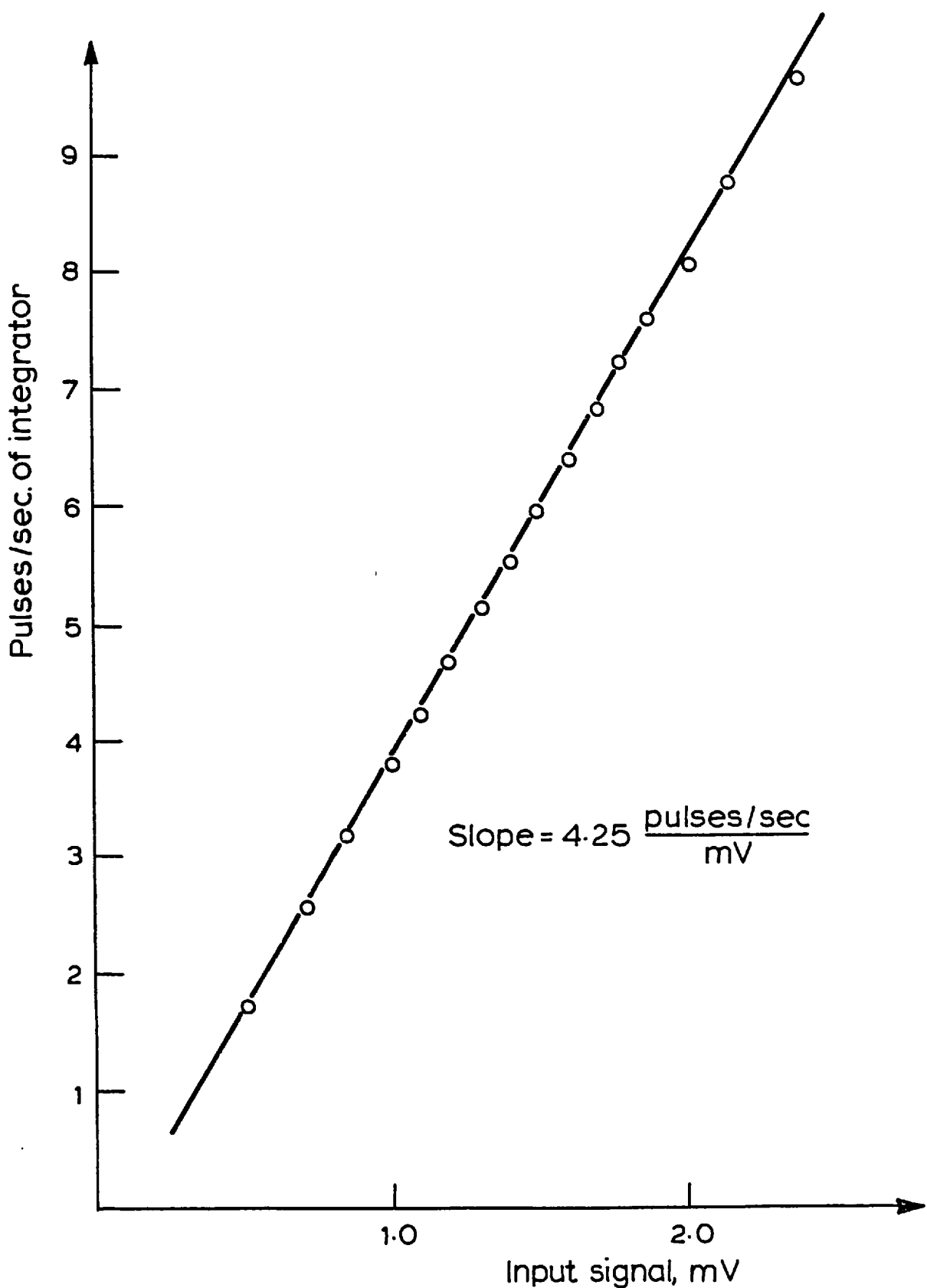


Fig. 3.16 Calibration graph of the series 400 converter

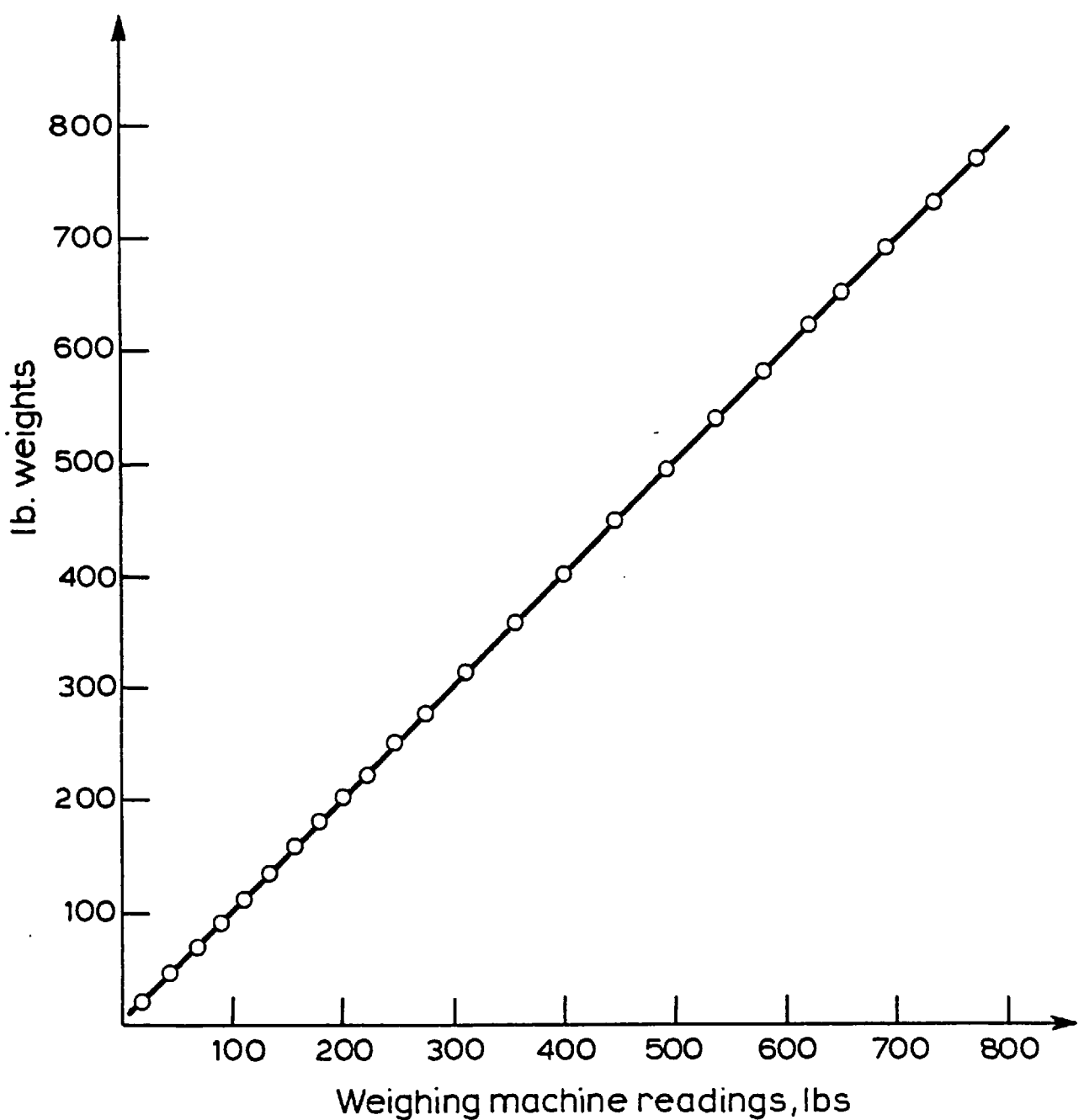


Fig. 3.17 The weighing machine linearity

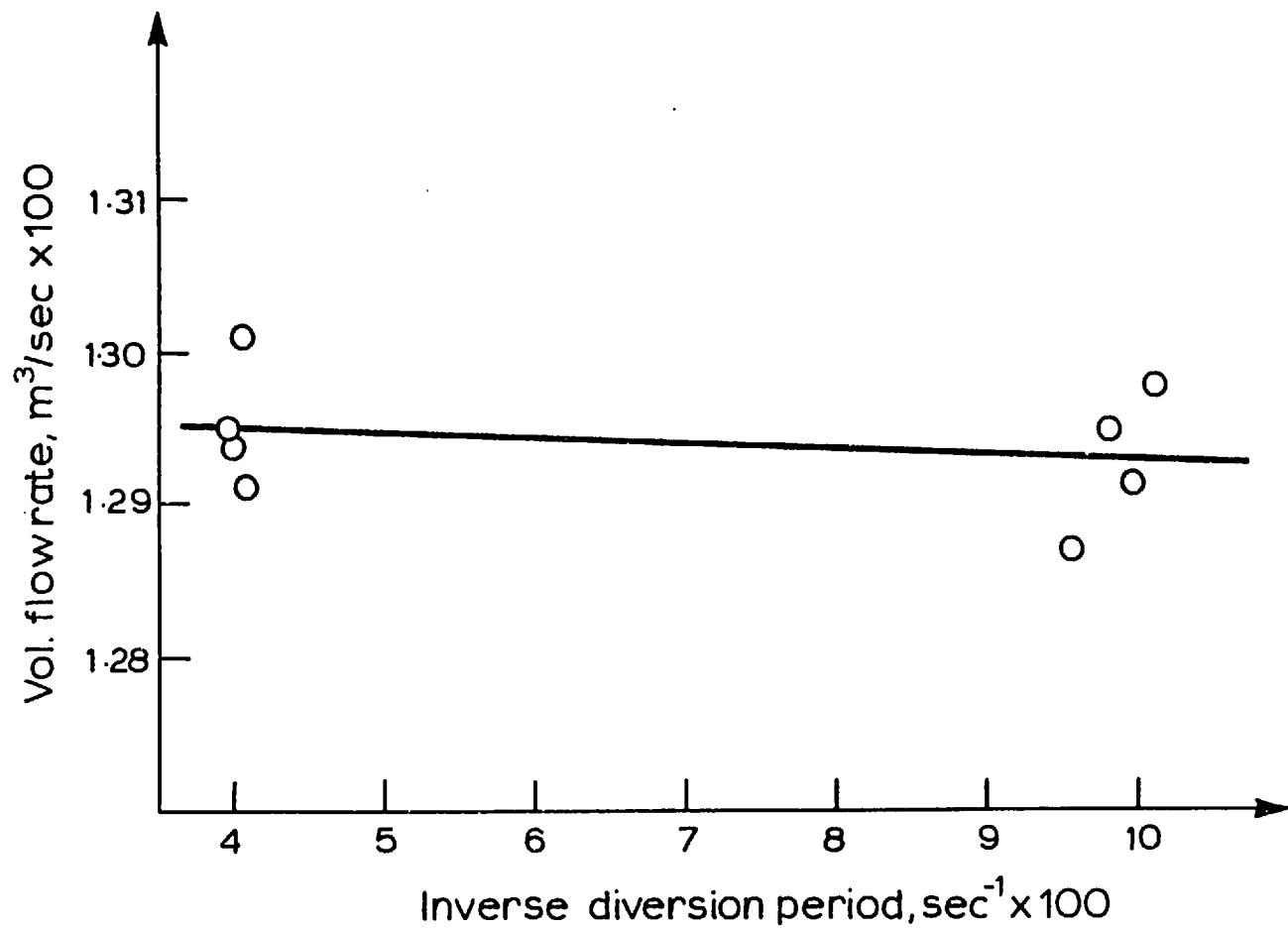


Fig. 3.18 Result of diverter adjustment tests

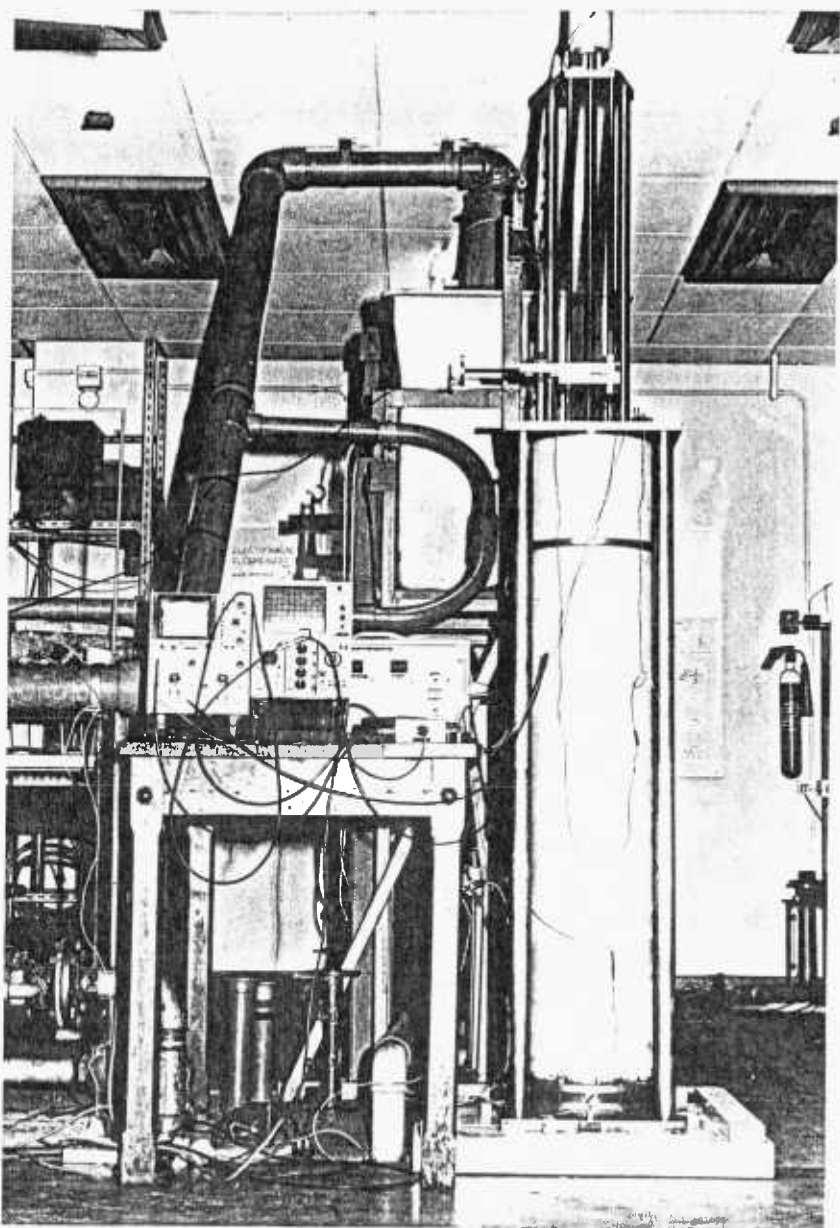


Fig. 4.1 Photograph of the virtual current tank and associated electronics.

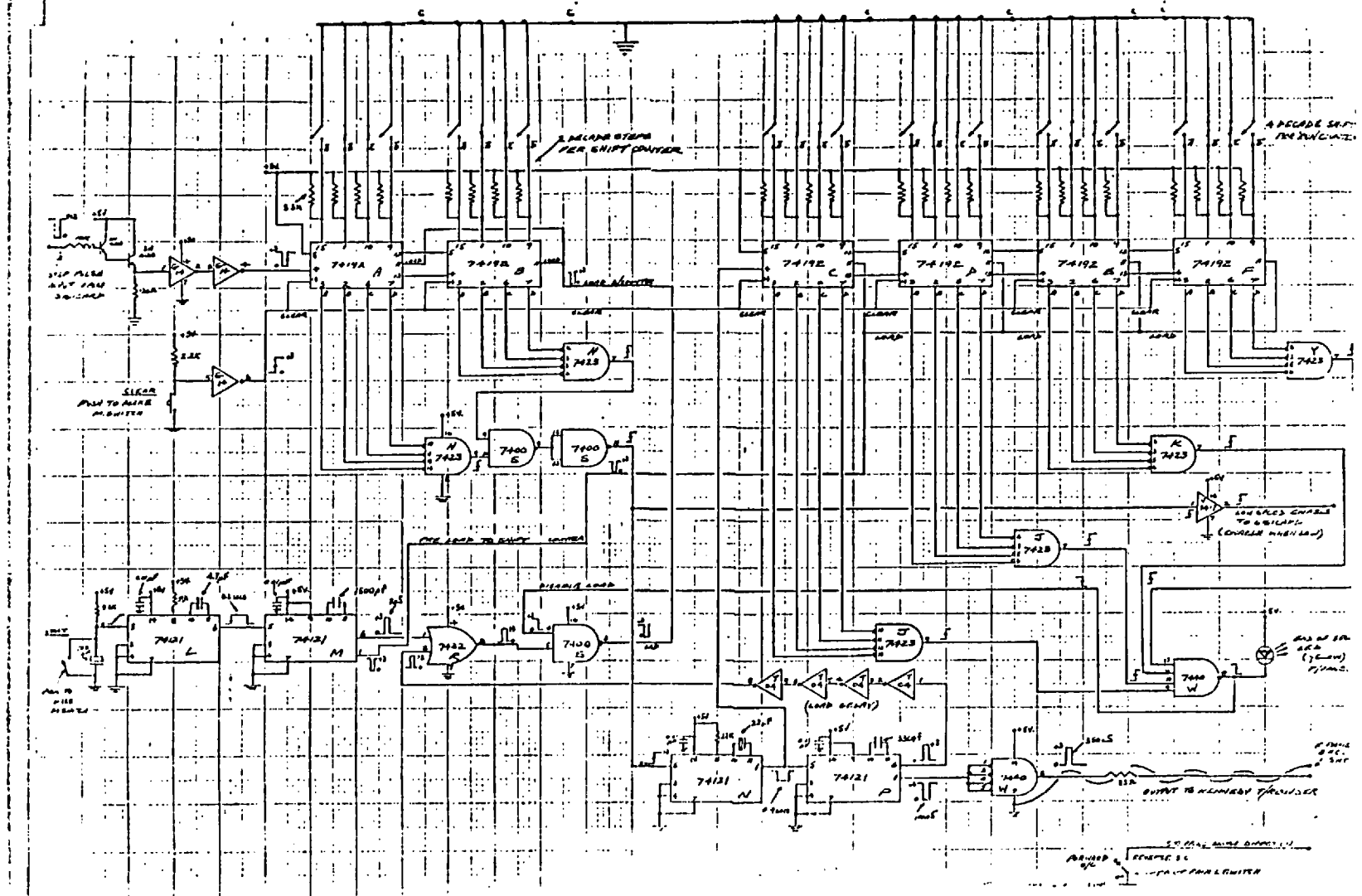
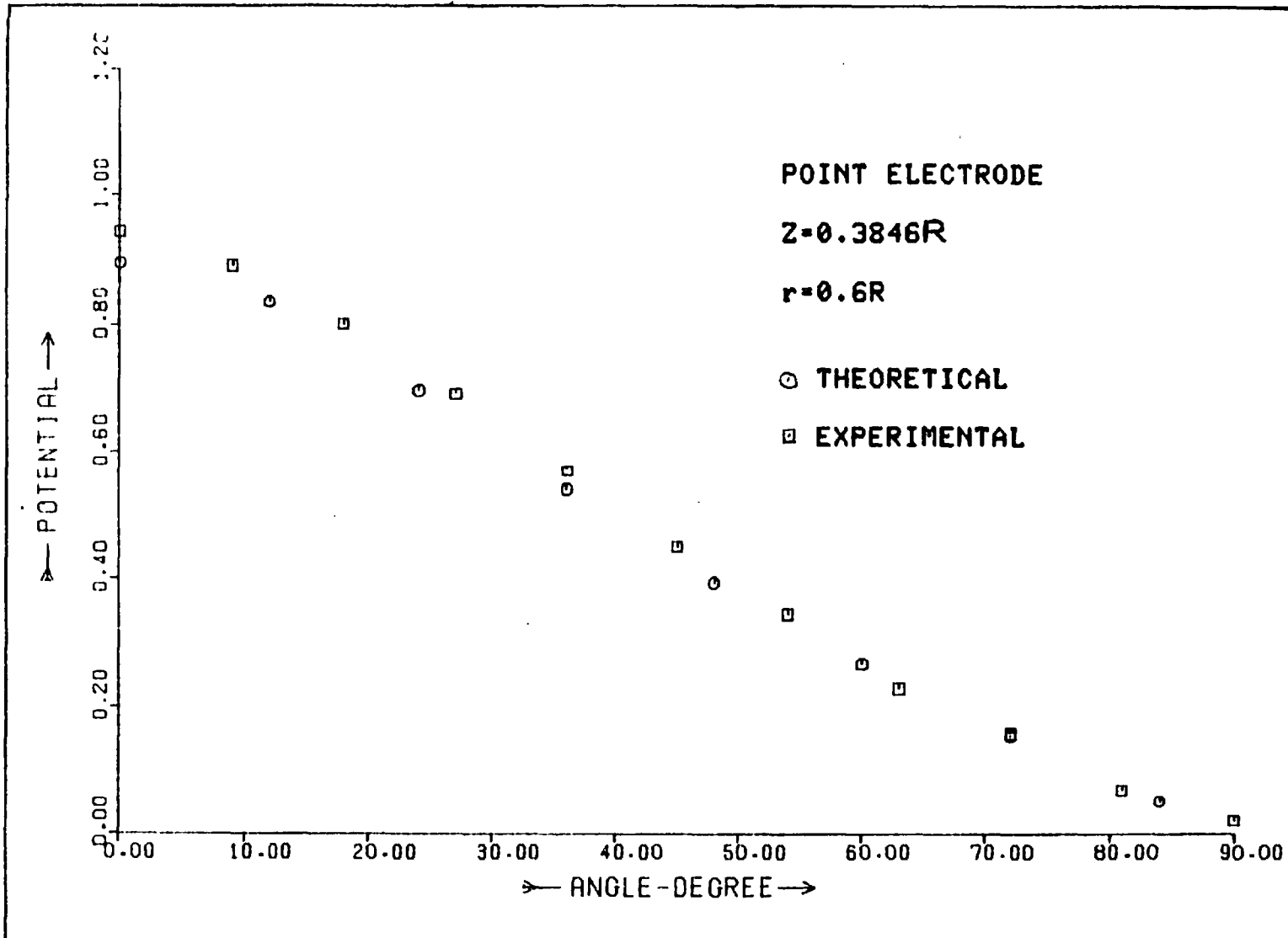
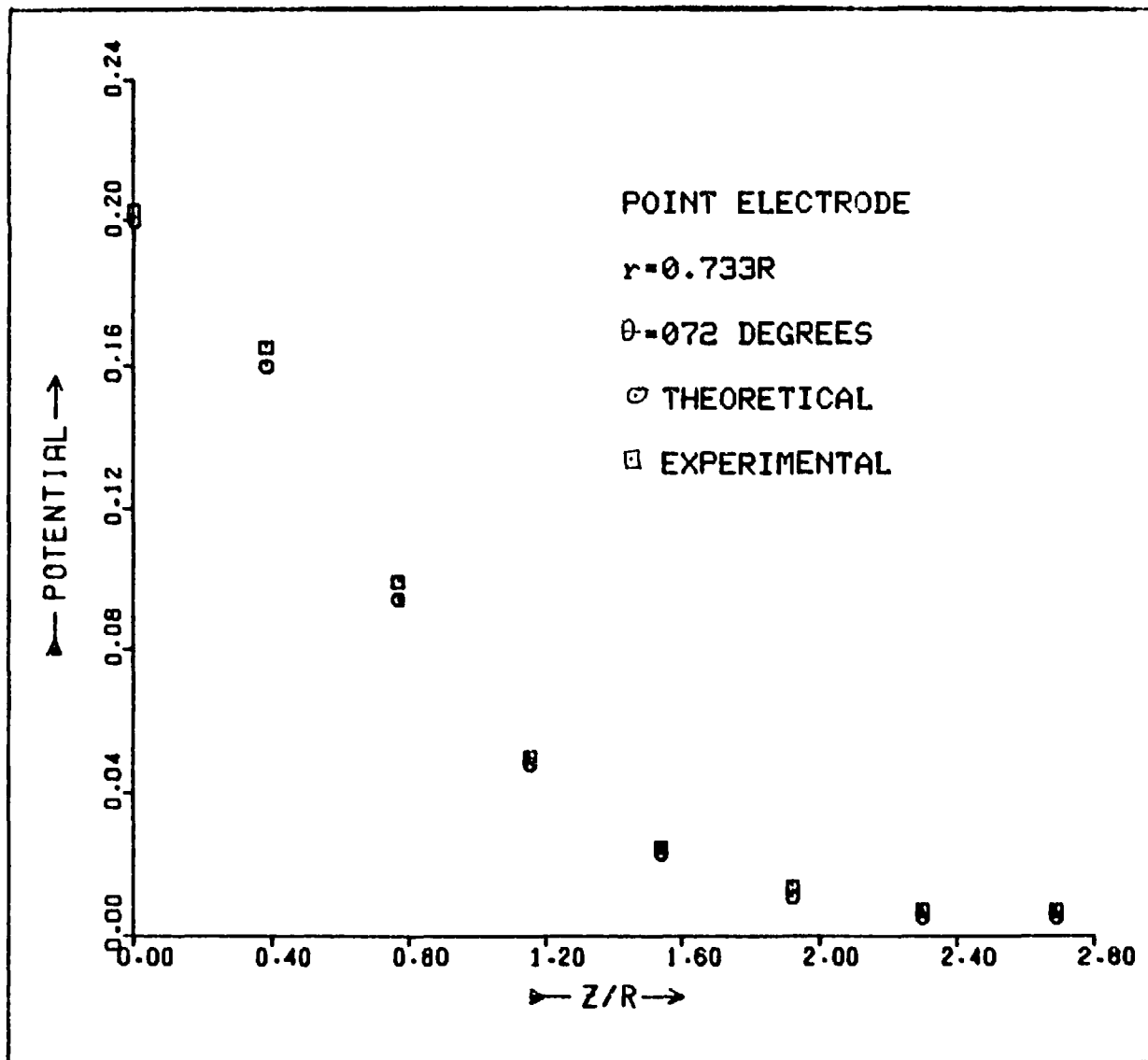


Fig. 4.2 Logic circuit for stepping motor controller



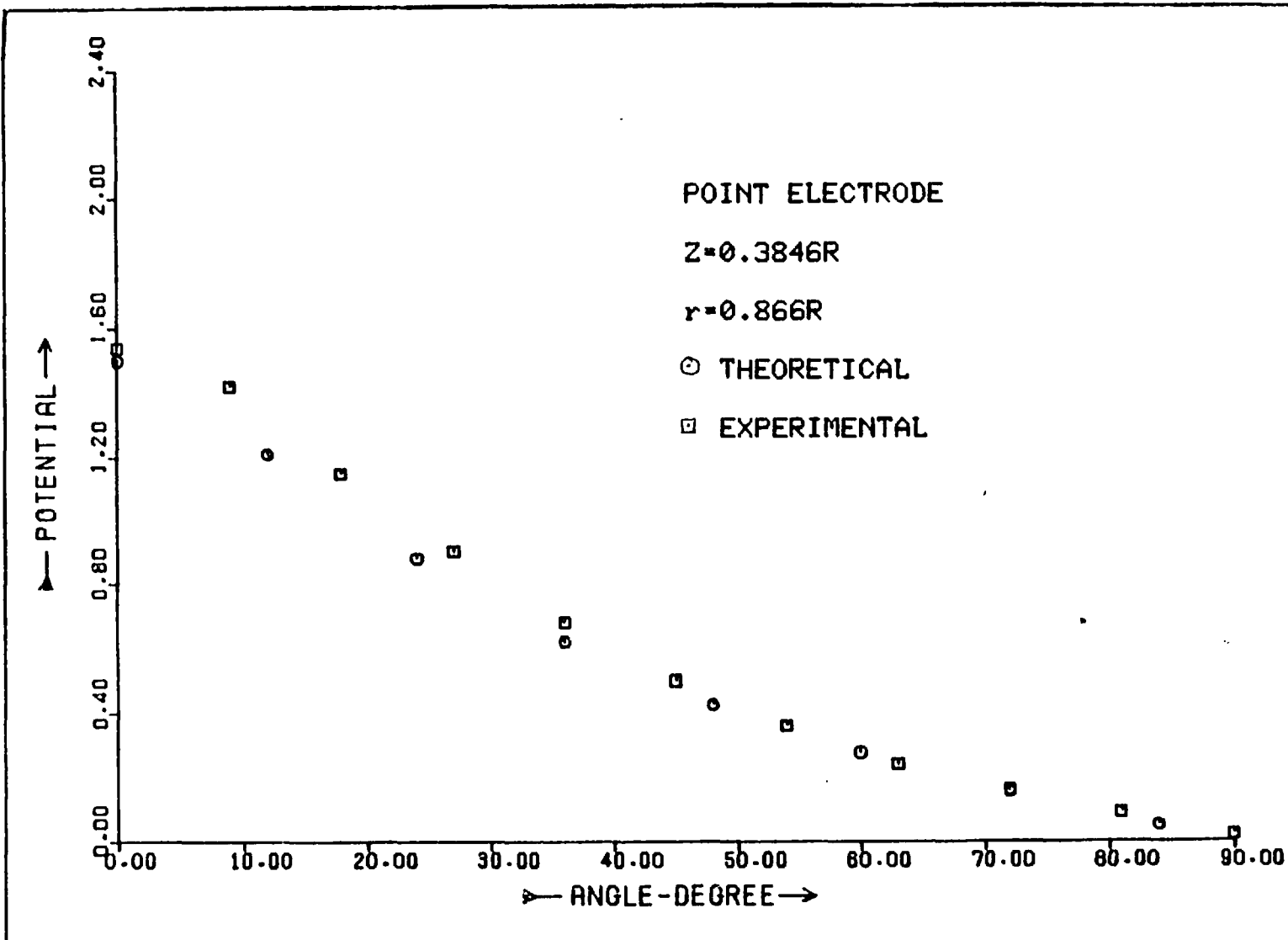
(a)

Fig. 4.3 Comparison of experimental values of virtual potential with computed values (point-electrodes flowmeter)



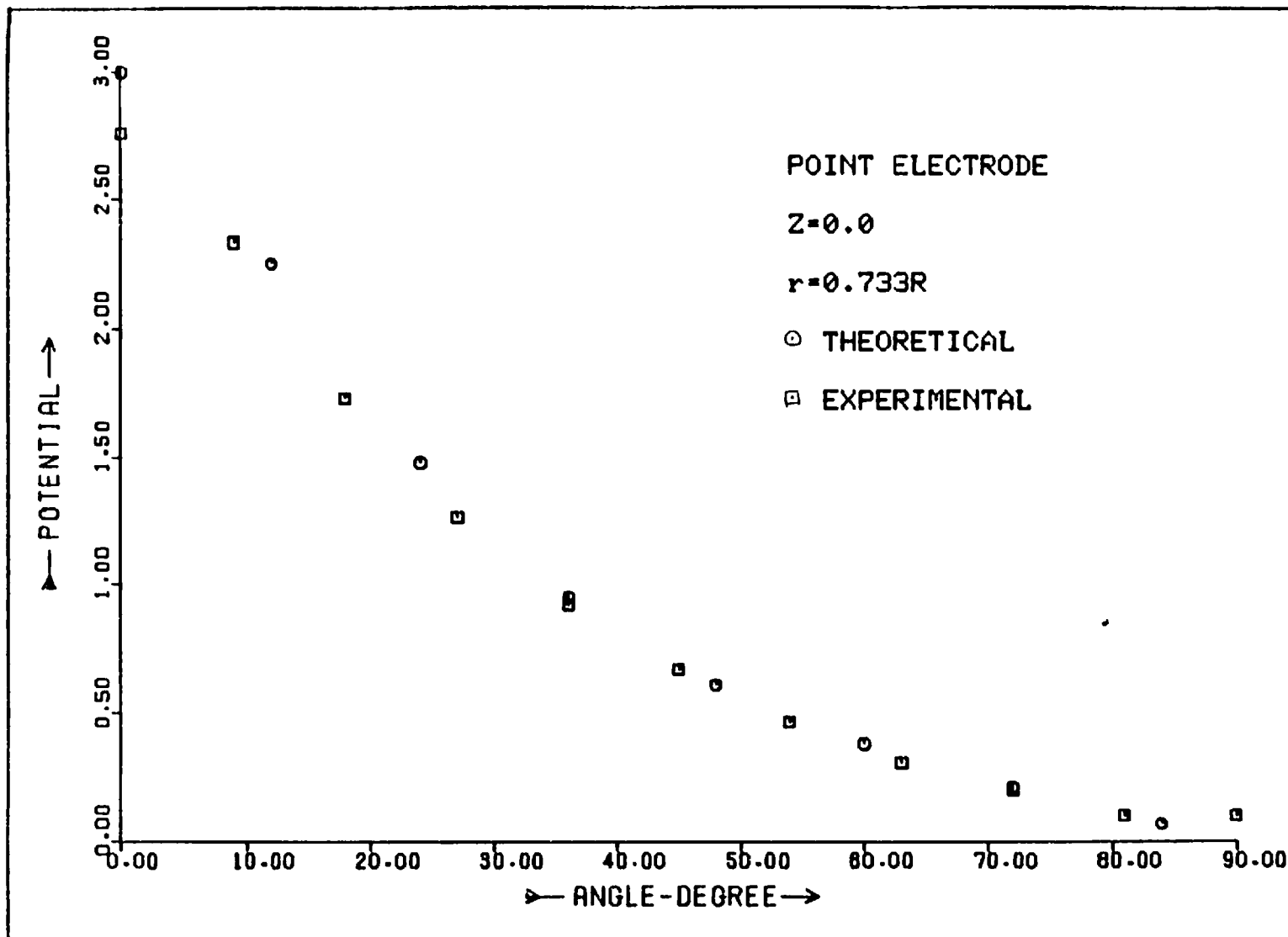
(b)

Fig. 4.3 (Continued)



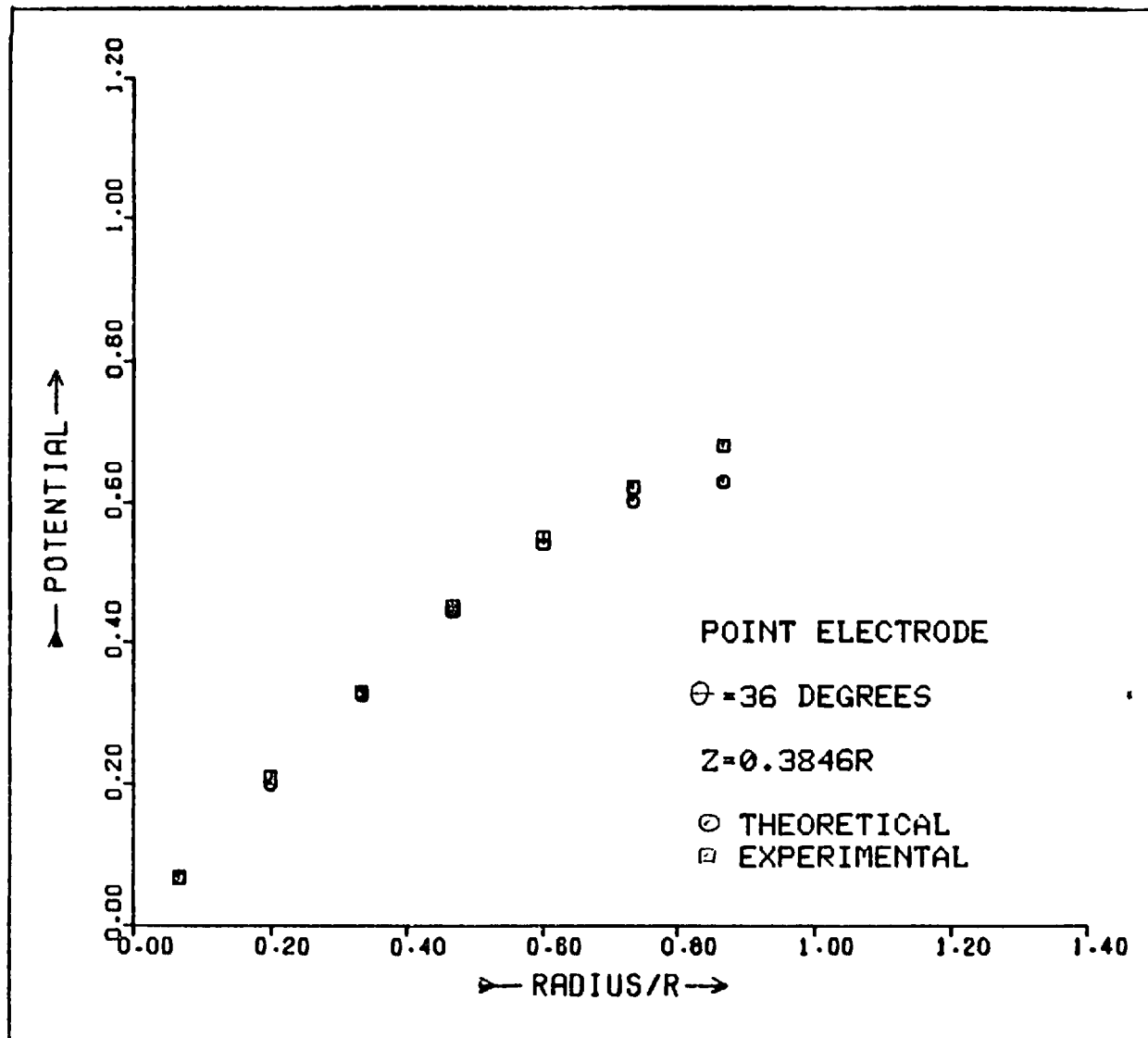
(c)

Fig. 4.3 (Continued)



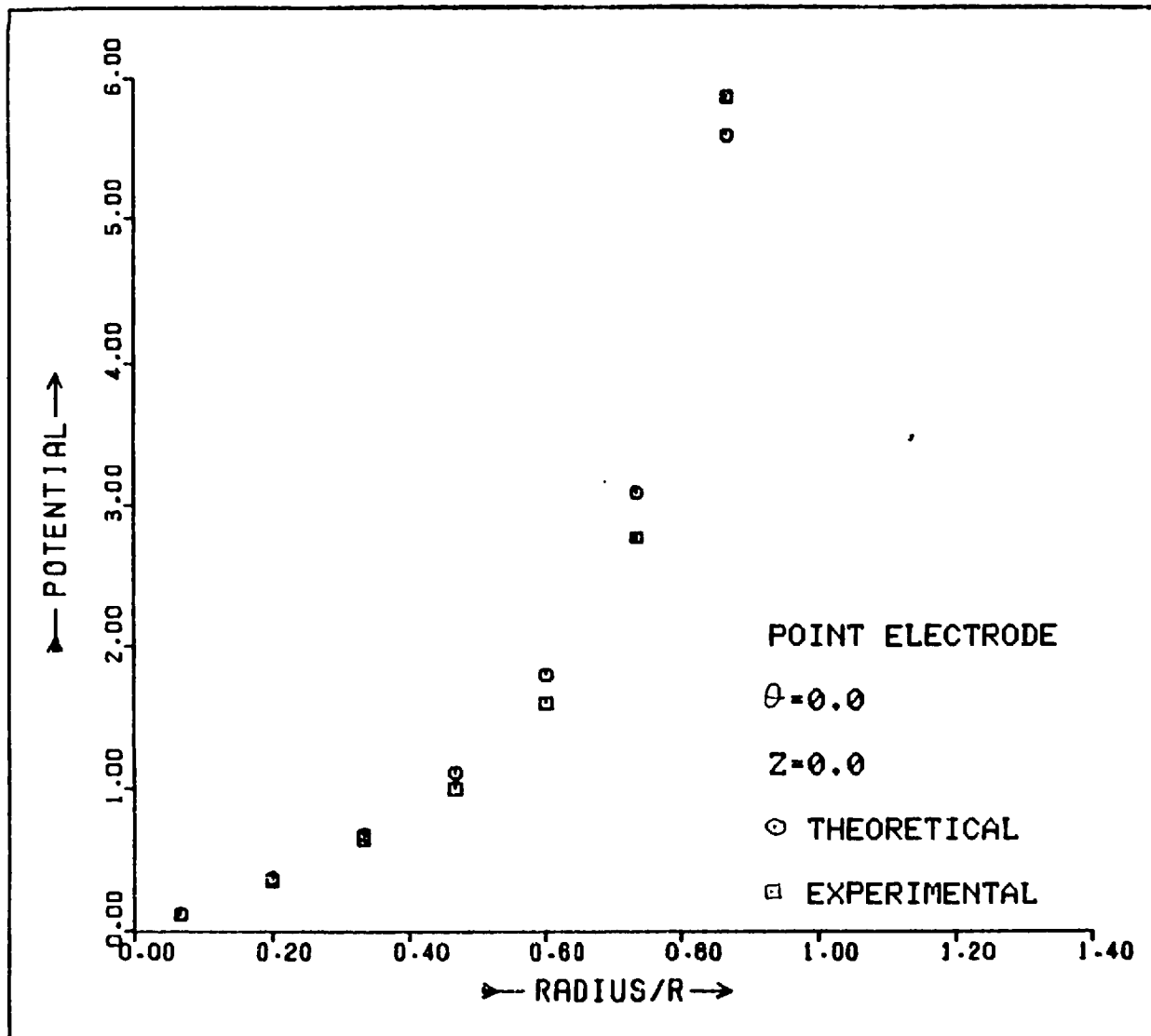
(d)

Fig. 4.3 (Continued)



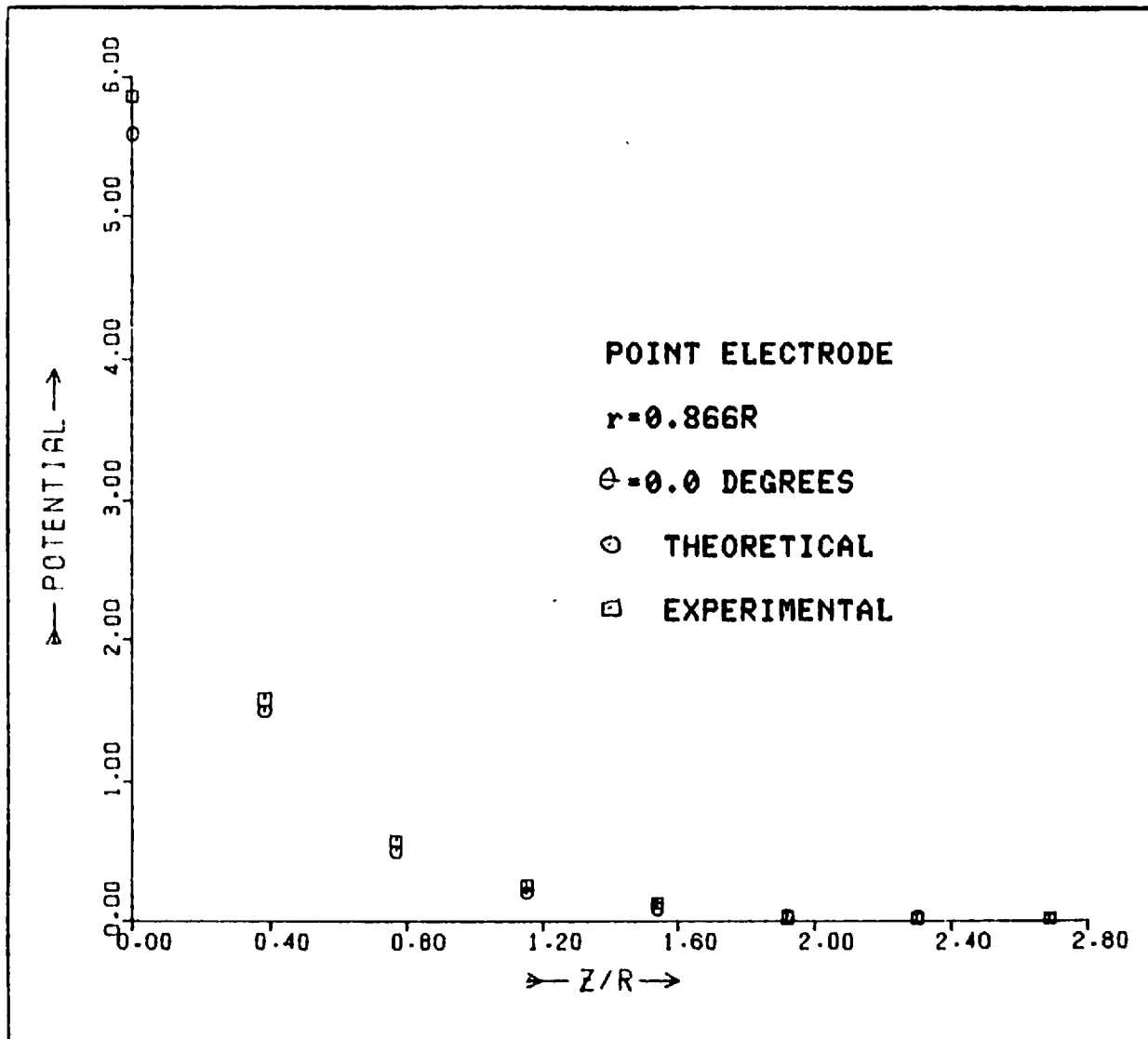
(e)

Fig. 4.3 (Continued)



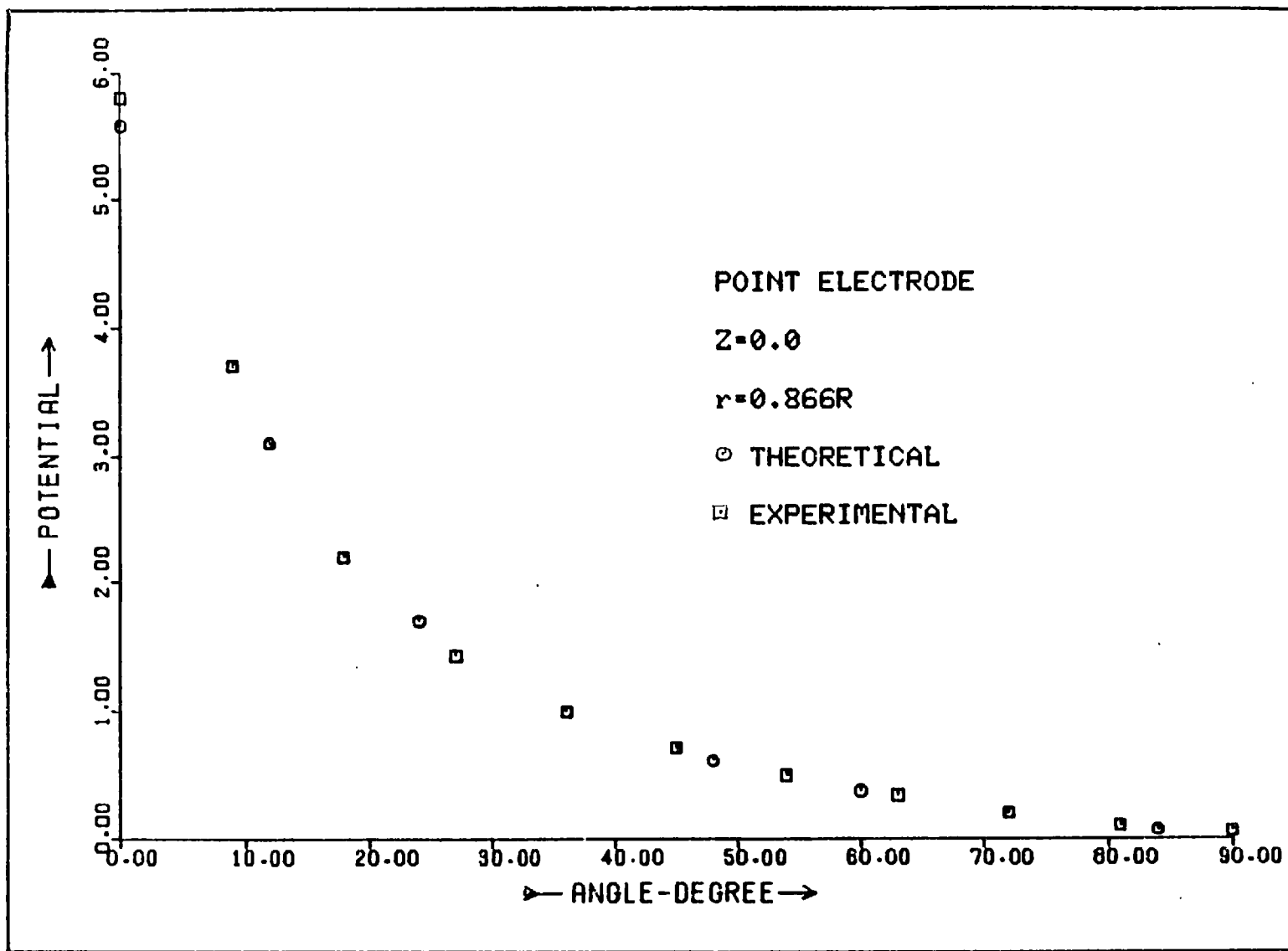
(f)

Fig. 4.3 (Continued)



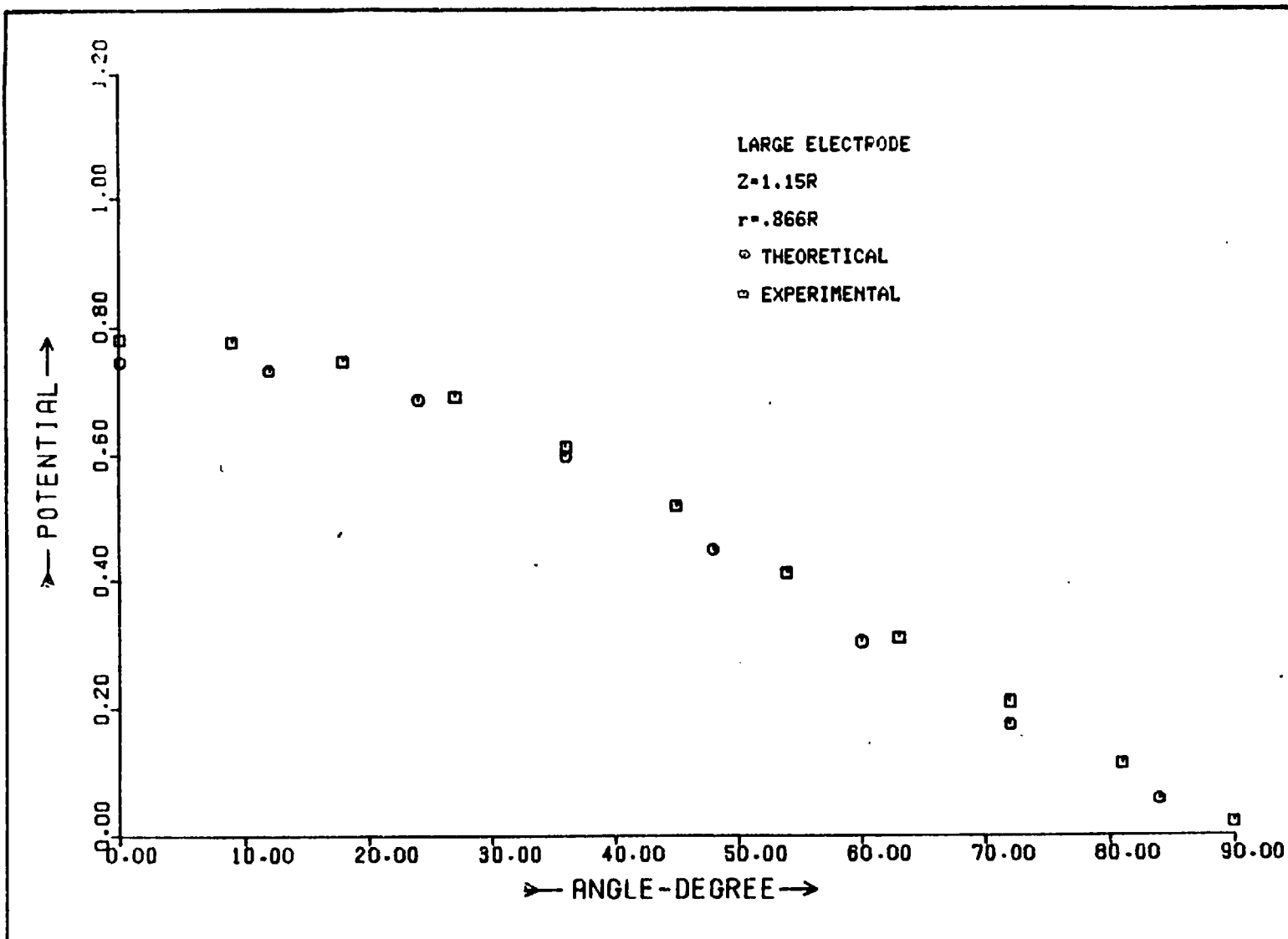
(g)

Fig. 4.3 (Continued)



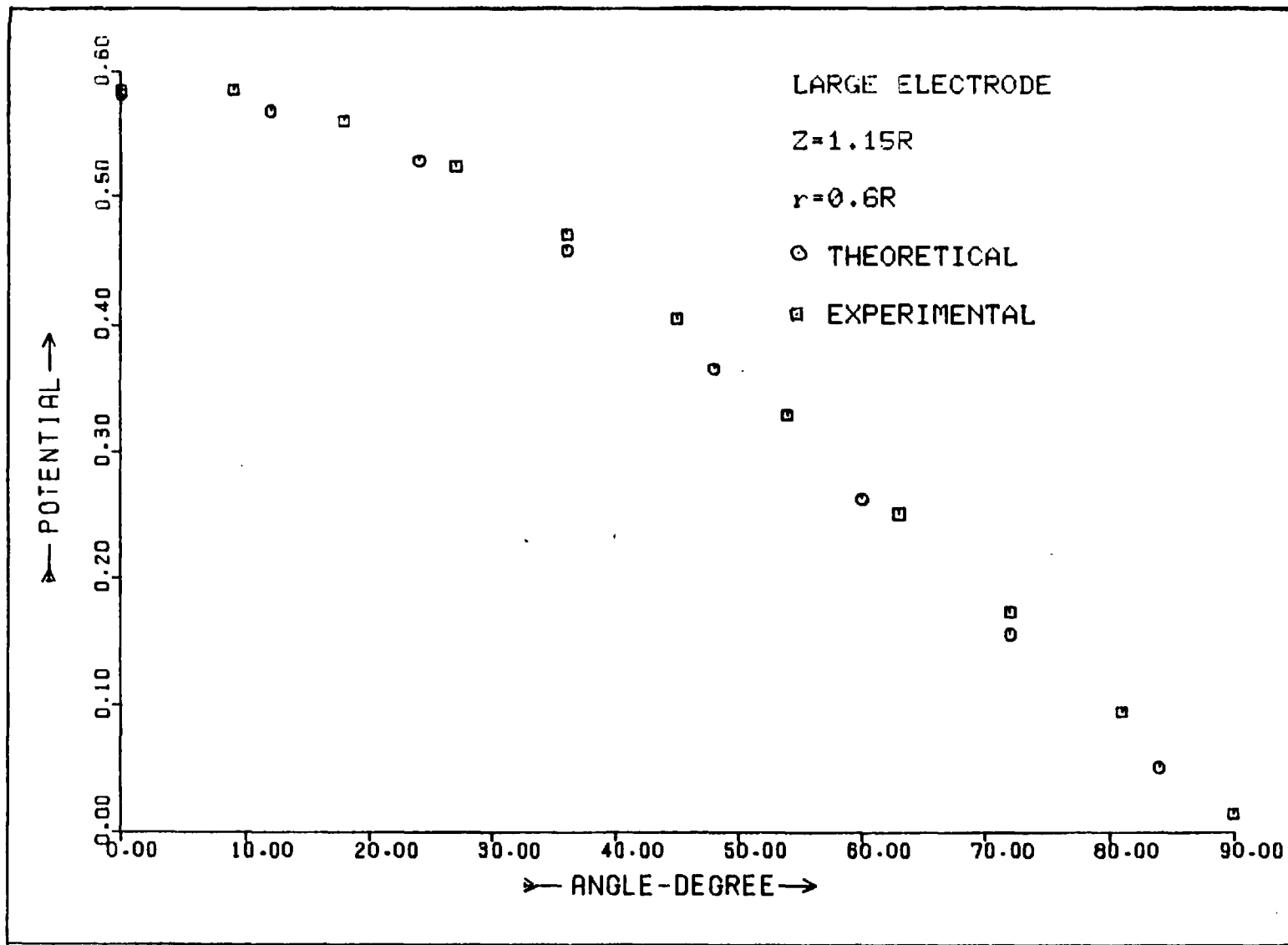
(h)

Fig. 4.3 (Continued)



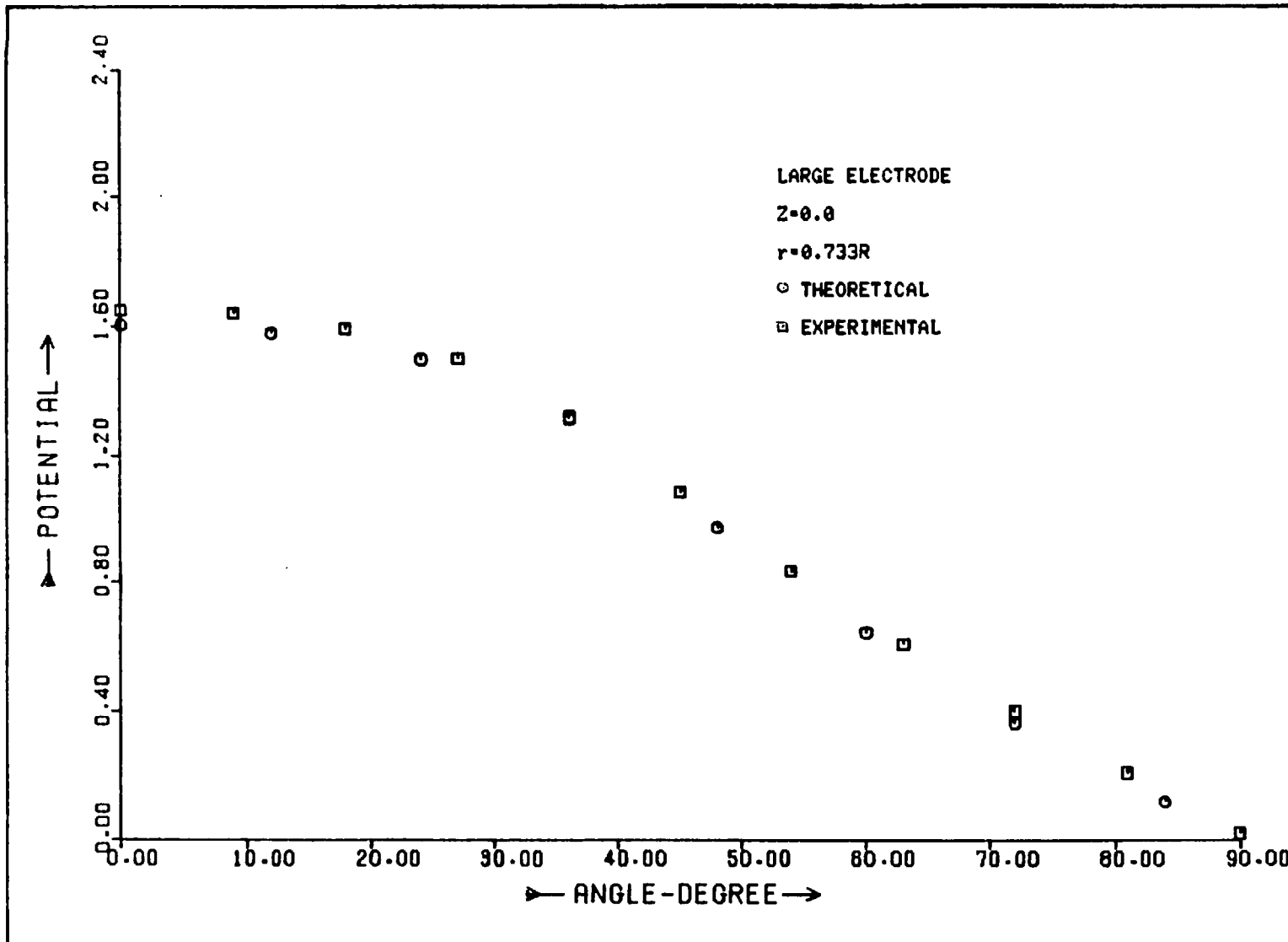
(a)

Fig. 4.4 Comparison of experimental values of virtual potential with computed values (large-electrodes flowmeter)



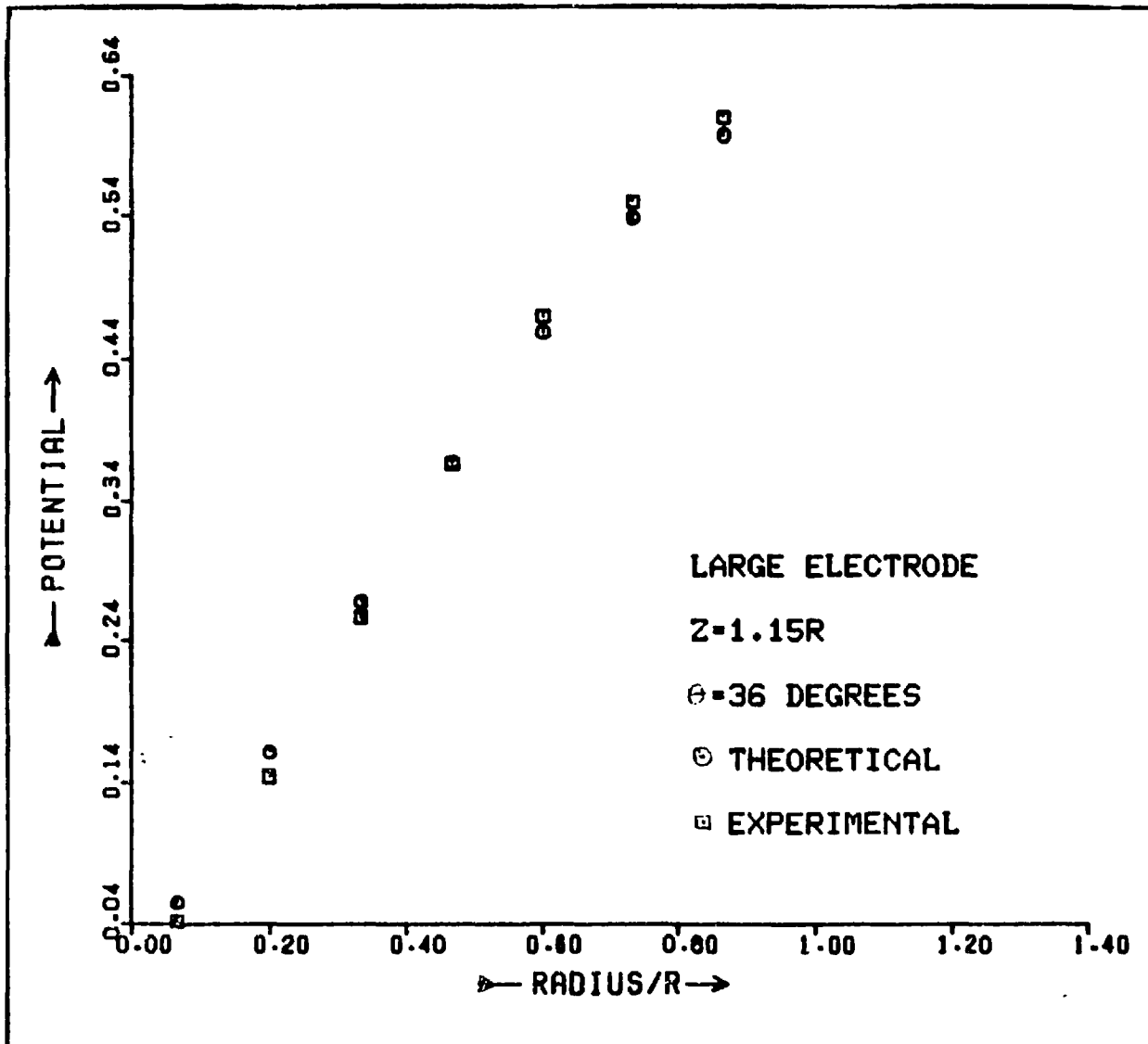
(b)

Fig. 4.4 (Continued)



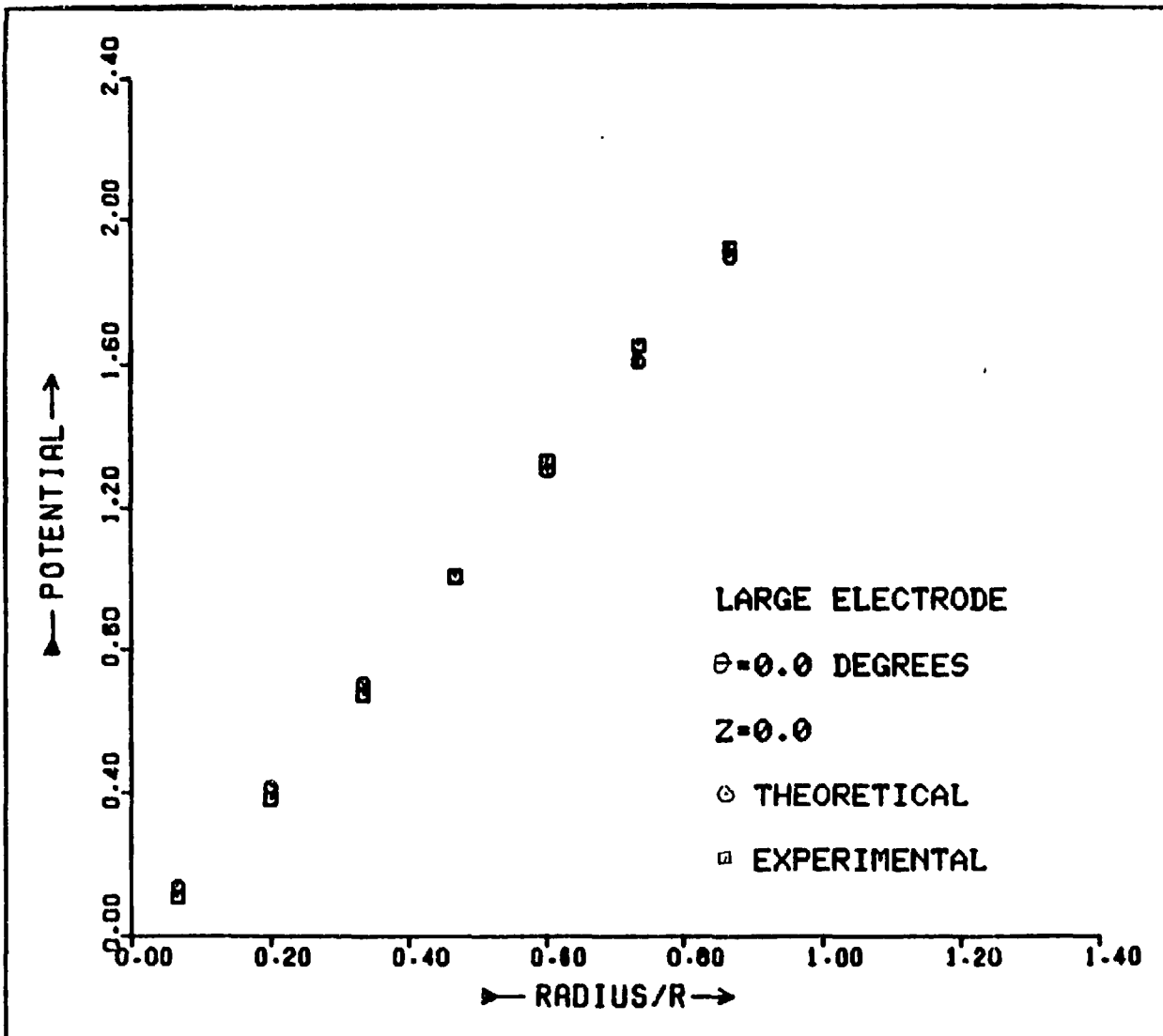
(c)

Fig. 4.4 (Continued)



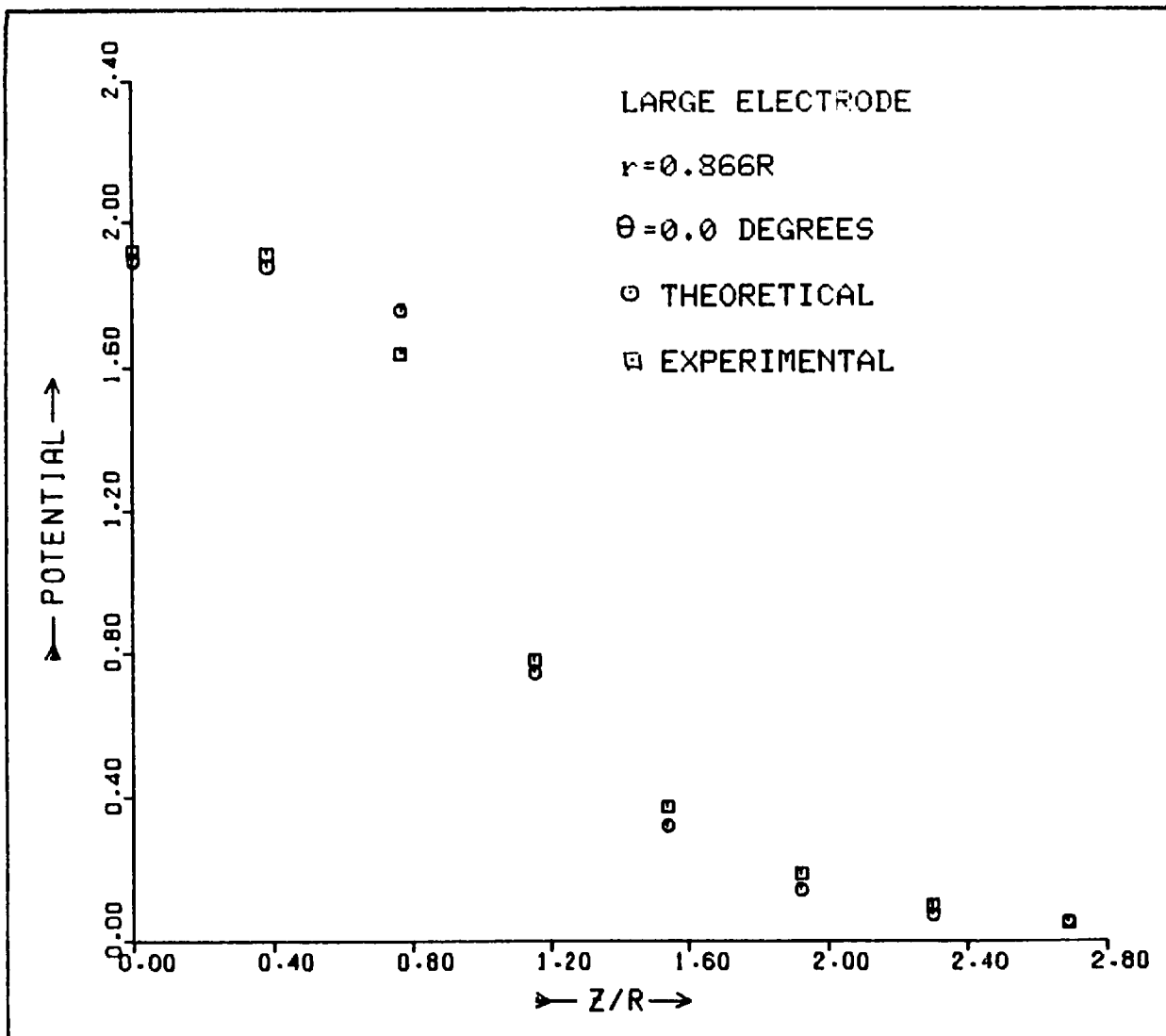
(d)

Fig. 4.4 (Continued)



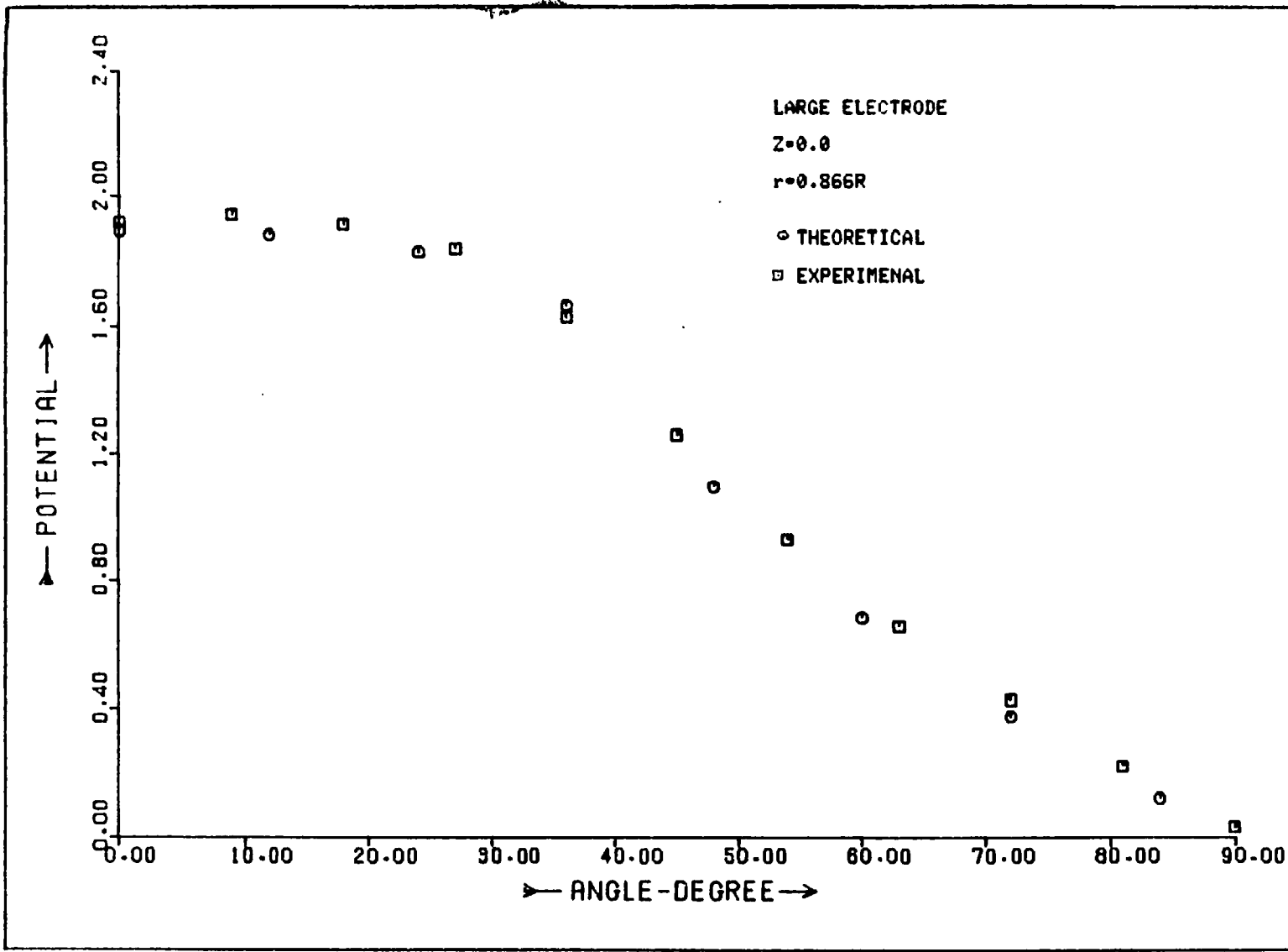
(e)

Fig. 4.4 (Continued)



(f)

Fig. 4.4 (Continued)



(g)

Fig. 4.4 (Continued)

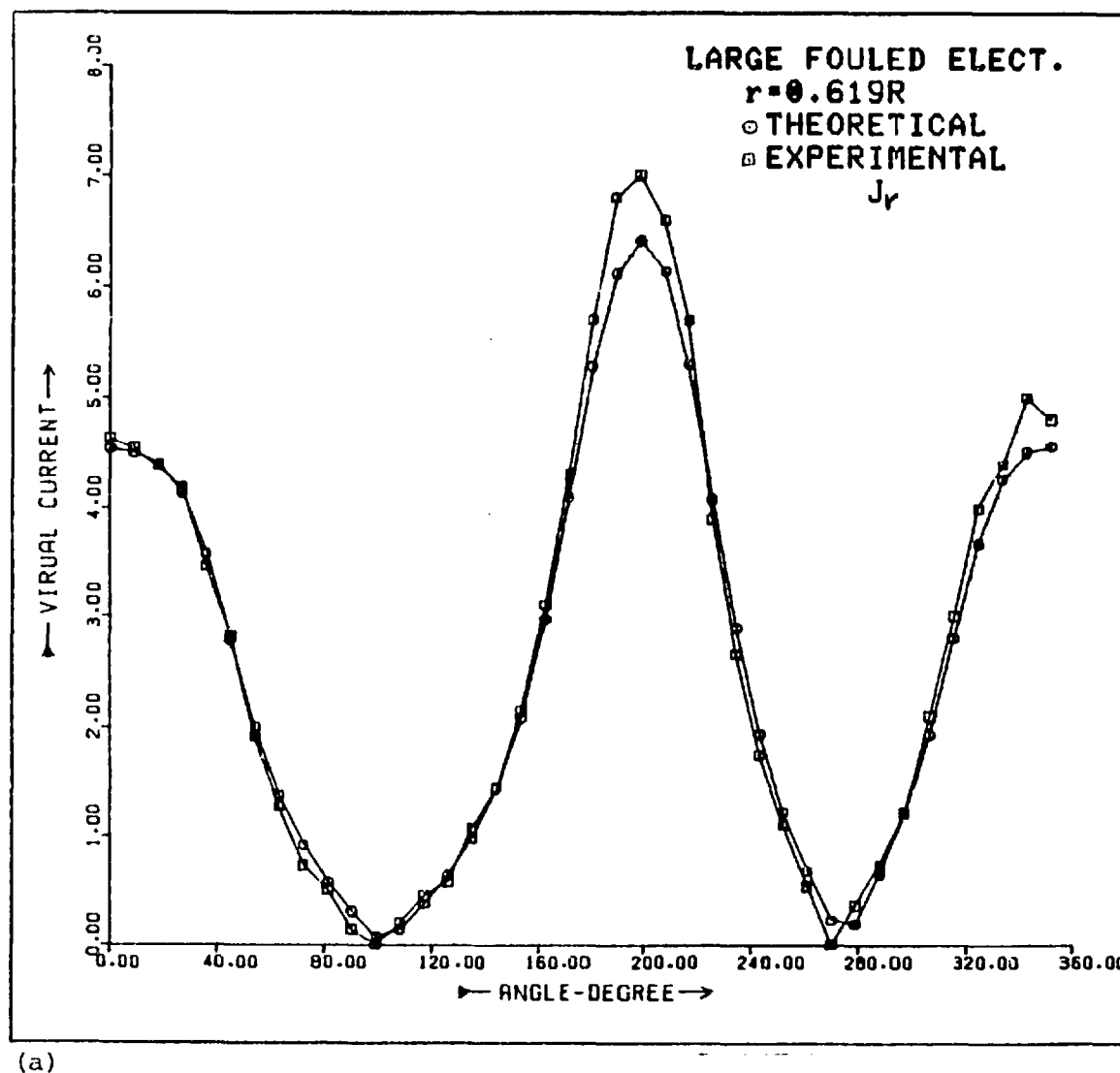
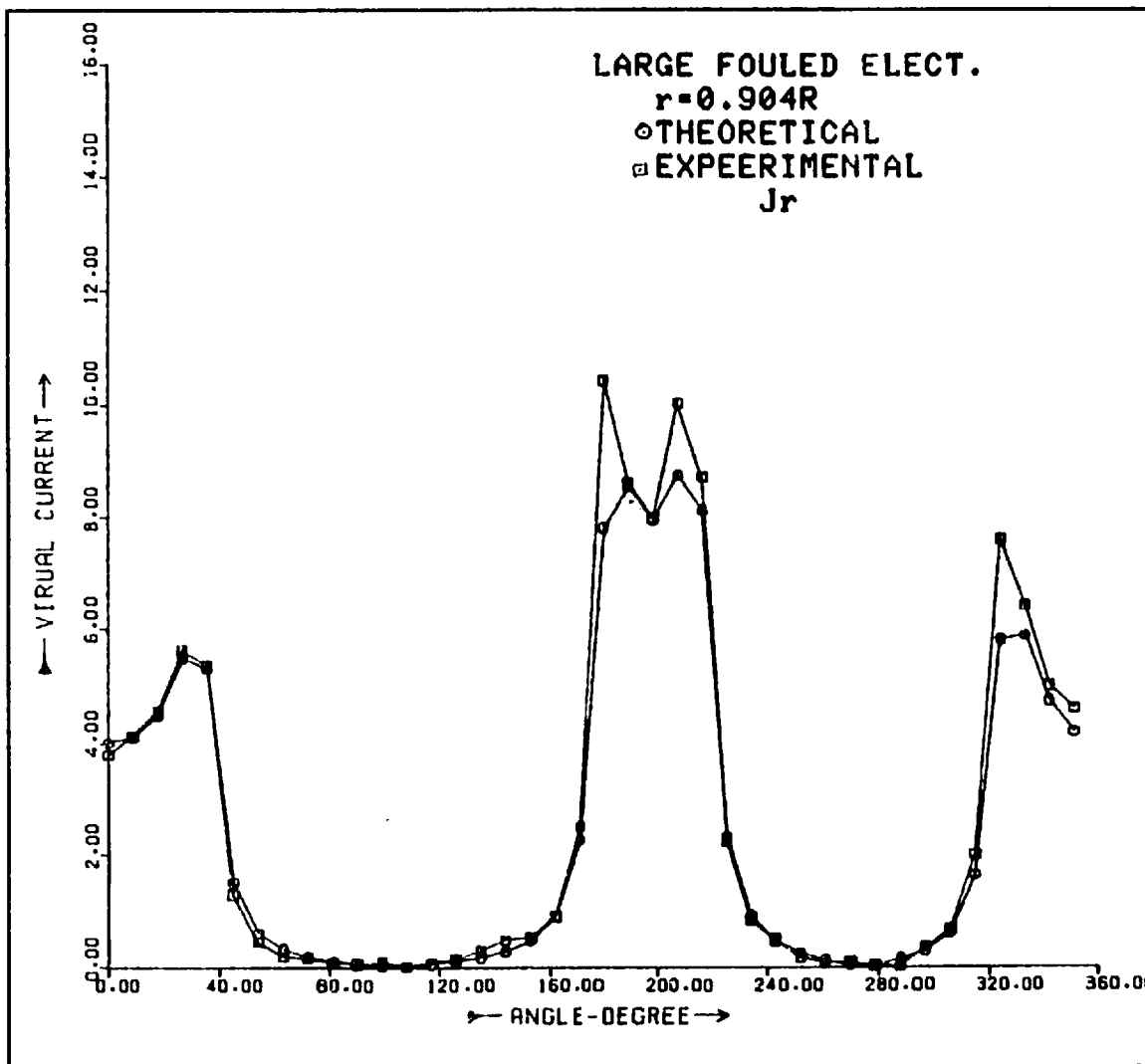
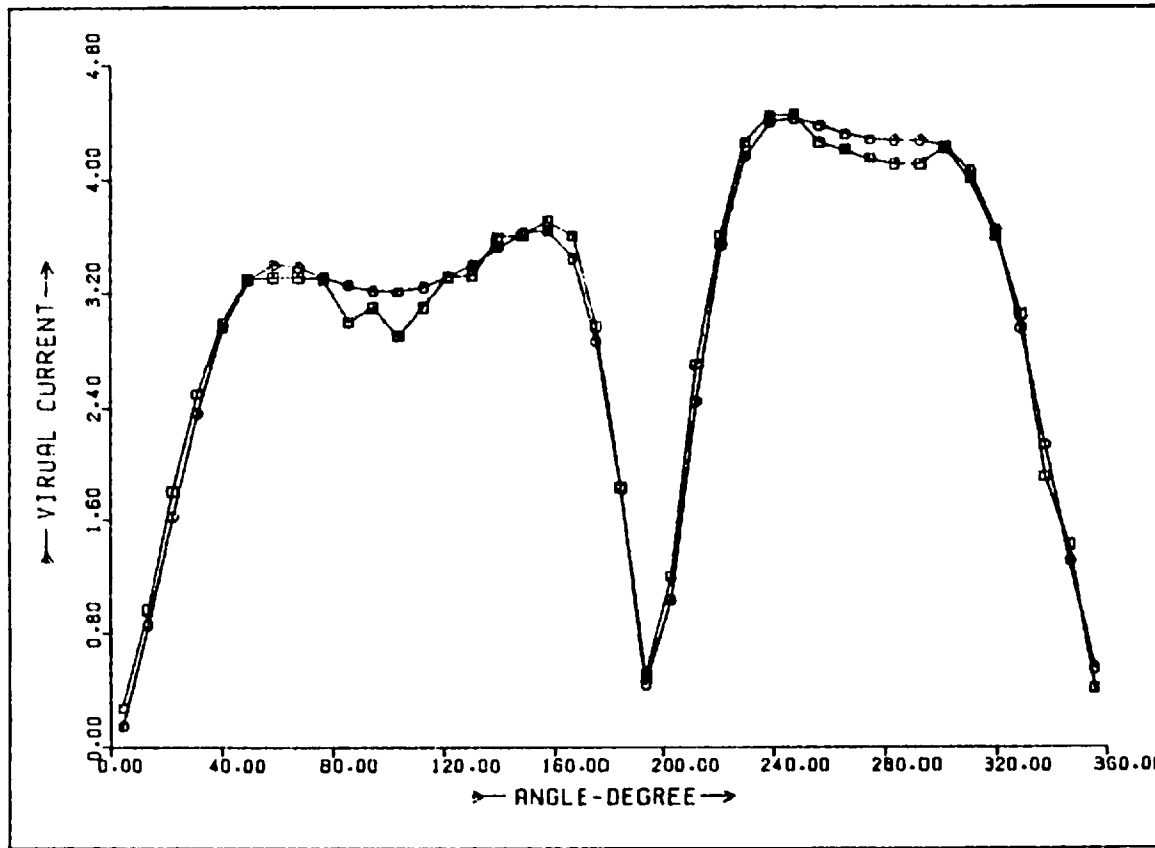


Fig. 4.5 Comparison of experimental values of virtual current with theoretical values (large-electrode flowmeter with moderate fouling)



(b)

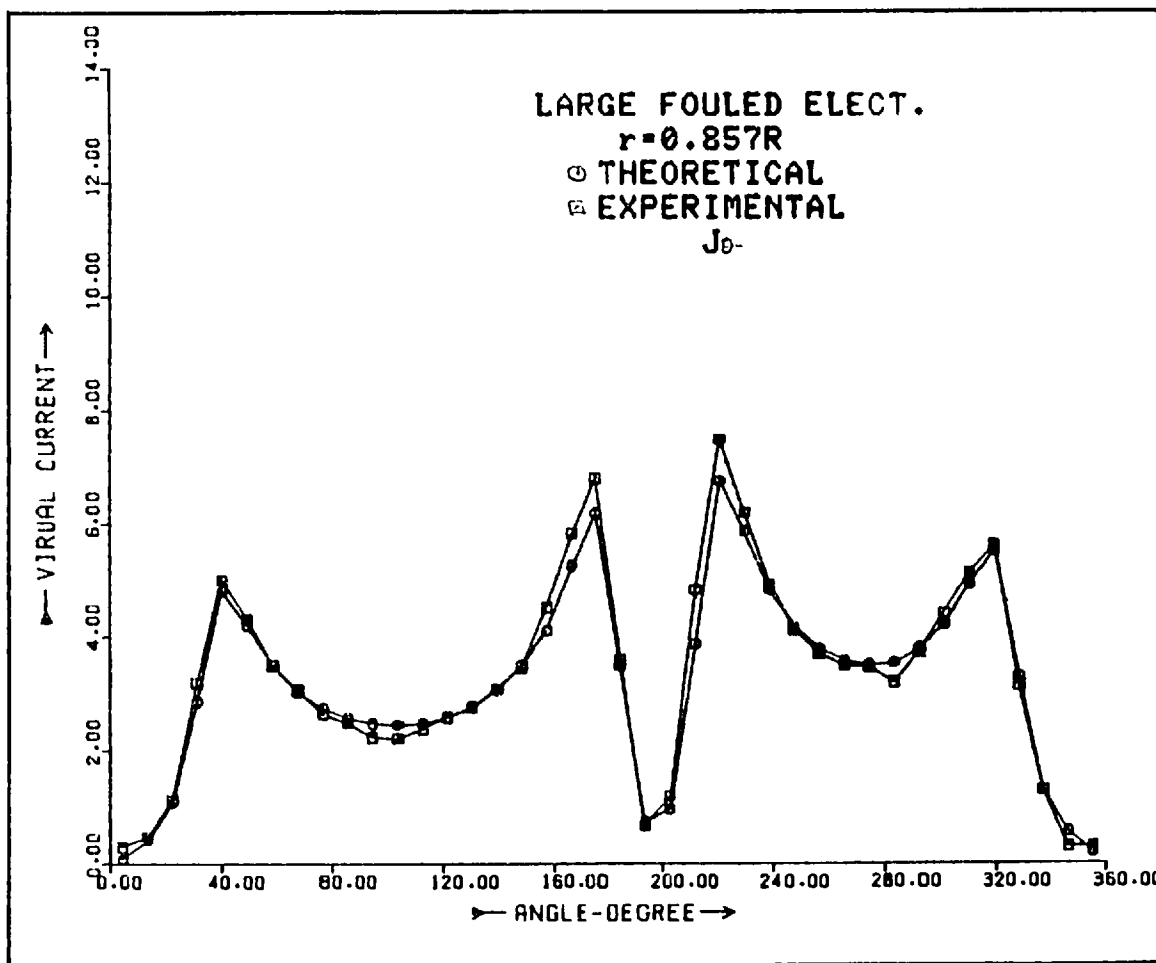
Fig. 4.5 (Continued)



(c)

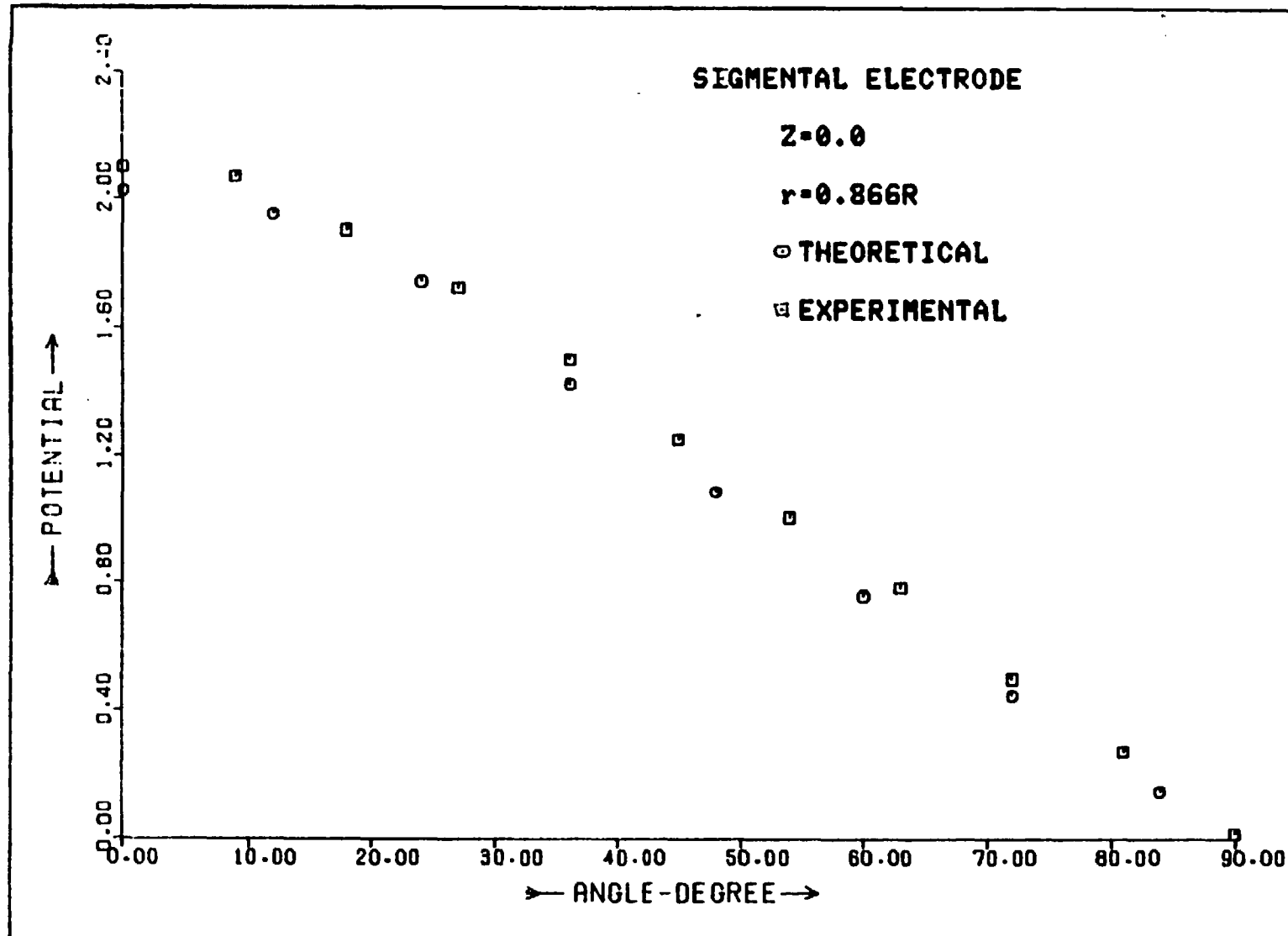
LARGE FOULED ELECT.
 $r = 0.57R$
○ THEORETICAL
■ EXPERIMENTAL J_θ

Fig. 4.5 (Continued)



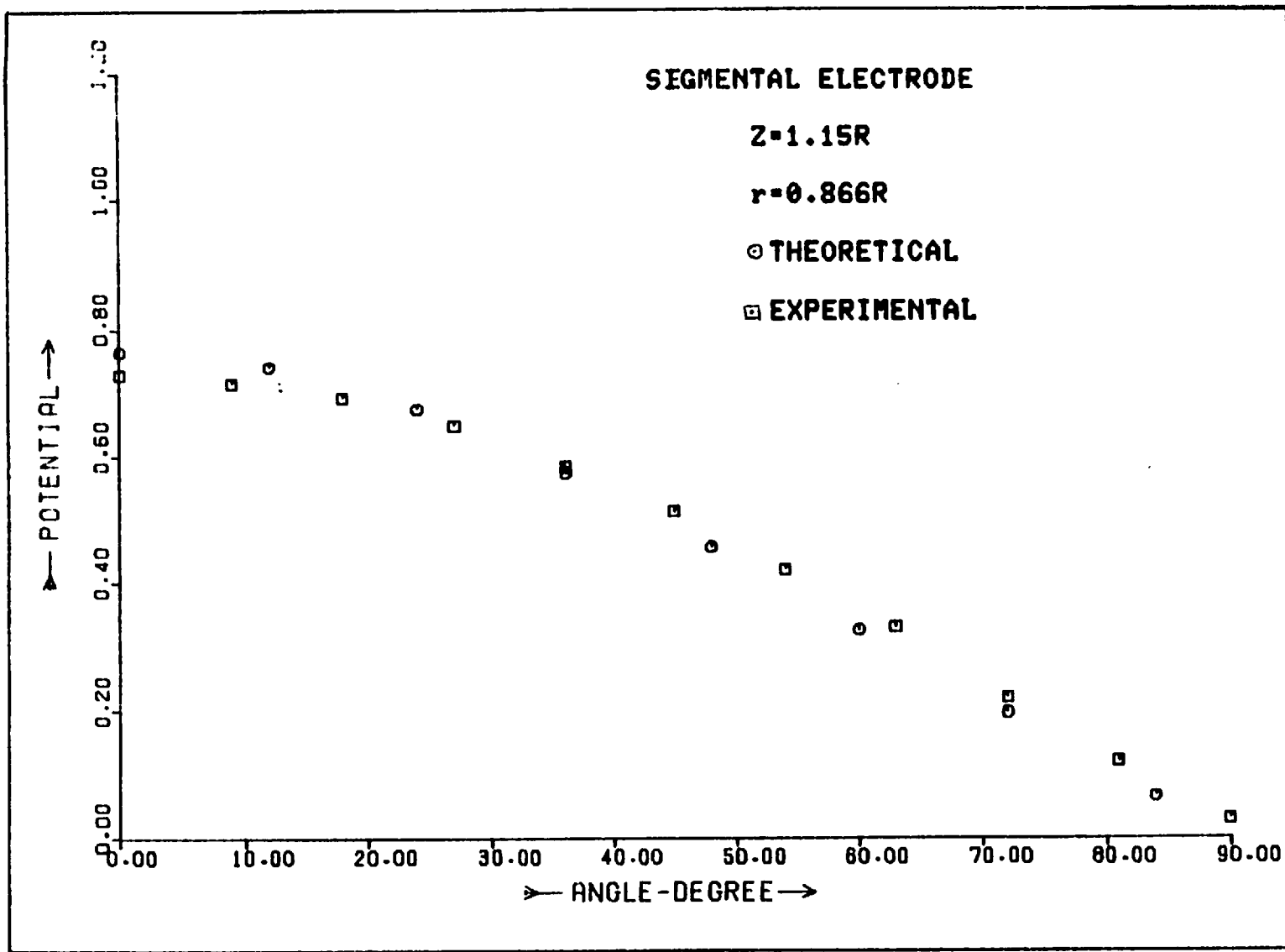
(d)

Fig. 4.5 (Continued)



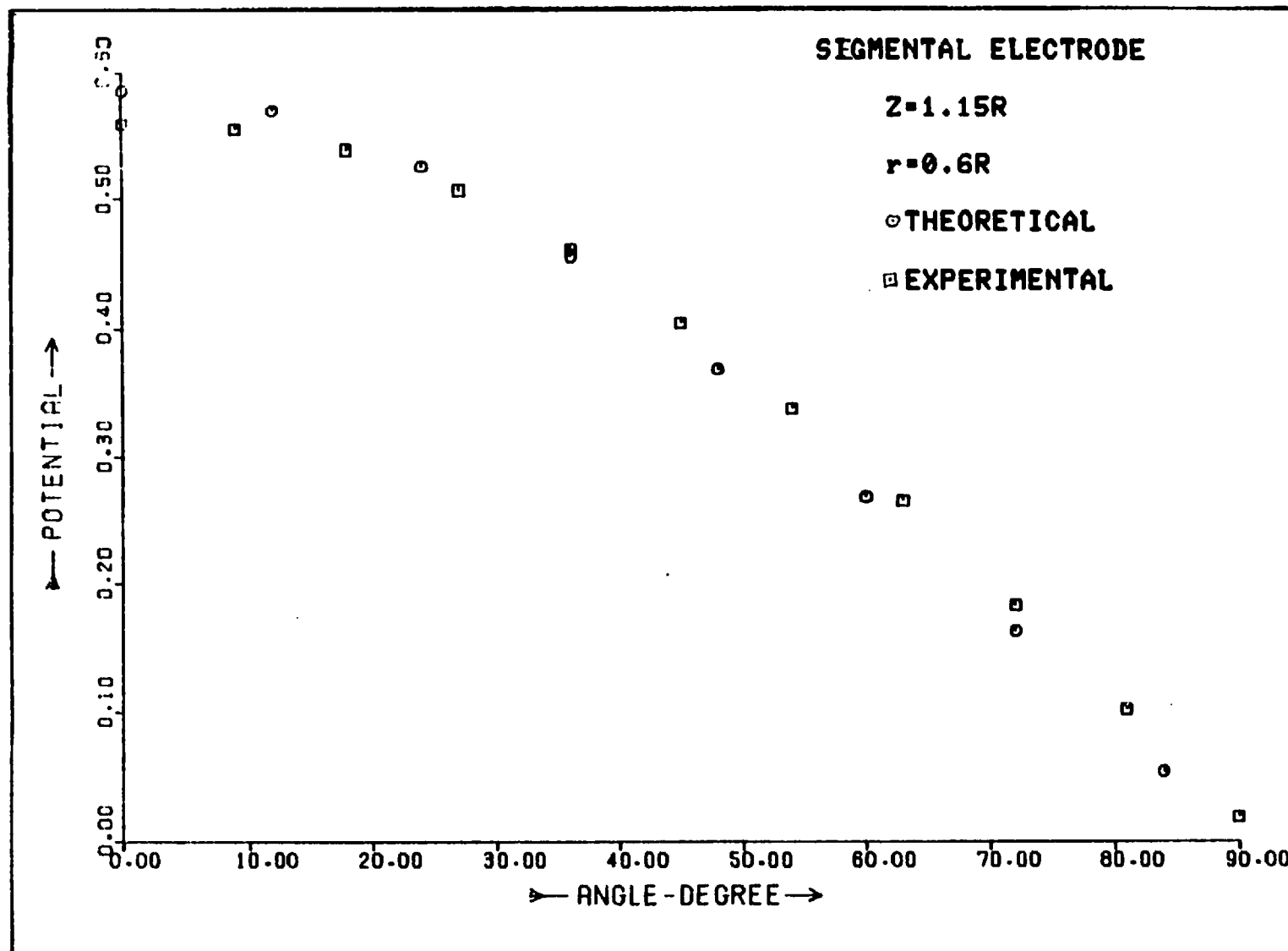
(a)

Fig. 4.6 Comparison of experimental values of virtual potential with computed values (segmental electrodes flowmeter)



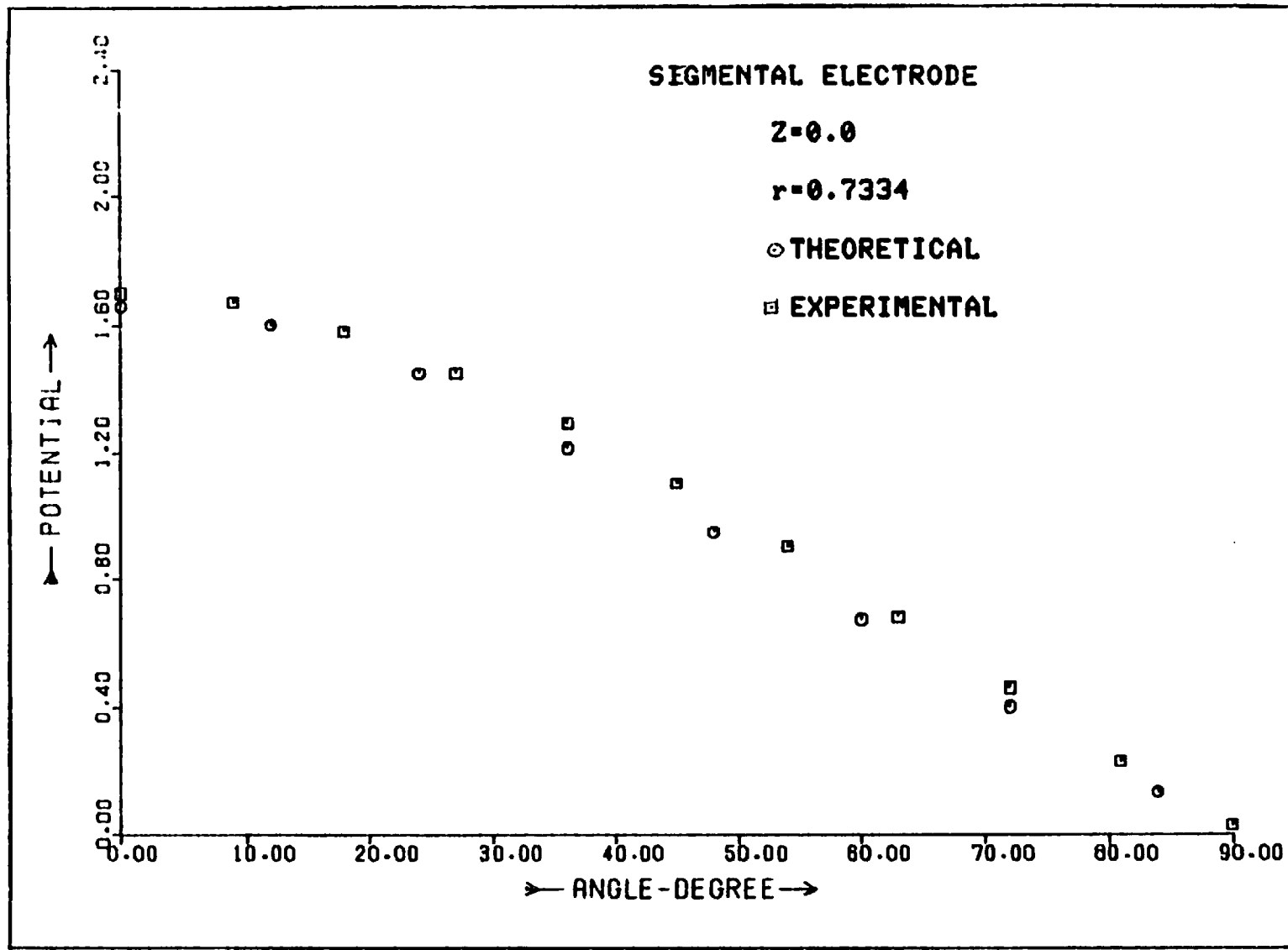
(b)

Fig. 4.6 (Continued)



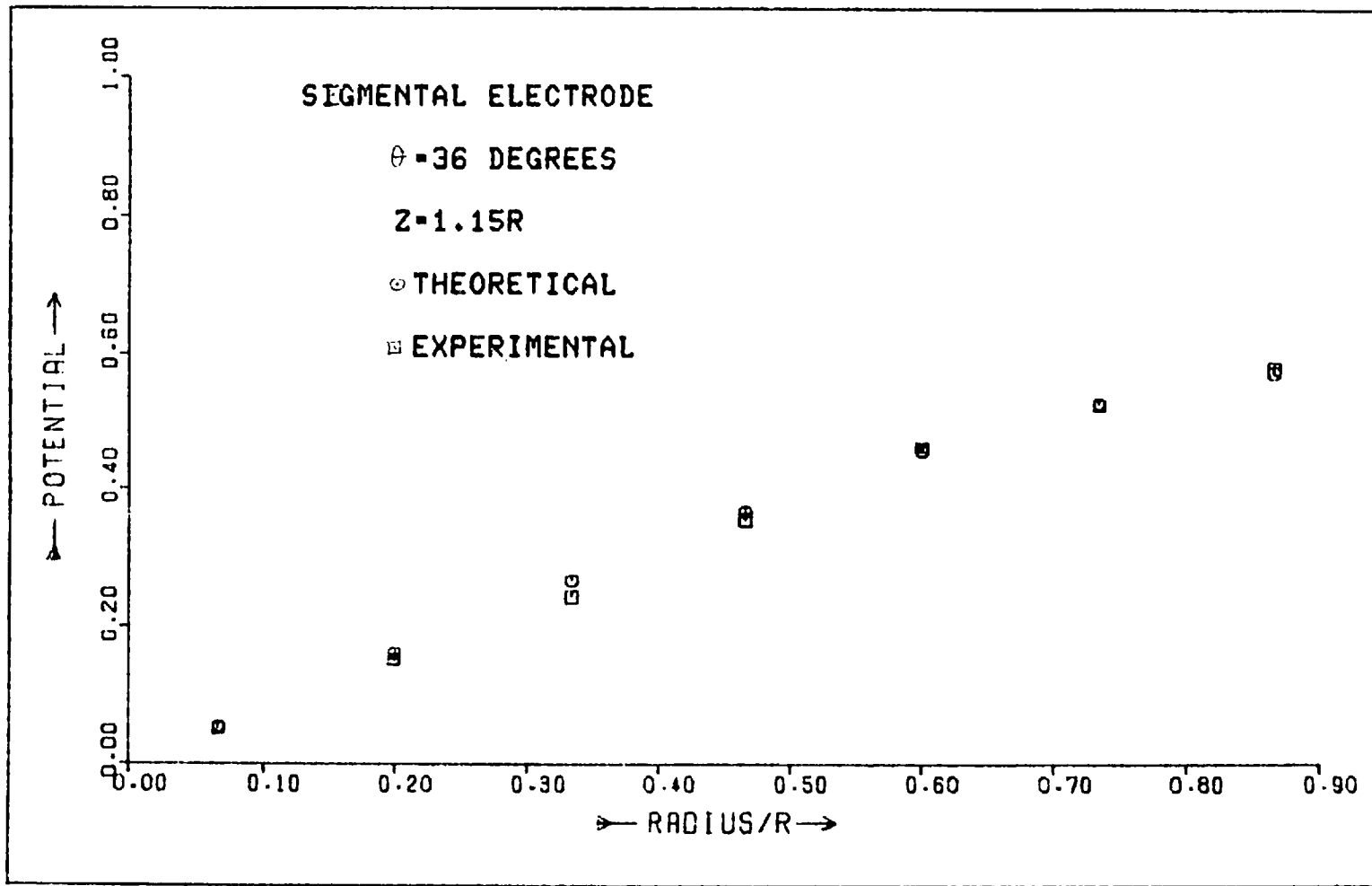
(c)

Fig. 4.6 (Continued)



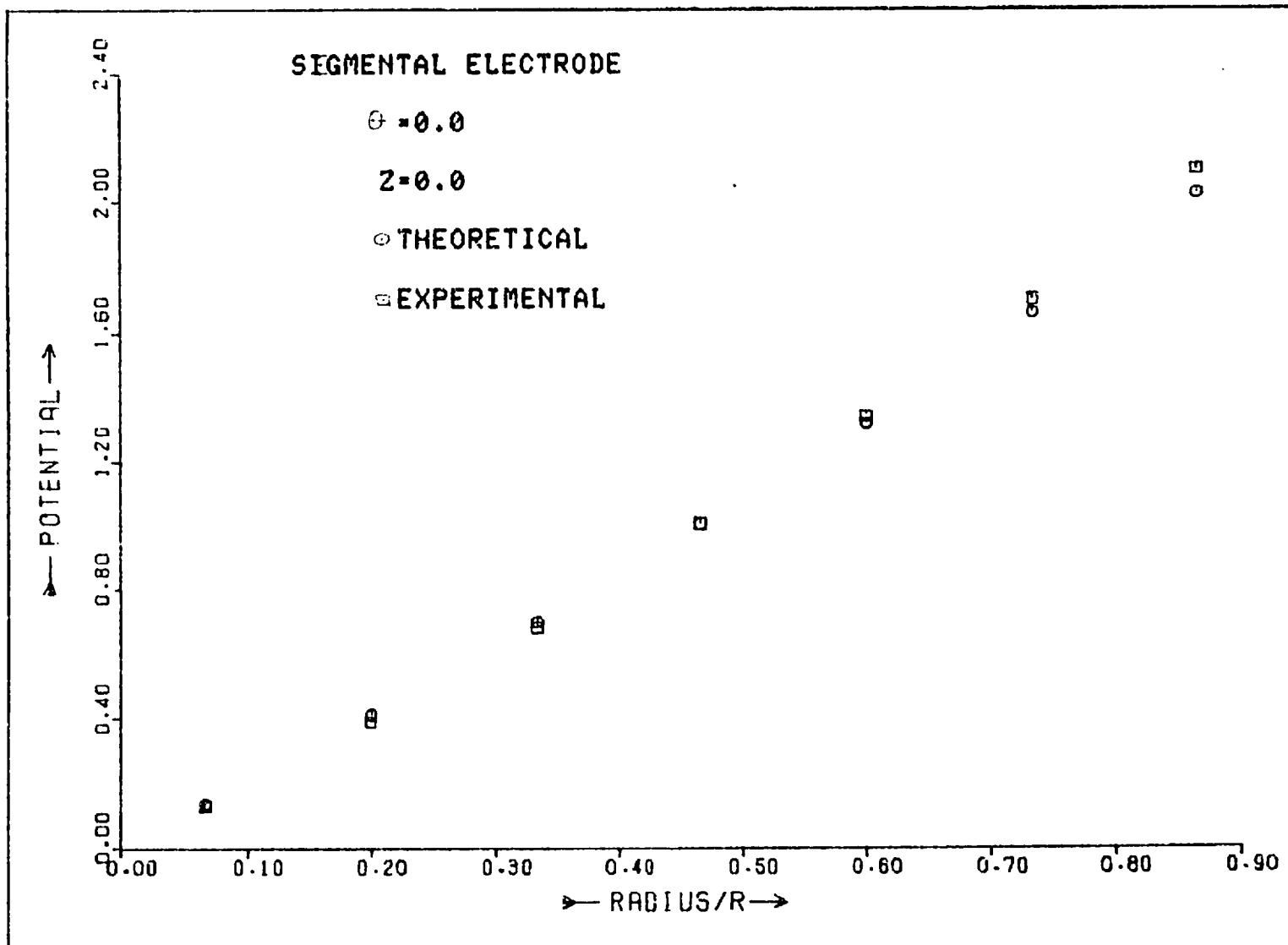
(d)

Fig. 4.6 (Continued)



(e)

Fig. 4.6 (Continued)



(f)

Fig. 4.6 (Continued)

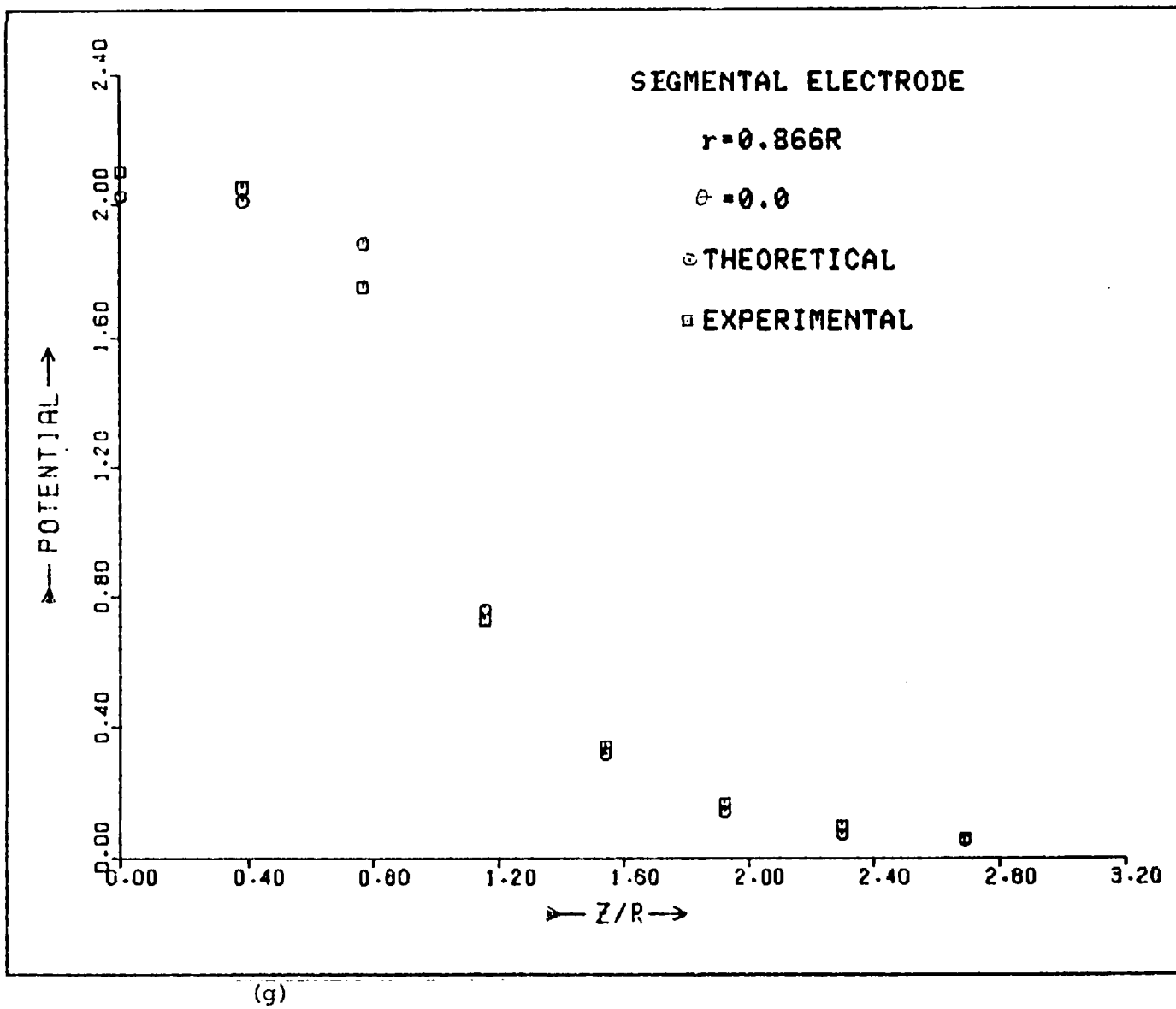


Fig. 4.6 (Continued)

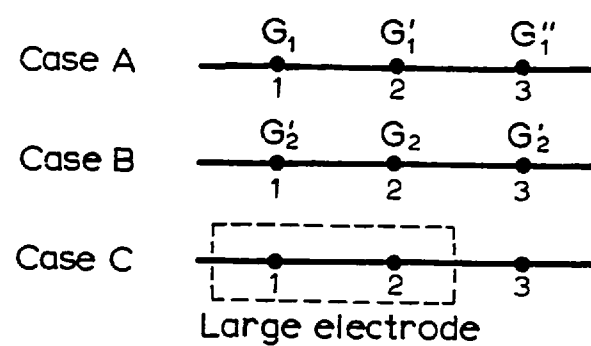


Fig. 5.1 Notation for the superposition method

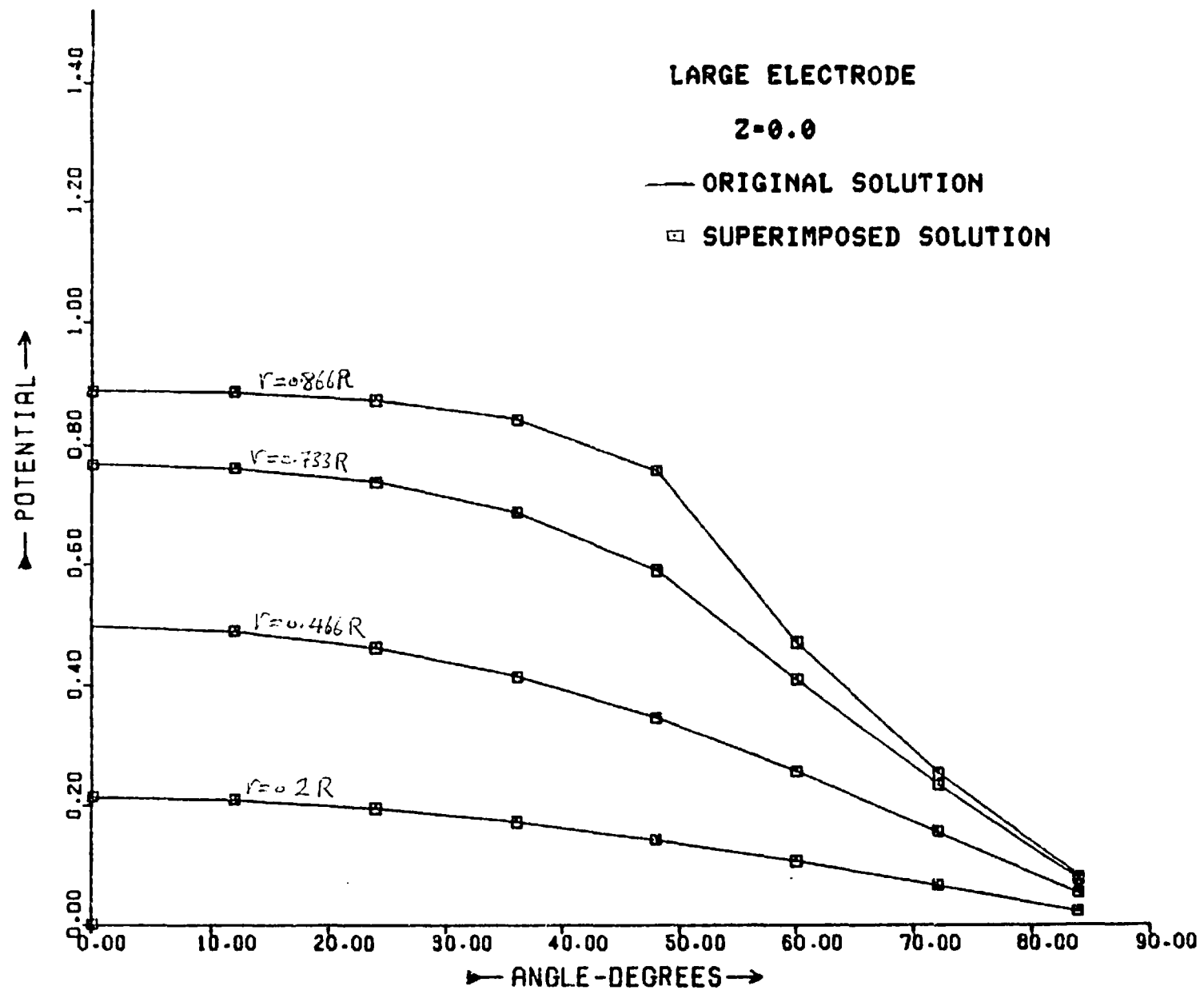


Fig. 5.2 Virtual potential variation with angle to show validity for superimposed solution

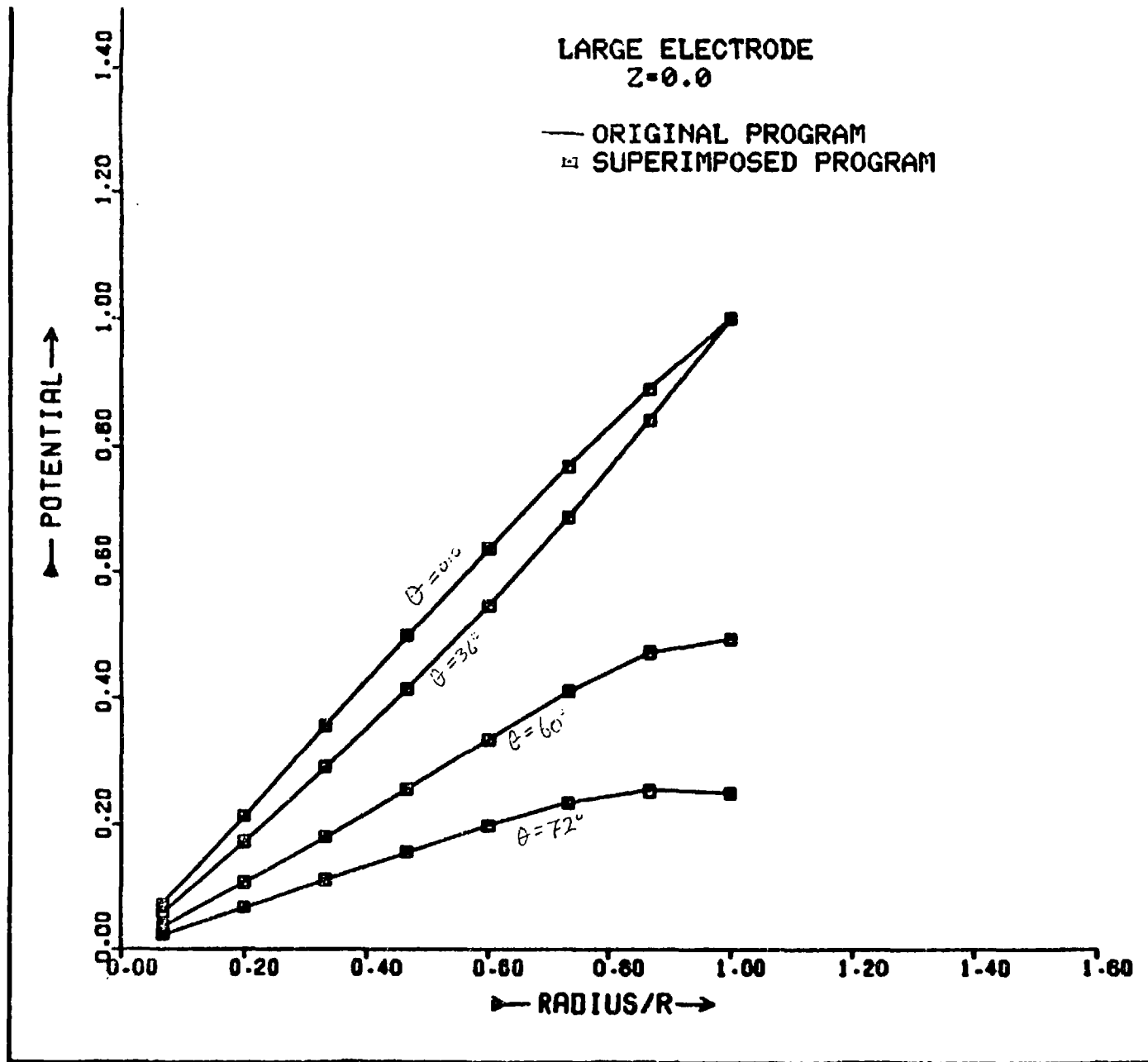


Fig. 5.3 Virtual potential variation with radius to show validity of superimposed solution

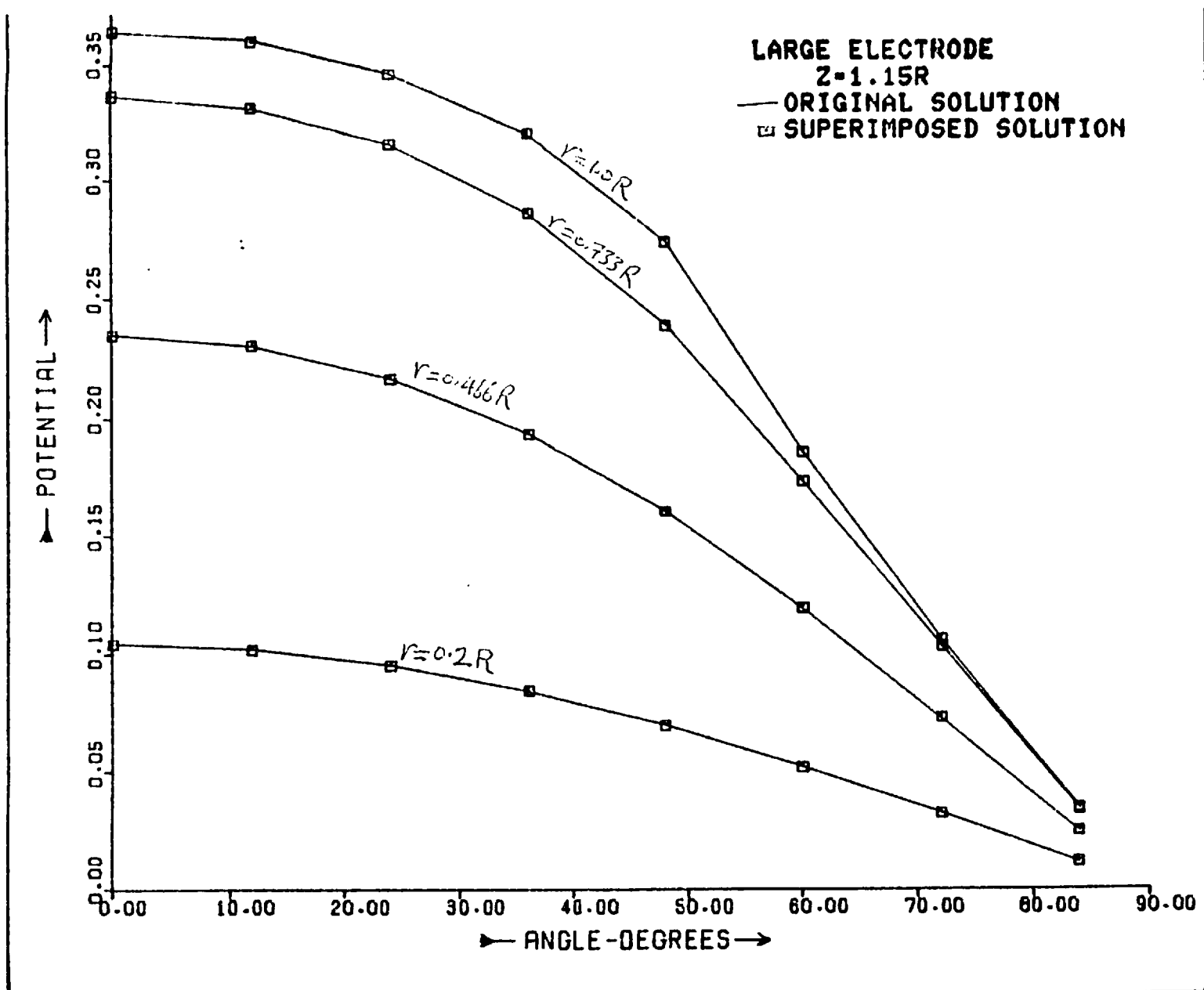


Fig. 5.4 Virtual potential variation with angle to show validity of superimposed solution

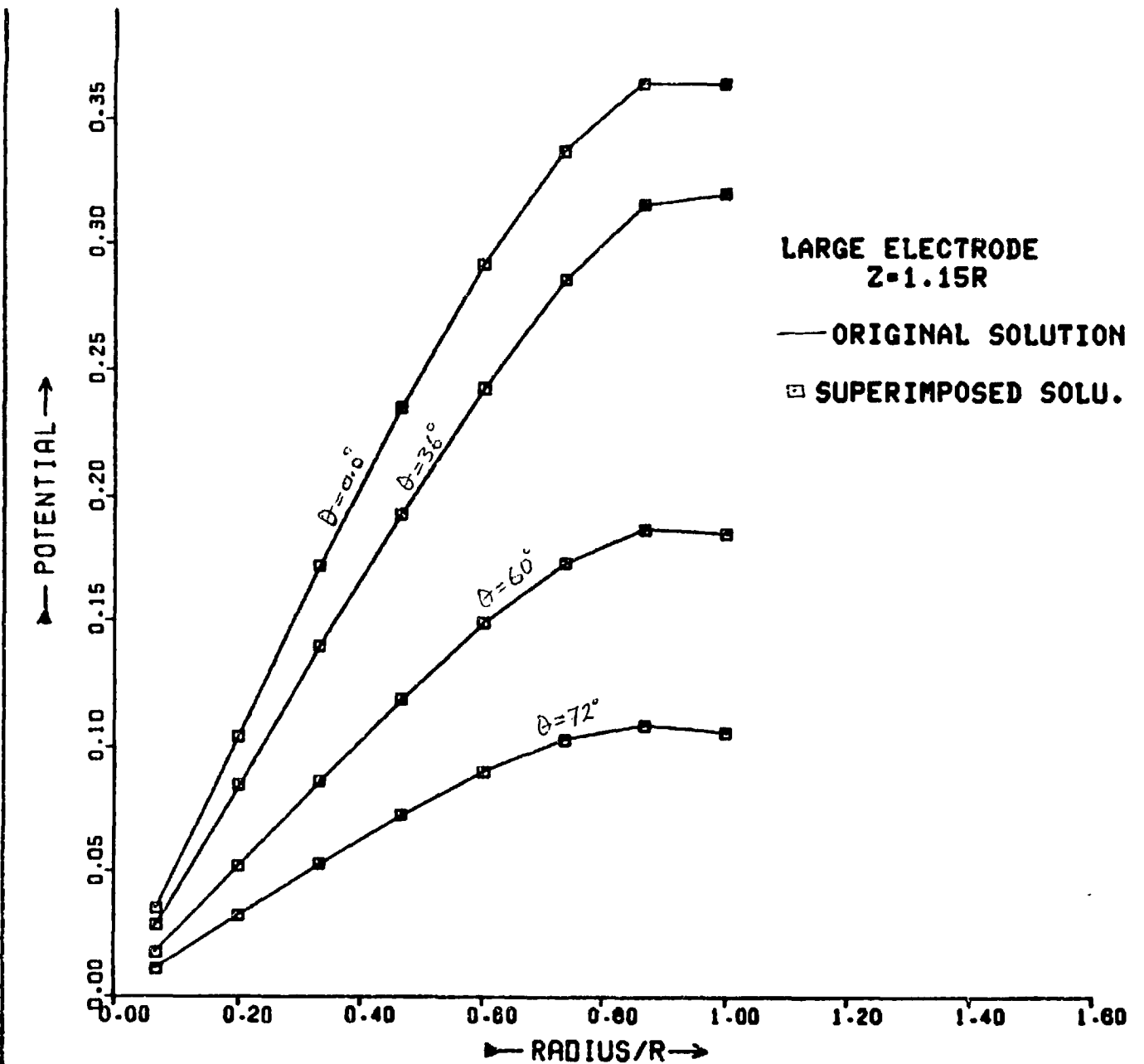


Fig. 5.5 Virtual potential variation with radius to show validity of superimposed solution

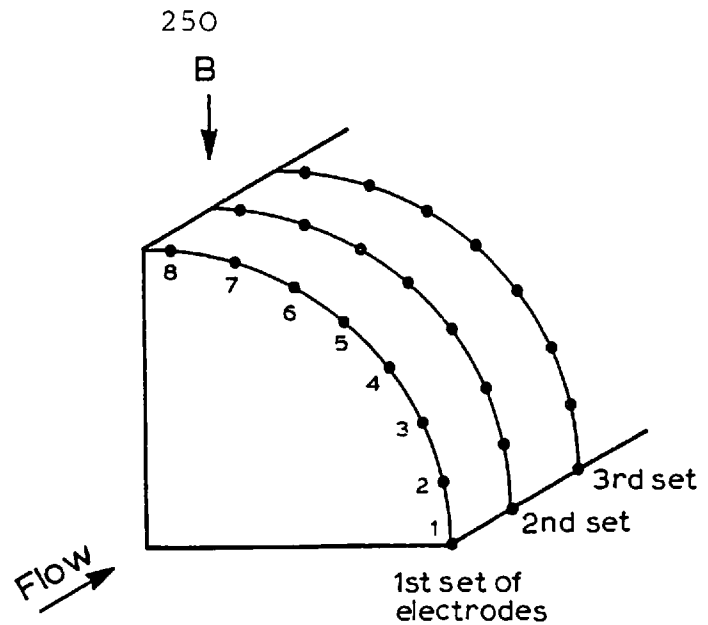


Fig. 5.6 Flowmeter tube showing the sets of electrodes

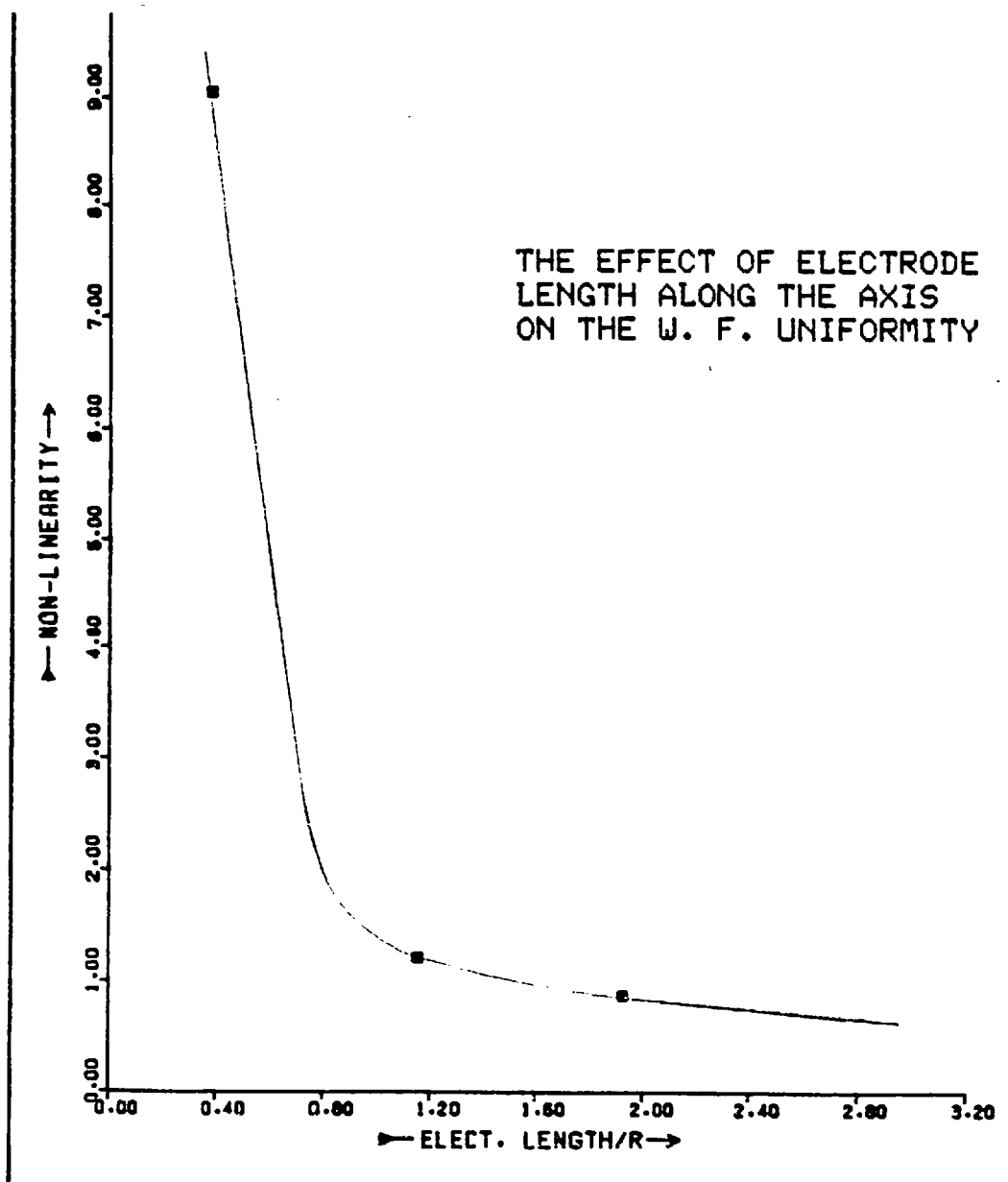


Fig. 5.7a

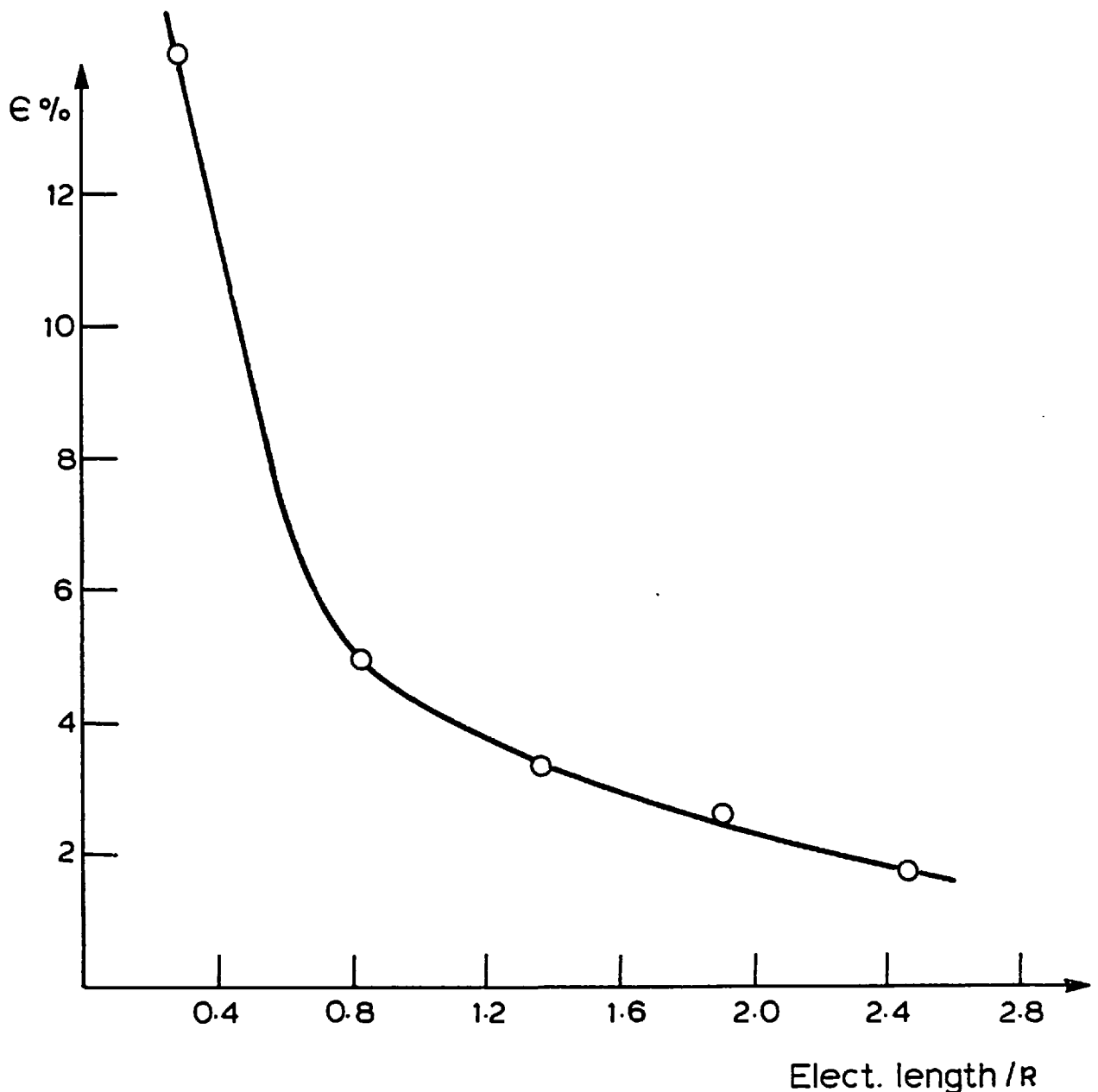


Fig. 5.7b The effect of electrode length along the axis on the weight function uniformity of the optimized-Type 2 flowmeter

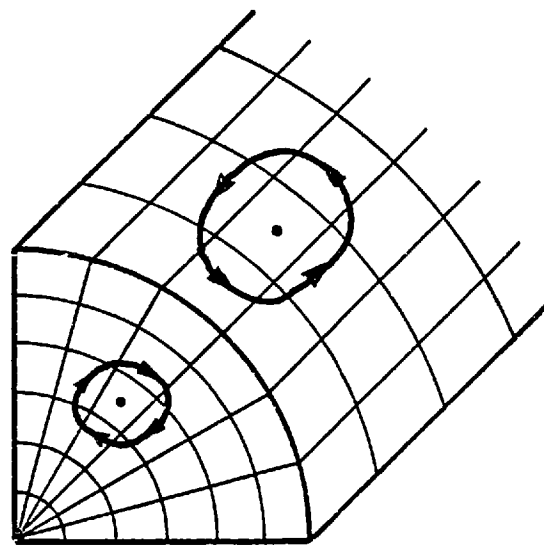


Fig. 5.8 The swirl loops for testing the performance of the flowmeter

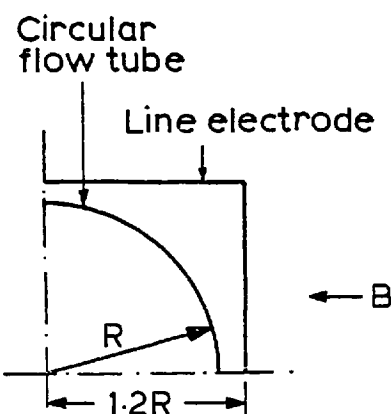


Fig. 5.9 Converting an ideal-rectangular flowmeter into a circular one

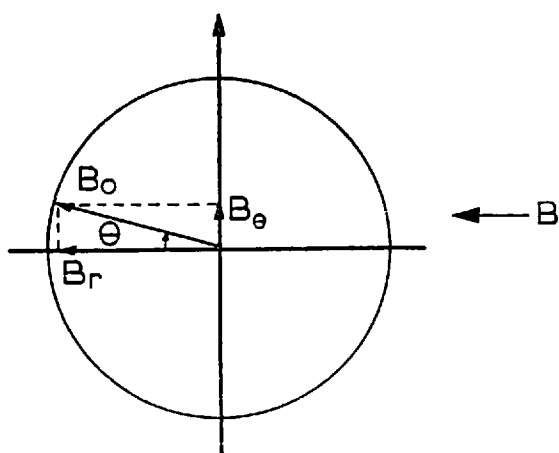


Fig. 5.10 The notation of a uniform magnetic field

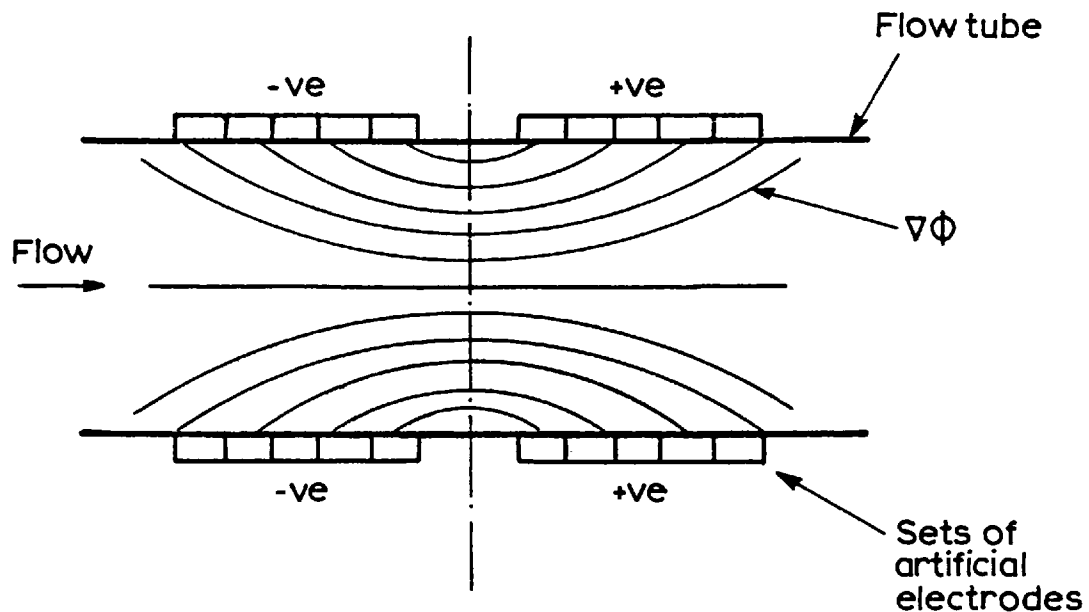


Fig. 5.11 Streamlines of weight function for an ideal flowmeter

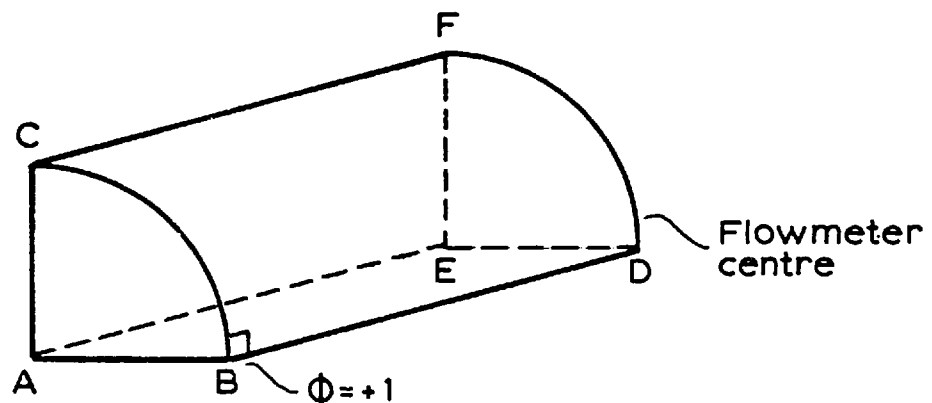


Fig. 5.12 The boundary conditions for solving the virtual potential of the artificial electrodes

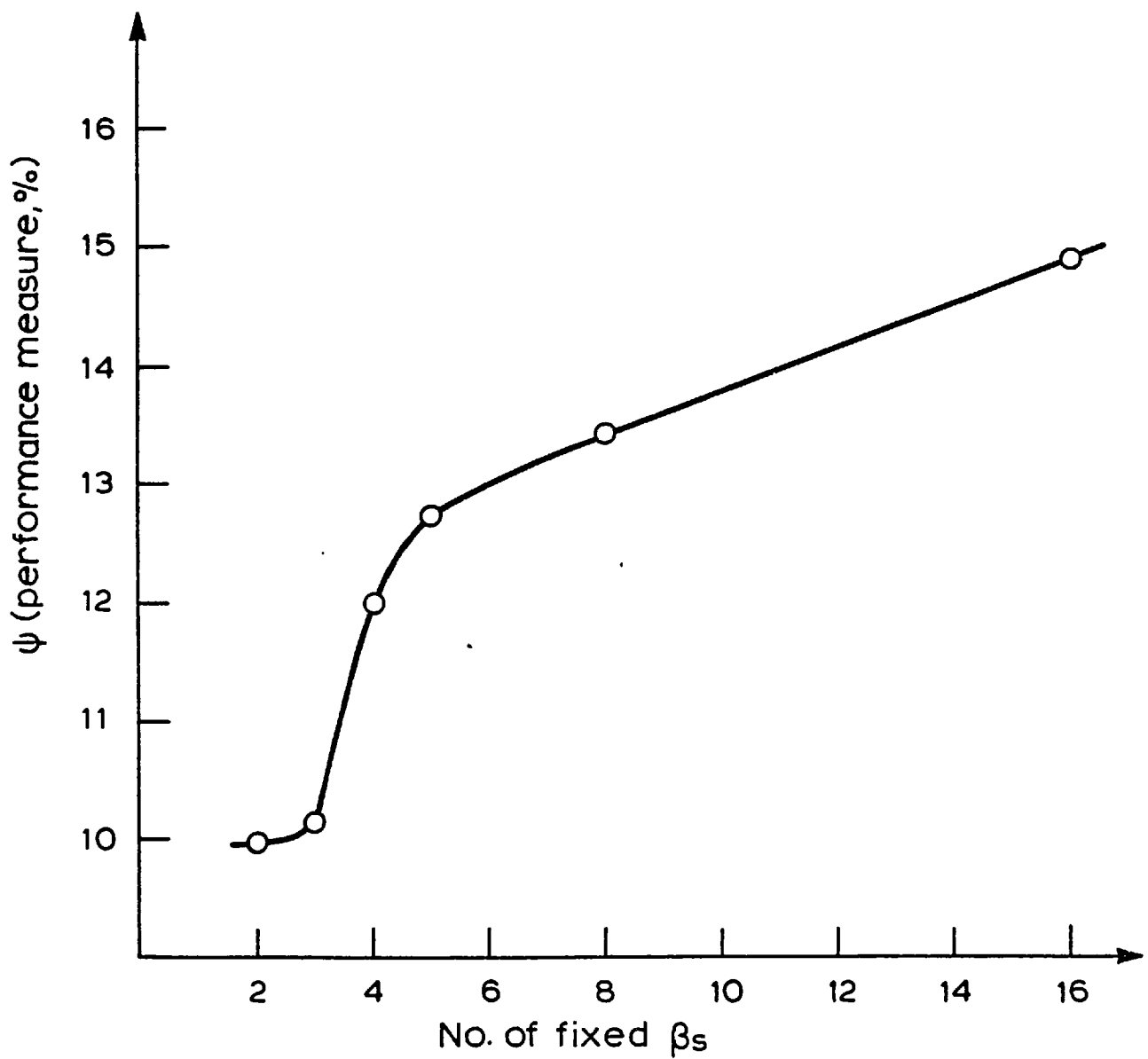


Fig. 5.13 The effect of the fixed β 's number on ψ (optimized-flowmeter designed for three-dimensional flow)

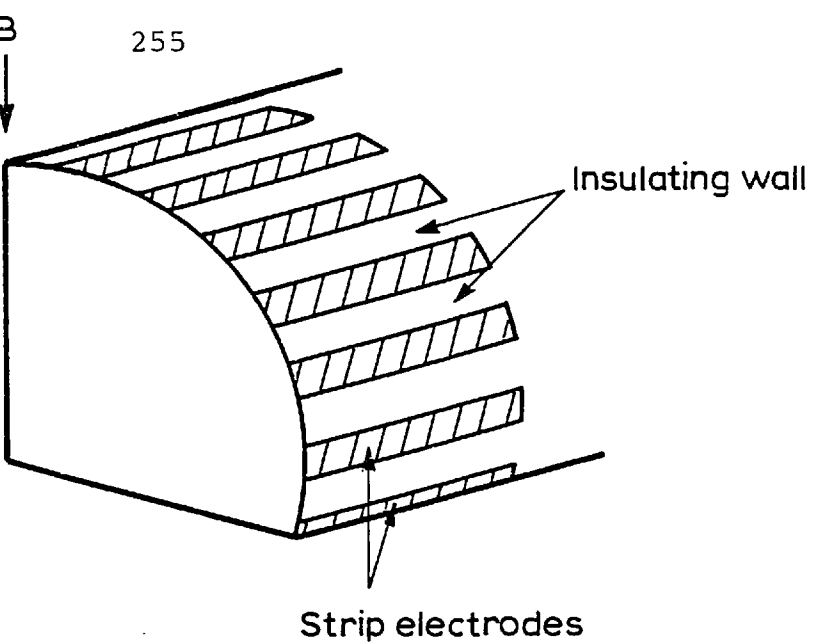


Fig. 6.1 Optimized flowmeter with the strip electrodes

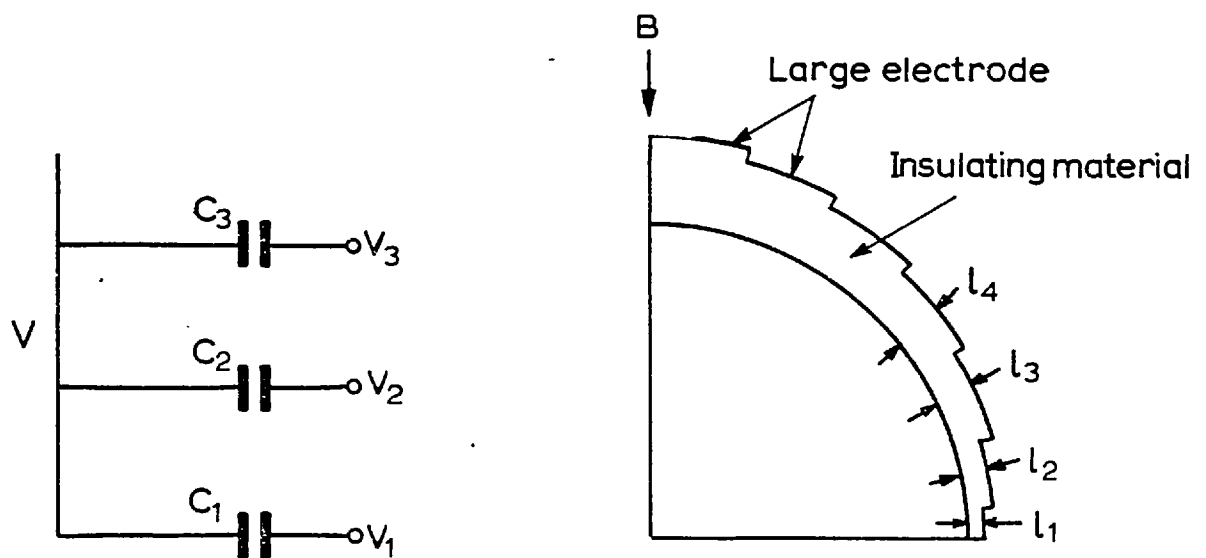


Fig. 6.2 Optimized flowmeter with different insulating wall thickness (different capacitance)

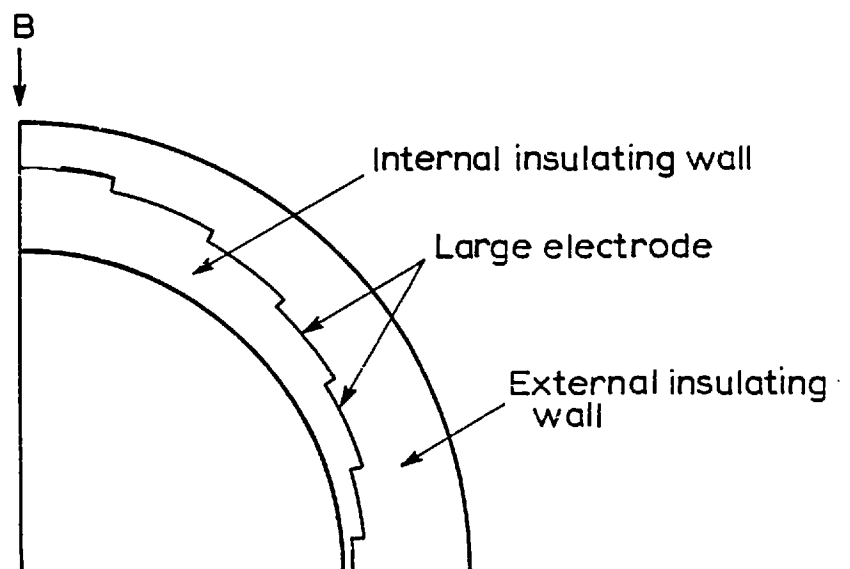


Fig. 6.3 The inner and outer insulating walls of the optimized flowmeter

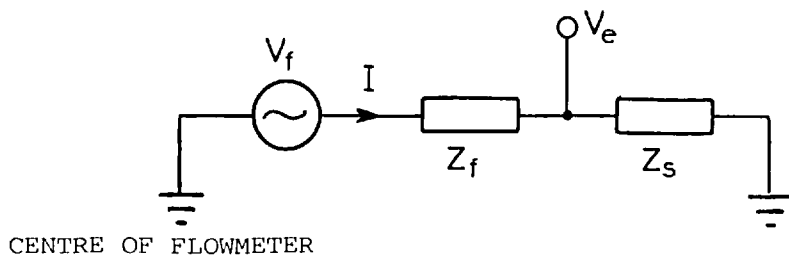


Fig. 6.4 The flowmeter circuit showing the internal and loss impedance

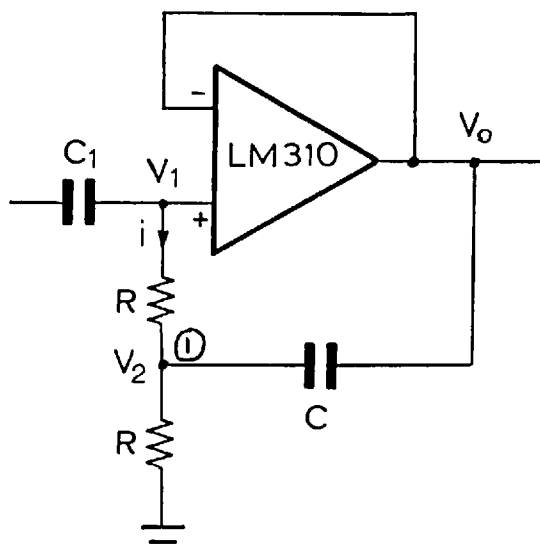


Fig. 6.5 Voltage follower circuit for half flowmeter

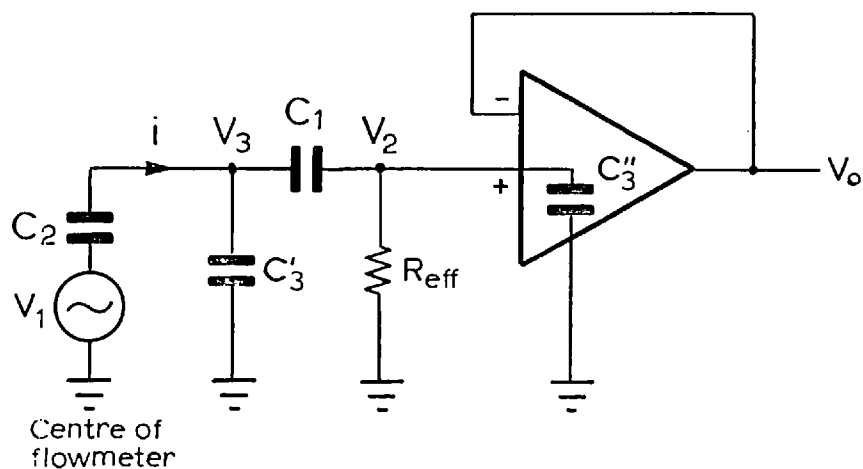
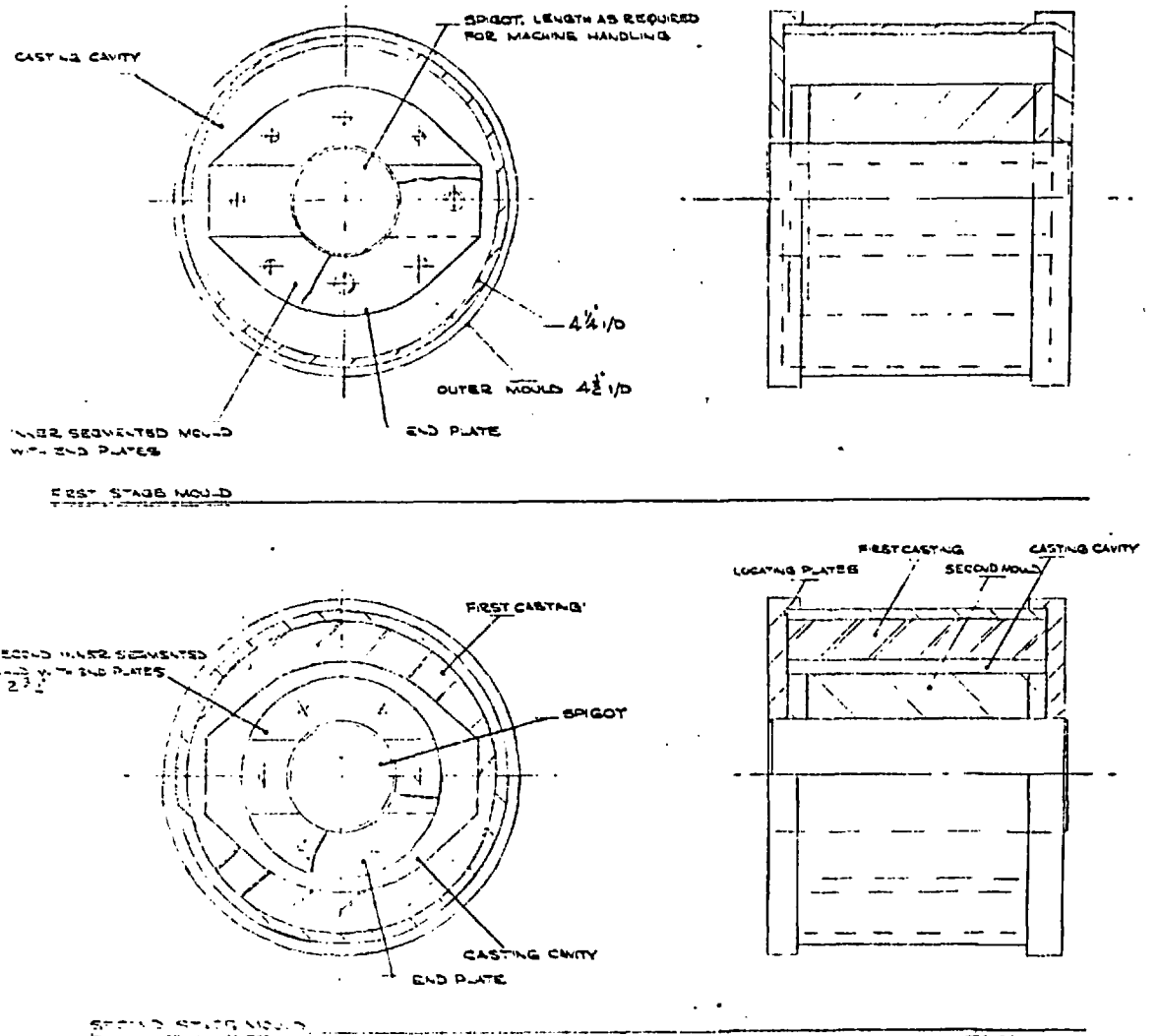


Fig. 6.6 The equivalent circuit of the contactless flowmeter

3 SDB C. EMA
11.12.1974

REF ID: A14194
REC'D: 2 NOV 1965
PAGE: 2 OF 2
DEC MM: 2 0.05MM
DEC IN: 2 0.05IN



NOTE:- BETWEEN CASTING STAGES 1 & 2
A COATING OF ELECTROLYTIC PAINT IS TO BE APPLIED 3/16" IN
ON THE INNER SURFACE OF FIRST CASTING.
IT IS IMPORTANT THAT THE COMPLETE ASSEMBLY IS SYMMETRICAL
CASTING MATERIAL ALUMINUM 15 HV 15
RELEASE AGENT FOR MOULDS SILICONE SPRAY
THE O.D. & I.D. TO BE MACHINED TO FINAL SIZE

Fig. 6.7 Mould of casting and constructing of contactless flowmeter electrode section

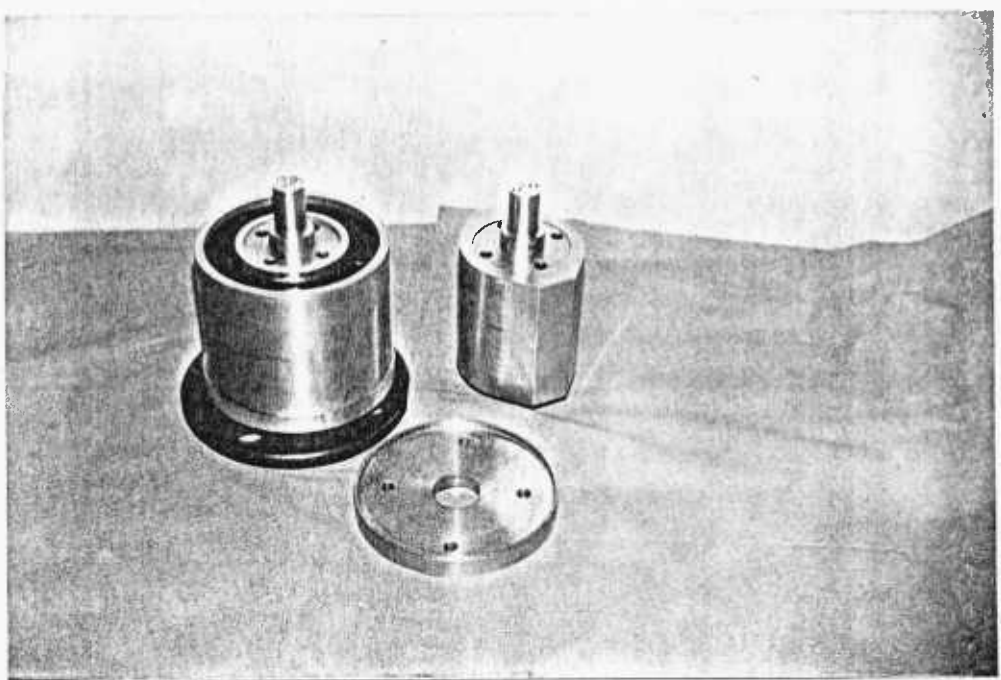


Fig. 6.8 The casting mould assembly

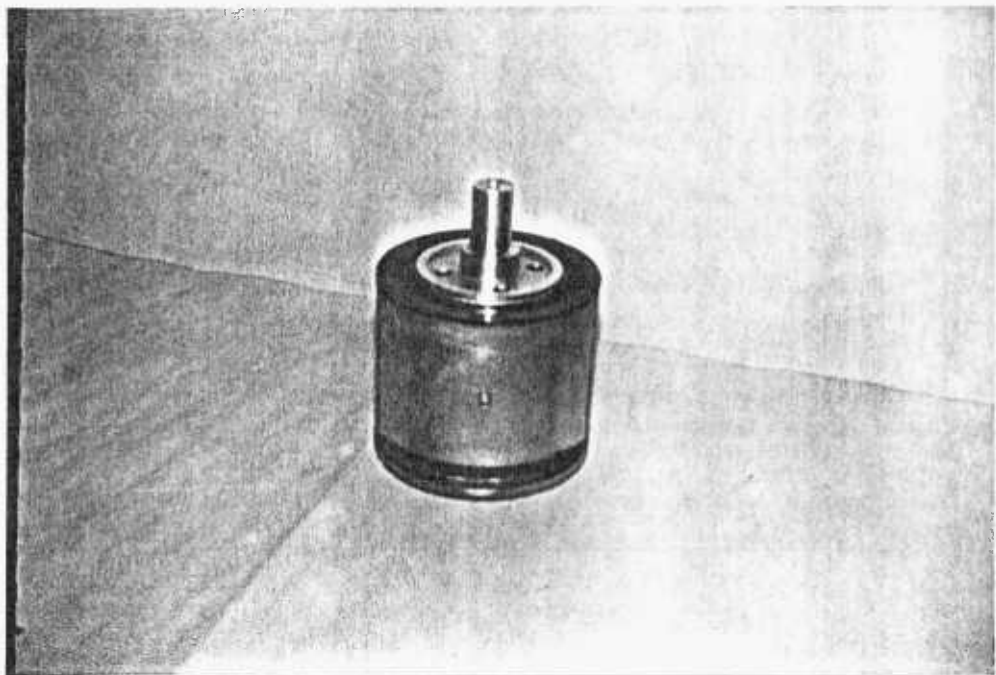


Fig. 6.9 Cast Araldite with the circular core

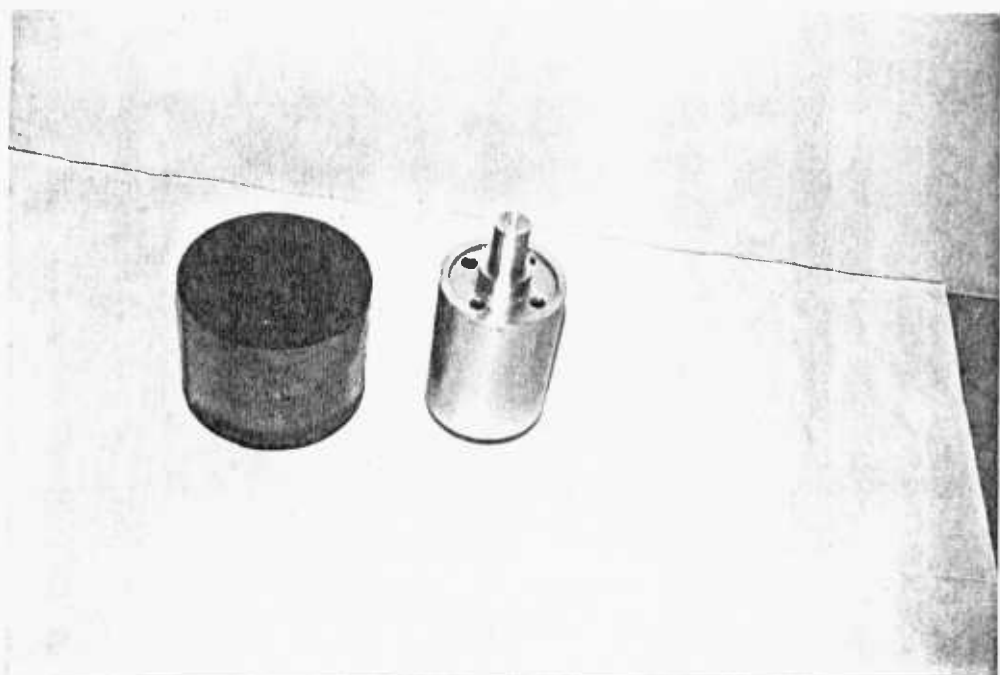


Fig. 6.10 The resulting-cast Araldite

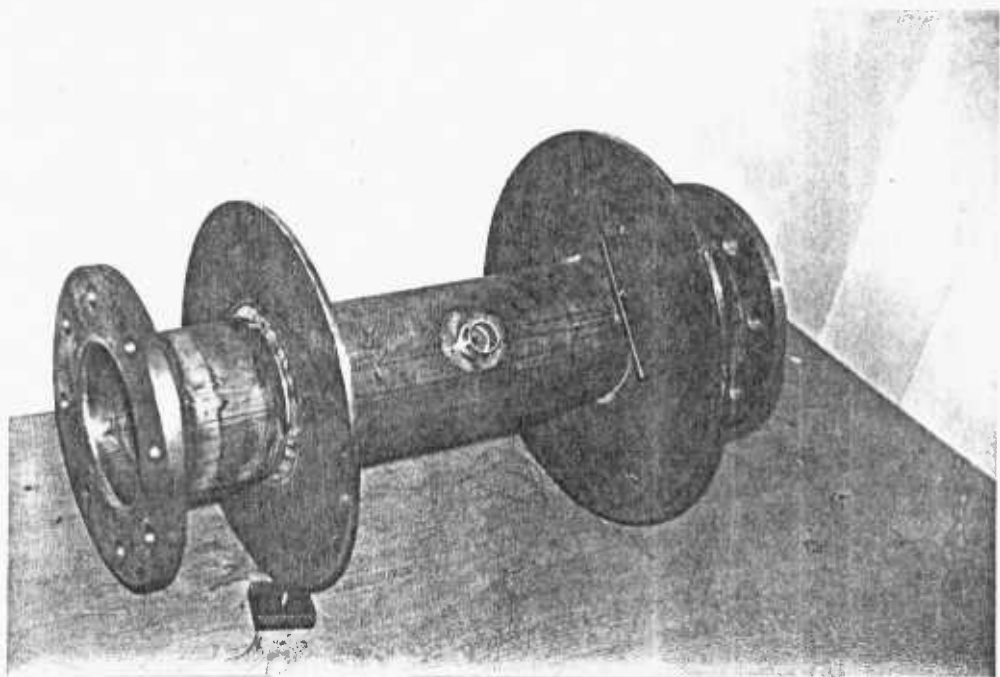


Fig. 6.11 Bare-flow tube for fabricating the optimized flowmeter

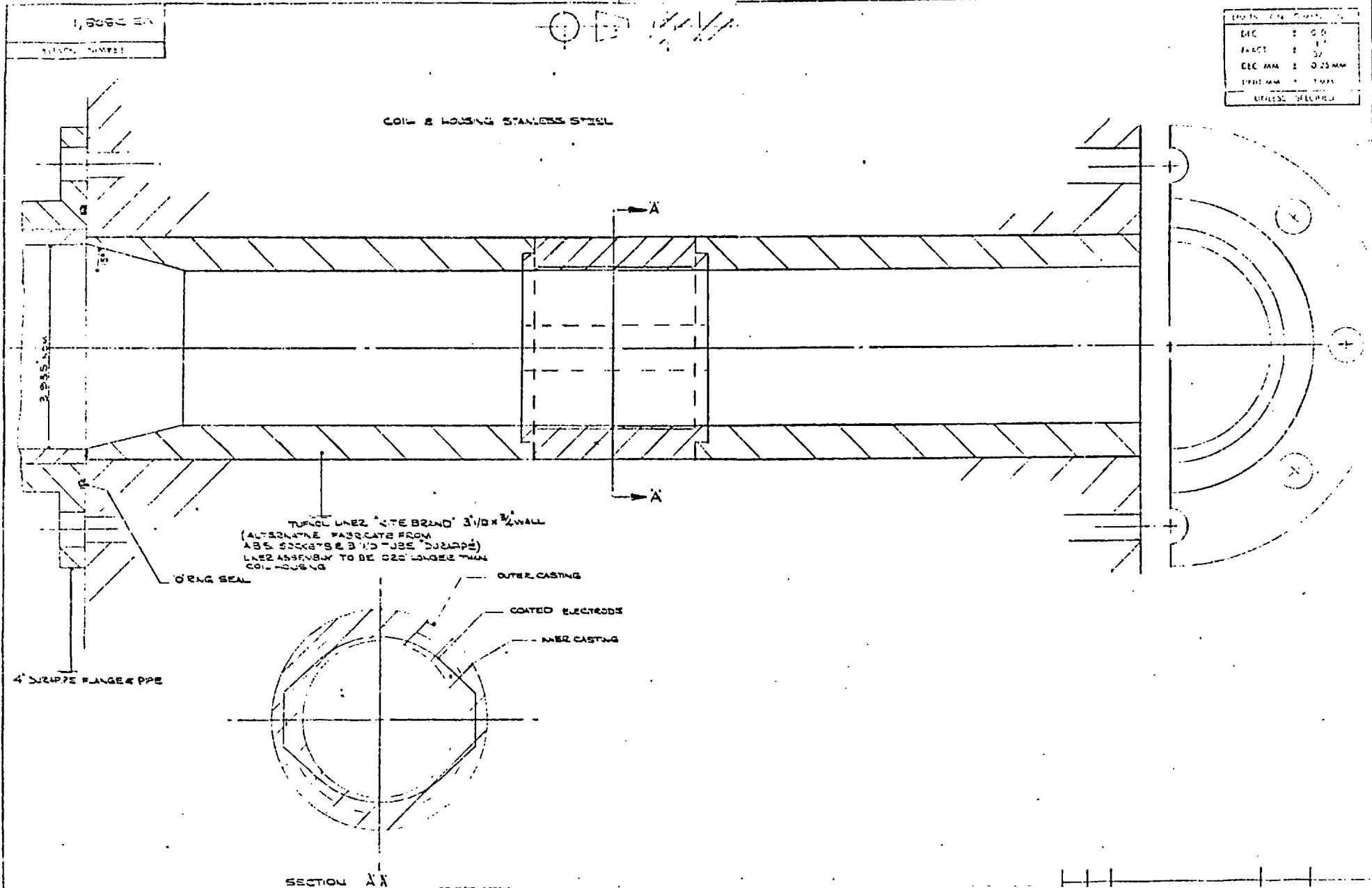


Fig. 6.12 Construction of optimized-contactless flowmeter

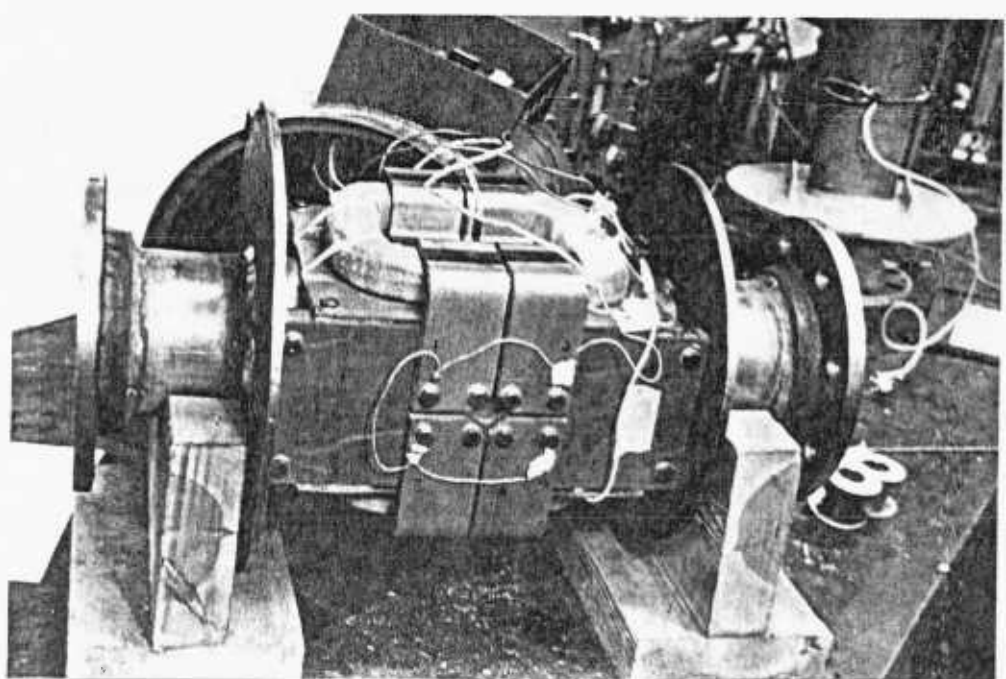


Fig. 6.13 Stage of fixing coils and yoke for the optimized-contactless flowmeter

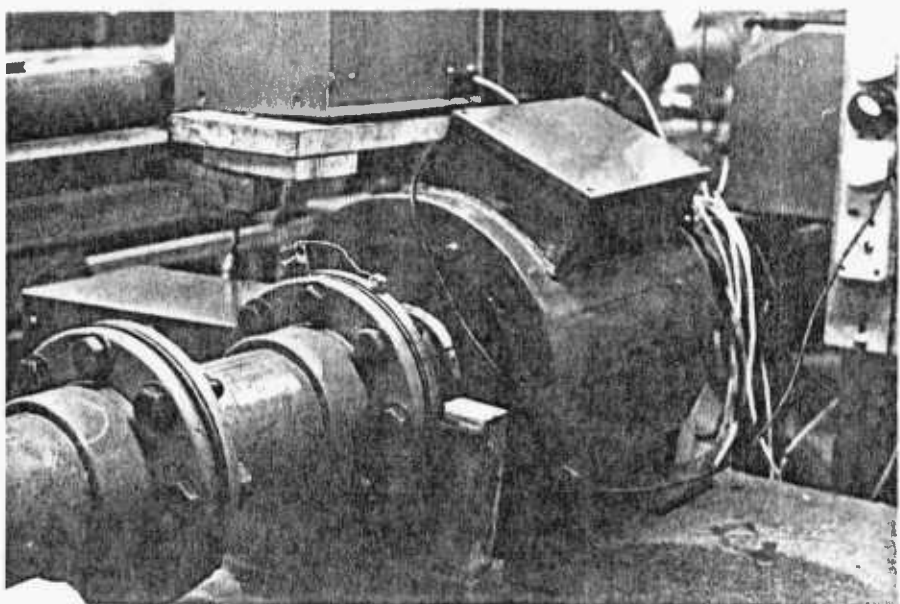


Fig. 7.1 Optimized-contactless flowmeter in 100 mm ID flow rig

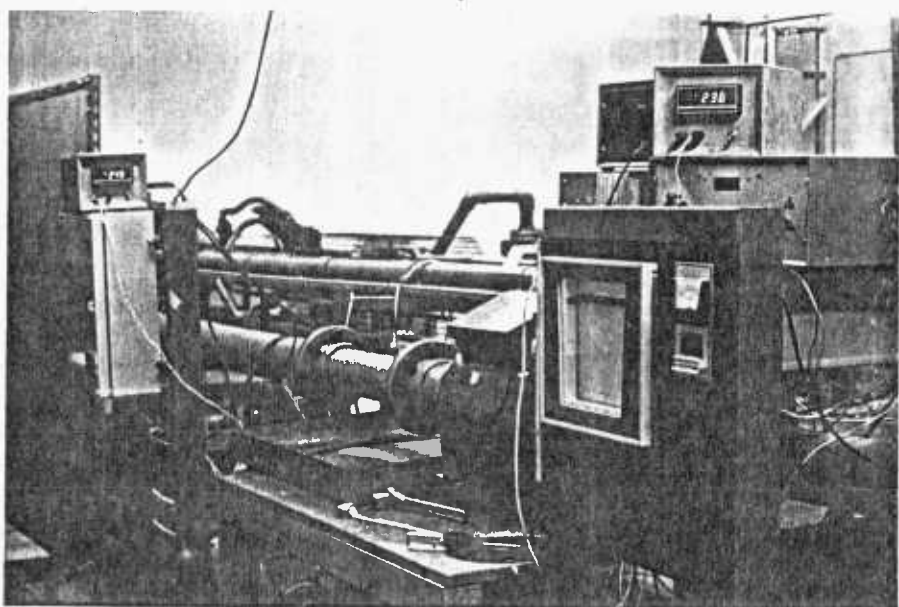


Fig. 7.2 Optimized-contactless flowmeter and instrumentation

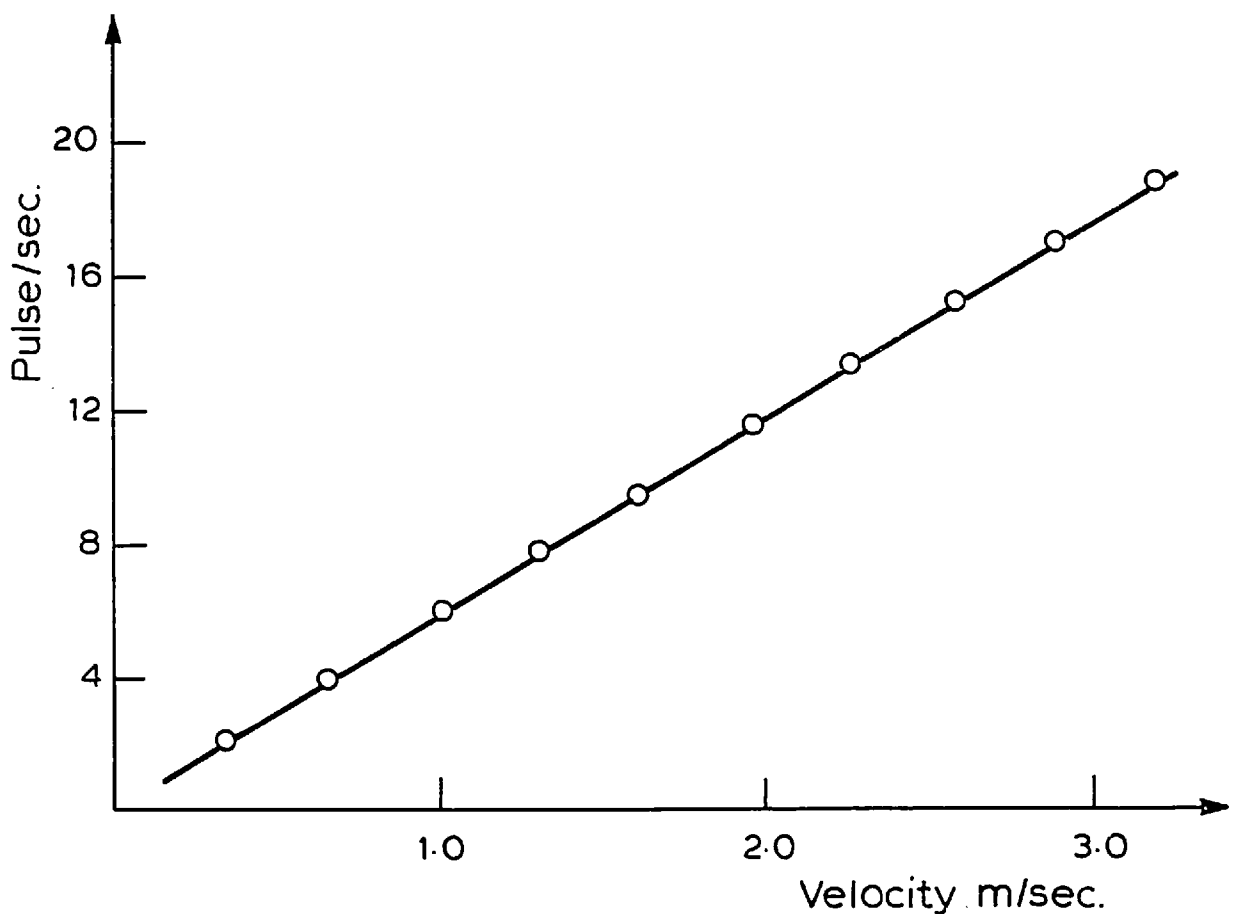


Fig. 7.3 Linearity of optimized-contactless flowmeter (converter-scale 1)

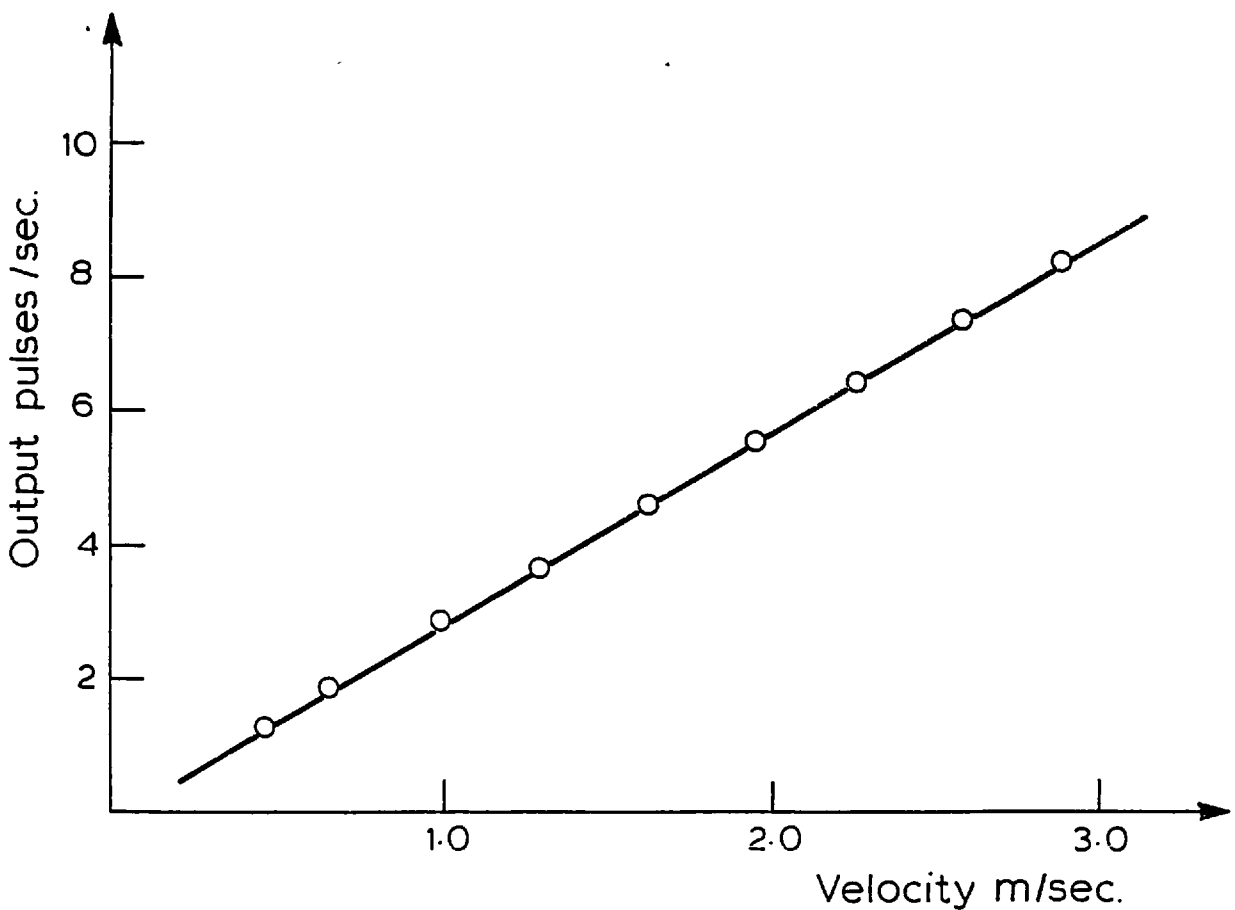


Fig. 7.4 Linearity of optimized-contactless flowmeter (converter-scale 2)

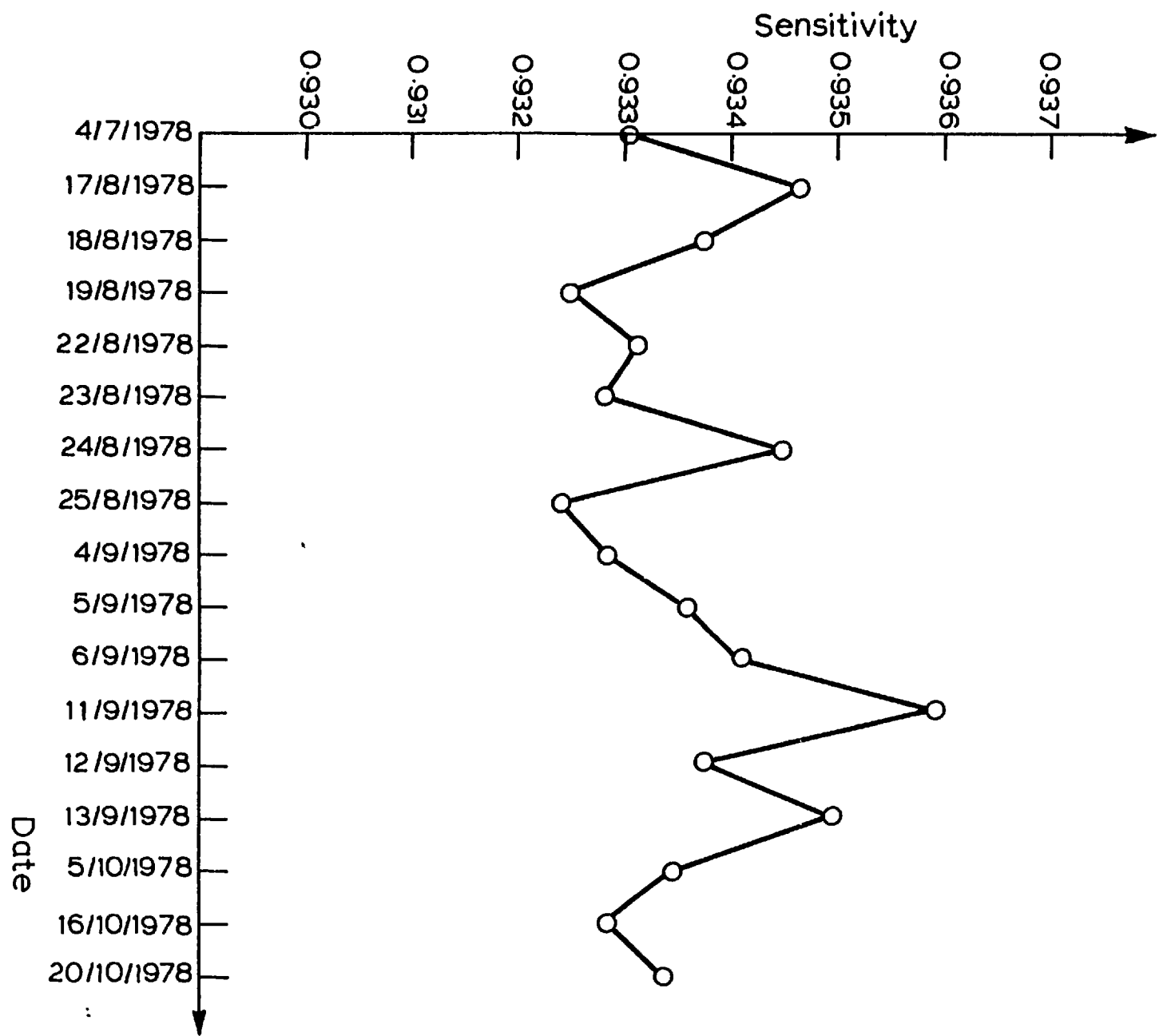


Fig. 7.5 Graph showing the repeatability of the optimized-contactless flowmeter

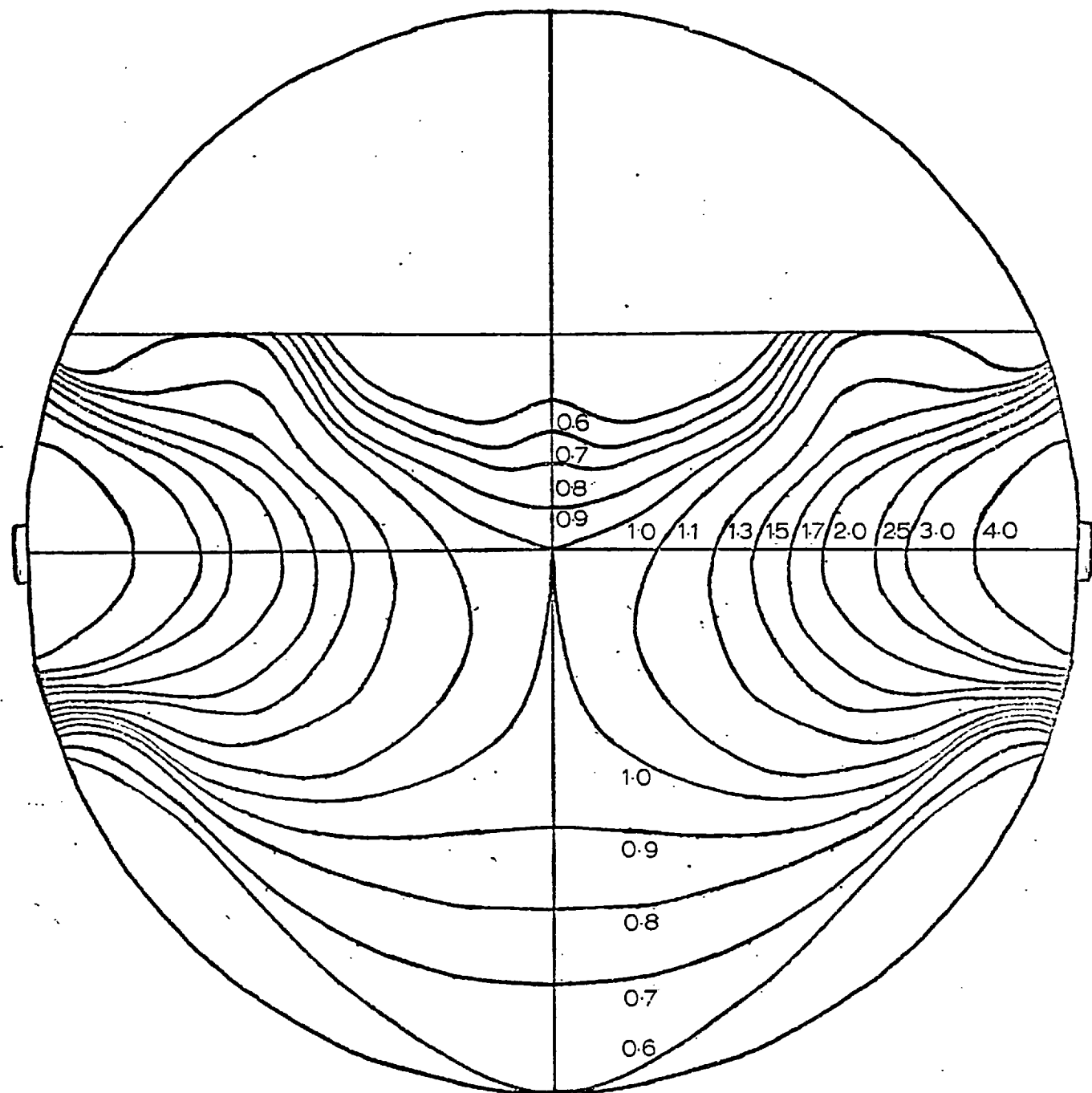


Fig. C.1 Weight function distribution for Type 1 flowmeter (with point electrodes) when a quarter of the flow tube is empty ($w_c = 0.031$)

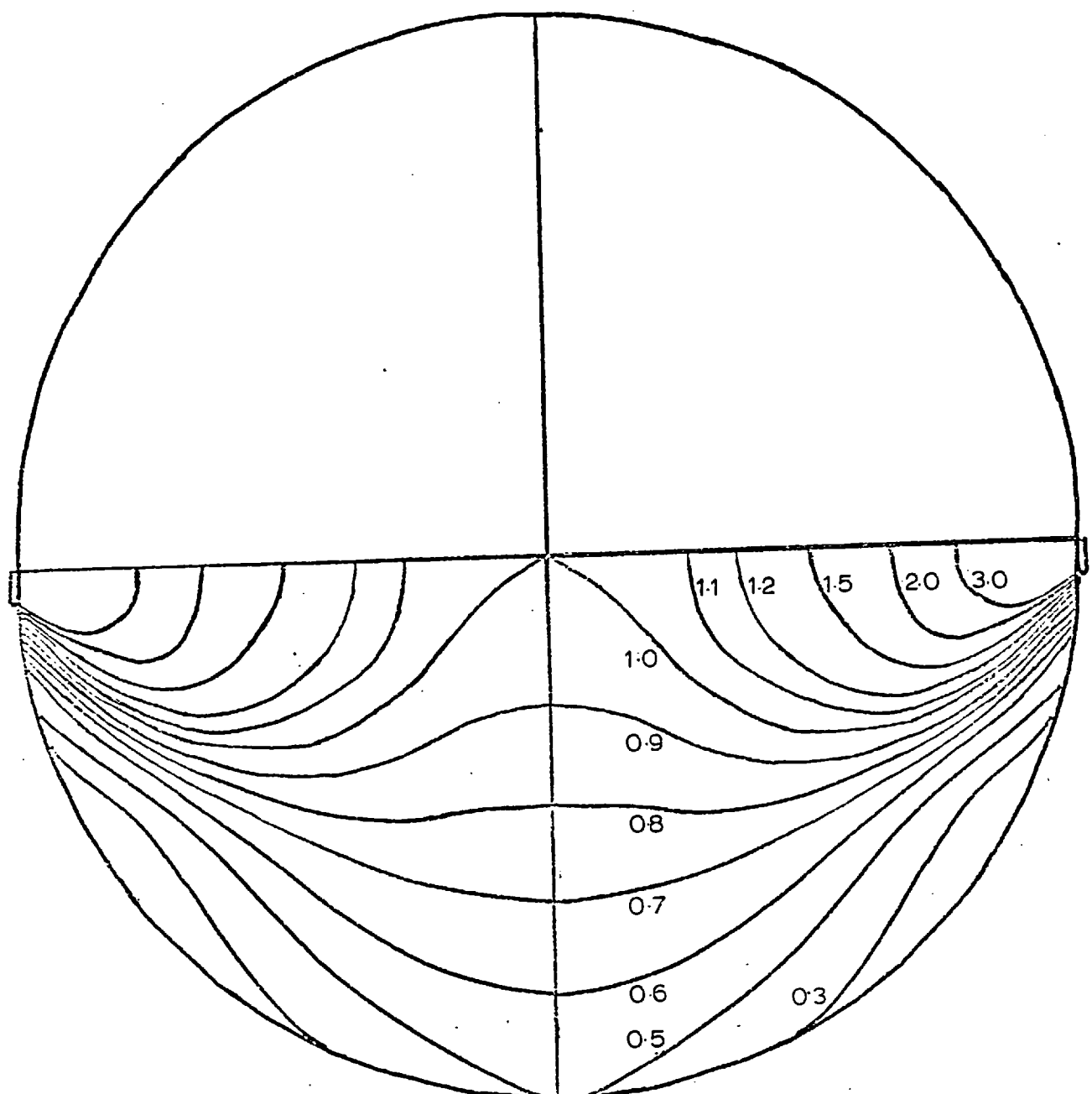


Fig. C.2 Weight function distribution for Type 1 flowmeter (with point electrodes) when half the flow tube is full ($w_c = 0.056$)

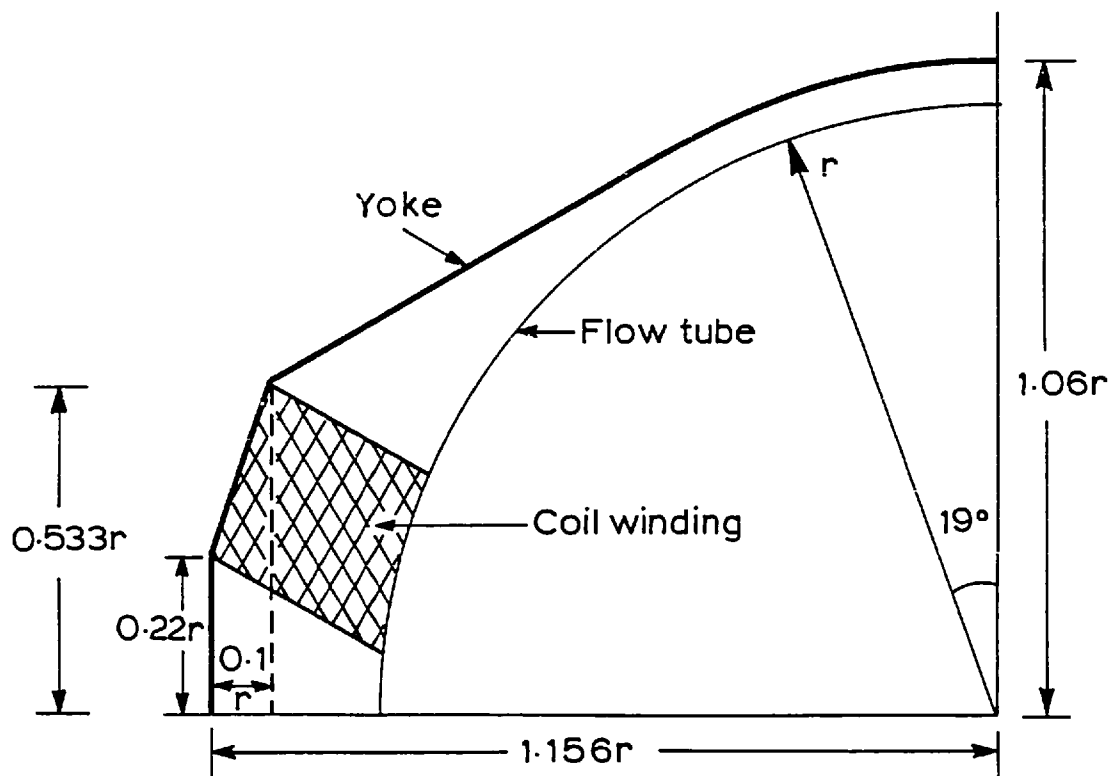


Fig. D.1 The large flowmeter assembly

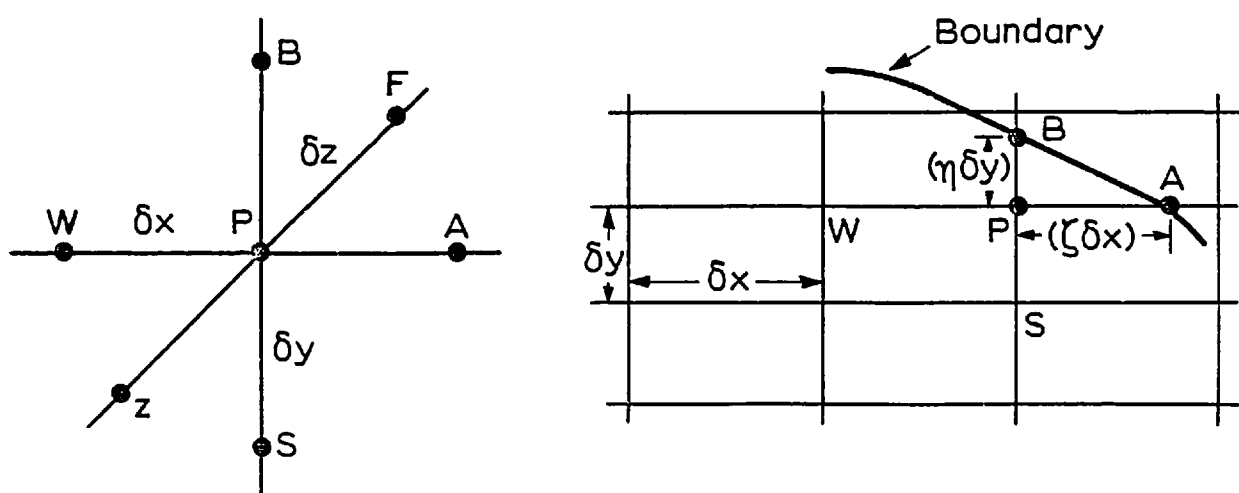


Fig. D.2 Notation for the mesh given in Appendix D

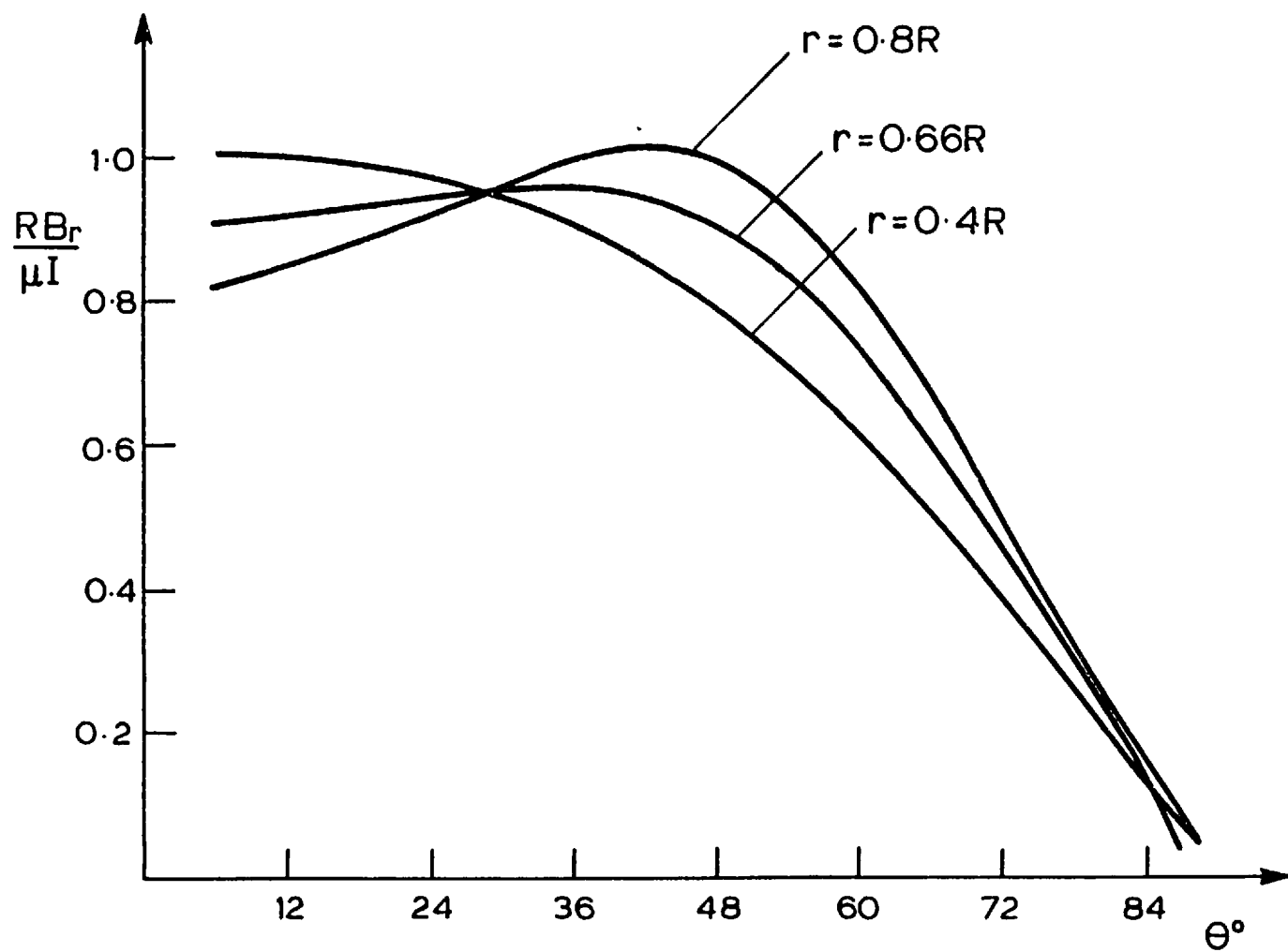


Fig. D.3a Three-dimensional solution for the magnetic field - radial component (large flowmeter)

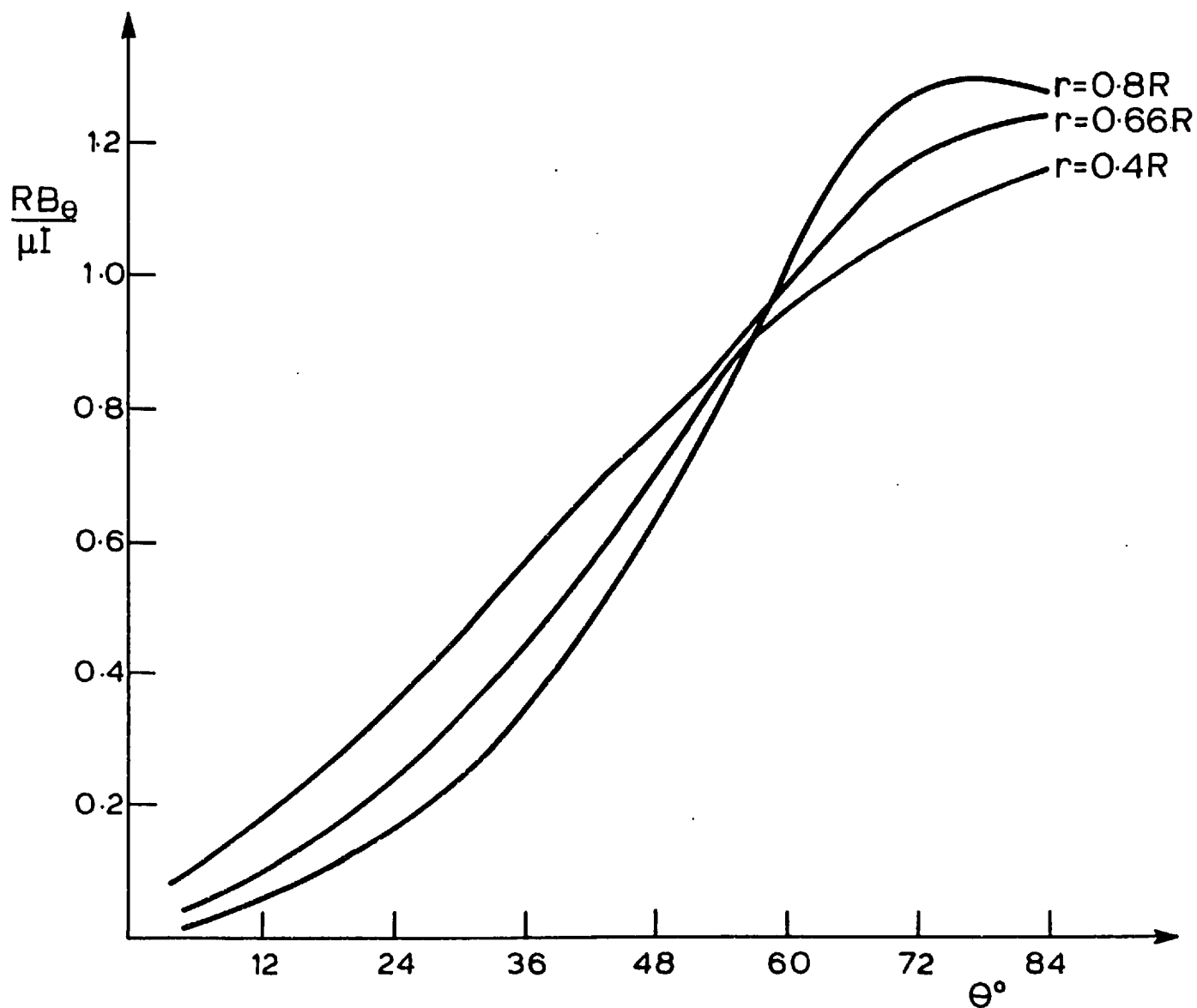


Fig. D.3b Three-dimensional solution for the magnetic field - circumferential component (large flowmeter)

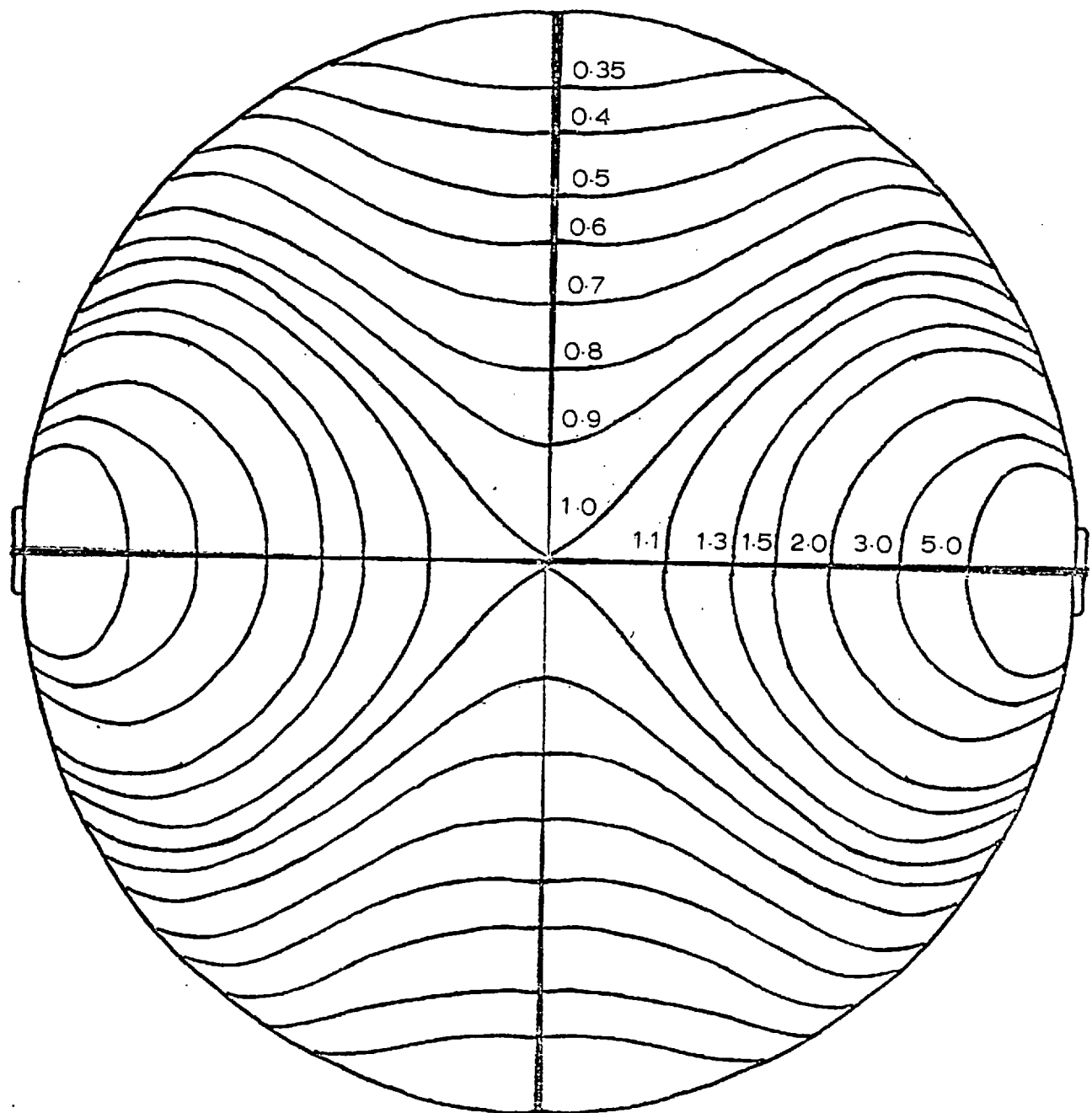


Fig. D.4 Weight function distribution for the large flowmeter with point electrodes ($w_c = 0.074$)

APPENDIX ATHREE-DIMENSIONAL SOLUTION OF
FLUX POTENTIAL DISTRIBUTION

The boundary condition at surface (ABCD) along the axial direction x could be divided into two parts: Part 1 when $0 \leq x \leq x_1$, the value of (γ) is assumed equal to 1; Part 2 when $x_1 \leq x \leq (L_1 + x_1)$, the value of (γ) is assumed to drop exponentially. The general form is:-

$$\gamma = e^{Ax} + B - 1$$

$$\text{at } x = x_1, \gamma = 1$$

$$\text{at } x = (x_1 + L_1), \gamma = 0$$

Therefore:-

$$\gamma = e^{\ln 2 \left[-\frac{x}{L_1} + 1 + \frac{x_1}{L_1} \right]} - 1$$

Hence the boundary conditions for surface (ABCD) at $y = L_2$:-

$$f(x) = 1$$

$$0 \leq x \leq x_1$$

$$f(x) = e^{\ln 2 \left[-\frac{x}{L_1} + 1 + \frac{x_1}{L_1} \right]} - 1 \quad x_1 \leq x \leq (L_1 + x_1) \quad \} \quad (1)$$

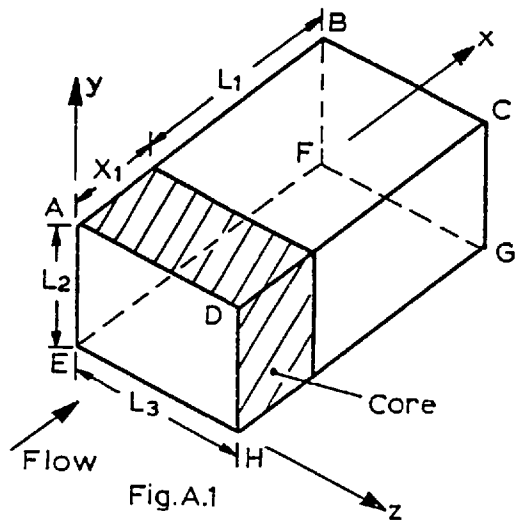


Fig.A.1

The rest of the boundary conditions are as follows:-

$$\text{at } y = 0 \quad \gamma = 0 \quad (2)$$

$$\text{at } x = \pm (x_1 + L_1) \quad \gamma = 0 \quad (3)$$

$$\text{at } z = \pm L_3 \quad \gamma = 0 \quad (4)$$

Laplace equation $\nabla^2 \gamma = 0 = \frac{\partial^2 \gamma}{\partial x^2} + \frac{\partial^2 \gamma}{\partial y^2} + \frac{\partial^2 \gamma}{\partial z^2}$ has to be solved.
Let the solution of this equation is of the product form as follows:-

$$\gamma_p = X \cdot Y \cdot Z \quad (5)$$

This equation becomes:-

$$-\frac{X''}{X} = \frac{Y''}{Y} + \frac{Z''}{Z} = K_1^2$$

Therefore:-

$$X'' + K_1^2 X = 0 \quad (6)$$

and:-

$$-\frac{Z''}{Z} = \left(\frac{Y''}{Y} - K_1^2 \right) = K_2^2$$

Therefore:-

$$Z'' + K_2^2 Z = 0 \quad (7)$$

Put $K_3^2 = K_1^2 + K_2^2$. Therefore:-

$$Y'' - K_3^2 Y = 0 \quad (8)$$

Solving Equations (6), (7) and (8) and substituting them in Equation (5), we obtain:-

$$\gamma = (A \cos K_1 x + B \sin K_1 x)(C \cos K_2 z + D \sin K_2 z) .$$

$$. (E \sinh K_3 y + F \cosh K_3 y) \quad (9)$$

From the boundary condition of Equation (3), the following are obtained:-

$$B = 0 \quad \text{and} \quad A \cos K_1 (x_1 + L_1) = 0$$

Therefore:-

$$K_1 = \frac{\left(n + \frac{1}{2}\right) \pi}{(L_1 + x_1)} \quad n = 0, 1, 2, \dots$$

Therefore:-

$$x = x_n = A_n \cos \frac{\left(n + \frac{1}{2}\right) \pi x}{(L_1 + x_1)} \quad (10)$$

Also from Equation (4) we obtain:-

$$D = 0 \quad \text{and} \quad C \cos K_2 L_3 = 0$$

Therefore:-

$$K_2 = \left(m + \frac{1}{2} \right) \frac{\pi}{L_3} \quad m = 0, 1, 2, \dots$$

Therefore:-

$$Z = Z_m = C_n \cos \left[\frac{\left(m + \frac{1}{2} \right) \pi z}{L_3} \right] \quad (11)$$

Since $K_3^2 = K_1^2 + K_2^2$, therefore:-

$$K_3 = \sqrt{K_1^2 + K_2^2} = \pi \sqrt{\left(\frac{\left(n + \frac{1}{2} \right)}{(x_i + L_1)} \right)^2 + \left(\frac{\left(m + \frac{1}{2} \right)}{L_3} \right)^2} \quad (12)$$

By applying the boundary condition of Equation (2), the following are obtained:-

$$F = 0 \quad \text{and} \quad Y = Y_{nm} = E_{nm} \sinh K_3 y \quad (13)$$

Writing $a_{nm} = A_n C_n E_{nm}$.

Substituting Equations (10), (11) and (13) in Equation (9), the desired solution is achieved in the form:-

$$\gamma(x, y, z) = \sum_{n=0}^{\infty} \sum_{m=0}^{\infty} a_{nm} \cdot \cos \frac{\left(n + \frac{1}{2}\right) \pi x}{(L_1 + x_1)} \cdot \\ \cdot \cos \frac{\left(m + \frac{1}{2}\right) \pi z}{L_3} \cdot \sinh K_3 y \quad (14)$$

We have to determine the coefficient a_{nm} in such a way that the remaining condition of Equation (1) is satisfied. By introducing the abbreviation:-

$$c_{nm} = a_{nm} \sinh K_3 L_2$$

this condition takes the following form:-

$$f(x) = \sum_{n=0}^{\infty} \sum_{m=0}^{\infty} c_{nm} \cos \left\{ \frac{\left(n + \frac{1}{2}\right) \pi x}{(L_1 + x_1)} \right\} \cdot \cos \left\{ \frac{\left(m + \frac{1}{2}\right) \pi z}{L_3} \right\} \quad (15)$$

Thus, c_{nm} are the coefficients of the double Fourier cosine-series expansion for $f(x)$ over the surface (ABCD).

By multiplying both sides of Equation (15) by:-

$$\left[\cos \left\{ \frac{\left(n + \frac{1}{2}\right) \pi x}{(L_1 + x_1)} \right\} \cdot \cos \left\{ \frac{\left(m + \frac{1}{2}\right) \pi z}{L_3} \right\} \right]$$

and then integrate over the surface (ABCD), the following expression is obtained:-

$$\int_0^{(L_1 + x_1)} \int_0^{L_3} f(x) \cdot \cos \left(\frac{\left(n + \frac{1}{2}\right) \pi x}{(L_1 + x_1)} \right) \cdot \cos \left(\frac{\left(m + \frac{1}{2}\right) \pi z}{L_3} \right) dx dz =$$

$$= \sum_{n=0}^{\infty} \sum_{m=0}^{\infty} c_{nm} \int_0^{(x_1 + L_1)} \int_0^{L_3} \cos^2 \left(\frac{\left(n + \frac{1}{2}\right) \pi x}{(L_1 + x_1)} \right)$$

$$\cdot \cos^2 \left(\frac{\left(m + \frac{1}{2}\right) \pi z}{L_3} \right) dx dz$$

Therefore:-

$$c_{nm} = \frac{4}{L_3 (L_1 + x_1)} \int_0^{(x_1 + L_1)} \int_0^{L_3} f(x) \cos \left(\frac{\left(n + \frac{1}{2}\right) \pi x}{(x_1 + L_1)} \right)$$

$$\cdot \cos \left(\frac{\left(m + \frac{1}{2}\right) \pi z}{L_3} \right) dx dz$$

$$c_{nm} = \frac{4 (-1)^m}{\pi (L_1 + x_1) \left(m + \frac{1}{2}\right)} \int_0^{(x_1 + L_1)} f(x) \cos \left(\frac{\left(n + \frac{1}{2}\right) \pi x}{(x_1 + L_1)} \right) dx$$

Substituting $f(x)$ by the Fourier series of Equation (1), we get:-

$$c_{nm} = \left[2G \sin \theta - G(-1)^n \right] + \\ + \left[P \left\{ \frac{E_1 \cdot E_3 \cdot (-1)^n}{Q} - \frac{E_2 \left\{ \frac{\left(n + \frac{1}{2} \right)}{x_1 + L_1} \sin \theta - \frac{\ln 2}{L_1} \cos \theta \right\}}{Q} \right\} \right]$$

where:-

$$\theta = \frac{\left(n + \frac{1}{2} \right) \pi x_1}{x_1 + L_1}$$

$$G = \frac{4(-1)^m}{\pi^2 \left(m + \frac{1}{2} \right) \left(n + \frac{1}{2} \right)}$$

$$P = \frac{4(-1)^m e^{\left(1 + \frac{x_1}{L_1} \right) \ln 2}}{\pi (x_1 + L_1) \left(m + \frac{1}{2} \right)}$$

$$Q = \left(\frac{\ln 2}{L_1} \right)^2 + \frac{\left(n + \frac{1}{2} \right)^2 \pi^2}{(x_1 + L_1)^2}$$

$$E_1 = e^{-\frac{\ln 2 (x_1 + L_1)}{L_1}}$$

$$E_2 = e^{-\frac{x_1 \ln 2}{L_1}}$$

$$E_3 = \frac{\left(n + \frac{1}{2}\right) \pi}{x_1 + L_1}$$

Hence the general form is:-

$$Y(x, y, z) = \sum_{n=0}^{\infty} \sum_{m=0}^{\infty} c_{nm} \cdot \cos \left(\frac{\left(n + \frac{1}{2}\right) \pi x}{(x_1 + L_1)} \right) \cdot$$

$$\cdot \cos \left(\frac{\left(m + \frac{1}{2}\right) \pi z}{L_3} \right) \cdot \frac{\sinh K_3 y}{\sinh K_3 L_2}$$

APPENDIX BTWO-DIMENSIONAL VIRTUAL CURRENT FOR
NON-SYMMETRIC LARGE ELECTRODES

The following two-dimensional analytical solution of the virtual current was derived with the help of Dr. J. Hemp*. If a , b , c and d are complex numbers defining the position of four points on a circle and (A) is a complex number, then the following term is a possibility for the virtual current $g'(z)$ to be defined, because this term has the right type of singularity at the points a , b , c and d to represent the edge of the large electrodes.

$$g'(z) = \frac{A}{[r_1 e^{i\theta_1} \cdot r_2 e^{-i\theta_2} \cdot r_3 e^{i\theta_3} \cdot r_4 e^{-i\theta_4}]^{1/2}} \quad (1)$$

where r_1 , θ_1 , r_2 , θ_2 , ... are the polar coordinates as illustrated in Fig. (B.1). As shown in Fig. (B.2), we have got:-

$$J_r = J_x \cos \theta + J_y \sin \theta$$

$$J_r = \frac{\partial G}{\partial x} \cos \theta + \frac{\partial G}{\partial y} \sin \theta$$

$$\text{but } g'(z) = \frac{\partial G}{\partial x} - i \frac{\partial G}{\partial y}$$

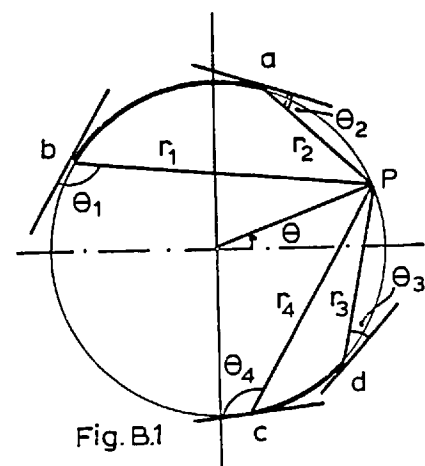


Fig. B.1

* Private communication

and $z = x + iy = e^{i\theta} = \cos \theta + i \sin \theta$

(where $r = \text{unity}$)

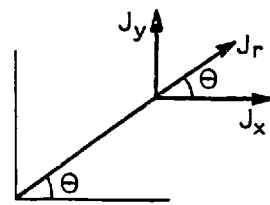


Fig. B.2

Therefore:-

$$g'(z) \cdot z = \left[\cos \theta \frac{\partial G}{\partial x} + \sin \theta \frac{\partial G}{\partial y} \right] + i \left[-\cos \theta \frac{\partial G}{\partial y} + \sin \theta \frac{\partial G}{\partial x} \right]$$

Therefore:-

$$J_r = \operatorname{Re} [g'(z) \cdot z]$$

and:-

$$J_\theta = \operatorname{Im} [g'(z) \cdot z]$$

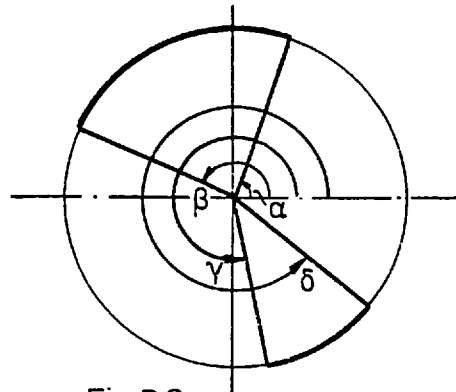


Fig. B.3

The angles α , β , γ and δ of the electrodes are shown in Fig. (B.3).

We must find the value of (A) which satisfies the following boundary conditions for a unit radius:-

$$\left. \begin{aligned} \operatorname{Re} [e^{i\theta} \cdot g'(z)] &= 0 && \text{on the insulator} \\ \operatorname{Im} [e^{i\theta} \cdot g'(z)] &= 0 && \text{on the electrode} \end{aligned} \right\} \quad (2)$$

From Equation (1), we get:-

$$e^{i\theta} \cdot g'(z) = \frac{A}{\sqrt{r_1 r_2 r_3 r_4}} \cdot e^{i\left(\theta - \frac{\theta_1}{2} + \frac{\theta_2}{2} - \frac{\theta_3}{2} + \frac{\theta_4}{2}\right)} \quad (3)$$

By geometry, where point (p) lies between a and d (on the insulator) or in other words $\left[-(2\pi - \delta) < \theta < \alpha\right]$, we get:-

$$\left. \begin{aligned} 2\theta_2 + \theta &= \alpha \\ 2\pi - 2\theta_1 + \theta &= \beta \\ 2\pi - 2\theta_4 - \theta &= 2\pi - \gamma \\ 2\theta_3 - \theta &= 2\pi - \delta \end{aligned} \right\} \quad (4)$$

Substituting the values of α , β , γ and δ from Equation (4) in Equation (3):-

$$e^{i\theta} \cdot g'(z) = \frac{A}{\sqrt{r_1 r_2 r_3 r_4}} e^{i\left[\frac{\alpha + \beta + \gamma + \delta}{4} - \frac{\pi}{2}\right]} \quad (5)$$

When point (p) lies between a and b (i.e. $\alpha < \theta < \beta$), the first of Equation (4) changes to $2\theta_2 - 2\pi + \theta = \alpha$, while the rest of Equation (4) remains the same. Therefore:-

$$e^{i\theta} \cdot g'(z) = \frac{A}{\sqrt{r_1 r_2 r_3 r_4}} e^{i \left[\frac{\alpha + \beta + \gamma + \delta}{4} - \pi + \frac{\pi}{2} \right]} \quad (6)$$

When point (p) lies between b and c (i.e. $\beta < \theta < \gamma$), the second of Equation (4) changes to $\theta - 2\theta_1 = \beta$. Therefore:-

$$e^{i\theta} \cdot g'(z) = \frac{A}{\sqrt{r_1 r_2 r_3 r_4}} e^{i \left[\frac{\alpha + \beta + \gamma + \delta}{4} - \pi + \frac{\pi}{2} \right]} \quad (7)$$

Similarly, when point (p) lies between c and d (i.e. $\gamma < \theta < \delta$), the third of Equation (4) changes to $\theta = \gamma + 2\pi - 2\theta_4$.

Therefore:-

$$e^{i\theta} \cdot g'(z) = \frac{A}{\sqrt{r_1 r_2 r_3 r_4}} e^{i \left[\frac{\alpha + \beta + \gamma + \delta}{4} - \pi + \frac{3\pi}{2} \right]} \quad (8)$$

The value of the complex number A can be rewritten as:-

$$A = iBe^{i \left[-\frac{\alpha + \beta + \gamma + \delta}{4} + \pi \right]} \quad \text{for } r = 1$$

where B is a real number. Since:-

$$e^{i\pi} = -1, \quad e^{i2\pi} = 1, \quad e^{i\pi/2} = i, \quad e^{i3\pi/2} = -i$$

therefore:-

$$e^{i\theta} \cdot g'(z) = \frac{iB}{\sqrt{r_1 r_2 r_3 r_4}}$$

$\begin{bmatrix} 1 \\ i \\ -1 \\ -i \end{bmatrix}$	for $(2\pi - \delta) < \theta < \alpha$
	$\alpha < \theta < \beta$
	$\beta < \theta < \gamma$
	$\gamma < \theta < \delta$

Hence, conditions of Equation (2) are met.

To express $g'(z)$ as a function of (z) , we have to do the following modification. In the rectangle (aeo), see Fig. (B.4):-

$$\left(\frac{\pi}{2} - \theta_2\right) + (\pi - \phi) + \alpha = \pi$$

$$\phi = \alpha + \frac{\pi}{2} - \theta_2$$

and:-

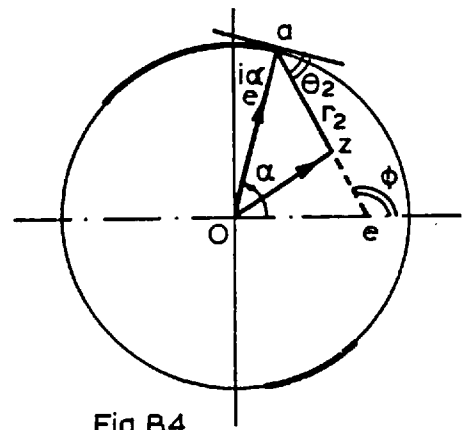


Fig.B.4

$$e^{i\alpha} = z + r_2 e^{i\phi} = z + r_2 e^{i\left(\alpha + \frac{\pi}{2} - \theta_2\right)}$$

Therefore:-

$$r_2 e^{-i\theta_2} = ie^{-i\alpha} (z - e^{i\alpha})$$

In the same way:-

$$r_1 e^{i\theta_1} = -ie^{-i\beta} (z - e^{i\beta})$$

$$r_3 e^{i\theta_3} = -ie^{-i\delta} (z - e^{i\delta})$$

$$r_4 e^{-i\theta_4} = ie^{-i\gamma} (z - e^{i\gamma})$$

Then, Equation (1) becomes:-

$$g'(z) = \frac{iB e^{i\left[\frac{\alpha + \beta + \gamma + \delta}{4} + \pi\right]}}{\left[(z - e^{i\alpha})(z - e^{i\beta})(z - e^{i\gamma})(z - e^{i\delta})\right]^{1/2}} \quad (9)$$

For the special case where the electrodes are symmetric, we have:-

$$\beta = \pi - \alpha$$

$$\gamma = \pi + \alpha$$

$$\delta = 2\pi - \alpha$$

$$(\alpha + \beta + \gamma + \delta) = 4\pi$$

Therefore:-

$$e^{i\left[\frac{\alpha + \beta + \gamma + \delta}{4} + \pi\right]} = e^{i2\pi} = 1$$

Hence, Equation (9) becomes:-

$$g'(z) = \frac{iB}{\left[(z - e^{i\alpha})(z - e^{i\beta})(z - e^{i\gamma})(z - e^{i\delta})\right]^{1/2}} \quad (10)$$

This equation agreed with Bevir's results of the virtual current for symmetric electrodes (Reference 9).

Now the value of the real number (B) is calculated as follows:-

$$J_r = \operatorname{Re} [e^{i\theta} \cdot g'(z)]$$

since the total current from one electrode is equal to unity.
Hence:-

$$\int_{\alpha}^{\beta} J_r d\theta = \int_{\alpha}^{\beta} \operatorname{Re} [e^{i\theta} \cdot g'(z)] d\theta = 1 \quad (\text{for unity radius})$$

Substituting the value of $g'(z)$ of Equation (9) in the above equation, we get:-

$$\frac{1}{B} = \int_{\alpha}^{\beta} \operatorname{Re} \left[\frac{i e^{i\theta} \cdot e^{i \left[\frac{\alpha + \beta + \gamma + \delta}{4} + \pi \right]}}{\left[(z - e^{i\alpha})(z - e^{i\beta})(z - e^{i\gamma})(z - e^{i\delta}) \right]^{1/2}} \right] d\theta \quad (11)$$

The value of B was calculated from this equation by using the computer.

APPENDIX CPARTIALLY EMPTY FLOWMETERS

A numerical analysis was developed to analyse the case when the flowmeter tube is not completely full. It is interesting to examine the characteristics of the electromagnetic flowmeter under this condition. For this particular situation, a design of type 1 flowmeter with point electrodes has been analysed. Two cases have been considered, one where a quarter of the flow tube was empty and the other where the flow tube was half full. The virtual current changed from the distribution for a full tube and it has been determined by assuming the normal component of the virtual current (J_n) at the flat surface of the liquid is zero. This is physically true, since no virtual current flows from the liquid to the air gap which has a high insulating impedance. Using the resulting virtual current, together with the known magnetic field, as previously explained, the value of W is obtained. The plots of these \bar{W} are given for a quarter and a half empty flowmeter in Figs. (C.1) and (C.2) respectively. The latter plot is identical to the plot of the normal point electrode (Fig. (2.24)). This is due to the symmetry in both the virtual current and the magnetic field across the line connecting the electrodes. The weight function non-uniformity (ϵ) of the quarter empty one has been calculated and it was 53.47% which is higher than for the flowmeters with a full pipe.

APPENDIX DLARGE ELECTROMAGNETIC FLOWMETERS

A large electromagnetic flowmeter with point electrodes has been proposed by Flowmetering Instruments Limited, Stroud, Gloucestershire. The design of this type of flowmeter has a different magnetic core shape and size than those discussed earlier. The magnetic field is produced by using a pair of coils wound around the yoke assembly as shown in Fig. (D.1). The flow tube diameter (D) is 300 mm and the core length along the flow direction is 2.22 diameters, while the other dimensions of the core are given in the figure.

The field equations are solved numerically (for cartesian coordinates) using the previous approach (by setting $\gamma = \pm 1$ on the yoke inside the winding area and $\gamma = 0$ on the yoke outside the winding area). In this particular case, the core shape creates a problem of having a curved boundary when using a rectangular mesh. The following expansion of the Laplace equation is used (Cohen⁽¹⁴⁾) :-

$$\nabla^2 \gamma = \frac{1}{\partial x^2} \left[\frac{2\gamma_A}{\zeta(1 - \zeta)} + \frac{2\gamma_W}{1 - \zeta} - \frac{2\gamma_P}{\zeta} \right] + \\ + \frac{1}{\partial y^2} \left[\frac{2\gamma_B}{\eta(1 + \eta)} + \frac{2\gamma_S}{1 + \eta} - \frac{2\gamma_P}{\eta} \right] + \frac{1}{\partial z^2} (\gamma_Z + \gamma_F - 2\gamma_P) = 0$$

The notation used in this equation is given in Fig. (D.2). Then by interpolating the resulting magnetic potential on the tube wall and using these values as boundary conditions, γ can be obtained by solving the Laplace equation inside the

flow tube (Polar Cylindrical Coordinate is used). The resulting magnetic field distribution inside the flow tube is shown in Figs. (D.3a) and (D.3b). By applying this magnetic field together with the virtual current (for point-electrodes), the value of \bar{W} is calculated at the grid points. Fig. (D.4) shows the plot of the weight function of this flowmeter design. Also, the value of (ϵ) has been calculated and it was 62.3%.

PUBLICATIONS

- AL-KHAZRAJI, Y., AL-RABEH, R., BAKER, R. and HEMP, J.
"Comparison of the effect of a distorted profile
on electromagnetic, ultrasonic and differential
pressure flowmeters".
FLOMEKO 1978, IMEKO-Conference on flow measurement
of fluids, Martinhal Centre Groningen/The Netherlands.
September 11 to 15, 1978
- AL-KHAZRAJI, Y. and BAKER, R.
"Analysis of the performance of three large electrode
electromagnetic flowmeters".
To be published in : Journal of Physics, D-Applied
Physics.
- AL-KHAZRAJI, J., AL-RABEH, R. and HEMP, J.
"New design concepts for electromagnetic and ultra-
sonic flowmeters for the process industries".
To be presented at : IMEKO Tokyo Flow Symposium, 1979.
The Society of Instrument and Control Engineers,
Tokyo, Japan, November 13 to 16, 1979.
- AL-KHAZRAJI, Y. and HEMP, J.
"Electromagnetic flowmeters and methods for measuring
flow".
British patent application made through NRDC, 1979.